PADERBORN UNIVERSITY

Faculty of Computer Science, Electrical Engineering and Mathematics

Model-Predictive Direct Self-Control for Optimal Voltage Utilization of Permanent Magnet Synchronous Machine Drives

From the Faculty of Electrical Engineering, Computer Science and Mathematics of Paderborn University

to obtain the academic degree

Doctor of Engineering (Dr.-Ing.)

approved dissertation
by

Mario Peña López

First Reviewer: Prof. Dr.-Ing. Joachim Böcker
Second Reviewer: Prof. Dr. Fernando Briz

Date of the dissertation defense: 21.09.2026

Paderborn 2026

Diss. EIM-E/405

Acknowledgements

This dissertation represents the outcome of a significant portion of my work as a research associate at the Department of Power Electronics and Electrical Drives (LEA) at Paderborn University, carried out within the framework of a research project commissioned by Volkswagen AG. While the project's development and eventual success were driven by my own efforts and independent contributions, the guidance and support surrounding this work were essential. Consequently, I would like to take this opportunity to thank those who contributed to this environment.

I am especially grateful to the supervising team: Prof. Dr.-Ing. Joachim Böcker (then head of the department, now emeritus), Dr.-Ing. Michael Meyer (project lead at Volkswagen AG), and my *Doktorvater*, Prof. Dr.-Ing. Oliver Wallscheid (then supervisor of the electric drives research within the group, now head of the IAS group at the University of Siegen). This project evolved through continuous and constructive dialogue with them, consistently guided by the goal of aligning academic research with the development objectives of our industrial partner. Beyond their technical expertise, I am especially appreciative of the opportunity they gave me to pursue this research and the examples they set in terms of character, rigour and leadership, which are lessons I will carry forward in my professional journey.

My journey to Paderborn would not have been possible without the opportunity to participate in the excellent Erasmus Mundus Joint Master Degree in Sustainable Transportation and Electric Power Systems. The technical and personal insights I gained through this program, both from colleagues and teaching staff, have proved invaluable and continue to influence both my personal and professional development. I would like to extend particular thanks to Prof. Pablo Garcia of the University of Oviedo, who was not directly involved in this dissertation, but was my first mentor and encouraged me to consider a research path during the early years of my undergraduate studies.

I am also thankful to the colleagues of the LEA department. The environment they created and continue to foster made the daily challenges of research both manageable and enjoyable.

Last but not least, I would like to thank my family and my partner. Since I cannot say enough about them, I will avoid saying too much. Their unwavering support, patience, and encouragement carried me to where I am.

Abstract

Electric drives are an integral part of transportation and industrial applications, and their importance continues to grow. The optimization of voltage utilization can significantly enhance their torque and power capabilities, as well as reduce losses in some operating points. However, most conventional control methods such as linear field-oriented control (FOC) in combination with standard pulse width modulation schemes face limitations in fully utilizing the available voltage. Despite these limitations, and due to its established history, relative simplicity, and other advantages such as robustness, FOC remains the industrial standard for controlling permanent magnet synchronous machine (PMSM) drives.

Within this context, the goal of this work is to provide a control solution with low computational burden that allows maximization of voltage utilization (i.e., six-step operation) as a complementary addition to the industrial standard FOC. For this, the model predictive direct self-control (MPDSC) strategy is proposed. This control strategy has been developed for discrete-time control of highly utilized PMSMs, including significant magnetic (cross-)saturation and low sampling-to-fundamental-frequency ratio. This strategy is intended for use at high speed when the machine is operated in the flux-weakening range.

Special focus is placed on the transition between MPDSC and FOC with minimal operational disruptions. Furthermore, enhancements to the strategy enabling the use of alternative switching patterns to six-step operation are considered. Finally, a comprehensive robustness analysis is provided to study the control performance when subjected to model inaccuracies, external disturbances and sensor noise.

The proposed solution is suitable not only for industrial and automation drives with almost linear magnetic behavior, but also for highly utilized machines typically found in transportation applications. It achieves six-step operation with accurate torque control as well as robustness against disturbances and model inaccuracies. Comprehensive simulation and experimental results demonstrate the performance of the proposed MPDSC while operating at the voltage limit.

Zusammenfassung

Elektrische Antriebe sind ein wesentlicher Bestandteil von Transport- und Industrieanwendungen, und ihre Bedeutung nimmt weiter zu. Die Optimierung der Spannungsausnutzung kann ihre Effizienz sowie ihre Drehmoment- und Leistungsfähigkeit deutlich verbessern. Allerdings stoßen die meisten konventionellen Regelverfahren, wie die lineare feldorienterite Regelung (eng.: field-oriented control, FOC) in Kombination mit gängigen Pulsweitenmodulationsverfahren, hierbei an Grenzen. Trotz dieser Einschränkungen bleibt die FOC aufgrund ihrer Etabliertheit, ihrer relativen Einfachheit und weiterer Vorteile wie Robustheit, der Industriestandard bezüglich der Regelung von Permanentmagnet-Synchronmotoren (PMSM).

Vor diesem Hintergrund besteht das Ziel dieser Arbeit darin, eine Regelung mit geringem Rechenaufwand bereitzustellen, die zur Maximierung der Spannungsausnutzung (d. h. Blocktaktung) als ergänzende Erweiterung der industriellen Standard-FOC eingesetzt werden kann. Hierfür wird die modellprädiktive direkte Selbstregelung (eng.: model predictive direct self-control, MPDSC) vorgeschlagen. Diese Regelstrategie wurde für die zeitdiskrete Regelung hochausgenutzter PMSM Antriebe entwickelt, welche starke magnetische (Kreuz-)Sättigungseffekte sowie ein geringes Verhältnis von Abtast- zu Grundfrequenz aufweisen können. Die Strategie ist für den Einsatz bei hohen Drehzahlen vorgesehen, wenn die Maschine im Feldschwächbereich betrieben wird.

Ein besonderer Fokus liegt auf dem Übergang zwischen MPDSC und FOC mit minimalen betrieblichen Beeinträchtigungen. Darüber hinaus werden Erweiterungen der Strategie betrachtet, die den Einsatz alternativer Schaltmuster im Vergleich zur Blocktaktung ermöglichen. Abschließend wird eine umfassende Robustheitsanalyse durchgeführt, um das Verhalten des Regelung gegenüber Parameterabweichung, Strögrößen und Messrauschen zu untersuchen.

Das vorgeschlagene Verfahren eignet sich nicht nur für Fertigungs- und Automatisierungsantriebe, welche nahezu lineares Magnetisierungsverhalten aufweisen, sondern auch für hochausgenutzte Maschinen, wie sie typischerweise in Transportanwendungen zu finden sind. Es erreicht Blocktaktungsbetrieb mit präziser Drehmomentregelung sowie Robustheit gegenüber Störungen und Modellabweichungen. Umfassende simulative und experimentelle Untersuchungen zeigen die Leistungsfähigkeit der vorgeschlagenen MPDSC im Betrieb an der Spannungsgrenze.

Own Publications

Relevant own Work for the Thesis

This thesis builds upon the author's prior publications, incorporating their core contributions in various forms. For ease of reading, explicit self-citations from these works are generally omitted.

- M. Peña, M. Meyer, O. Wallscheid and J. Böcker, "Model Predictive Direct Self-Control for Six-Step Operation of Permanent-Magnet Synchronous Machines," in IEEE Transactions on Power Electronics, vol. 38, no. 10, pp. 12416-12429, Oct. 2023, doi: 10.1109/TPEL.2023.3286713.
- M. Peña, M. Meyer, O. Wallscheid and J. Böcker, "Fade-Over Strategy for use of Model Predictive Direct Self-Control with Field-Oriented Control," 2023 IEEE International Electric Machines & Drives Conference (IEMDC), San Francisco, CA, USA, 2023, pp. 1-7, doi: 10.1109/IEMDC55163.2023.10239056.

Further, the following patent has been filed regarding key components of this work.

- M. Meyer, M. Peña, J. Böcker and O. Wallscheid, "Verfahren zum Ansteuern einer leistungselektronischen Vorrichtung eines elektrischen Antriebs, Kontroll-Einheit für einen elektrischen Antrieb sowie elektrischer Antrieb," Reference No. 10 2021 202 868.3, filing date 24 March 2021, url: https://patents.google.com/patent/DE102021202868A1.

Further Own Work

As Main Author

- M. Peña, M. Schenke, D. Jakobeit, B. Haucke-Korber and O. Wallscheid, "Reinforcement Learning Control of Three-Level Converter Permanent Magnet Synchronous Machine Drives," 2025 IEEE International Electric Machines & Drives Conference (IEMDC), Houston, TX, USA, 2025, pp. 57-64, doi: 10.1109/IEMDC60492.2025.11061032.

As Co-Author

- D. Jakobeit, M. Peña, M. Schenke, B. Haucke-Korber and O. Wallscheid, "Structural Optimization of Meta-Reinforcement Learning-based Finite-Control-Set Direct Torque Control of Permanent Magnet Synchronous Motors," 2025 IEEE International Electric Machines & Drives Conference (IEMDC), Houston, TX, USA, 2025, pp. 673-678, doi: 10.1109/IEMDC60492.2025.11061179.
- H. Vater, M. Peña and O. Wallscheid, "Optimal System Excitation of a Permanent Magnet Synchronous Motor Using Differentiable Model Predictive Excitation," 2025 IEEE International Electric Machines & Drives Conference (IEMDC), Houston, TX, USA, 2025, pp. 245-251, doi: 10.1109/IEMDC60492.2025.11061126.
- B. Haucke-Korber, N. N. Aung, M. Schenke, M. Peña, D. Jakobeit and O. Wallscheid, "Reinforcement Learning-based Direct Torque Control of Externally Excited Synchronous Motors: a Proof of Concept," 2025 IEEE International Electric Machines & Drives Conference (IEMDC), Houston, TX, USA, 2025, pp. 916-921, doi: 10.1109/IEMDC60492.2025.11061093.

Externally Affiliated Work

- H. El Khatib, M. Peña, B. Grothmann, E. Gedlu and M. Saur, "Applying the Square-Root-Condition combined with DB-DTFC as a Flux Observer-Based Maximum Torque per Flux Strategy," 2019 IEEE 10th International Symposium on Sensorless Control for Electrical Drives (SLED), Turin, Italy, 2019, pp. 1-6, doi: 10.1109/SLED.2019.8896256.
- H. El Khatib, M. Peña, B. Grothmann, E. Gedlu and M. Saur, "Flux Observer-Based MTPF/MTPV-Operation With Low Parameter Sensitivity Applying Deadbeat-Direct Torque and Flux Control," in IEEE Transactions on Industry Applications, vol. 57, no. 3, pp. 2494-2504, May-June 2021, doi: 10.1109/TIA.2021.3056630

Nomenclature

Abbreviations

AW	Anti-windup
DBFC	Deadbeat flux control
DSC	Direct self-control
DTC	Direct torque control
EOT	End of transition
EV	Electric vehicle
FOC	Field-oriented control
IM	Induction machine
IPMSM	Interior permanent magnet synchronous machine
LAC	Load-angle control
LPF	Low-pass filter
LUT	Look-up table
MAE	Mean-absolute error
MAEE	Mean-absolute estimation error
MPC	Model predictive control
MPDSC	Model-predictive direct self-control
MPFC	Model-predictive flux control
MTPF	Maximum torque per flux
MTPA	Maximum torque per ampere
MTPC	Maximum torque per current
MVSC	Modulated voltage-scale controller
OC	Own contributions
PEE	Parameter estimation error
PI	Proportional-integral (controller)
PLL	Phase-locked loop

PMSM	Permanent magnet synchronous machine
PR	Passive rectifier
PT_1	*Proportionaler Tiefpassfilter erster Ordnung*, i.e., proportional first-order low-pass filter
PWM	Pulse-width modulation
RMS	Root-mean-square
SOT	Start of transition
SVM	Space-vector modulation
VAC	Voltage-angle control
VSI	Voltage-source inverter
ZVI	Zero-voltage injection

Notation

$\boldsymbol{x}$	Vectorial variable
$\boldsymbol{X}$	Matrix variable
x	Scalar variable
$\boldsymbol{x}_{\mathrm{dq}}$	Vectorial variable in the rotor-synchronous dq-reference frame
$\boldsymbol{x}_{\mathrm{abc}}$	Vectorial variable in the stationary abc-reference frame
$\boldsymbol{x}_{\alpha\beta}$	Vectorial variable in the stationary αβ-reference frame
$\boldsymbol{x}_{\mathrm{L\text{-}L}}$	Vectorial variable in the stationary line-to-line reference frame
x^*, $\boldsymbol{x}^*$	Reference variable
x', X'	Variable or parameter subject to model deviations
$\widehat{x}$, $\widehat{\boldsymbol{x}}$	Estimated variable
$\boldsymbol{X}^\top$	Matrix transposition
$\boldsymbol{X}^{-1}$, $\boldsymbol{X}^\dagger$	Matrix inverse and pseudo-inverse
$\wedge$	Logic AND operator
$\vee$	Logic OR operator
$\neg$	Logic NOT operator

Symbols

α_{e}	Electrical angular acceleration
α_{fold}	Fundamental component reduction for three-fold modulation

$\alpha_{\alpha_{\Psi_{\mathrm{PM}}}}$, $\alpha_{L_{\mathrm{d}}}$, $\alpha_{L_{\mathrm{q}}}$, $\alpha_{R_{\mathrm{s}}}$	Deviation factors considered for model deviation analysis
$c\,(\,\Psi_{ij})$	Switching criteria for the line-to-line flux Ψ_{ij} , with $(i,j) \in \{(a,b),(b,c),(c,a)\}$
c_{to}	Logic signal indicating operation at or towards MPDSC
c_{from}	Logic signal indicating operation at or towards FOC
c_{aux}	Auxiliary logic signal for fade-over logic between MPDSC and FOC
c_{FW}	Logic signal indicating that the operating point belongs to the flux weakening region
c_{ini}	Logic signal initiating the fade-over between FOC and MPDSC
c_{angle}	Logic signal indicating that the flux angle is appropriate for the start-of-transition between FOC and MPDSC
$c_{\mathrm{time,1}}$, $c_{\mathrm{time,2}}$	Logic signals indicating a waiting time condition for ensuring the fade-over is completed
$\boldsymbol{d}^*_{\mathrm{abc}}$	Duty cycle command
δ	Load angle
δ_{rip}	Load angle ripple
$\Delta_{\Psi_{\mathrm{PM}}}$, $\Delta_{L_{\mathrm{d}}}$, $\Delta_{L_{\mathrm{q}}}$, $\Delta_{R_{\mathrm{s}}}$	Biases considered for model deviation analysis
I_{n}	Nominal stator current
I_{max}	Stator current limit
$\boldsymbol{i}_{\mathrm{abc}}$	Vector of phase currents in the abc-reference frame
$\boldsymbol{i}_{\alpha\beta}$	Vector of phase currents in the $\alpha\beta$-reference frame
$\boldsymbol{i}_{\mathrm{dq}}$	Vector of phase currents in the dq-reference frame
$i_{\mathrm{PR,thr}}$	Threshold for confidence in current polarity detection
$\boldsymbol{J}$	Rotation matrix
k	Sampling instant
$k_{p,\mathrm{i}}$	Confidence factor of current polarity for dead-time compensation
$k_{\mathrm{f}\to\mathrm{h}}$	Fundamental to hexagonal amplitude transformation
k_{f}	Folding ratio for three-fold switching
$k_{u_{\mathrm{DC}}}$, $k_{\theta_{\mathrm{r}}}$, k_{i_p}	Standard deviation of sensor noise injection
L_{s}	Stator inductance
L_{d},L_{q}	Stator absolute inductance in the d and q-axes, respectively
$\boldsymbol{L}_{\mathrm{dq}}$	Matrix of absolute inductances in the dq-reference frame
$\boldsymbol{L}_{\mathrm{dq},\Delta}$	Matrix of differential inductances in the dq-reference frame

M_{idx}	Modulation index
μ	Mean value
N_{p}	Number of pole pairs
N_{s}	Switching horizon for three-fold modulation implementation
n_{n}	Nominal mechanical speed
p_m	Percentile m$^{\mathrm{th}}$
Ψ_{PM}	Permanent magnet flux linkage
Ψ_{s}	Flux linkage amplitude
Ψ_{h}	Radius of the circle inscribed in the hexagonal flux trajectory for phase coordinates
Ψ_{hc}	Flux linkage amplitude at the corner of the hexagonal flux trajectory for phase coordinates
Ψ_{H}	Radius of the circle inscribed in the hexagonal flux trajectory for line-to-line coordinates
$\Psi_{\mathrm{h,MTPC}}$	Hexagonal flux linkage amplitude for MTPC operation
Ψ_{f}	Flux amplitude of folded corner in the 18-corner flux trajectory for phase coordinates
$\boldsymbol{\Psi}_{\mathrm{abc}}$	Vector of phase magnetic flux linkages in the abc-reference frame
$\boldsymbol{\Psi}_{\alpha\beta}$	Vector of phase magnetic flux linkages in the αβ-reference frame
$\boldsymbol{\Psi}_{\mathrm{dq}}$	Vector of phase magnetic flux linkages in the dq-reference frame
Ψ_{mod}	Flux reference reduction generated by the modulation controller
$\boldsymbol{\Psi}_{\mathrm{s}}$	Stator flux vector
$\boldsymbol{\Psi}_{\mathrm{r}}$	Rotor flux vector
ψ_α, ψ_β	Flux components in αβ-reference for a unit-corner amplitude hexagonal trajectory
$\boldsymbol{\psi}_{\mathrm{s}}$	Flux vector in αβ-reference frame for a unit-corner amplitude hexagonal trajectory
$\boldsymbol{\psi}_{\mathrm{s,1}}$	Vector of the fundamental component of the flux in αβ-reference frame for a unit-corner amplitude hexagonal trajectory
φ_{fold}	Angles at which the additional corners appear in the 18-corner flux trajectory
$\boldsymbol{R}_{\mathrm{abc}}$	Matrix of stator resistances in the abc-reference frame
$\boldsymbol{R}_{\alpha\beta}$	Matrix of stator resistances in the αβ-reference frame
$\boldsymbol{R}_{\mathrm{dq}}$	Matrix of stator resistances in the dq-reference frame
ρ	Range
s_p	Switching state of inverter leg $p \in \{\mathrm{a,b,c}\}$

$s_{p,\mathrm{U/L}}$	Switching state of the upper (U) or lower (L) semiconductor in the inverter leg $p \in \{\mathrm{a,b,c}\}$
$s_{p,\mathrm{PR}}$	Switching state the inverter leg $p \in \{\mathrm{a,b,c}\}$ during passive rectifier operation
σ	Standard deviation
T_e	Electric rotation period
T_s	Sampling period
T_del	Inverter delay time
T_dt	Inverter interlock dead-time
T_m	Time margin
T_swi	Time between switching events
T	Airgap torque
T^*	Torque reference
T^*_lim	Limited torque reference
T_n	Nominal torque
$\boldsymbol{T}_{\mathrm{abc}\to\alpha\beta}$, $\boldsymbol{T}_{\alpha\beta\to\mathrm{abc}}$	Transformation matrix from abc to αβ-reference frame and vice-versa, respectively
$\boldsymbol{T}_{\alpha\beta\to\mathrm{dq}}$, $\boldsymbol{T}_{\mathrm{dq}\to\alpha\beta}$	Transformation matrix from αβ to dq-reference frame and vice-versa, respectively
t	Time
$\boldsymbol{t}^*_{\mathrm{s,abc}}$	Switching time commands for each of the semiconductors
$\boldsymbol{t}^*_{\mathrm{s,FOC}}$	Switching time commands for each of the semiconductors from FOC
$\boldsymbol{t}^*_{\mathrm{s,MPFC}}$	Switching time commands for each of the semiconductors from MPFC
$\boldsymbol{t}^*_{\mathrm{abc,on/off}}$	Ideal on and off switching time commands
t^*_ZVI	Reference zero-voltage injection time
t_f	Time for the edge modulation during three-fold switching
t_mid	Switching time for the middle switching event in three-fold modulation
$\boldsymbol{t}_\mathrm{up}$, $\boldsymbol{t}_\mathrm{low}$	Times until line-to-line flux linkages reach the upper and lower reference
τ	Time constant
Θ	Temperature
θ_e	Electric angle
$\theta_\mathrm{e,pred}$	One-step-ahead predicted electric angle
θ_r	Mechanical angle
θ_s	Stator flux angle in the αβ-reference frame

$\theta_{\mathrm{s,1}}$	Angle of the fundamental component of the stator flux in the $\alpha\beta$-reference frame
θ_{thr}	Threshold angle determining the valid range of flux linkage location for fade-over
U_{DC}	Nominal DC-bus voltage
u_{DC}	DC-bus voltage
u_p	Line voltage of line $p \in \{\mathrm{a,b,c}\}$
$\boldsymbol{u}_{\mathrm{abc}}$	Vector of phase voltages in the abc-reference frame
u_α, u_β	Stator voltage in the α or β axis, respectively
$\boldsymbol{u}_{\alpha\beta}$	Vector of phase voltages in the $\alpha\beta$-reference frame
$\boldsymbol{u}_i$	Voltage vectors achievable with three-phase two-level VSI, with $i \in [0, 7]$
$\boldsymbol{u}_{\mathrm{dq}}$	Vector of phase voltages in the dq-reference frame
$\tilde{u}^*_\Delta$	Zero-component addition to normalized voltage references in FOC
ω_{e}	Electrical angular frequency
$\omega_{\mathrm{e,n}}$	Nominal electrical angular frequency
ω_Ψ	Flux linkage rotational frequency

Contents

Acknowledgements **i**

Abstract **iii**

Zusammenfassung **iv**

Own Publications **v**

Nomenclature **vii**

1 Introduction **1**
1.1 Motivation 1
1.2 Maximum Voltage Utilization 3
1.2.1 Field-Oriented Control 4
1.2.2 Alternative Control Strategies 5
1.2.3 Summary 6
1.3 Direct Self-Control 7
1.3.1 Adaptations to DSC 8
1.4 Goal and Content Structure 9

2 Fundamentals **11**
2.1 Electric Drive System 11
2.1.1 Three-Phase Two-Level Inverter 12
2.1.2 Permanent Magnet Synchronous Machine 14
2.2 Control Frameworks 18
2.2.1 Field-Oriented Control 19
2.2.2 Direct Self-Control 21

3 MPDSC for Six-Step Operation **23**
3.1 Modifications to DSC 23
3.1.1 Torque Control 23
3.1.2 Delay Compensation 26
3.2 Overview of MPDSC 28
3.2.1 Model Predictive Flux Control 29
3.2.2 Load Angle Control 34
3.2.3 Operating Point Selection 41

3.2.4 Voltage and Flux Estimation . . . 43
3.3 Simulation Results . . . 47
3.3.1 Steady-State Operation . . . 47
3.3.2 Torque Transient Response . . . 50
3.3.3 Speed Transient Response . . . 51
3.4 Experimental Results . . . 55
3.4.1 Computational Load . . . 55
3.4.2 Steady-State Operation . . . 55
3.4.3 Torque-Transient Operation . . . 60
3.4.4 Speed-Transient Operation . . . 61
3.5 Summary . . . 63

4 Fade-Over Strategy **65**
4.1 Fade-Over Control Strategy . . . 66
4.1.1 Fade-Over Logic . . . 67
4.1.2 Load Angle Control through Zero-Voltage Injection . . . 69
4.1.3 Flux Amplitude Reference . . . 70
4.1.4 MPFC with Zero-Voltage Injection . . . 71
4.1.5 Load Angle Reference Selection . . . 72
4.2 Simulation Results . . . 72
4.3 Experimental Results . . . 74
4.4 Summary . . . 75

5 Alternative Switching Patterns **77**
5.1 Three-Fold Switching Pattern . . . 77
5.2 Three-Fold MPDSC Control Strategy . . . 81
5.2.1 Three-Fold Reference Generation . . . 82
5.2.2 Switching Time Calculation . . . 85
5.2.3 Switching Pulse Generation . . . 86
5.2.4 Voltage and Flux Estimation . . . 88
5.3 Simulation Results . . . 88
5.4 Experimental Results . . . 93
5.5 Summary . . . 95

6 Robustness Analysis **97**
6.1 Simulation Evaluation . . . 98
6.1.1 Parameter Estimation Errors . . . 98
6.1.2 Sensor Noise . . . 103
6.1.3 Monte Carlo Simulations . . . 103
6.1.4 Response to Exogenous Transients . . . 106
6.2 Experimental Results . . . 112
6.3 Summary . . . 114

7 Conclusions **115**

7.1 Outlook 116

Appendix **125**
A Simulation Setup 125
A.1 Machine Model for Simulation Evaluation 125
A.2 Pulse Generation for Simulation Evaluation 126
A.3 Inverter Model for Simulation Evaluation 126
B Experimental Evaluation 128
C Voltage estimation algorithm 131
D Fade Over Logic Truth Tables 133
E Switching Criteria Modification for ZVI 134
F Machine Parameter Deviations 134

Lists **137**
List of Tables 137
List of Figures 137

1 Introduction

1.1 Motivation

Electric drives are essential components in modern industrial, transportation, and energy systems, generating the vast majority and consuming between 30 % and 40 % of electrical energy worldwide [1]. The electrification of the transportation sector continues to accelerate (cf. Fig. 1.1), with electric vehicle (EV) sales reaching 17 million units in 2024, making up over 20 % of global new car sales [2]. Looking ahead, global EV sales are expected to surpass 20 million in 2025 and reach 40 % of new car sales by 2030 under current policies. This transition is projected to displace over 5 million barrels of oil per day by 2030, driven by growing EV adoption and expanding charging infrastructure. Similar trends can be observed in other types of electric mobility, e.g., e-micromobility [3]. Within this context, optimizing the efficiency, maximizing utilization of available resources (e.g., voltage), and enhancing robustness of electric drives is critical to maximizing energy savings, ensuring user satisfaction, and maintaining safety. To achieve these objectives, the development of control strategies plays a pivotal role.

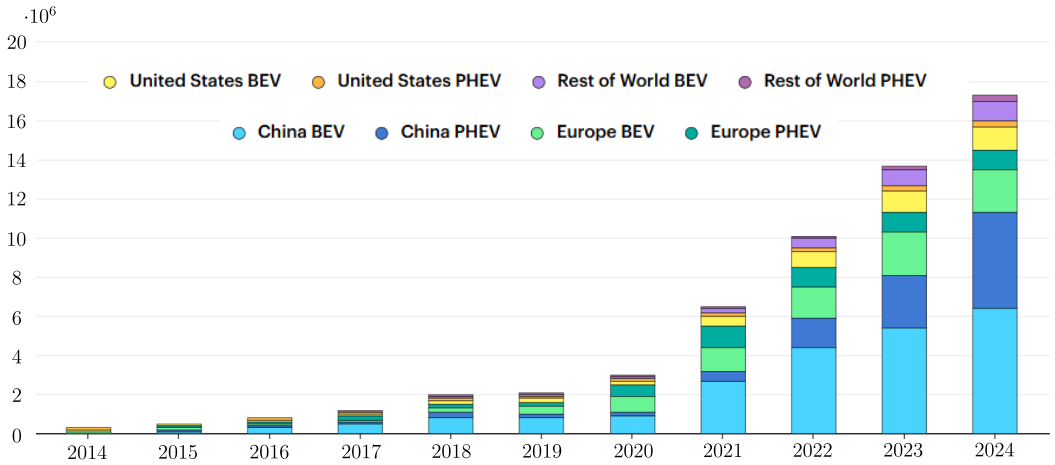


Fig. 1.1: Global electric car sales for battery electric vehicles (BEVs) and plug-in hybrid electric vehicles (PHEVs), 2014-2024 [2]

The control of AC drives has been a prominent research topic for over five decades, driven by the demand for high-efficiency, high-performance electric motor systems. A foundational breakthrough occurred with the introduction of field-oriented control (FOC) by Blaschke in 1972 [4], which decoupled the flux and torque components of AC machines, enabling control characteristics similar to those of separately excited DC motors. This was followed by the development of direct torque control (DTC) in 1985 by Takahashi and Noguchi [5], offering faster torque response and reduced computational complexity by eliminating coordinate transformations and modulation stages. In 1988, direct self-control (DSC) was proposed by Depenbrock [6], introducing a switching logic-based approach that further improved the dynamic behavior of induction motor drives. Model predictive control (MPC) received some initial attention for AC drive control in the 1980s, notably by Holtz [7], and Schröder and Kennel [8]. With the advent of powerful microprocessors, MPC re-emerged as a powerful alternative in the early 2000s [9], offering a predictive, constraint-aware framework capable of optimizing system performance over a future time horizon. More recently, AI-based strategies such as reinforcement learning have been proposed as valid strategies for electric drive control [10].

Despite these advances in the field, proportional-integral (PI)-based FOC continues to be at the core of the preferred control strategies and industry standards for control of AC drives. This stems from its long established history and proven balance of performance, reliability, and implementation complexity, making it suitable for a wide range of applications. FOC has been extensively studied, validated, and standardized, and has a widespread availability of development tools, reference designs, and robust tuning procedures that can reduce implementation effort. The main drawbacks of FOC stem from its inherently linear and decoupled interpretation of the machine dynamics and constraints, and its suboptimal dynamic response[1]. The latter can be dismissed in certain applications such as automotive drives, when the dynamic requirements for functionality and mechanic considerations can be far below the drive's capabilities. Furthermore, despite the linear control law in PI-based FOC implementations, some of the nonlinear characteristics of the drive can be considered within ancillary systems such as the operating point selection, flux prediction for the decoupling network, and current prediction, enhancing its performance especially in the context of highly utilized[2] machines.

However, a key drawback remains: the inherent decoupled and linear interpretation of the machine dynamics and the actuation constraints. FOC assumes the existence of two separate degrees of freedom for control of the machine, which is not accurate for the neighborhood of the drive voltage limit. While several strategies have been proposed that enable the use of FOC in this region, their applicability within the context of highly utilized machines with relatively low sampling-to-fundamental-frequency ratio is questionable. Nevertheless, the ability to operate at and around the voltage limit offers significant advantages, such as increasing the maximum drive torque and power output, and reduc-

[1]The optimal dynamic response would be that which brings about the desired steady state in the minimum time within the drive's constraints.

[2]This term refers to drives frequently operated near or at their constraints, often exhibiting large magnetic (cross-)saturation in these conditions.

ing copper losses for partial load operation, without any change to the actual hardware. This enhancement is represented in Fig. 1.2 for the motoring operation of the machine utilized in this investigation. The standard FOC control strategy is limited to the linear modulation range in steady state. In contrast, achieving maximum voltage utilization increases the maximum torque and power output in the flux weakening region.

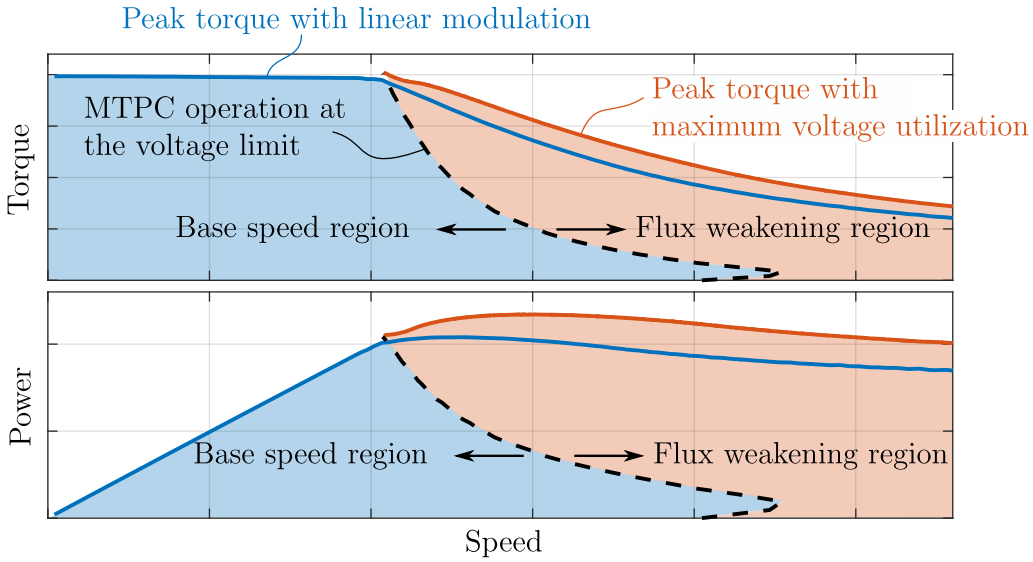


Fig. 1.2: Operating regions for exemplary PMSM, highlighting the maximum torque and power output according to voltage utilization

The goal of this investigation then is to achieve a control solution that

- achieves maximum voltage utilization,
- attains dynamic performance metrics comparable to, or surpassing, those of the industry-standard FOC solution,
- can be implemented as a complementary addition to the industry-standard FOC solution, i.e., is not computationally expensive, does not require additional sensors, and appropriately handles the fade-over to and from FOC, and
- is stable and robust within the context of highly-utilized permanent magnet synchronous machines (PMSMs), making it appropriate for automotive applications.

The following summarizes the state-of-the-art approaches for attaining maximum voltage utilization in PMSMs, and provides the background for the proposed solution: model predictive direct self-control (MPDSC).

1.2 Maximum Voltage Utilization

The problem of voltage utilization has been the subject of extensive research for industrial and transportation applications. The primary challenge does not lie in the synthesis of the output voltage itself. Indeed, maximum voltage utilization is achieved through

the simplest switching strategy, namely six-step operation. Rather, the difficulty arises from its interaction with the control scheme, which constitutes the focus of this section. Operating around and beyond the linear voltage limit introduces several issues that need to be considered to maintain the drive's controllability and performance.

To attain maximum voltage utilization, six-step modulation must be applied, i.e., sequentially switching between the six active voltage vectors during one fundamental period. This means that the degrees of freedom for control are severely limited, as the applied voltage has a fixed amplitude, and the control strategy can only choose when to switch to the next active voltage vector[3]. No further voltage utilization improvements are physically possible beyond this strategy, regardless of the control method.

Six-step modulation introduces additional consequences, notably increased harmonic content in current, voltage, torque, and flux linkage. When operating in this mode, as well as in the overmodulation region, the system inevitably exhibits increased ripple in both controlled and uncontrolled variables, thereby complicating control design and signal sampling, and ultimately degrading overall performance [11], [12], [13], [14].

The control structure cannot address these disadvantages, as they are inherent properties of the modulation strategy required to maximize the utilization of the voltage given the physical constraints of the voltage-source inverter (VSI), i.e., any deviations would require an introduction of additional switching events, which would reduce the voltage utilization. As they are inevitable, the trade-off between additional ripple and voltage-utilization is not a role of the proposed controller but of an upper-level strategy accounting for the drive's desired performance. In the following, established control strategies are briefly introduced, and the state of the art regarding their effectiveness in addressing maximum voltage utilization is discussed.

1.2.1 Field-Oriented Control

The industry's most established control strategy for electric motors is FOC (cf. [11], [13], [15], [16], [17], [18], [19]), which independently controls the rotor-synchronous-reference-frame dq-currents. Standard approaches such as pulse-width modulation (PWM) or space-vector modulation (SVM) can synthesize, on average over a switching period, voltage commands below the linear voltage limit. This is no longer the case when the voltage command goes beyond the limit of the linear modulation range. The unavailability of an arbitrary dq-voltage command of such amplitude reduces the practical degrees of freedom of the system in that region, i.e., the dq-currents can no longer be independently controlled, violating the underlying assumption for standard FOC.

FOC schemes require a safety voltage margin to enable dynamic current control [12], [18], which is inherently unavailable at the voltage limit. Consequently, appropriate saturation

[3]It should be noted that this differs from finite-control-set (FCS) approaches: for six-step operation the switching transitions may occur at arbitrary continuous times, rather than being restricted to the sampling instants, as is the case with FCS.

handling and anti-windup (AW) strategies become necessary [18]. Under these conditions, the effective bandwidth of the employed PI controllers is reduced [11].

In the overmodulation region, increased ripple and noise appear in both controlled and uncontrolled variables, thereby complicating control and signal sampling, and reducing machine efficiency [11], [12], [13], [14]. The application of filters to attenuate harmonic content in the measured signals further degrades the achievable bandwidth [11].

Furthermore, cross-coupling between the current components intensifies with increasing speed [18]. Beyond the base speed, flux-weakening strategies become necessary, such as dynamic modulation control [16].

The simultaneous implementation of multiple strategies addressing the aforementioned conditions may lead to conflicts, particularly when they attempt to modify the current references supplied to the controllers [19]. Moreover, when multiple operating modes are employed, appropriate transition mechanisms must be ensured to maintain stability and performance [12], [14].

Several FOC-based contributions tackling enhanced voltage utilization focus primarily on voltage synthesis at or near the voltage limit, without explicitly addressing the management of the associated challenges [20], [21], [22], [23]. In addition, research on overmodulation and six-step operation is often conducted using induction machines [13], [18], or PMSMs with high inductance values [11] or low power ratings [19]. Furthermore, these studies typically consider systems with relatively low fundamental electrical frequencies and high switching frequencies, resulting in a high number of samples per electrical revolution (often exceeding 50) [11]. When such conditions do not apply, the practical applicability of FOC overmodulation and six-step strategies may be limited.

Among them, [11] was identified as a particularly promising approach, and is included in the selected examples from the literature in Fig. 1.3. It achieves six-step operation by effectively creating a voltage margin through the exploitation of the induced voltage, enabled by a dynamic adjustment of the current references based on Bolognani's overmodulation scheme [21]. In [19], high-voltage utilization operation is achieved through a similar principle.

1.2.2 Alternative Control Strategies

Alternative control strategies have been used in conjunction with FOC to avoid the issues discussed previously, such as load-angle control (LAC) [12], voltage-angle control (VAC) [14], or modulating voltage-scaled control (MVSC) [24]. However, the examples found in the literature for these strategies do not include applications with comparable drives to the one considered here in terms of dynamic response and number of measurement samples per electrical revolution (cf. Fig. 1.3).

MPC utilizes a dynamic model of the motor and inverter system to predict future behavior and optimize control actions over a specified prediction horizon. In contrast to conventional PI controllers, MPC explicitly considers system constraints, such as voltage

and current limits, and offers improved dynamic performance, which makes it suitable for applications requiring high precision and fast response. Several MPC methods reach six-step operation [25], [26], [27], [28], some only achieve high-voltage utilization but not full six step operation [29], [30]. In either case, the methods generally require high processing power and high fundamental-to-sampling frequency ratio.

Several notable approaches have been developed concurrently with this work, pursuing similar objectives. In particular, the solutions presented in [25] and [31] are of significant relevance, as they demonstrate strategies capable of operating across the entire modulation range, including seemingly stable and robust six-step operation with highly utilized drives. In [25], a MPC scheme is proposed, which achieves this by pre-modifying the reference in order to account for harmonic distortion during overmodulation and six-step operation. Similarly, the deadbeat flux control (DBFC) strategy introduced in [31], based on [32] and [33], exhibits strong conceptual parallels to the present work. This method employs deadbeat-control principles to synthesize a stator flux trajectory through closed-loop regulation of the load angle.

1.2.3 Summary

The machines employed in traction applications have specific characteristics, such as relatively low inductance values[4], operating point-depending magnetic (cross-)saturation, operation at high electric fundamental frequencies (up to 1-2 kHz), and relatively high voltage and power rating. Relevant examples of the strategies in the literature that have demonstrated to be capable of achieving six-step operation with PMSMs, and which disclose the parameters required for this comparison[5], are depicted in Fig. 1.3[6] regarding the challenges related to highly utilized machines. The minimum number of measurement samples per electrical revolution ($\min(T_\mathrm{e}/T_\mathrm{s})$, where T_e is the electric rotation period and T_s is the sampling period) relates to the challenge of achieving robust control at high speeds when the measurements are only sampled and the actuating commands only updated a few times per electrical rotation. The normalized current transient achieved in one sampling period when applying maximum voltage neglecting the ohmic voltage drop ($2u_\mathrm{DC}T_\mathrm{s}/(3L_\mathrm{s}I_\mathrm{max})$, where u_DC is the DC-bus voltage, L_s is the nominal inductance, and I_max is the current limit) relates to the dynamic behavior between sampling instants. Highly utilized machines have relatively small inductances leading to a large current transient. Furthermore, the depicted comparison considers nominal inductance values, the maximum current transient would be even more significant in the high-saturation region.

[4]This results from the high-rated-speed design requirements of traction drives. However, the inductance must remain sufficiently large to enable flux weakening within the current limits and to limit the short-circuit current, as determined by the other system parameters and constraints.

[5]The strategy in [31] is excluded from this comparison for lack of machine information, although from the results provided, the conditions seem to approach that of this work.

[6]It should be noted that only strategies fulfilling the conditions listed in the caption are considered in this comparison, i.e., strategies capable of only achieving quasi-six-step operation, or applied to different machine types, are excluded.

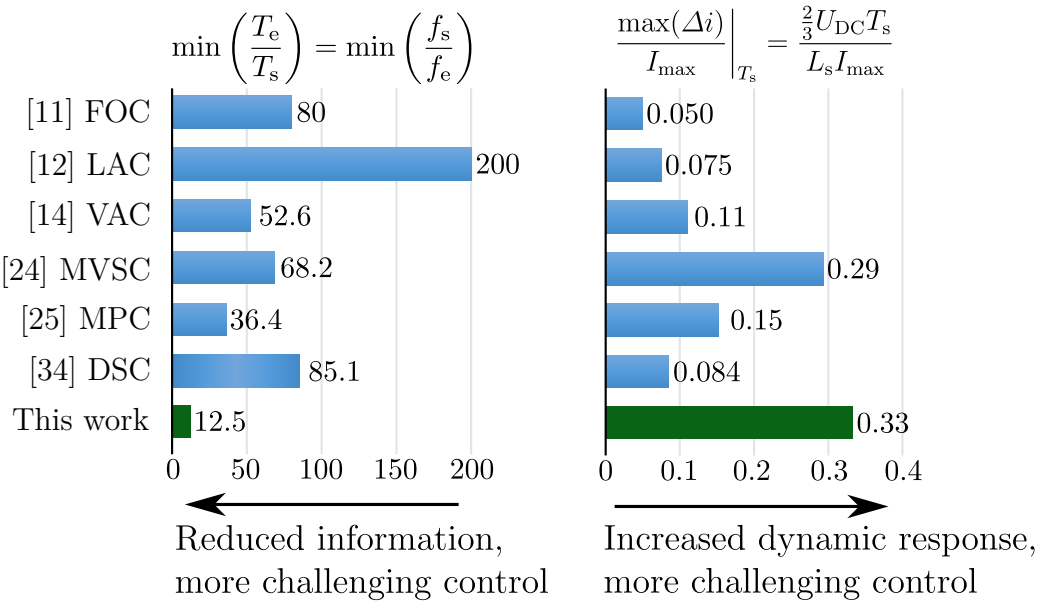


Fig. 1.3: Comparison of drives and control strategies used in the literature for six-step operation of PMSMs [OC1]: left - number of samples (each $T_s = 1/f_s$) per electrical revolution ($T_e = 1/f_e$); right - normalized current transient (with respect to I_{max}) achieved in one sampling period (T_s) when applying maximum voltage ($2u_{DC}/3$) considering nominal stator inductance (L_s)

The attempts to adapt the strategies discussed in Fig. 1.3, focusing on [11], to control the considered highly utilized PMSM-based automotive drive in six-step operation were unsuccessful. While the author does not claim that the efforts have been fully exhaustive, e.g., it might be possible to adapt the control strategy from [11] further to enable its use, direct adaption did not seem feasible. This is likely due to the more challenging control characteristics that are encountered for the given drive (shown in Fig. 1.3 in green). Hence, there is a need for computational lightweight and robust six-step control schemes, which can apply to highly utilized PMSM drives under these conditions. For this, an adaptation of the DSC strategy was considered.

1.3 Direct Self-Control

The DSC strategy was introduced in [6] for analog (i.e., continuous-time) control of induction machines. This strategy generates the switching pulses according to the comparison between the line-to-line flux and an externally generated reference. The ideal evolution of the line-to-line fluxes during six-step operation is shown in Fig. 1.4, where s_a, s_b, s_c are the switching states of each of the phases, Ψ_h is the radius of the circle inscribed in the hexagonal flux trajectory for phase coordinates, and Ψ_H for line-to-line coordinates.

Once the flux reference is reached for a given axis, the appropriate switching is triggered to maintain the flux at the reference value. In this way, pulse generation is integrated

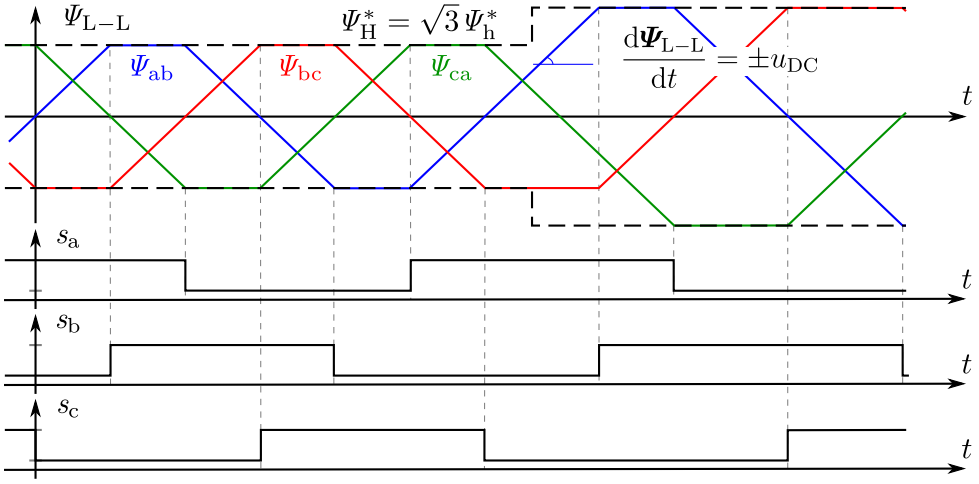


Fig. 1.4: Switching pulse generation by the DSC algorithm under ideal conditions in continuous time

with the control strategy, whose actuating variable is the time between switching events. This effectively removes the need for voltage margin to ensure controllability and enables control at the voltage limit. The controlled variables are the line-to-line (or β-axes) fluxes in the stationary reference frame. This removes the complications for control that harmonic distortion introduces in the synchronous reference frame variables during six-step operation. A change in the flux reference value is only accounted for in the next switching event, and the six-step voltage sequence is always followed without modulation between switching states. In steady-state, the flux reference amplitude dictates the angular frequency of the stator according to the DC-bus voltage.

1.3.1 Adaptations to DSC

The DSC control structure has been explored for six-step operation in the literature since [6] in 1988, almost exclusively applied to induction machine (IM) control (e.g., [35], [36], [37]), with different inverter configurations [37] and modifications to the original control strategy [36]. In [35], the superior performance of DSC compared to FOC with synchronous PWM is highlighted for a low switching-frequency to motor-frequency ratio, including improvements in peak currents, motor losses, torque ripple, and DC-link current harmonics, as well as better voltage and switching frequency utilization. The same study also notes the greater robustness of DSC against input voltage disturbances.

Control methods based on DSC have been applied to PMSMs [38], though their working principles deviate from the original control strategy in [6]. Concurrent with this investigation, an example of DSC six-step operation control for an IPMSM was also independently achieved in [34] by the combined action of modifying the estimated flux linkage according to the reference load angle, and a torque control scheme for improved high-speed operation. The reference flux amplitude appears to be set by a feed-forward calculation.

However, the system proposed is not tested for a highly utilized machine, nor at very high speeds with low samples per electrical revolution (cf., Fig. 1.3). Flux control is executed with hysteresis comparators in discrete time, which introduces flux control errors that would become more significant at high speeds. Likely due to this issue, substantial deviations are noticeable between current peak values in the results shown operating in six-step in steady state. The fade-over to alternative control strategies appears smooth but is not explained or tested at high speeds, and the response to incorrect parameter or flux estimation is not analyzed. This work addresses these issues and deviates from [34] in its core control principles. Nevertheless, both employ similar ancillary strategies (e.g., flux estimation via an observer) and share their conceptual approach, i.e., to achieve torque control based on the load angle.

1.4 Goal and Content Structure

The goal of this work is to develop, analyze, and validate an ancillary control strategy to FOC that enables maximum voltage utilization in the flux-weakening range. Although techniques have emerged that enable a continuous transition through linear modulation, overmodulation, and six-step operation, this work maintains FOC as the strategy for the linear modulation range, according to the industrial preference.

At the beginning of this research, a review of the literature and an evaluation of the specific challenges associated with the chosen drive system were carried out. These challenges include high voltage utilization requirements, significant magnetic (cross-)saturation, and a relatively low number of sampling events per electrical cycle. Based on this assessment, the most suitable approach was identified as a modification of the DSC method, adapted for use in discrete time control of PMSMs. This decision was motivated by the inherent robustness of the DSC framework, which is essential for the intended transportation application, as well as its relatively low computational requirements.

To address this objective, the dissertation proposes and evaluates the model predictive direct self-control (MPDSC) strategy. The structure of the document is organized as follows:

- Chapter 1 introduces the motivation for this work, provides a review of related research, and outlines the structure of the dissertation,
- Chapter 2 presents the theoretical foundations and essential background required to understand the control approach,
- Chapter 3 describes the main control strategy, including its core principles and the supporting ancillary systems,
- Chapter 4 explains the transition mechanisms between the proposed method and conventional FOC,
- Chapter 5 introduces alternative switching patterns within the MPDSC methodology,

- Chapter 6 presents a robustness analysis, covering sensitivity to parameter estimation errors, measurement noise, and external disturbances, and
- Chapter 7 provides the conclusions and outlook of this research.

Each chapter provides simulation and experimental results validating the presented content.

2 Fundamentals

This chapter provides the theoretical foundation for the algorithms examined in the remainder of the document. It begins with a description of the key components of the electric drive system. The inverter is analyzed with respect to its modeling, inherent limitations, and modulation strategies. The electric machine is then discussed in detail, covering its modeling, reference frame transformations, magnetic saturation, loss mechanisms, and operational constraints. Finally, the chapter introduces the relevant control frameworks, outlining the established FOC method and the DSC approach, which provided the basis for the proposed MPDSC strategy. All results throughout this document are normalized with respect to the nominal drive values given in Tab. 2.1[1]. Unless otherwise stated, angles are given in radians.

Variable	Parameter	Symbol	Value	Unit
Current	Nominal current	I_n	840	A
Voltage	DC-bus voltage	U_DC	320	V
Torque	Nominal torque	T_n	310	Nm
Speed	Nominal speed	n_n	5000	min^{-1}
Flux linkage	Permanent magnet flux linkage	Ψ_PM	45	mVs

Tab. 2.1: Normalization values

2.1 Electric Drive System

Electric drive systems have the following main components, represented in the simplified diagram of Fig. 2.1:

- the electric machine, converting electric to mechanical energy,
- the inverter and electric supply, including the power electronics executing the switching commands to produce the desired voltages at the machine terminals,

[1]Reported values in Tab. 2.1 are approximate to ensure confidentiality.

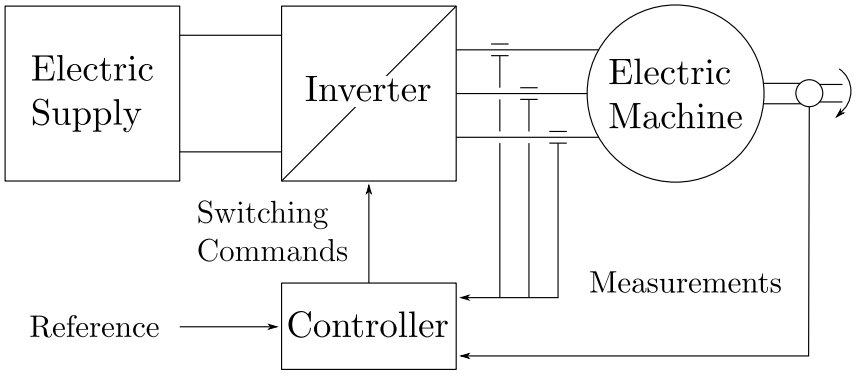


Fig. 2.1: Simplified diagram of an electric drive system

- the controller, generating switching commands from measurements obtained from the environment and a given reference for the desired operating point,
- sensors for obtaining the relevant data from the environment.

In transportation applications, a classical two-level VSI is typically used. Interior permanent magnet synchronous machines (IPMSM) are preferred to other machine typologies in some applications due to their high torque, power density, power factor, and mechanical design, allowing for high-speed operation. In the application considered in this investigation, phase current, DC-bus voltage, and rotor angle measurements are available to the control strategy. In the following, each of these components is explored in detail.

2.1.1 Three-Phase Two-Level Inverter

Among other constraints, the performance and specifications of the drive are limited by the voltage supply. The three-phase two-level inverter feeding the circuit of the machine's stator is represented in Fig. 2.2, where u_{DC} is the instantaneous DC-bus voltage, and $s_{p,\mathrm{U/L}}$ is the switching state of the upper (U) or lower (L) semiconductor in the inverter leg corresponding to line $p \in \{\mathrm{a,b,c}\}$, achieving the line voltages u_{a}, u_{b}, and u_{c}, respectively. The combination of these switching states results in the values depicted in Tab. 2.2.

In this investigation, inverter nonlinearities are considered in terms of delay and interlock deadtime, and passive rectifier operation therein (more details are provided in Sec. 3.2.1.3 and App. A.3). Further nonideal switching behavior is not modeled or compensated, including conduction and switching losses.

2.1.1.1 Modulation Regions

The combination of the switching states in the three-phase system, averaged over the switching period, results in the voltage space depicted in Fig. 2.3. The voltage at the inverter output can be expressed in the three-phase stationary reference frame (abc), the equivalent two-phase stationary reference frame ($\alpha\beta$), or a two-phase arbitrary reference

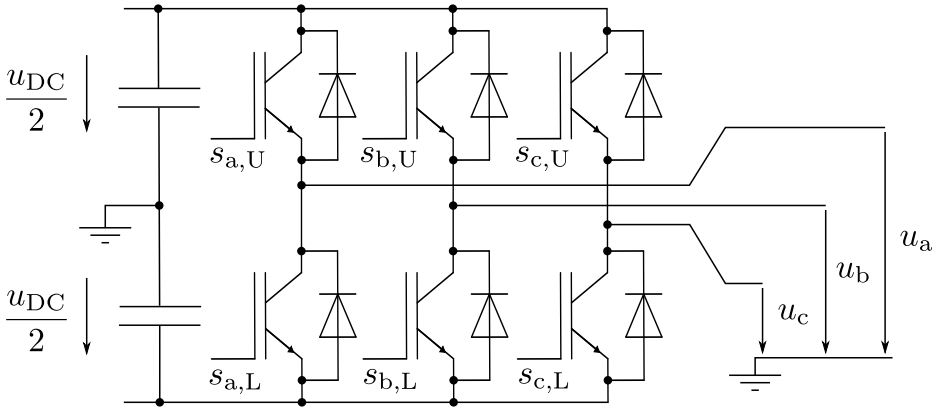


Fig. 2.2: Three-phase two-level VSI

Voltage vector	s_{a}	s_{b}	s_{c}	u_{a}	u_{b}	u_{c}	u_{α}	u_{β}
$\boldsymbol{u}_0$	-	-	-	$-\frac{u_{\mathrm{DC}}}{2}$	$-\frac{u_{\mathrm{DC}}}{2}$	$-\frac{u_{\mathrm{DC}}}{2}$	0	0
$\boldsymbol{u}_1$	+	-	-	$\frac{u_{\mathrm{DC}}}{2}$	$-\frac{u_{\mathrm{DC}}}{2}$	$-\frac{u_{\mathrm{DC}}}{2}$	$\frac{2u_{\mathrm{DC}}}{3}$	0
$\boldsymbol{u}_2$	+	+	-	$\frac{u_{\mathrm{DC}}}{2}$	$\frac{u_{\mathrm{DC}}}{2}$	$-\frac{u_{\mathrm{DC}}}{2}$	$\frac{u_{\mathrm{DC}}}{3}$	$\frac{u_{\mathrm{DC}}}{\sqrt{3}}$
$\boldsymbol{u}_3$	-	+	-	$-\frac{u_{\mathrm{DC}}}{2}$	$\frac{u_{\mathrm{DC}}}{2}$	$-\frac{u_{\mathrm{DC}}}{2}$	$-\frac{u_{\mathrm{DC}}}{3}$	$\frac{u_{\mathrm{DC}}}{\sqrt{3}}$
$\boldsymbol{u}_4$	-	+	+	$-\frac{u_{\mathrm{DC}}}{2}$	$\frac{u_{\mathrm{DC}}}{2}$	$\frac{u_{\mathrm{DC}}}{2}$	$-\frac{2u_{\mathrm{DC}}}{3}$	0
$\boldsymbol{u}_5$	-	-	+	$-\frac{u_{\mathrm{DC}}}{2}$	$-\frac{u_{\mathrm{DC}}}{2}$	$\frac{u_{\mathrm{DC}}}{2}$	$-\frac{u_{\mathrm{DC}}}{3}$	$-\frac{u_{\mathrm{DC}}}{\sqrt{3}}$
$\boldsymbol{u}_6$	+	-	+	$\frac{u_{\mathrm{DC}}}{2}$	$-\frac{u_{\mathrm{DC}}}{2}$	$\frac{u_{\mathrm{DC}}}{2}$	$\frac{u_{\mathrm{DC}}}{3}$	$-\frac{u_{\mathrm{DC}}}{\sqrt{3}}$
$\boldsymbol{u}_7$	+	+	+	$\frac{u_{\mathrm{DC}}}{2}$	$\frac{u_{\mathrm{DC}}}{2}$	$\frac{u_{\mathrm{DC}}}{2}$	0	0

Tab. 2.2: Switching states

frame (dq). The dq-frame rotates at the electrical angular speed ω_{e}, and its d-axis is shifted by an angle θ_{e} relative to the a-axis (or equivalently the α-axis).

Depending on the magnitude of the commanded voltage vector within Fig. 2.3, three operating regions can be distinguished: linear region, overmodulation region, and six-step operation. In the linear region, any dq-voltage can be synthesized in average using standard approaches such as PWM or SVM, and can achieve a maximum fundamental component of $u_{\mathrm{DC}}/\sqrt{3}$.

In the overmodulation region a constant dq-voltage output is not possible for the full electric period. Thus, this region involves a trade-off between further increase of the fun-

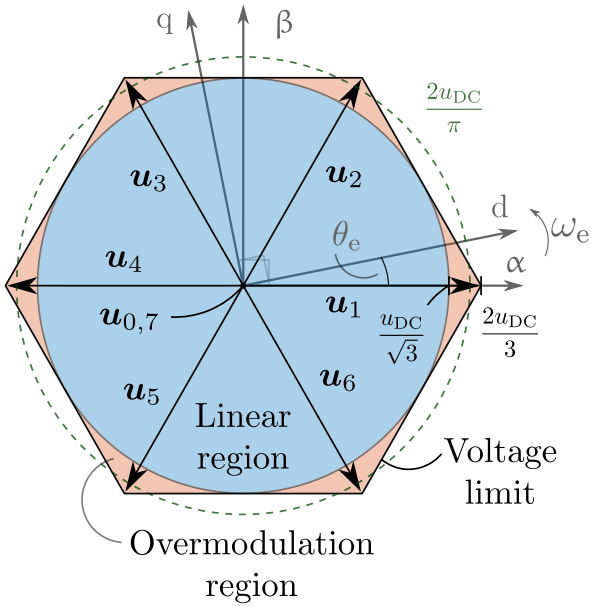


Fig. 2.3: Operating regions and limits of inverter in the αβ-voltage plane

damental component of the voltage and increased harmonic content. The combination of a lack of voltage margin and the inability to independently set the two voltage components is one of the main reasons for which conventional PI-FOC is challenging in this region. Several overmodulation strategies exist that attempt to minimize different aspects of the voltage output distortion [20], [21], [22], [23]. In this investigation the overmodulation region is solely utilized within FOC for transient control voltage margin (details in Sec. 2.2.1). The reference voltage saturation method utilized achieves the minimum voltage error [18], [39] by projecting the voltage vector upon the hexagonal boundary when the reference is out of bounds. The maximum fundamental voltage output, $2u_{DC}/\pi$, is achieved with six-step operation, i.e., operating only at the hexagon corners by switching sequentially from voltage vectors 1 to 6 for counter-clockwise rotation, and in the reverse order for clockwise rotation.

2.1.2 Permanent Magnet Synchronous Machine

The simplified scheme of a single pole PMSM can be seen in Fig. 2.4. For a multi-pole machine, the electric angle (θ_e) is related to the mechanical angle (θ_r) as

$$\theta_e = N_p \theta_r, \tag{2.1}$$

where N_p is the number of pole pairs. The machine can be described in the stationary reference frame considering the fundamental wave[2] model as [40]

[2]In this work, this assumption refers solely to spatially periodic behavior. Specifically, fields in the air gap that vary sinusoidally with the circumferential coordinate [40]. It does not imply any assumption of fundamental temporal oscillation or linear magnetization.

$$\boldsymbol{u}_{\mathrm{abc}} = \boldsymbol{R}_{\mathrm{abc}}\boldsymbol{i}_{\mathrm{abc}} + \frac{\mathrm{d}\boldsymbol{\Psi}_{\mathrm{abc}}}{\mathrm{d}t}, \tag{2.2}$$

where $\boldsymbol{u}_{\mathrm{abc}} = [u_{\mathrm{a}}\ u_{\mathrm{b}}\ u_{\mathrm{c}}]^{\top}$ is the vector of phase voltages, $\boldsymbol{i}_{\mathrm{abc}} = [i_{\mathrm{a}}\ i_{\mathrm{b}}\ i_{\mathrm{c}}]^{\top}$ is the vector of phase currents, $\boldsymbol{\Psi}_{\mathrm{abc}} = [\Psi_{\mathrm{a}}\ \Psi_{\mathrm{b}}\ \Psi_{\mathrm{c}}]^{\top}$ is the vector of phase flux linkages, and $\boldsymbol{R}_{\mathrm{abc}} = \mathrm{diag}([R_{\mathrm{a}}\ R_{\mathrm{b}}\ R_{\mathrm{c}}])$ is the resistance matrix, in the abc-reference frame. In general, the flux linkage depends on the currents, the rotor electric angle (θ_{e}), and the temperature (Θ), while the resistance is likewise temperature dependent, i.e.,

$$\boldsymbol{\Psi}_{\mathrm{abc}} = \boldsymbol{\Psi}_{\mathrm{abc}}(i_{\mathrm{a}}, i_{\mathrm{b}}, i_{\mathrm{c}}, \theta_{\mathrm{e}}, \Theta), \tag{2.3}$$

$$\boldsymbol{R}_{\mathrm{abc}} = \boldsymbol{R}_{\mathrm{abc}}(\Theta). \tag{2.4}$$

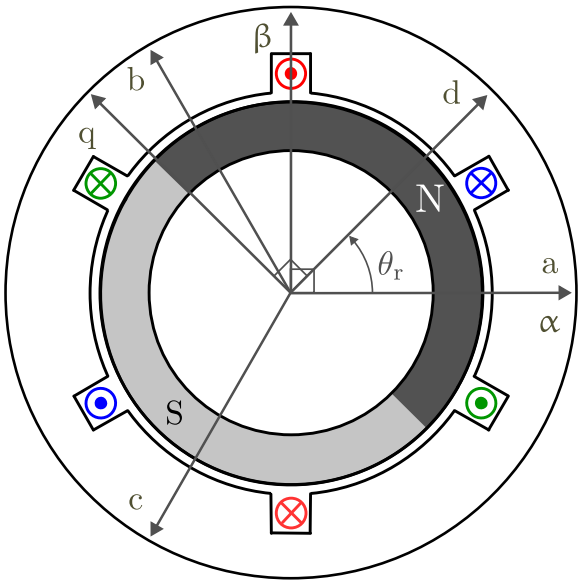


Fig. 2.4: Single-pole PMSM schematic cross-section

It is advantageous to transform the equations describing the machine behavior between the stationary abc-reference frame, a stationary two-phase system ($\alpha\beta$), and a rotating reference frame (dq). This can be done through the following transformation matrices

$$\boldsymbol{T}_{\mathrm{abc}\to\alpha\beta} = \frac{2}{3}\begin{bmatrix} 1 & -\frac{1}{2} & -\frac{1}{2} \\ 0 & \frac{\sqrt{3}}{2} & -\frac{\sqrt{3}}{2} \end{bmatrix}, \quad \boldsymbol{T}_{\alpha\beta\to\mathrm{abc}} = \boldsymbol{T}^{\dagger}_{\mathrm{abc}\to\alpha\beta} = \frac{3}{2}\begin{bmatrix} \frac{2}{3} & -\frac{1}{3} & -\frac{1}{3} \\ 0 & \frac{\sqrt{3}}{3} & -\frac{\sqrt{3}}{3} \end{bmatrix}^{\top}, \tag{2.5}$$

$$\boldsymbol{T}_{\alpha\beta\to\mathrm{dq}}(\theta_{\mathrm{e}}) = \begin{bmatrix} \cos\theta_{\mathrm{e}} & \sin\theta_{\mathrm{e}} \\ -\sin\theta_{\mathrm{e}} & \cos\theta_{\mathrm{e}} \end{bmatrix}, \quad \boldsymbol{T}_{\mathrm{dq}\to\alpha\beta}(\theta_{\mathrm{e}}) = \boldsymbol{T}^{-1}_{\alpha\beta\to\mathrm{dq}}(\theta_{\mathrm{e}}) = \begin{bmatrix} \cos\theta_{\mathrm{e}} & -\sin\theta_{\mathrm{e}} \\ \sin\theta_{\mathrm{e}} & \cos\theta_{\mathrm{e}} \end{bmatrix}, \tag{2.6}$$

where † depicts the matrix pseudo-inverse (for non-square matrices). Thus, the transformed voltage equations for the $\alpha\beta$-reference frame result in

$$\boldsymbol{u}_{\alpha\beta} = \boldsymbol{R}_{\alpha\beta}\boldsymbol{i}_{\alpha\beta} + \frac{\mathrm{d}\boldsymbol{\Psi}_{\alpha\beta}}{\mathrm{d}t}, \tag{2.7a}$$

$$\boldsymbol{x}_{\alpha\beta} = \boldsymbol{T}_{\mathrm{abc}\to\alpha\beta}\boldsymbol{x}_{\mathrm{abc}}, \tag{2.7b}$$

and for the dq-reference frame in

$$\boldsymbol{u}_{\mathrm{dq}} = \boldsymbol{R}_{\mathrm{dq}}\boldsymbol{i}_{\mathrm{dq}} + \frac{\mathrm{d}\boldsymbol{\Psi}_{\mathrm{dq}}}{\mathrm{d}t} + \omega_{\mathrm{e}}\boldsymbol{J}\boldsymbol{\Psi}_{\mathrm{dq}}, \tag{2.8a}$$

$$\boldsymbol{x}_{\mathrm{dq}} = \boldsymbol{T}_{\alpha\beta\to\mathrm{dq}}\boldsymbol{x}_{\alpha\beta}, \tag{2.8b}$$

$$\boldsymbol{J} = \begin{bmatrix} 0 & -1 \\ 1 & 0 \end{bmatrix}, \ \omega_{\mathrm{e}} = \frac{\mathrm{d}\theta_{\mathrm{e}}}{\mathrm{d}t}, \tag{2.8c}$$

where $\boldsymbol{x}$ and $\boldsymbol{X}$ represent the vectorial variables in the corresponding reference frame, respectively. For the control method described in this work, it is also useful to consider line to line (L-L) variables, as

$$x_{ij} = x_i - x_j, \tag{2.9}$$

$$\boldsymbol{x}_{\text{L-L}} = \begin{bmatrix} x_{\mathrm{ab}} & x_{\mathrm{bc}} & x_{\mathrm{ca}} \end{bmatrix}^{\top}, \tag{2.10}$$

where x_{ij} is the variable for (i, j), which corresponds to phase pairs (a,b), (b,c) and (c,a) for each of the line-to-line axes.

The airgap torque can be expressed as

$$T = \frac{3N_{\mathrm{p}}}{2}\left(\Psi_{\mathrm{d}}i_{\mathrm{q}} - \Psi_{\mathrm{q}}i_{\mathrm{d}}\right), \tag{2.11}$$

and the load angle δ is defined in this work as

$$\delta = \angle\boldsymbol{\Psi}_{\mathrm{dq}}. \tag{2.12}$$

The flux linkage for a machine with linear magnetization can be modeled as

$$\boldsymbol{\Psi}_{\mathrm{dq}} = \boldsymbol{L}_{\mathrm{dq}}\boldsymbol{i}_{\mathrm{dq}} + \begin{bmatrix} \Psi_{\mathrm{PM}} & 0 \end{bmatrix}^{\top}, \tag{2.13a}$$

$$\boldsymbol{L}_{\mathrm{dq}} = \begin{bmatrix} L_{\mathrm{d}} & 0 \\ 0 & L_{\mathrm{q}} \end{bmatrix}, \tag{2.13b}$$

where $\boldsymbol{L}_{\mathrm{dq}}$ is the matrix of absolute inductances. However, for highly utilized machines, the magnetic (cross-)saturation effects are not negligible. Thus, in this work the flux is considered as a nonlinear static function of the operating point, as

$$\boldsymbol{\Psi}_{\mathrm{dq}} = \boldsymbol{\Psi}_{\mathrm{dq}}(\boldsymbol{i}_{\mathrm{dq}}). \tag{2.14}$$

Within (2.8a) this can be incorporated as

$$\boldsymbol{u}_{\mathrm{dq}} = \boldsymbol{R}_{\mathrm{dq}}\boldsymbol{i}_{\mathrm{dq}} + \boldsymbol{L}_{\mathrm{dq},\Delta}(\boldsymbol{i}_{\mathrm{dq}})\frac{\mathrm{d}\boldsymbol{i}_{\mathrm{dq}}}{\mathrm{d}t} + \omega_{\mathrm{e}}\boldsymbol{J}\boldsymbol{\Psi}_{\mathrm{dq}}(\boldsymbol{i}_{\mathrm{dq}}), \tag{2.15a}$$

$$\boldsymbol{L}_{\mathrm{dq},\Delta}(\boldsymbol{i}_{\mathrm{dq}}) = \begin{bmatrix} \dfrac{\partial\Psi_{\mathrm{d}}(\boldsymbol{i}_{\mathrm{dq}})}{\partial i_{\mathrm{d}}} & \dfrac{\partial\Psi_{\mathrm{d}}(\boldsymbol{i}_{\mathrm{dq}})}{\partial i_{\mathrm{q}}} \\ \dfrac{\partial\Psi_{\mathrm{q}}(\boldsymbol{i}_{\mathrm{dq}})}{\partial i_{\mathrm{d}}} & \dfrac{\partial\Psi_{\mathrm{q}}(\boldsymbol{i}_{\mathrm{dq}})}{\partial i_{\mathrm{q}}} \end{bmatrix} = \begin{bmatrix} L_{\mathrm{dd}}(\boldsymbol{i}_{\mathrm{dq}}) & L_{\mathrm{dq}}(\boldsymbol{i}_{\mathrm{dq}}) \\ L_{\mathrm{qd}}(\boldsymbol{i}_{\mathrm{dq}}) & L_{\mathrm{qq}}(\boldsymbol{i}_{\mathrm{dq}}) \end{bmatrix}, \tag{2.15b}$$

where $\boldsymbol{L}_{\mathrm{dq},\Delta}$ is the differential inductance matrix. The normalized flux maps for the machine considered in this investigation are depicted in Fig. 2.5. All other nonlinear effects (e.g., temperature dependencies, slotting effect) are neglected. Further, only copper losses are considered (i.e., iron losses and their effect on optimal operating paths [41] are neglected)[3].

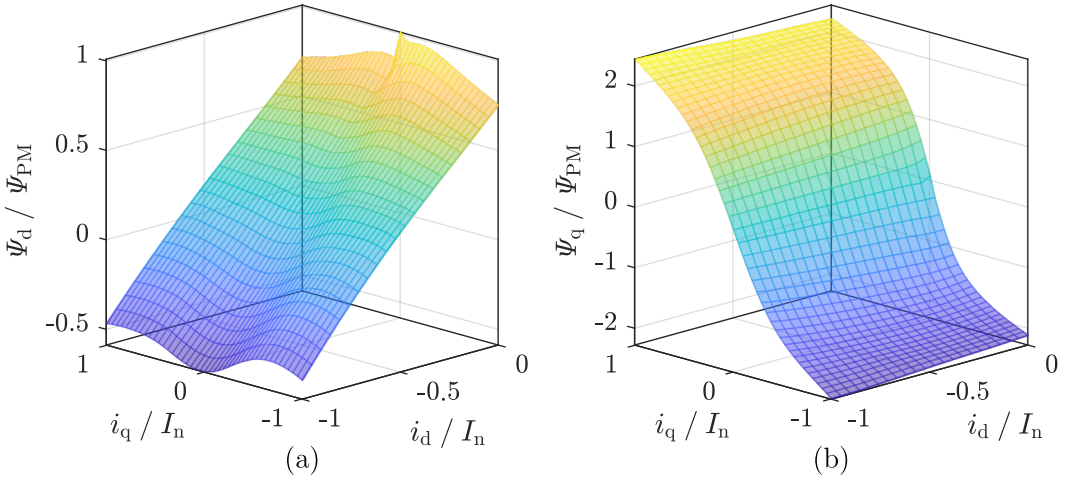


Fig. 2.5: Normalized d- (a) and q- (b) flux linkage maps

The operation of such a machine can be divided in two areas: base speed and flux-weakening region (cf. Fig. 1.2). Maximum torque-per-current (MTPC)[4] is applied at low speeds in order to produce the desired torque output with minimum ohmic losses. With increasing speed, the back-emf induced voltage increases. When the voltage limit is reached, the desired torque can no longer be achieved with MTPC, since some current

[3]This assumption may not apply for all drives and modulation strategies. Furthermore, it is usually the case in practice that overall loss minimization is not necessarily the desired objective, but rather the allocation of the losses to different systems (e.g., inverter or machine) or elements within a system (e.g., copper, iron, or magnets). Some strategies may be unwanted, even if they improve the overall efficiency, when they introduce unwanted effects, e.g., increasing magnet losses leading to high temperature and demagnetization. These considerations are not within the scope of this work, and they should be accounted for by a higher level system-control strategy.

[4]This operation mode is commonly referred to in the literature as maximum-torque-per-ampere (MTPA). This terminology is avoided here to preserve the author's continued well-being among colleagues.

must be invested in weakening the flux linkage to reduce the induced voltage, i.e., flux weakening region. If speed increases further, at some point the maximum torque operation is no longer obtained at the current limit but at the maximum torque-per-flux (MTPF) locus. The MTPC, MTPF, current limit, voltage limits for various speeds, and trajectory for maximum torque operation with increasing speed for an exemplary PMSM are depicted in Fig. 2.6.

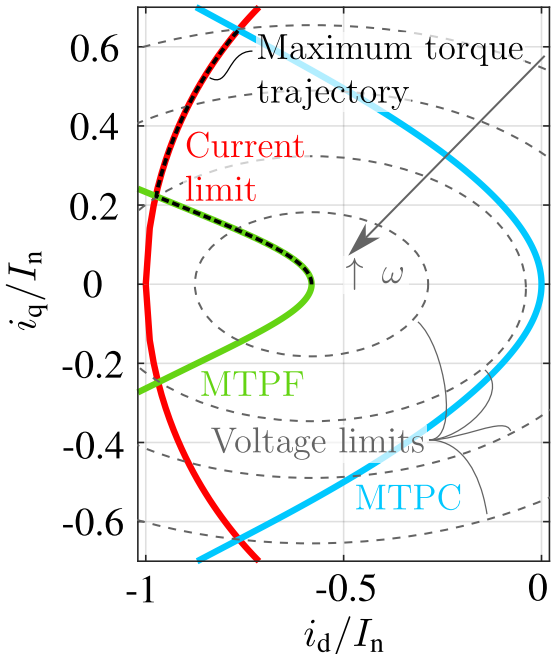


Fig. 2.6: Operating regions of PMSMs in the dq-current plane

It should be clear that increased voltage utilization is only advantageous in steady-state in the flux weakening region. For the base speed region, i.e., at or below base speed, the only advantage would come from an increased voltage margin for transient control. Once the available voltage becomes the limiting factor, however, operating with increased voltage utilization enables both higher maximum torque, and operation at lower current amplitude for partial load, leading to higher efficiency (assuming copper losses are dominant).

2.2 Control Frameworks

The control strategy is responsible for processing the information from the sensors and generate action commands for the inverter to achieve the desired operating point, according to the set reference (e.g., torque), operating constraints (e.g., current and voltage) and optimization criteria (e.g., fast dynamic response, reduced losses). The controller must ensure stable operation throughout the operating range, robustness against disturbances, proper reference tracking, and adequate dynamic performance. If degrees of freedom are available, other concerns such as reducing losses can be taken into account. Modern drives

utilize digital signal processors and thus must be implemented accounting sampling effects and actuation delays. For this purpose, the drive dynamics in (2.7a) can be discretized applying the forward Euler method as

$$\boldsymbol{\Psi}_{\alpha\beta}[k+1] = \boldsymbol{\Psi}_{\alpha\beta}[k] + T_\mathrm{s}\left(\boldsymbol{u}_{\alpha\beta}[k] - \boldsymbol{R}_{\alpha\beta}\boldsymbol{i}_{\alpha\beta}[k]\right), \tag{2.16}$$

where k is the sampling instant and T_s is the sampling period.

Prior to the control task implementation, the data from the sensors must be processed. Other than appropriate scaling of the received signals, two ancillary systems are worth noting in this implementation. First, the DC-bus voltage measurement is filtered, as it is assumed not to change significantly and this would protect against measurement noise. The low-pass filter (LPF) utilized was tuned to $\tau_{u_\mathrm{DC},\mathrm{filt}} = 9T_\mathrm{s}$ to provide sufficient noise attenuation without introducing excessive delay. Secondly, to obtain reliable speed information from the resolver angle measurement, a phase-locked-loop (PLL) is implemented. Its tuning is set as $K_{\mathrm{P,PLL}} = 2\omega_\mathrm{PLL}$, $K_{\mathrm{I,PLL}} = \omega_\mathrm{PLL}^2$, achieving unit damping for fast, non-oscillatory convergence. The natural frequency is set at $\omega_\mathrm{PLL} = \sqrt{\alpha_\mathrm{e}/e_{\theta_\mathrm{e}}}$, obtained via the final-value theorem upon the angle-error transfer function for a constant acceleration, and considering a reasonably low angle tracking error of $e_{\theta_\mathrm{e}} = 4°$ at a large acceleration of $\alpha_\mathrm{e} = \omega_{\mathrm{e,max}}/1\,\mathrm{s}$, with

$$\omega_{\mathrm{e,max}} = n_\mathrm{max} N_\mathrm{p} \frac{2\pi\ \mathrm{s}^{-1}}{60\ \mathrm{min}^{-1}}. \tag{2.17}$$

This tuning choice ensures adequate speed and angle tracking within the expected operating conditions.

2.2.1 Field-Oriented Control

The proposed MPDSC is intended as an extension of the preferred industry control strategy, i.e., FOC. A simplified diagram of the implemented strategy is depicted in Fig. 2.7. The generation of dq-current references is accomplished as described in [41], [42]. The PI-controllers and induced voltage compensation are implemented according to a discrete plant model, and considering the machine's nonlinear flux maps and appropriate values for the differential inductances to ensure stability as in [42]. The PI controllers are tuned via pole placement to achieve a PT_1[5] behavior with time constant $\tau = -T_\mathrm{s}/\ln(r_\mathrm{goal})$, with r_goal being the desired pole location in the z-plane, chosen as 0.95 to balance dynamic response and noise rejection. The modulation strategy, explained in the following, synthesizes the reference switching time commands for each of the semiconductors ($\boldsymbol{t}^*_{\mathrm{s,FOC}}$), limits the reference action, and calculates the modulation index (M_idx). This value is considered within the modulation controller, which slowly adapts the flux reference to prevent steady-state operation with low voltage margin while allowing short-term use of the overmodulation region for transient control.

[5] This terminology refers to *proportionaler Tiefpassfilter erster Ordnung*, i.e., first-order low-pass filter.

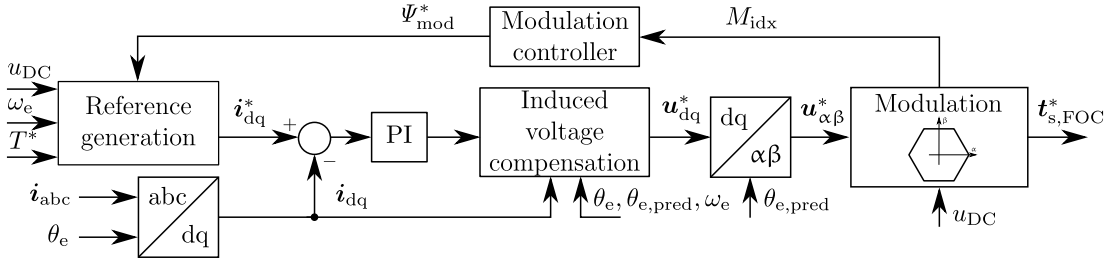


Fig. 2.7: Simplified FOC control diagram

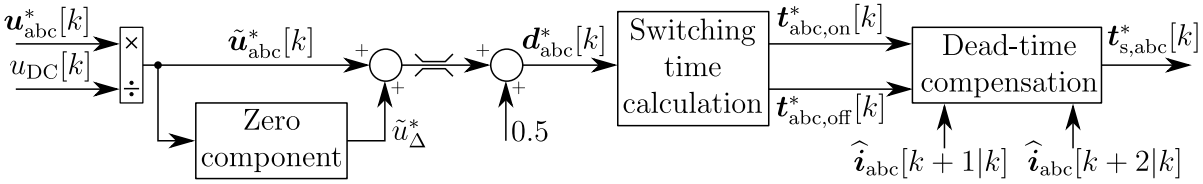


Fig. 2.8: Modulation strategy for FOC

2.2.1.1 Modulation Strategy

The structural visualization of the voltage reference adaptation, switching time command generation, and dead-time compensation is given in Fig. 2.8. First, the reference voltage is normalized and a zero component is added to all three phases, which does not affect the line voltages and thus the currents, due to the floating neutral point of the machine [40]. This zero component can be calculated as

$$\tilde{u}^*_{\Delta} = \frac{1}{2}\left(\max(\tilde{\boldsymbol{u}}^*_{\mathrm{abc}}) + \min(\tilde{\boldsymbol{u}}^*_{\mathrm{abc}})\right), \tag{2.18}$$

which symmetrizes the null-voltage component achieving symmetrical sine-triangle modulation. This is the method utilized for the experimental evaluation.

Alternatively, the references can be adapted to prevent duty cycle commands $\boldsymbol{d}^*_{\mathrm{abc}}$ close but not equal to 0 or 1, as those commands require good resolution for narrow pulses, which is sometimes not possible when delay and dead-time effects are at play. One method that achieves this is flat top modulation, here implemented as

$$\tilde{u}^*_{\Delta} = \begin{cases} 0.5 - \max\left(\tilde{\boldsymbol{u}}^*_{\mathrm{abc}}\right) & \text{if } |\max(\tilde{\boldsymbol{u}}^*_{\mathrm{abc}})| \geq |\min(\tilde{\boldsymbol{u}}^*_{\mathrm{abc}})|, \\ -0.5 - \min\left(\tilde{\boldsymbol{u}}^*_{\mathrm{abc}}\right) & \text{otherwise.} \end{cases} \tag{2.19}$$

This method was utilized in the simulation evaluation to improve the FOC results. Experimental evaluation of this modulation method was not possible as explained in App. B.

After the reference adaptation, the duty cycles $\boldsymbol{d}^*_{\mathrm{abc}}$ are calculated in a range of 0 to 1, and the ideal switching times are calculated as

$$\boldsymbol{t}^*_{\mathrm{abc,on}}[k] = \frac{T_\mathrm{s}}{2}(1 - \boldsymbol{d}^*_{\mathrm{abc}}[k]), \tag{2.20}$$

$$\boldsymbol{t}^*_{\mathrm{abc,off}}[k] = \frac{T_\mathrm{s}}{2}(1 + \boldsymbol{d}^*_{\mathrm{abc}}[k]). \tag{2.21}$$

Finally, the dead-time compensation is performed as explained in Sec. 3.2.1.3.

2.2.2 Direct Self-Control

The continuous time implementation of DSC [6], considering perfect flux knowledge and instantaneous actuation on the inverter switches, can be achieved according to Fig. 2.9. A hysteresis comparator can be established for each of the phases, turning on when the upper limit is reached and turning off when the lower limit is reached. A one-to-one relation can be established between the change of state required in each inverter phase and the limits (U for upper, L for lower) being reached in each of the line-to-line fluxes. An example of this switching process is shown in Fig. 1.4, where reaching the ab-flux linkage threshold triggers the transition from voltage vector 1 to 2.

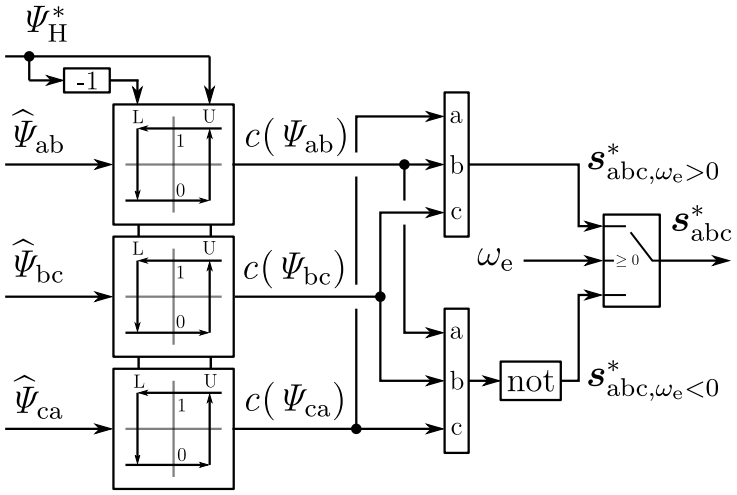


Fig. 2.9: Flux control diagram for continuous-time implementation of DSC

The time derivative of the line-to-line flux during six-step operation with DSC can be considered as

$$\frac{\mathrm{d}\boldsymbol{\Psi}_\mathrm{L\text{-}L}}{\mathrm{d}t} = \begin{cases} \pm u_\mathrm{DC} - \boldsymbol{u}_\mathrm{R,L\text{-}L} \mp \boldsymbol{u}_\mathrm{drop} & \text{when evolving between the limits,} \\ 0 & \text{otherwise,} \end{cases} \tag{2.22}$$

where $\boldsymbol{u}_\mathrm{R,L\text{-}L}$ is the resistive voltage drop in the machine and $\boldsymbol{u}_\mathrm{drop}$ is the voltage drop in the inverter. This value, when non-zero, is largely dominated by the DC-bus voltage, which can be considered constant within a short time horizon. Thus, flux rotational frequency depends on the size of the hexagon path, providing the basis for load angle control introduced in the following chapter.

3 Model Predictive Direct Self-Control for Six-Step Operation

This chapter presents the proposed MPDSC strategy, a solution for operation in the flux-weakening range achieving maximum voltage utilization. Despite the control method being intended as an enhancement of FOC, this chapter focuses on MPDSC operation individually. The adaptation from the original concept [6], core working principles as well as ancillary systems are explored. Finally, the presented approach is validated with simulation and experimental results.

3.1 Modifications to DSC

As discussed in Sec. 1.3, the DSC strategy was originally intended for analog implementation with induction machines. The transfer of this strategy to digital control of PMSMs involved certain modifications, namely

- torque control through load angle control,
- flux reference generation ensuring synchronous rotation of stator and rotor flux, and
- model prediction to enable discrete-time implementation avoiding flux amplitude fluctuations and compensating for the sampling-to-actuation delay,

These are explained in detail in the following.

3.1.1 Torque Control

The control strategy aims to attain the reference torque set by the upper-level control. From a simplified linear PMSM model as given by (2.11), (2.12), and (2.13), it can be shown that torque production can be controlled by means of flux amplitude and load angle, as given by

$$T = \frac{3N_\mathrm{p}\Psi_\mathrm{s}}{2L_\mathrm{d}L_\mathrm{q}}\left(L_\mathrm{q}\Psi_\mathrm{PM}\sin\delta + \frac{\Psi_\mathrm{s}}{2}(L_\mathrm{d}-L_\mathrm{q})\sin 2\delta\right), \tag{3.1}$$

where Ψ_s is the flux linkage amplitude. The flux differential equation in the stator reference frame is, from (2.2),

$$\frac{\mathrm{d}\boldsymbol{\Psi}_{abc}}{\mathrm{d}t} = \boldsymbol{u}_{abc} - R_s \boldsymbol{i}_{abc}, \tag{3.2}$$

where $\boldsymbol{\Psi}_{abc}$ is the flux in the abc-reference frame. Neglecting resistive voltage drop, the flux variation depends only on stator voltage. During six-step operation the voltage amplitude is fixed (equal to $2u_{DC}/3$ in the abc-reference frame, or u_{DC} in the line-to-line reference frame), only changing its phase. This results in the hexagonal flux path observed in Fig. 3.1, where $\boldsymbol{\Psi}_r$ is the rotor flux vector, $\boldsymbol{\Psi}_s$ the stator flux vector, θ_e the rotor flux angle in the stationary reference frame, and θ_s the stator flux angle in the stationary reference frame. The size of the hexagonal flux path can be considered by the amplitude at the middle of the hexagon side (Ψ_h) or at the corner ($\Psi_{hc} = 2\Psi_h/\sqrt{3}$).

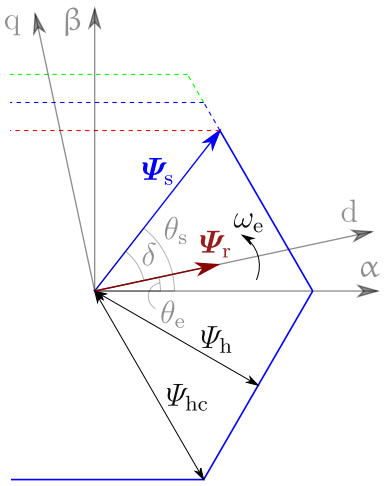


Fig. 3.1: Ideal flux path during six-step operation in PMSM

Since the voltage amplitude does not change, the tip of the flux space vector travels at a constant rate through the hexagonal path during six-step operation. From (2.22) and Fig. 1.4, the average flux linkage rotational frequency can be approximated based on the size of the hexagon as

$$\omega_\Psi = \frac{\mathrm{d}}{\mathrm{d}t}\theta_s, \tag{3.3}$$

$$\overline{\omega}_\Psi \approx \frac{2\pi u_{DC}}{6\sqrt{3}\,\Psi_h}, \tag{3.4}$$

where ω_Ψ is the stator flux linkage rotational frequency. Considering the machine rotational frequency as an external input, the load angle is dynamically modified depending on flux amplitude in six-step operation as

$$\frac{\mathrm{d}}{\mathrm{d}t}\delta = \omega_\Psi - \omega_e \approx \overline{\omega}_\Psi(\Psi_h, u_{DC}) - \omega_e. \tag{3.5}$$

The DSC strategy is capable of controlling the stator flux amplitude following the six-step voltage sequence. From the instant shown in Fig. 3.1, different flux paths are possible that achieve this while increasing (green), maintaining (blue), or reducing (red) the hexagon path size. This provides a control strategy capable of operating in six-step with a single degree-of-freedom.

The flux reference fed to the flux control should ensure stability, accurate torque reference tracking during steady-state operation, control of torque transients, and rejection of disturbances caused by changes in speed, machine parameters, or other sources. A closed-loop torque controller could directly generate this reference. However, the relation between load angle and torque is highly nonlinear and depends on the operating point, as shown in Fig. 3.2. This figure is based on (2.11) and machine data available shown in Fig. 2.5.

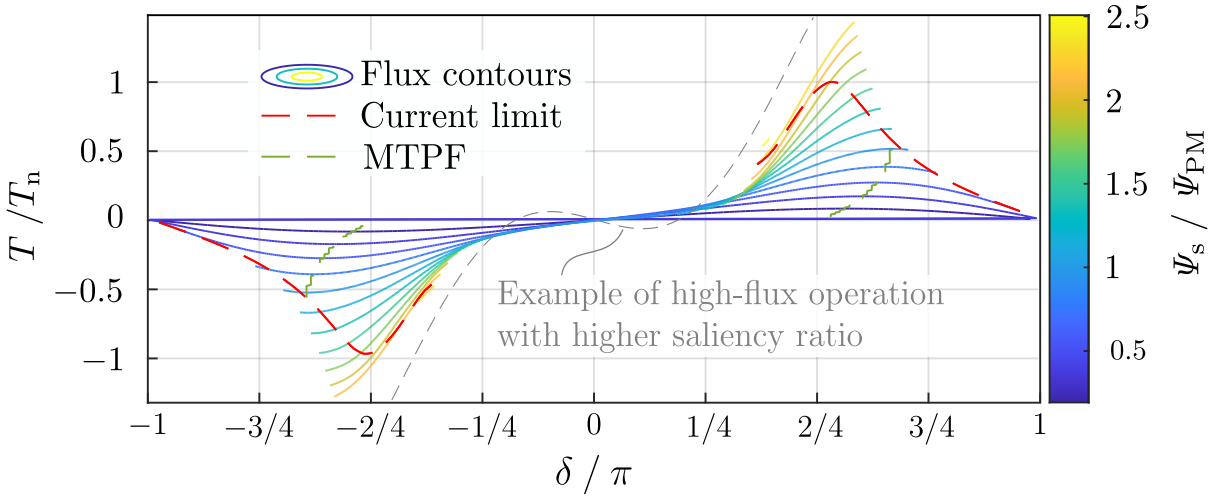


Fig. 3.2: Torque relation with load angle depending on flux amplitude for the machine model considered, and example for higher saliency ratio

For high flux amplitude (only attainable at low speed), an increase in load angle increases torque in all operating points within the drive capabilities. Although this is not the case for the machine represented, this relation can be inverted in the neighborhood of null load angle depending on the machine parameters, i.e., the slope of the curve would be negative around zero load angle. This occurs for

$$\frac{\Psi_\mathrm{PM}}{\Psi_\mathrm{s}} + \frac{L_\mathrm{d}}{L_\mathrm{q}} < 1. \tag{3.6}$$

An example of this is shown in a dashed grey line in Fig. 3.2 for high-flux operation in a similar machine with a higher saliency ratio. For low flux amplitude (as is the case for high speed in the flux-weakening range), the relation is also inverted after a certain load angle value, i.e., an increase in load angle produces a decrease in torque. The point at which this change occurs denotes the MTPF operation. A linear torque controller that does not account for these effects would cause instability.

To manage these nonlinearities, torque control could be achieved by a nonlinear controller or linear with scheduled gains. These options would complicate the control strategy, make it difficult to tune accurately, and be especially problematic around the MTPF region.

Alternatively, a simpler load angle controller may be implemented. This way, the system's dynamic behavior does not change in the neighborhood of the MTPF operating point (cf. Fig. 3.10). Divergence from the correct MTPF operation would only introduce a steady-state torque deviation. The load angle reference can be generated taking into account the reference torque and flux amplitude. This relation can be transformed into a look-up table (LUT) in order to generate a load angle reference that would bring about the reference torque. The nonlinearities observed in Fig. 3.2 are embedded in this relation and thus no longer need to be addressed by the control strategy. Furthermore, for a constant load angle reference, the feedback load angle control ensures the synchronous rotation of the stator flux with the rotor.

3.1.2 Delay Compensation

In the discrete-time domain, the controller does not have continuous access to the line-to-line flux values, nor can the switching commands be generated and achieved instantaneously. The sequence of events is shown in Fig. 3.3, where T_s is the sampling period duration. At the start of each sampling period, the measurements from the machine are sampled. During each sampling period, the times at which each of the inverter switches will turn on and off during the next sampling period is calculated. Therefore, the need to command a switching event must be detected, and the switching times calculated, more than one sampling period before the switching happens (one sampling period for the sampling delay, and less than one sampling period until the switching sequence command is executed). Not doing so would result in a large variance in the duration for which each of the voltage vectors is applied (cf. comparison with [34] in Sec. 3.4.2). Consequently, the discrete-time implementation must follow a model predictive flux control (MPFC) approach.

An example of the MPFC operation is shown in Fig. 3.4, where Ψ_H^* is the hexagonal flux amplitude reference for the line-to-line flux and $\widehat{x}$ depicts estimation or prediction. The figure depicts the flux prediction for various sampling instants (k, $k+1$, $k+2$) from the information available at time k. For the prediction at $k+2$, it is assumed the voltage does not change after $k+1$. In the top plot, the intervals highlighted in yellow correspond to those in which, for the ab-flux, the need for a switching event (i.e., $|\widehat{\Psi}_\mathrm{ab}[k+2|k]| > \Psi_\mathrm{H}^*$) is detected, and the appropriate switching time command for inverter leg b is calculated. The execution of this command is also highlighted in the third plot.

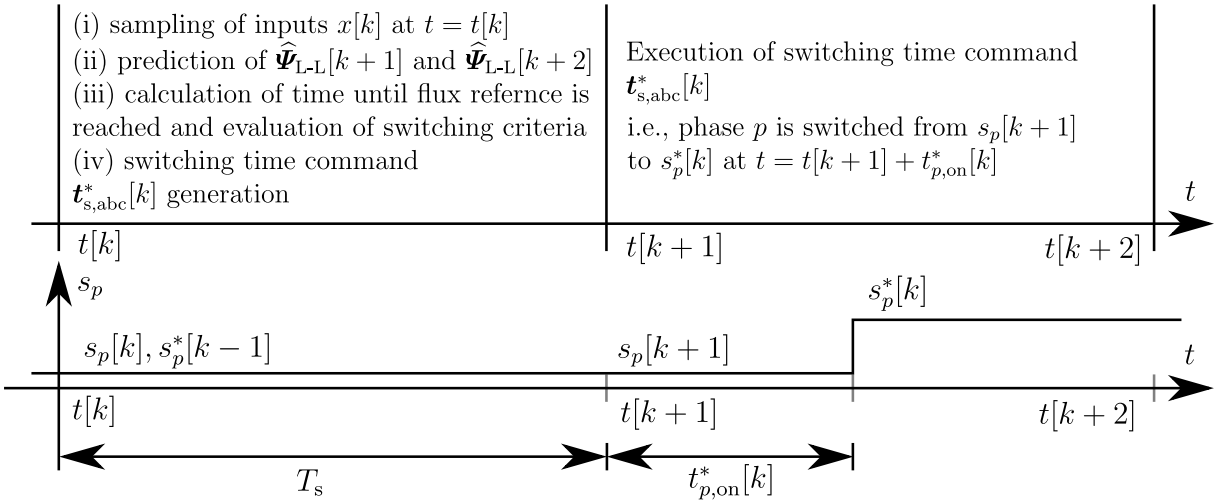


Fig. 3.3: Event sequence for discrete-time implementation of MPDSC

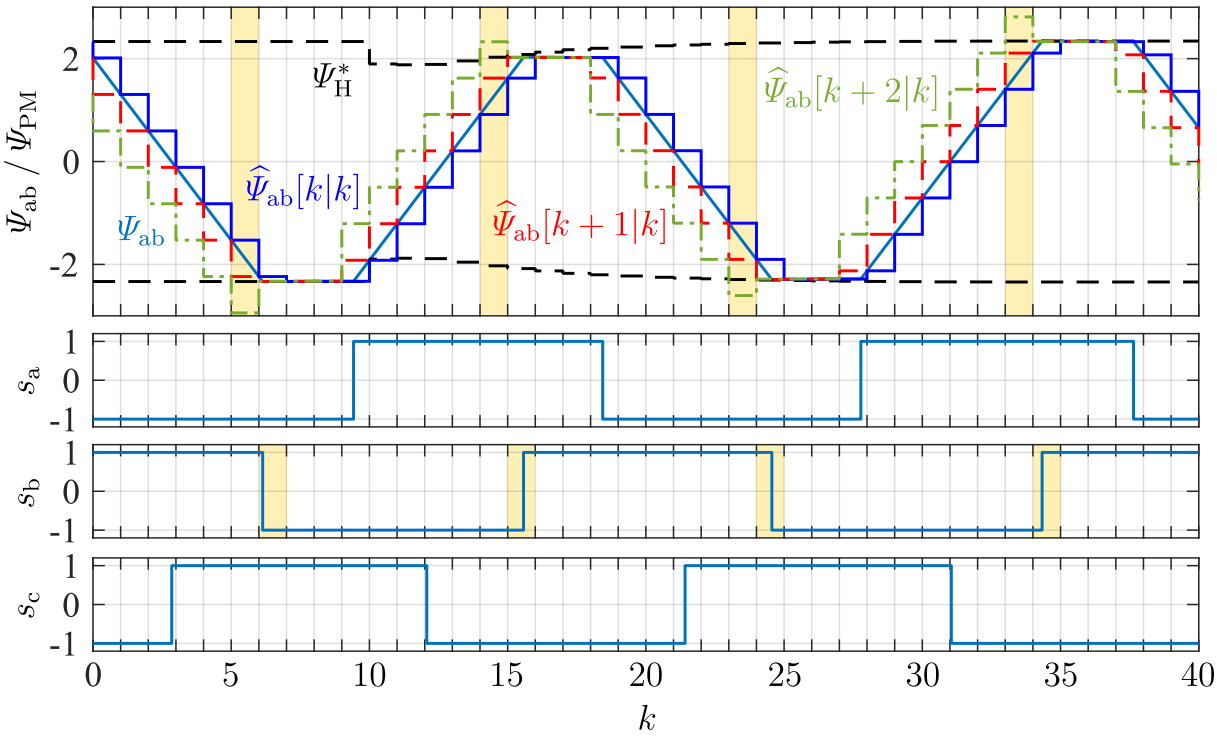


Fig. 3.4: Example of the switching pulse generation by the proposed MPFC. From top to bottom: ab-flux linkage (with reference, estimation, and prediction one and two-steps ahead), switching pulses in phases a, b, and c

3.2 Overview of MPDSC

The stator flux angular frequency during the six-step operation depends on the flux amplitude. Hence, the flux amplitude can be used as an actuating variable to control the load angle. The control is simplified by first generating a load angle reference from the torque reference information, which is used as the controller's input that produces the flux amplitude reference. Fig. 3.5 shows the discrete-time MPDSC implementation, with its four basic subfunctionalities highlighted.

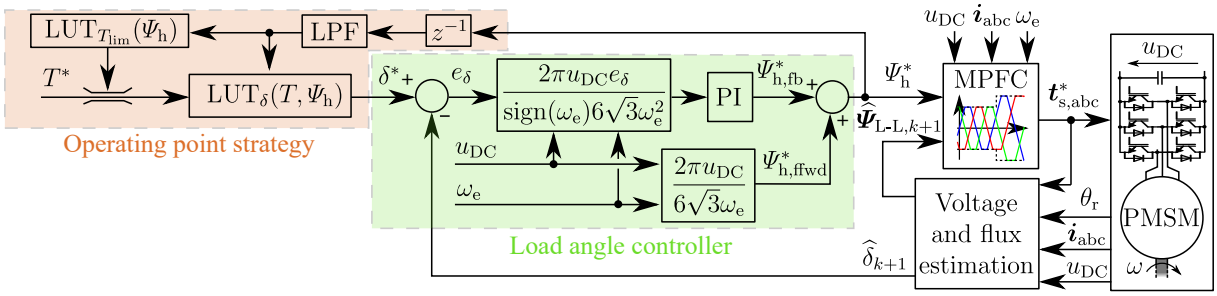


Fig. 3.5: Control diagram for torque control in the flux-weakening region with MPDSC

- MPFC: This strategy generates switching-time commands based on comparing the predicted machine flux in the line-to-line reference frame with an externally generated reference. When the predicted flux reaches the reference value, a switching is triggered towards the next active voltage in the six-step sequence. For discrete-time implementation, model prediction is required to account for the variable delay between sampling and actuation.
- Load angle controller: The flux amplitude reference is achieved through a combination of feed-forward control (estimating the steady-state flux amplitude for six-step operation based on DC-bus voltage and electric frequency) and feedback control (through a PI-controller with constant gains and an operating-point-dependent scaling).
- Operating point strategy: The relation between torque and load angle embedded into LUT_{δ} can be obtained using the machine characteristic information (current-flux relation accounting for saturation phenomena) and a fundamental machine model or via a specific application protocol. Torque and flux amplitude uniquely define the operating point in the desired operating region. The latter is estimated from the flux amplitude reference (Ψ^*_{h}) fed to the MPFC algorithm via an LPF.
- Voltage and flux estimation: This control strategy requires knowledge of the machine flux, both for load angle feedback control and flux control. This, in turn, involves voltage estimation from the switching time commands. The flux is estimated using a Gopinath-style flux observer, and appropriate coordinate transformations are applied to obtain the desired output variables. Moreover, the inherent load angle ripple present in six-step is compensated, enhancing the performance of the controller in discrete time.

It must be noted that the control strategy presented in this chapter is only intended for six-step operation in the flux weakening range. Enhancements to handle the operation below base speed and the fade-over to other strategies are discussed in Ch. 4, and the generation of alternative switching patterns is discussed in Ch. 5.

3.2.1 Model Predictive Flux Control

The proposed MPFC modifies the strategy detailed in Sec. 1.3 and 2.2.2 for its implementation in discrete time for processor-based applications with a low sampling rate. The MPFC follows the algorithm represented in Fig. 3.6, where k is the discrete-time sampling index. A crucial aspect of this solution is the application of flux prediction based on the machine model (2.22), allowing for minimal flux amplitude tracking errors down to extremely low sampling-to-fundamental-frequency ratio ($3 < \min(T_\mathrm{e}/T_\mathrm{s}) < 4$)[1]. Such an operating point, depicting the variables involved and their interaction for switching command generation, is shown in Fig. 3.7, where $c\,(\Psi_{ij})$ is the switching criteria as described in Sec. 3.2.1.2.

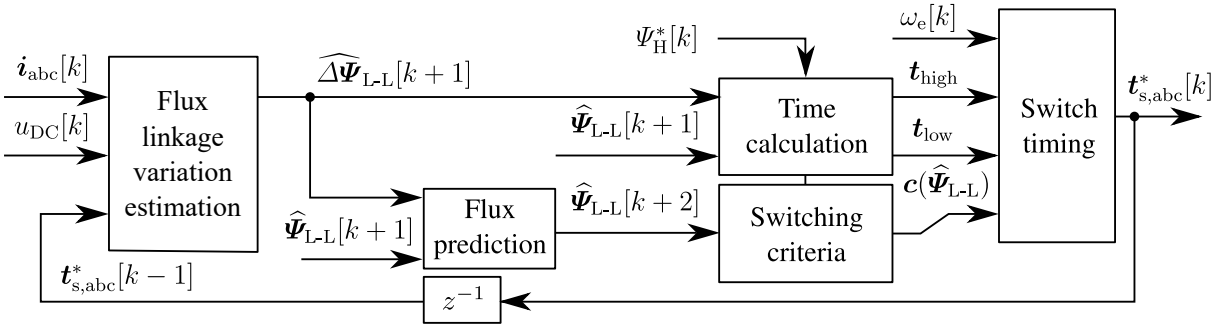


Fig. 3.6: Model predictive flux control schematic

For MPFC, perfect flux knowledge is assumed at the end of the momentary sampling period. The prediction is done in two stages. First, the flux at the end of the next sampling period is predicted using the flux at the start of the sampling period, the previous switching state command, and the current information. Then, the time required to reach the reference flux from the end of the present sampling period, maintaining the same voltage, is calculated. This time-until-next-switching is used to generate the switching time commands for the inverter semiconductors. The requirement of a minimum of three measurement samples per electric rotation stems from the usage of a two steps-ahead prediction of the flux.

[1]In this report, the number of samples per electrical revolution demonstrated experimentally is constrained to a minimum of 12.5 by the load machine's maximum speed in the utilized testbench. Thus, the capabilities of the algorithm to operate with under 4 samples per fundamental period is only demonstrated through simulation results in Fig. 3.7.

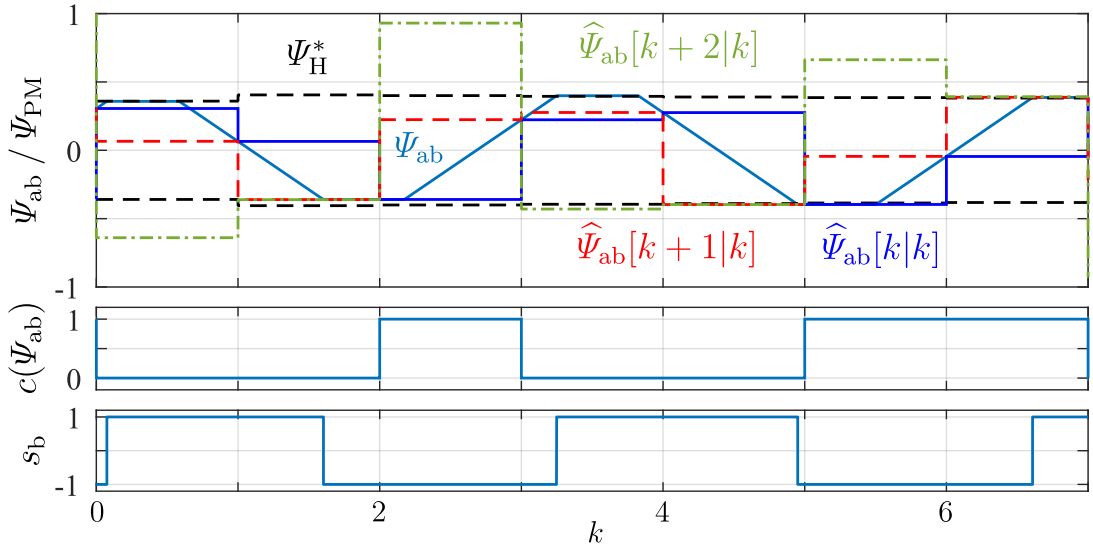


Fig. 3.7: Switching pulse generation by the MPFC algorithm operating at 3.05 samples per electrical revolution. From top to bottom: ab-flux linkage, ab-switching condition, and switching pulses for phase b

3.2.1.1 Flux Linkage Prediction

Assuming there will be at least three samples per electrical revolution, a maximum of two switching events will occur during a sampling period for six-step operation. The line-to-line flux machine model is obtained from equation (3.2), discretized as

$$\boldsymbol{\Psi}_{\mathrm{abc}}[k+1] = \boldsymbol{\Psi}_{\mathrm{abc}}[k] + T_{\mathrm{s}}\left(\boldsymbol{u}_{\mathrm{abc}}[k] - R_{\mathrm{s}}\boldsymbol{i}_{\mathrm{abc}}[k]\right), \tag{3.7}$$

following the forward or explicit Euler method. Considering an ideal inverter model (i.e., with no voltage drop), the expected line-to-line voltage variation can be calculated from $s_p[k+1]$, which is the switching state in each phase p at the end of the momentary sampling period (i.e., at instant $k+1$). For improved accuracy, the predicted phase resistive voltage drop (cf. Sec. 3.2.4.2) can also be considered, as

$$\Delta\widehat{\Psi}_{\mathrm{ab}}[k+1] = T_{\mathrm{s}}\left[(s_{\mathrm{a}}[k+1] - s_{\mathrm{b}}[k+1])/2 \cdot u_{\mathrm{DC}}[k] - (\widehat{i}_{\mathrm{a}}[k+1] - \widehat{i}_{\mathrm{b}}[k+1])R_{\mathrm{s}}\right], \tag{3.8a}$$

$$\Delta\widehat{\Psi}_{\mathrm{bc}}[k+1] = T_{\mathrm{s}}\left[(s_{\mathrm{b}}[k+1] - s_{\mathrm{c}}[k+1])/2 \cdot u_{\mathrm{DC}}[k] - (\widehat{i}_{\mathrm{b}}[k+1] - \widehat{i}_{\mathrm{c}}[k+1])R_{\mathrm{s}}\right], \tag{3.8b}$$

$$\Delta\widehat{\Psi}_{\mathrm{ca}}[k+1] = T_{\mathrm{s}}\left[(s_{\mathrm{c}}[k+1] - s_{\mathrm{a}}[k+1])/2 \cdot u_{\mathrm{DC}}[k] - (\widehat{i}_{\mathrm{c}}[k+1] - \widehat{i}_{\mathrm{a}}[k+1])R_{\mathrm{s}}\right]. \tag{3.8c}$$

For this algorithm, it is sufficient to predict the expected line-to-line flux variation assuming the voltage at the end of the present sampling period is maintained. This consideration ensures that the prediction is accurate in the sampling period before a switching event, even for operation at a very low (up to three) samples per electrical revolution, as seen in Fig. 3.7.

Using the information of the expected flux linkage variation, the flux at the end of the next sampling period can be predicted (i.e., $\widehat{\boldsymbol{\Psi}}_{\text{L-L}}[k+2]$). The flux prediction one-step-ahead

$\hat{\boldsymbol{\Psi}}_{\text{L-L}}[k+1]$ should consider the switching sequence generated in the previous sampling period, and it is used for other parts of the algorithm that require large accuracy. Therefore, the method considers a comprehensive model of the inverter, for which details are provided in Sec. 3.2.4.3. The two-steps-ahead flux prediction is achieved as

$$\hat{\boldsymbol{\Psi}}_{\text{L-L}}[k+2] = \hat{\boldsymbol{\Psi}}_{\text{L-L}}[k+1] + \Delta\hat{\boldsymbol{\Psi}}_{\text{L-L}}[k+1], \tag{3.9}$$

where $\hat{\boldsymbol{\Psi}}_{\text{L-L}}$ is the vector of estimated or predicted line-to-line fluxes.

3.2.1.2 Switching Time Setting

The time that it would take the flux in each of the line-to-line axes to reach the upper $\boldsymbol{t}_{\text{up}}$ and lower $\boldsymbol{t}_{\text{low}}$ line-to-line flux linkage reference Ψ^*_{H} from the end of the momentary sampling period if the voltage was maintained are calculated as

$$\hat{t}_{\text{up},ij}[k] = T_{\text{s}} \frac{\Psi^*{}_{\text{H}}[k] - \widehat{\Psi}_{ij}[k+1]}{\Delta\widehat{\Psi}_{ij}[k+1]}, \tag{3.10}$$

$$\hat{t}_{\text{low},ij}[k] = T_{\text{s}} \frac{-\Psi^*{}_{\text{H}}[k] - \widehat{\Psi}_{ij}[k+1]}{\Delta\widehat{\Psi}_{ij}[k+1]}. \tag{3.11}$$

The switching criteria $\boldsymbol{c}(\boldsymbol{\Psi}_{\text{L-L}})$ determines whether, before the end of the next sampling period, a switching is required to keep the flux within the reference boundaries. Equivalently to continuous-time implementation, it is generated based on the hysteresis comparison between the two-step-ahead flux prediction and the flux reference as given by

$$c(\Psi_{ij})[k] = 0 \quad \text{if} \;\; c(\Psi_{ij})[k-1] = 1 \;\wedge\; \widehat{\Psi}_{\text{ij}}[k+2] \leq -\Psi^*{}_{\text{H}}[k], \tag{3.12a}$$

$$c(\Psi_{ij})[k] = 1 \quad \text{if} \;\; c(\Psi_{ij})[k-1] = 0 \;\wedge\; \widehat{\Psi}_{\text{ij}}[k+2] \geq \Psi^*{}_{\text{H}}[k], \tag{3.12b}$$

$$c(\Psi_{ij})[k] = c(\Psi_{ij})[k-1] \quad \text{otherwise.} \tag{3.12c}$$

These signals are equivalent to the switching pulse commands in the continuous-time implementation shown in Fig. 1.4. The collective output of these comparators is referenced as $\boldsymbol{c}(\boldsymbol{\Psi}_{\text{L-L}})$, and for each axis as $c\,(\Psi_{\text{ab}})$, $c\,(\Psi_{\text{bc}})$, and $c\,(\Psi_{\text{ca}})$, respectively. Two-steps-ahead flux prediction accuracy is, therefore, only relevant in the sampling period before the switching event that the prediction will trigger, and for which the time calculated from the one-step-ahead prediction will be used. The estimation remains accurate under these conditions despite a switching in other phases occurring in the meantime. The initialization of these signals is performed according to the flux location (e.g., for the situation depicted in Fig. 3.1, with $\hat{\boldsymbol{\Psi}}_{\text{s}}[k]$ located between $\boldsymbol{u}_1$ and $\boldsymbol{u}_2$, the initialization value would be $\boldsymbol{c}(\boldsymbol{\Psi}_{\text{L-L}})[k] = [1\,0\,1]^\top$).

Selecting the appropriate switching time for each semiconductor ensures that the estimated line-to-line flux is kept in the reference boundary. Tab. 3.1 summarizes the process for selection of the switching on and off time for an ideal inverter $t^*_{p,\text{on/off,ideal}}$, where p is the relevant inverter leg and c_p is the switching criteria used.

	$\omega_\mathrm{e}[k] \geq 0$			$\omega_\mathrm{e}[k] < 0$		
p	$c_p[k]$	$t^*_{p,\mathrm{on,ideal}}[k]$	$t^*_{p,\mathrm{off,ideal}}[k]$	$c_p[k]$	$t^*_{p,\mathrm{on,ideal}}[k]$	$t^*_{p,\mathrm{off,ideal}}[k]$
a	$c\left(\Psi_\mathrm{ca}\right)[k]$	$\widehat{t}_\mathrm{up,ca}[k]$	$\widehat{t}_\mathrm{low,ca}[k]$	$\overline{c\left(\Psi_\mathrm{ab}\right)}[k]$	$\widehat{t}_\mathrm{low,ab}[k]$	$\widehat{t}_\mathrm{up,ab}[k]$
b	$c\left(\Psi_\mathrm{ab}\right)[k]$	$\widehat{t}_\mathrm{up,ab}[k]$	$\widehat{t}_\mathrm{low,ab}[k]$	$\overline{c\left(\Psi_\mathrm{bc}\right)}[k]$	$\widehat{t}_\mathrm{low,bc}[k]$	$\widehat{t}_\mathrm{up,bc}[k]$
c	$c\left(\Psi_\mathrm{bc}\right)[k]$	$\widehat{t}_\mathrm{up,bc}[k]$	$\widehat{t}_\mathrm{low,bc}[k]$	$\overline{c\left(\Psi_\mathrm{ca}\right)}[k]$	$\widehat{t}_\mathrm{low,ca}[k]$	$\widehat{t}_\mathrm{up,ca}[k]$

Tab. 3.1: Switching criteria and switching times to be used in each phase according to rotation direction

As in MPDSC the actuating variable is switching time, the inverter delay (T_del) should be subtracted from the switching time command to improve the accuracy of the actuation and, therefore, of the flux control. The resulting reference switching time is

$$t^*_{p,\mathrm{on/off}}[k] = t^*_{p,\mathrm{on/off,ideal}}[k] - T_\mathrm{del}. \tag{3.13}$$

Tab. 3.2 depicts the reference on and off switching time for each semiconductor[2] in phase p, according to the switching criteria c_p as given by Tab. 3.1 and (3.13). Moreover, the necessary dead-time T_dt to avoid short-circuit in the inverter leg is also imposed by software at this stage as given in the following subsection to prevent mismatches to the desired effective switching instant. A time margin T_m introduced to ensure that the switching state at the beginning and end of the sampling period matches the desired state, in accordance with the pulse generation implementation employed[3]. The output of this process is, for each phase p, the vector $\boldsymbol{t}^*_{p,\mathrm{s}} = \left[t^*_{p,\mathrm{U,on}}\ t^*_{p,\mathrm{U,off}}\ t^*_{p,\mathrm{L,on}}\ t^*_{p,\mathrm{L,off}}\right]^\top$.

Action	$c_p[k-1]$	$c_p[k]$	$t^*_{p,\mathrm{U,on}}[k]$	$t^*_{p,\mathrm{U,off}}[k]$	$t^*_{p,\mathrm{L,on}}[k]$	$t^*_{p,\mathrm{L,off}}[k]$
Keep off	0	0	$T_\mathrm{s}+T_\mathrm{m}$	$-T_\mathrm{m}$	$-T_\mathrm{m}$	$T_\mathrm{s}+T_\mathrm{m}$
Switch on	0	1	$t^*_{p,\mathrm{on}}[k]$	$-T_\mathrm{m}$	$-T_\mathrm{m}$	$t^*_{p,\mathrm{on}}[k]$
Keep off	1	1	$-T_\mathrm{m}$	$T_\mathrm{s}+T_\mathrm{m}$	$T_\mathrm{s}+T_\mathrm{m}$	$-T_\mathrm{m}$
Switch on	1	0	$-T_\mathrm{m}$	$t^*_{p,\mathrm{off}}[k]$	$t^*_{p,\mathrm{off}}[k]$	$-T_\mathrm{m}$

Tab. 3.2: Switching time command generation according to switching criteria and switching times in each phase

[2]It should be noted that the subindexes "up" and "low" in (3.11), (3.10), and Tab. 3.1 refer to the upper and lower reference for the flux, while the subscript U and L in (3.14) to (3.19), and Tab. 3.1 and 3.2 denote the upper and lower semiconductors in each inverter leg.

[3]Switching pulse generation is performed based on the comparison of the switching time command with a carrier signal. By setting a time margin from of 0 or T_s, the command is placed beyond the carrier limits, thereby preventing the interaction with the carrier.

Alternative switching patterns can be implemented as is explored in Ch. 5. For this purpose, the switching pulse vector for each phase $\boldsymbol{t}^*_{p,\mathrm{s}}$ is expanded as

$$\boldsymbol{t}^*_{p,\mathrm{s}} = \left[t^*_{p,\mathrm{U,on},1}\; t^*_{p,\mathrm{U,on},2}\; t^*_{p,\mathrm{U,off},1}\; t^*_{p,\mathrm{U,off},2}\; t^*_{p,\mathrm{L,on},1}\; t^*_{p,\mathrm{L,on},2}\; t^*_{p,\mathrm{L,off},1}\; t^*_{p,\mathrm{L,off},2}\right]^\top, \tag{3.14}$$

where

$$t^*_{p,\mathrm{U/L,on/off},1} = t^*_{p,\mathrm{U/L,on/off}}, \tag{3.15a}$$
$$t^*_{p,\mathrm{U/L,on/off},2} = T_\mathrm{s} + T_\mathrm{m}. \tag{3.15b}$$

3.2.1.3 Dead-time Compensation

For safety reasons, it is necessary to maintain a dead-time between the switch-on of the semiconductors in the same inverter leg, during which both semiconductors are in the off state. Under these conditions, the leg operates as a passive rectifier (PR), with the anti-parallel diodes conducting according to the sign of the line current. To account for this effect and prevent distortion to the desired switching time instants, and depending on the switching scenario, the switching time commands can be modified as depicted in Fig. 3.8 and as follows. This algorithm necessitates current prediction two steps ahead, which is done equivalently to Sec. 3.2.4.2, i.e., assuming the switching state at the start of the considered sampling period is maintained.

For the turn-on behavior, switching times for the upper and lower semiconductors are calculated as

$$t^*_{p,\mathrm{on,U}}(\widehat{i}_p[k+1|k], \widehat{i}_p[k+2|k], t^*_{p,\mathrm{on}}[k]) = \begin{cases} t^*_{p,\mathrm{on}}[k] + T_\mathrm{dt} k_{p,\mathrm{i}} & \text{if } s_{p,\mathrm{PR}} = 1, \\ t^*_{p,\mathrm{on}}[k] & \text{otherwise,} \end{cases} \tag{3.16a}$$

$$t^*_{p,\mathrm{off,L}}(\widehat{i}_p[k+1|k], \widehat{i}_p[k+2|k], t^*_{p,\mathrm{on}}[k]) = \begin{cases} t^*_{p,\mathrm{on}}[k] & \text{if } s_{p,\mathrm{PR}} = 1, \\ t^*_{p,\mathrm{on}}[k] - T_\mathrm{dt} k_{p,\mathrm{i}} & \text{otherwise,} \end{cases} \tag{3.16b}$$

and for the turn-off behavior as

$$t^*_{p,\mathrm{off,U}}(\widehat{i}_p[k+1|k], \widehat{i}_p[k+2|k], t^*_{p,\mathrm{off}}[k]) = \begin{cases} t^*_{p,\mathrm{off}}[k] - T_\mathrm{dt} k_{p,\mathrm{i}} & \text{if } s_{p,\mathrm{PR}} = 1, \\ t^*_{p,\mathrm{off}}[k] & \text{otherwise,} \end{cases} \tag{3.17a}$$

$$t^*_{p,\mathrm{on,L}}(\widehat{i}_p[k+1|k], \widehat{i}_p[k+2|k], t^*_{p,\mathrm{off}}[k]) = \begin{cases} t^*_{p,\mathrm{off}}[k] & \text{if } s_{p,\mathrm{PR}} = 1, \\ t^*_{p,\mathrm{off}}[k] + T_\mathrm{dt} k_{p,\mathrm{i}} & \text{otherwise.} \end{cases} \tag{3.17b}$$

Therein, $s_{p,\mathrm{PR}}$ is the PR switching state during the dead-time and $k_{p,\mathrm{i}}$ is a gain based on the phase current that decreases the confidence of the deadtime compensation for low currents, calculated as

$$s_{p,\mathrm{PR}}(\widehat{i}_p[k+1|k], \widehat{i}_p[k+2|k], t_\mathrm{s}) = -\mathrm{sign}\left(\widehat{i}_p[k+1|k] + (\widehat{i}_p[k+2|k] - \widehat{i}_p[k+1|k])\frac{t_\mathrm{s}}{T_\mathrm{s}}\right), \tag{3.18}$$

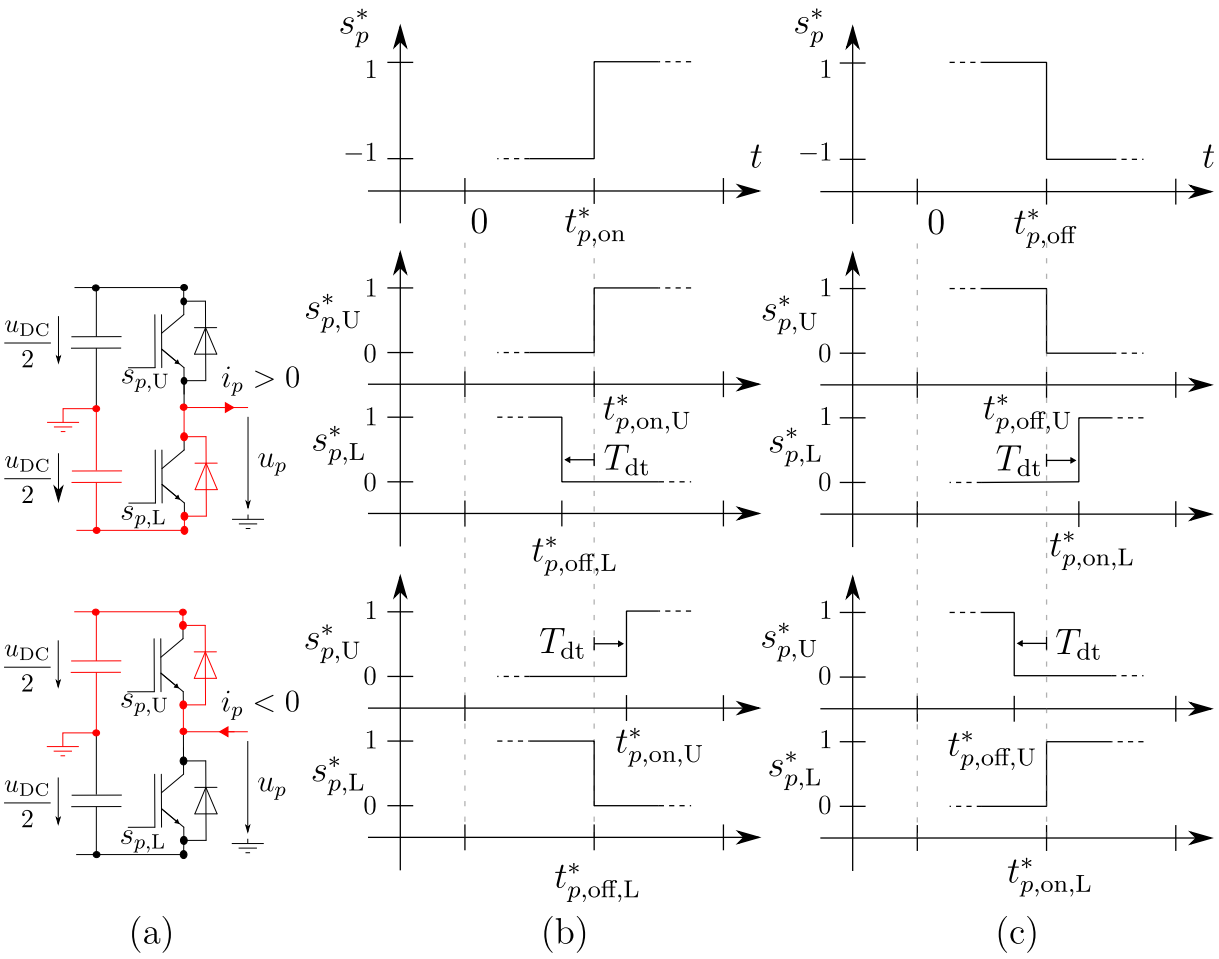


Fig. 3.8: Inverter leg diagram highlighting in red the current path (a) and dead-time compensation for turn-on (b) and turn-off (c) behavior depending on the PR operation. Desired switching behavior (top), necessary upper and lower semiconductor reference pulses for positive phase current (middle), and for negative phase current (bottom)

$$k_{p,\mathrm{i}}(\widehat{i}_p[k+1|k], \widehat{i}_p[k+2|k], t_\mathrm{s}) = \frac{1}{i_{\mathrm{PR,thr}}} \min\left(\left|\widehat{i}_p[k+1|k] + (\widehat{i}_p[k+2|k] - \widehat{i}_p[k+1|k])\frac{t_\mathrm{s}}{T_\mathrm{s}}\right|, i_{\mathrm{PR,thr}}\right), \quad (3.19)$$

where $i_{\mathrm{PR,thr}}$ is the threshold for confidence in current polarity detection, tuned as $i_{\mathrm{PR,thr}} = 0.025 I_\mathrm{n}$ (i.e., uncertainty in current polarity is considered negligible above 2.5 % of the nominal value), and t_s is the unmodified switching time, i.e., $t^*_{p,\mathrm{on}}$ and $t^*_{p,\mathrm{off}}$ for the switching on and off, respectively.

3.2.2 Load Angle Control

Load angle control is achieved through a combination of feed-forward and feedback control actions, which generate the flux amplitude reference for the MPFC. The feed-forward

action estimates the steady-state flux linkage amplitude for six-step operation based on DC-bus voltage and electric frequency based on (3.4) as

$$\Psi^*_{\mathrm{h,ffwd}} = \frac{2\pi u_{\mathrm{DC}}}{6\sqrt{3}\omega_{\mathrm{e}}}. \tag{3.20}$$

The feedback action is generated through a combination of a PI controller with constant gains with an adaptable gain according to the speed and DC-bus voltage. Using such a structure provides a very robust strategy, as the controller adjusts the flux linkage amplitude following changes in the operating point to maintain the desired load angle, ensuring a stable six-step operation. The load angle control implementation diagram is shown in Fig. 3.9.

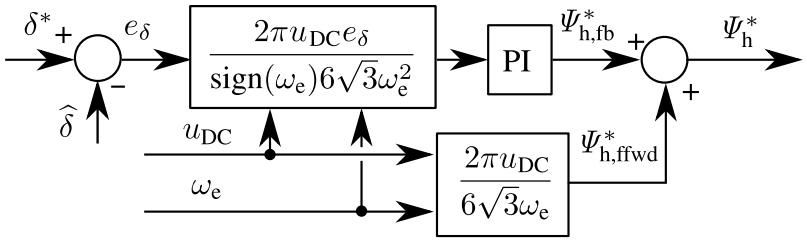


Fig. 3.9: Load angle control diagram

The following subsections explore the controller design, providing details about the plant model, the controller gain tuning, saturation, and the AW implementation.

3.2.2.1 Plant Model

The plant from the load angle controller point of view can be modeled as Fig. 3.10.

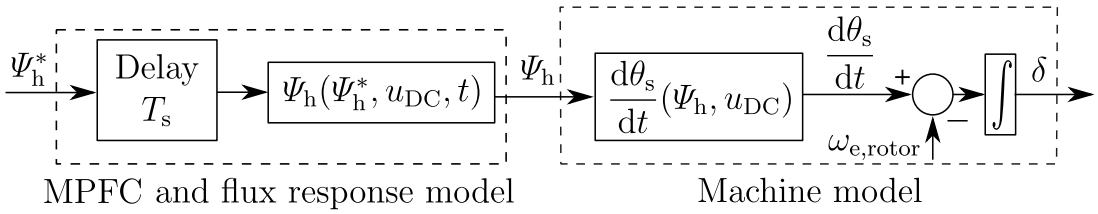


Fig. 3.10: Plant model for load angle controller tuning

This model can be linearized as

$$G_{\mathrm{Plant}}(s) = \frac{\Delta\delta(s)}{\Delta\Psi^*_{\mathrm{h}}(s)} \approx \frac{1}{\frac{sT_{\mathrm{s}}}{2}+1} \cdot \frac{1}{s\tau_{\mathrm{MFPC}}+1} \cdot K \cdot \frac{1}{s}, \tag{3.21}$$

where s is the Laplace complex variable. The first term in (3.21) models the sampling-to-actuation delay T_{s}. It is linearized as a PT_1 element with the time constant $T_{\mathrm{s}}/2$.

Secondly, the nonlinear MPFC response is considered. The line-to-line flux linkage evolves at a constant rate with slope u_{DC}. The initial location of the stator flux linkage when the reference changes also affects the response time, as the next reference will not be achieved until the next flux hexagon corner is reached. For its linearization, it was chosen to approximate this behavior as a PT_1 response, with a time constant τ_{MPFC}. To consider the differences in the flux amplitude response time, and simplifying according to (3.4), this value ranges as

$$\tau_{\mathrm{MPFC,min}} = \frac{1}{3}\frac{\Psi_{\mathrm{h}} \cdot 0.1}{u_{\mathrm{DC}}/\sqrt{3}} \approx \frac{\pi}{90 \cdot \omega_{\mathrm{e},0}}, \tag{3.22a}$$

$$\tau_{\mathrm{MPFC,max}} = \frac{1}{3}\frac{T_{\mathrm{e}}}{3} \approx \frac{\pi}{4.5 \cdot \omega_{\mathrm{e},0}}. \tag{3.22b}$$

The minimum considered time constant is chosen to reach 95% of the reference for a reference step of 10% of the steady-state flux value applied just before the flux reaches the next corner (i.e., no delay between reference change and MPFC response). For its maximum, it is considered that 95% of the reference is achieved after the flux has gone across two sectors (i.e., one third of the electrical period), considering that the reference could change significantly between sampling periods in a transient. This response approximation is illustrated in Fig. 3.11, with the expected responses by the MPFC according to the location of the flux linkage vector in the hexagonal trajectory when the reference change is applied.

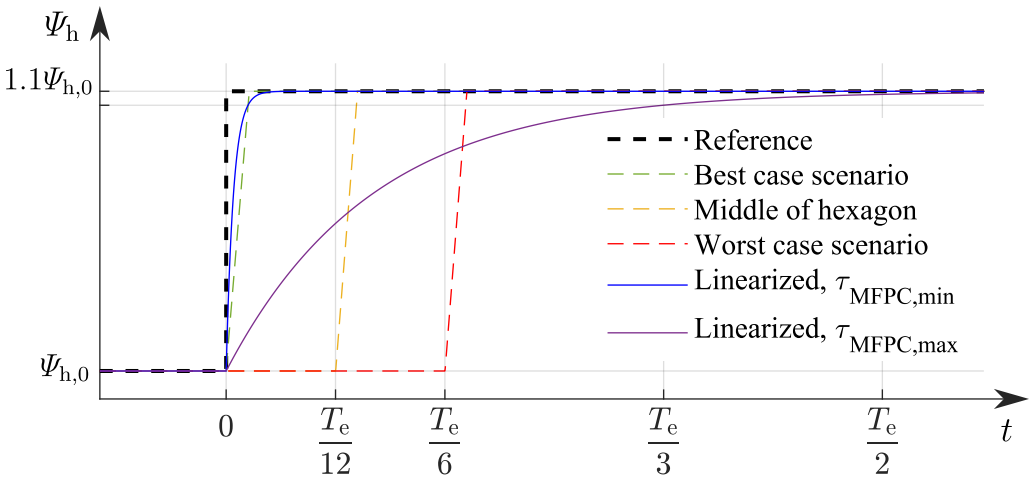


Fig. 3.11: Example MPFC response according to the instantaneous flux location when the new reference is applied

The third term in (3.21) represents the flux rotational frequency variation with the flux amplitude during six-step operation, as given by (3.4). This relationship is linearized around a specific speed and DC-bus voltage operating point as

$$\left.\frac{\partial \omega_{\Psi}}{\partial \Psi_{\mathrm{h}}}\right|_{\Psi_{\mathrm{h},0} \approx \frac{2\pi u_{\mathrm{DC},0}}{6\sqrt{3}\omega_{\mathrm{e},0}}} \approx \frac{-6\sqrt{3}\omega_{\mathrm{e},0}^2}{2\pi u_{\mathrm{DC},0}} = K. \tag{3.23}$$

Finally, for controller tuning purposes, (3.21) can be discretized with the Tustin method as

$$G_{\mathrm{Plant}}(z) \approx \frac{z^{-1} \cdot K \cdot T_{\mathrm{s}}(z+1)}{\left(\dfrac{2\pi}{\omega_{\mathrm{e},0} 6\sqrt{3}} \dfrac{2(z-1)}{T_{\mathrm{s}}(z+1)} + 1\right) 2(z-1)}, \tag{3.24}$$

where z is the z-transform complex variable. The equivalence between the functionalities in Fig. 3.10, the linearized relationship, and the discretized version are summarized in Tab. 3.3.

Model	Linearized	Discretized
Delay	$\dfrac{1}{\dfrac{sT_{\mathrm{s}}}{2}+1}$	z^{-1}
MPFC	$\dfrac{1}{s\tau_{\mathrm{MPFC}}(\omega_{\mathrm{e},0})+1}$	$\dfrac{1}{\dfrac{2(z-1)\tau_{\mathrm{MFPC}}(\omega_{\mathrm{e},0})}{T_{\mathrm{s}}(z+1)}+1}$
Flux angular frequency	$\dfrac{-6\sqrt{3}\omega_{\mathrm{e},0}^2}{2\pi u_{\mathrm{DC},0}}$	$\dfrac{-6\sqrt{3}\omega_{\mathrm{e},0}^2}{2\pi u_{\mathrm{DC},0}}$
Integrator	$\dfrac{1}{s}$	$\dfrac{T_{\mathrm{s}}(z+1)}{2(z-1)}$

Tab. 3.3: Switching time command generation according to switching criteria and switching times in each phase

It should be noted that all systems considered in Fig. 3.10, (3.21), and (3.24) are independent of machine parameters. Therefore, so is the controller tuning. A controller design can be executed in a quasi-continuous way using (3.21) or directly in the discrete-time domain using (3.24). The control (G_{c}), plant (G_{plant}), open-loop (G_{OL}), and closed-loop (G_{CL}) transfer functions are depicted in Fig. 3.12.

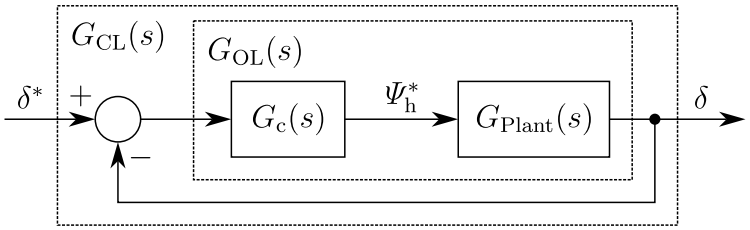


Fig. 3.12: Control diagram depicting the control (G_{c}), plant (G_{plant}), open-loop (G_{OL}), and closed-loop (G_{CL}) transfer functions

3.2.2.2 Controller Design

The feed-forward control is introduced to reduce the burden on the feedback control to arrive at a steady state and accounts for most of the effect of speed changes in flux amplitude. It is generated according to the estimated steady-state flux amplitude for six-step operation from the rotor electric frequency and DC-bus voltage as shown in (3.4). This way, the feedback controller is only responsible for handling deviations from the estimated operating point and reference changes.

The feedback controller chosen was a PI controller with fixed gains. Moreover, by accounting for (3.23), inverted, in the load angle controller as seen in Fig. 3.10, the operating-point dependency of the response with constant controller gains is significantly reduced. The sign of the speed must also be considered, as the change in load angle has opposite polarity to changes in flux linkage amplitude depending on the direction of rotation. The required transient change of flux amplitude to control the load angle depending on the direction of rotation is shown in Tab. 3.4.

	$\omega_\mathrm{e} > 0$	$\omega_\mathrm{e} < 0$
$\delta^* - \delta > 0$	$\downarrow \Psi$	$\uparrow \Psi$
$\delta^* - \delta < 0$	$\uparrow \Psi$	$\downarrow \Psi$

Tab. 3.4: Controller output depending on controller input sign and direction of rotation

Using as a reference case the counter-clockwise rotation ($\omega_\mathrm{e} > 0$), the PI-controller will include a negative sign and the load-angle error fed to the PI-controller is multiplied by

$$K_\mathrm{cont} = \frac{\mathrm{sign}(\omega_\mathrm{e}) 2\pi u_\mathrm{DC}}{6\sqrt{3}\omega_\mathrm{e}^2}. \tag{3.25}$$

The following explains the formal process for tuning the PI controller gains. The chosen feedback controller is defined in the Laplace domain as

$$G_\mathrm{c}(s) = -K_\mathrm{p,c}\frac{\tau_\mathrm{n,c}s + 1}{\tau_\mathrm{n,c}s}K_\mathrm{cont} \tag{3.26}$$

where $K_\mathrm{p,c}$ is the controller gain and $\tau_\mathrm{n,c}$ provides the location of the controller zero. Thus, from (3.24), the open-loop transfer function G_OL (cf. Fig. 3.12) results in

$$G_\mathrm{OL}(s) = \left(K_\mathrm{p,c}\frac{\tau_\mathrm{n,c}s + 1}{\tau_\mathrm{n,c}s}K_\mathrm{cont}\right)\left(\frac{1}{\frac{sT_\mathrm{s}}{2} + 1} \cdot \frac{1}{s\tau_\mathrm{MFPC} + 1} \cdot K \cdot \frac{1}{s}\right). \tag{3.27}$$

The time constants for the sampling delay and the MPFC response are combined as

$$\tau_\sigma = \frac{T_\mathrm{s}}{2} + \tau_\mathrm{MFPC,max} = \frac{T_\mathrm{s}}{2} + \frac{\pi}{4.5 \cdot \omega_\mathrm{e,0}}. \tag{3.28}$$

The maximum value of τ_MPFC is used to consider the worst-case scenario. To provide sufficient phase margin, the location of the controller's zero is chosen as

$$\tau_\mathrm{n,c} = 20 \cdot \tau_\mathrm{\sigma,max} = 20 \cdot \left(\frac{T_\mathrm{s}}{2} + \frac{\pi}{4.5 \cdot \omega_\mathrm{e,min}} \right) = 0.0092\,\mathrm{s}. \tag{3.29}$$

The lower limit for the speed is chosen as $0.8\omega_\mathrm{e,n}$, as the MPDSC strategy is only intended for operation in the flux weakening range. The effect of this zero location for the whole speed range (considered from $0.8\omega_\mathrm{e,n}$ to $3\omega_\mathrm{e,n}$) and for the entire range of τ_MFPC is shown in Fig. 3.13.

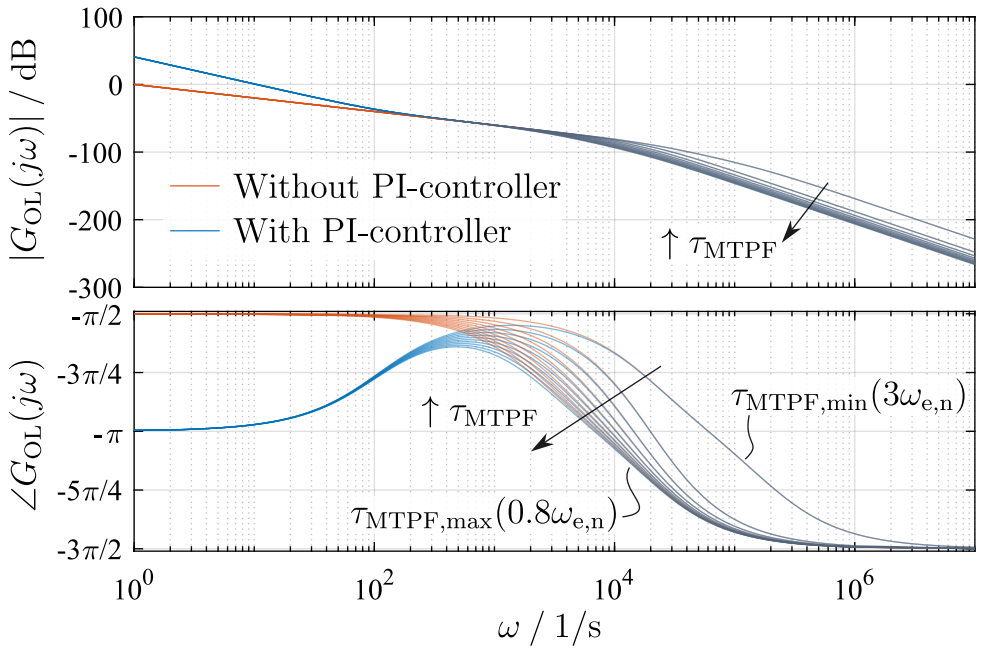


Fig. 3.13: Amplitude (top) and phase (bottom) frequency response of the open-loop transfer function for the whole range of speed and τ_MPFC, without (blue) and with (orange) the PI controller with the chosen zero location ($\tau_\mathrm{n} = 0.0092$) and $K_\mathrm{p,c} = 1$

Having selected the zero location, the controller gain is selected considering a trade-off between high crossover frequency (for fast response) and low resonance (for limited overshoot in the response). Furthermore, it must be remembered that the ultimate goal of MPDSC is to achieve the desired torque reference, and the transient response of both the load angle (controlled variable) and flux amplitude (actuating variable) will affect the transient response in torque. In Fig. 3.14, the crossover frequency of the open-loop transfer function and maximum overshoot of the closed-loop transfer function G_CL is plotted for various values of $K_\mathrm{p,c}$ for different values of speed and τ_MPFC including the considered range limits. To limit the overshoot while achieving a fast transient, the maximum overshoot is set to 1 dB, resulting in a controller gain as $K_\mathrm{p,c} = 1508\,1/\mathrm{s}$.

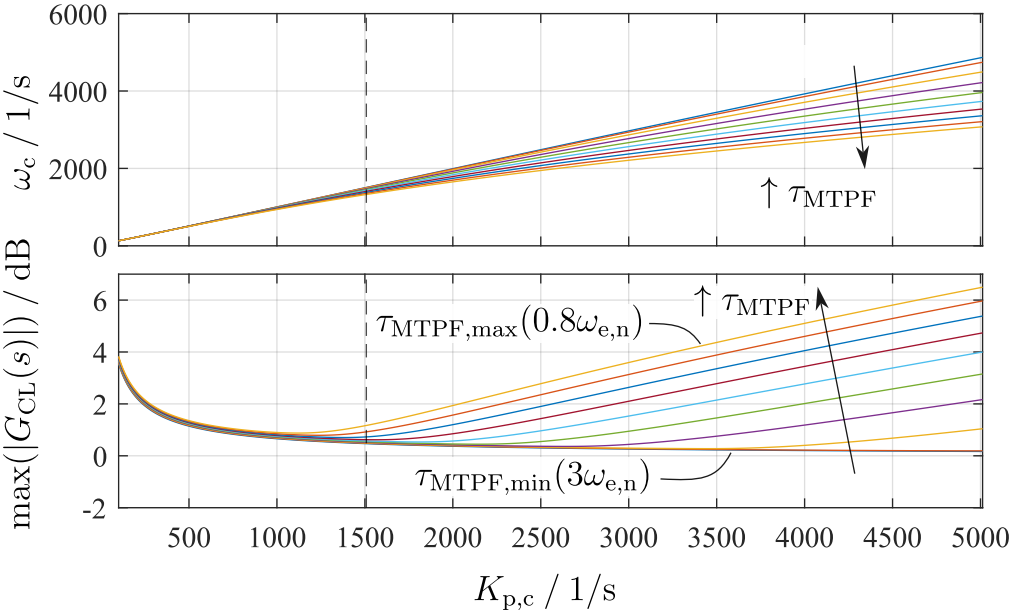


Fig. 3.14: Crossover frequency of the open-loop transfer function (top) and maximum gain of the closed-loop transfer function (bottom) depending on the controller proportional gain, for the whole range of speed and τ_{MPFC}

3.2.2.3 Saturation and Anti-Windup

The resulting reference after the combination of feedback and feed-forward control actions is bounded, with the limits for the flux reference being chosen according to physics and control criteria. When the output of this saturation differs from the original reference, the AW is triggered. The clamping AW strategy is implemented, by nullifying the error fed to the integral part of the controller when the output is saturated or the control loop is opened (e.g., while another control strategy controls the machine).

The physical lower limit for the flux reference is null flux. However, the lower limit should be defined as a sufficiently small value that does not disrupt the control of the machine, but ensures that switching pulses can still be generated when a drastic reduction of flux is commanded. The minimum flux amplitude that can be applied, leading to a hexagonal flux path with the suggested implementation, is

$$\Psi^*_{h,min} = \frac{u_{DC} T_s}{2\sqrt{3}}. \tag{3.30}$$

The physical upper limit for the flux reference depends on the machine itself. For the machine model used in simulation, the operating range includes flux amplitudes up to around $2\Psi_{PM}$.

Moreover, the MPDSC control strategy is intended for use in the flux-weakening range. In this operation mode, if the torque reference or the speed is reduced sufficiently, the flux amplitude required for operation with MPDSC will be higher than that of MTPC oper-

ation, i.e., the same torque at the same speed could be achieved with lower current, and not with maximum voltage utilization. Therefore, the flux reference for MTPC operation ($\Psi_{\mathrm{h,MTPC}}$) should be considered as an upper limit for the steady-state operation.

In this instance, a different control strategy must take over control of the machine, as the flux reference can no longer be used for load angle control in six-step operation. This can be done by extending the MPDSC strategy to include other switching patterns (cf. Ch. 5) or initiating a transition to FOC (cf. Ch. 4). The comparison between the reference flux (or some alternative value as the estimated flux amplitude) and the flux for MTPC operation can also provide a criterion for ensuring the operating point is in the flux-weakening region before commanding a transition towards operation with the standard MPDSC strategy explored in this chapter.

3.2.3 Operating Point Selection

The load angle reference generation implementation diagram is shown in Fig. 3.15. The flux amplitude is estimated from the flux amplitude reference fed to the MPFC, Ψ_{h}^*. The signal is filtered through an LPF (tuned at 100 Hz), in order to decouple the load angle reference generation from fast transients in reference flux amplitude by the load angle controller.

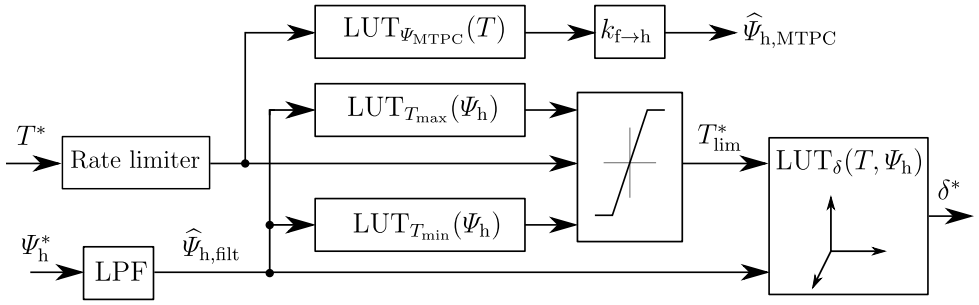


Fig. 3.15: Load angle reference generation diagram

Before accessing the 2D-LUT generating the load angle reference δ^* for the desired operating point defined by the reference torque and estimated flux amplitude, the reference torque is limited according to the maximum torque given the operating limits. Thus, the LUT will not be accessed to pursue an unachievable torque for the momentary estimated flux amplitude in the machine and the current constraints.

The fundamental flux that would achieve the reference torque in MTPC operation $\Psi_{\mathrm{h,MTPC}}$ is also estimated from a LUT based on the reference torque. For its use by the saturation part of the load angle controller, the LUT output, which provides the amplitude of the fundamental component, is scaled by $k_{\mathrm{f}\to\mathrm{h}}$ to consider the corresponding amplitude of the hexagonal flux path, with

$$k_{\mathrm{f}\to\mathrm{h}} = \frac{\Psi_{\mathrm{h}}}{|\boldsymbol{\Psi}_{\mathrm{s},1}|} = \frac{\pi^2}{6\sqrt{3}}, \tag{3.31}$$

obtained by a Fourier analysis of the ideal flux waveform, which has a trapezoidal shape (see Fig. 1.4) whose first harmonic amplitude can be calculated analytically.

3.2.3.1 Look-Up Table Generation

The reference generation implementation is based on look-up tables embedding the relations between the different variables ($T_{\max}(\Psi_h)$, $T_{\min}(\Psi_h)$, $\Psi_{MTPC}(T)$, and $\delta(T, \Psi_h)$). The output values for the load angle reference generation, the MTPC flux, and the limit torque boundaries are represented in Fig. 3.16, for the simulation machine model data. The torque boundaries consider both current limitation and MTPF. These LUTs are precalculated offline, using machine data relating current and flux (as (2.14), according to the operating point and accounting for saturation effects) and an ideal fundamental mode machine model (as (2.11)).

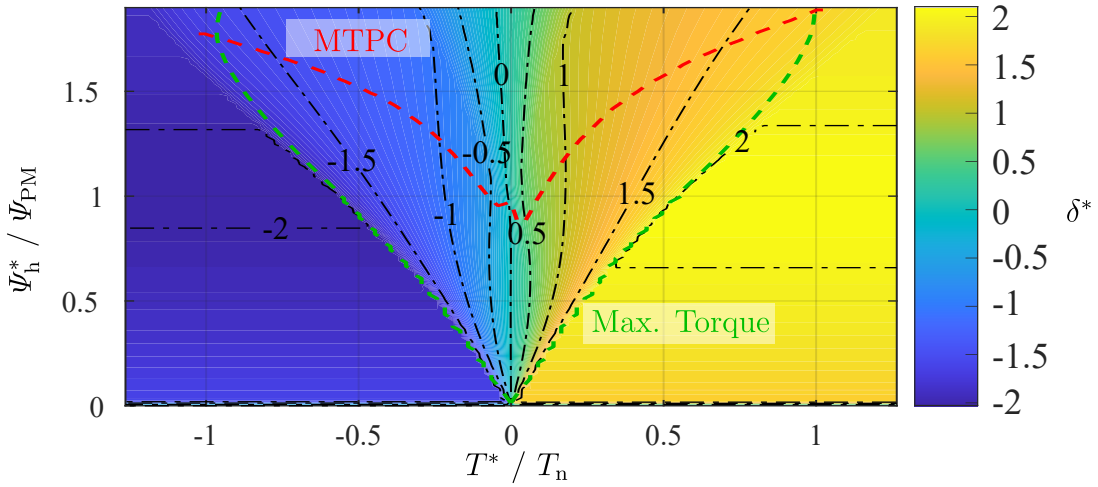


Fig. 3.16: Load angle reference generation LUT values with MTPF and MTPC loci

The direct use of FEM-analysis-based data for testbench operation led to poor torque accuracy upon experimental evaluation. Consequently, an experimental characterization using MPDSC for machine control was performed. For this approach, a grid of data was generated for multiple load angle reference values at different speeds and DC-bus voltage operating points, resulting in different flux amplitude values, and for which the torque output was measured in steady-state operation. This procedure also allows for the identification of the MTPF path. The stored (T, Ψ_h^*, δ^*) tuples are processed offline to generate the load angle reference LUT (i.e., $\text{LUT}_\delta : (T, \Psi_h^*) \mapsto \delta^*$). Another alternative would be to perform online adaptation of an initial LUT guess, as proposed in [43], but this approach was not pursued in the present work.

This MPDSC-specific characterization provides relatively accurate torque control even with inaccurate flux-current LUTs in the flux observer. The torque accuracy achieved is, nevertheless, dependent on rotor temperature, and the normalized steady-state torque

error can reach up to 10 % within the considered temperature range of the machine. More details of this and other dependencies are explored in Ch. 6.

3.2.4 Voltage and Flux Estimation

Accurate flux estimation and prediction is critical for both control loops, providing the load angle estimation for load angle control and the line-to-line flux estimation for MPFC. The sections above have been discussed assuming perfect flux knowledge. This is an ideal scenario, but in any real implementation, the flux needs to be estimated from the machine information available for the inverter control logic (DC-bus voltage, switching time commands, measured currents, machine angle, and speed). The diagram in Fig. 3.17 depicts the basic functionalities of the voltage and flux estimation algorithm, which are explained in detail in the following subsections.

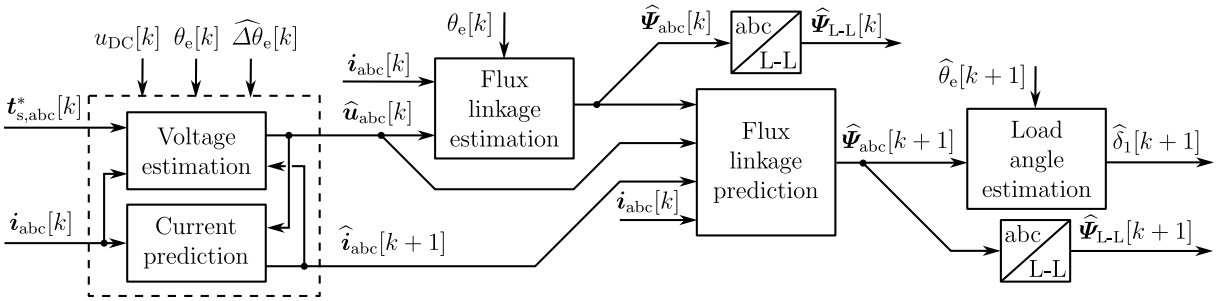


Fig. 3.17: Voltage and flux estimation and prediction diagram

3.2.4.1 Voltage Estimation

The implementation is intended for a three-phase two-level inverter (cf. Fig. 2.2). The inverter and its integrated drivers introduce distortions to the desired switching times, due to inaccessible operating modes (e.g., short pulse removal), forward and resistive voltage drop, sampling and actuation delays, and required safety interlock time. These issues, particularly the time delays, must be accounted for in the switch-time calculation and voltage-estimation systems.

The voltage estimation is performed as presented in Alg. C.1 in App. C. The algorithm first determines the ideal switching sequence based on the commanded switching times of each inverter leg semiconductor ($\boldsymbol{s}_{\mathrm{u}}$, $\boldsymbol{s}_{\mathrm{d}}$), inserting dead-time as needed to guarantee a minimum off-time before turn-on, consistent with inverter behavior. It then estimates the actual switching sequence by considering passive rectifier operation from the measured and predicted current, and uses this to estimate the leg voltage during the sampling period. Finally, the delay effect is incorporated through a residual voltage (u_{res}), which adjusts the voltage estimation for the next sampling period.

3.2.4.2 Current Prediction

As discussed above, current prediction one step ahead is necessary for accurate estimation of the current polarity at the switching instant. For this, the flux one-step ahead is estimated as

$$\widehat{\Psi}_{\mathrm{dq}}[k+1|k] = \boldsymbol{T}_{\alpha\beta\to\mathrm{dq}}\left(-\widehat{\Delta\theta}[k]\right)\left(T_{\mathrm{s}}\boldsymbol{T}_{\mathrm{abc}\to\mathrm{dq}}\left(\widehat{\theta}[k]\right)\widehat{\boldsymbol{u}}_{\mathrm{abc}}[k] + \boldsymbol{\Psi}_{\mathrm{dq}}(\boldsymbol{i}_{\mathrm{dq}}[k])\right) - R_{\mathrm{s}}\frac{T_{\mathrm{s}}}{2}(\boldsymbol{i}_{\mathrm{dq}}[k] + \widehat{\boldsymbol{i}}_{\mathrm{dq}}[k+1|k]). \quad (3.32)$$

This estimation, based on the flux-to-current LUTs ($\boldsymbol{\Psi}_{\mathrm{dq}}(\boldsymbol{i}_{\mathrm{dq}})$), is employed for current prediction as

$$\widehat{\boldsymbol{i}}_{\mathrm{abc}}[k+1|k] = \boldsymbol{T}_{\mathrm{dq}\to\mathrm{abc}}\left(\widehat{\theta}[k+1|k]\right)\boldsymbol{i}_{\mathrm{dq}}\left(\widehat{\Psi}_{\mathrm{dq}}[k+1|k]\right). \quad (3.33)$$

The current prediction is used within the voltage estimation algorithm discussed above, and the process is repeated for four[4] iterations within the sampling period.

3.2.4.3 Flux Linkage Estimation

The voltage estimation is used for estimating the stator flux with a Gopinath-style flux observer [44] as Fig. 3.18. The observer PI-controller is tuned so that the fade-over frequency between the current mode (2.14) and the voltage mode (3.2) is placed below 10% of the base speed as

$$\boldsymbol{u}^{\mathrm{corr}}_{\alpha\beta}[k] = \left(\boldsymbol{\Psi}^{\boldsymbol{i}_{\mathrm{obs}}}_{\alpha\beta}[k] - \boldsymbol{\Psi}^{\boldsymbol{u}_{\mathrm{obs}}}_{\alpha\beta}[k]\right)\left(K_{\mathrm{p,obs}} + K_{\mathrm{i,obs}}\frac{T_{\mathrm{s}}z^{-1}}{1-z^{-1}}\right), \quad (3.34)$$

$$K_{\mathrm{p,obs}} = 2\frac{\omega_{\mathrm{e,n}}}{10}, \quad (3.35a)$$

$$K_{\mathrm{i,obs}} = \left(\frac{\omega_{\mathrm{e,n}}}{10}\right)^2. \quad (3.35b)$$

This results in two identical real poles placed at $\sigma = -\omega_{\mathrm{e,n}}/10$ in the continuous s-domain for the closed-loop transfer functions $\boldsymbol{\Psi}^{\boldsymbol{u}_{\mathrm{obs}}}_{\alpha\beta}(s)/\boldsymbol{\Psi}^{\boldsymbol{i}_{\mathrm{obs}}}_{\alpha\beta}(s)$, and ensures that the less parameter-sensitive voltage model is dominant in the flux-weakening region.

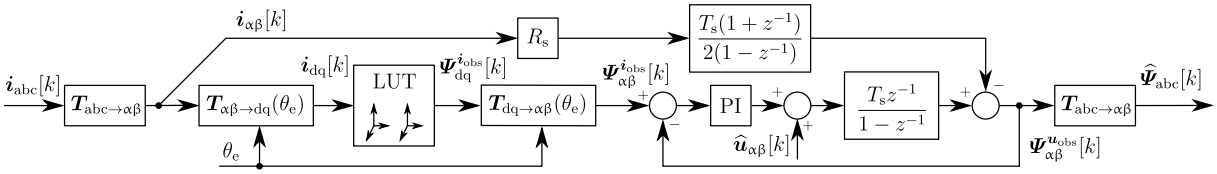


Fig. 3.18: Gopinath-style flux observer

[4]Further repetition were not observed to affect the results.

3.2.4.4 Flux Linkage Prediction

Flux linkage prediction is done based on the voltage and flux estimation, and current prediction as

$$\widehat{\boldsymbol{\Psi}}_{\mathrm{abc}}[k+1] = \widehat{\boldsymbol{\Psi}}_{\mathrm{abc}}[k] + T_{\mathrm{s}} \left(\widehat{\boldsymbol{u}}_{\mathrm{abc}}[k] - R_{\mathrm{s}} \frac{\widehat{\boldsymbol{i}}_{\mathrm{abc}}[k+1] + \boldsymbol{i}_{\mathrm{abc}}[k]}{2} \right). \tag{3.36}$$

This enables the flux prediction to accurately account for the switching commands being executed during the present sampling period.

3.2.4.5 Load Angle Estimation

During six-step operation, the load angle presents an inherent ripple due to the dependency of the stator flux rotational frequency on its location on the hexagon path. This ripple is independent of flux amplitude and can be calculated from the difference between the instantaneous stator flux angle and the angle of its fundamental component. Removing this value from the estimated load angle before feeding this signal to the load angle controller prevents the controller from generating a control action (flux amplitude reference) attempting to compensate for this ripple. Moreover, due to aliasing effects and depending on sampling frequency and rotational frequency, this ripple could otherwise be amplified through closed loop control and result in unwanted low-frequency ripple in the rest of the machine variables. The load angle ripple compensation allows for the discrete-time implementation of the control strategy presented with arbitrarily chosen sampling frequency within reasonable bandwidth boundaries. Thus, the angle of the fundamental component of the predicted flux linkage is estimated as

$$\widehat{\delta}_1[k+1] = \angle \left(\widehat{\boldsymbol{\Psi}}_{\mathrm{dq}}[k+1] \right) - \delta_{\mathrm{rip}} \left(\widehat{\boldsymbol{\Psi}}_{\mathrm{abc}}[k+1] \right). \tag{3.37}$$

The following considers only the first $\pi/3$ sector since the relations repeat for every sector. A normalized flux path (corner amplitude equal to 1) can be considered as Fig. 3.19.

The six-step flux vector and its fundamental component are parallel at the corners and middle of the hexagon sides. Also, the stator flux moves at a constant rate (determined by the DC-bus voltage) through the flux path, and the fundamental flux component rotates with constant angular speed. The stator flux components in the first sector in the αβ-reference frame are given by

$$\psi_\alpha = 1 - \cos\left(\frac{\pi}{3}\right) \frac{6\,\overline{\omega}_\Psi}{2\pi} t, \tag{3.38a}$$

$$\psi_\beta = \sin\left(\frac{\pi}{3}\right) \frac{6\,\overline{\omega}_\Psi}{2\pi} t, \tag{3.38b}$$

where ψ_α and ψ_β are the normalized flux in αβ-coordinates, $\overline{\omega}_\Psi$ the stator flux average frequency (i.e., its fundamental frequency) and t the time. The flux angle θ_{s} and the angle of the fundamental component $\theta_{\mathrm{s},1}$ can then be calculated as

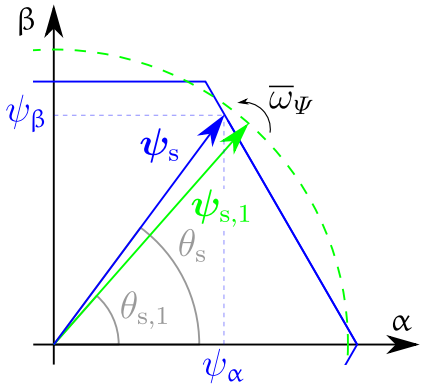


Fig. 3.19: Normalized flux path during six-step operation compared to its fundamental component

$$\theta_\mathrm{s} = \tan^{-1}\left(\frac{3\sqrt{3}\,\overline{\omega}_\Psi t}{2\pi - 3\,\overline{\omega}_\Psi t}\right), \tag{3.39a}$$

$$\theta_{\mathrm{s},1} = \overline{\omega}_\Psi t, \tag{3.39b}$$

The difference between them provides the ripple in load angle. This relation can be generalized for all angles for online estimation of the inherent load angle ripple during six-step operation, as represented in Fig. 3.20 and calculated as

$$\delta_\mathrm{rip} = \mathrm{mod}\left(\widehat{\theta}_\mathrm{s}, \frac{\pi}{3}\right) - \frac{2\pi \tan\left(\mathrm{mod}\left(\widehat{\theta}_\mathrm{s}, \frac{\pi}{3}\right)\right)}{3\left(\sqrt{3} + \tan\left(\mathrm{mod}\left(\widehat{\theta}_\mathrm{s}, \frac{\pi}{3}\right)\right)\right)}. \tag{3.40}$$

This relationship can be calculated online or stored in a LUT.

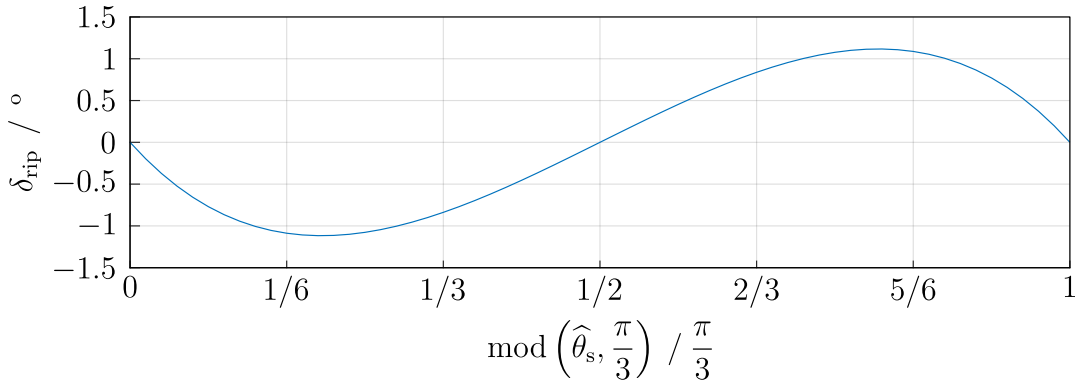


Fig. 3.20: Load angle ripple estimation during six-step operation referred to the first sector of the flux hexagon trajectory

3.3 Simulation Results

The control strategy presented in the previous sections has been demonstrated to be capable of achieving six-step operation with a PMSM through simulation results. The following results focus on the behavior of the developed MPDSC strategy and its ancillary systems in steady state, and through transients in torque reference and speed. As the control strategy is intended for implementation in parallel to a FOC controller, some figures also include the FOC behavior for the same torque reference and speed. It should be noted, however, that the FOC implementation has not been optimized for overmodulation operation, and thus the results shown could be further improved. The FOC results are presented for context and to provide a benchmark to the capabilities of a system limited to the linear modulation range in steady-state, not as a representation of the optimized capabilities of FOC itself. The simulation setup is detailed in App. A.

3.3.1 Steady-State Operation

An example of the voltage and flux linkage estimation performance is shown to be extremely accurate in Fig. 3.21. The error in voltage estimation is near zero with peaks under 10^{-11} of the nominal DC voltage. Such errors can be attributed to numerical issues during the simulation. This leads to a very small error in the line-to-line flux estimation and prediction of under 0.025 % of the peak value. The notable errors in two-steps-ahead line-to-line flux prediction which exceed the figure axis correspond to the instant before a switching occurs, since this prediction is done under the assumptions that switching would not occur, i.e., the same voltage would have been applied throughout that sampling period.

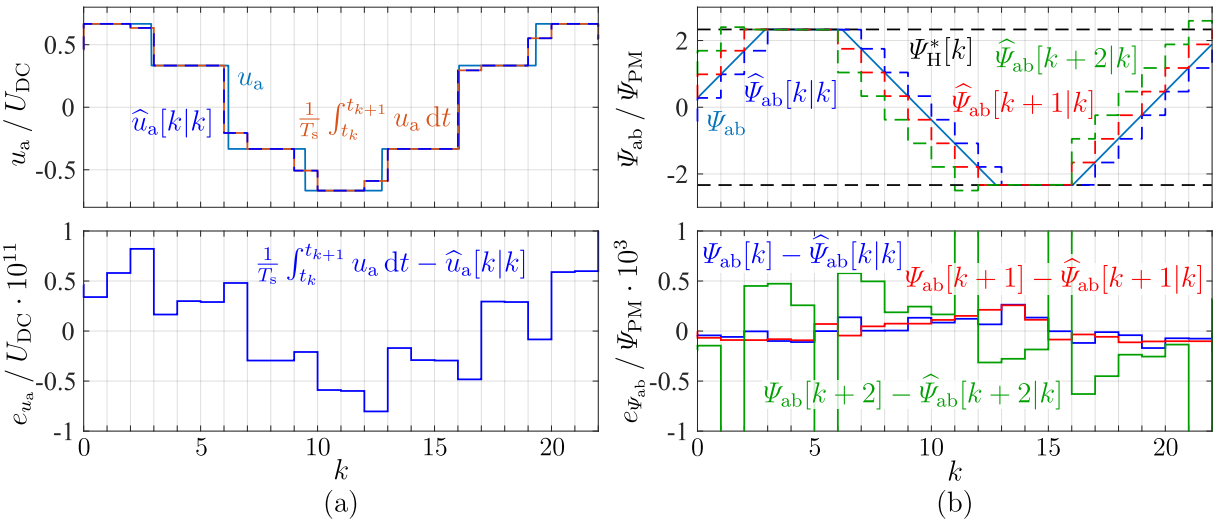


Fig. 3.21: Phase voltage (a) and line-to-line flux (b) estimation and prediction (top), and error (bottom), during steady-state MPDSC operation. Operating point: $n = 1.5 n_\mathrm{n}$, $T^* = 0.3 T_\mathrm{n}$

The steady-state response regarding torque, flux amplitude, load angle, and switching state is shown in Fig. 3.22. The ripple observed in torque results from the inevitable flux amplitude and load angle ripple during six-step operation. However, no oscillations can be observed in its average value, which accurately follows the reference. The load angle response can be observed in the lower-left sub-figure, where the load angle ripple compensation is shown to adequately estimate the average value regardless of the location of the sampling point in the signal ripple. This enables the load angle control to maintain the controlled variable (estimated load angle after compensation) equal to the reference set. The upper right plot shows the flux amplitude, with the minimum value corresponding to the flux amplitude set by the load angle controller. The lower right plot shows the switching state or active voltage vector applied, clearly depicting the six-step voltage sequence. Furthermore, Fig. 3.23 shows the dq-current path with the contour lines for iso-torque, current, and flux for reference. The dq-current operating point, which is not a controlled variable in this strategy, follows the tear-shaped trajectory characteristic of six-step operation, and repeats this path for each voltage of the sequence, i.e., it follows that path six times per electric period.

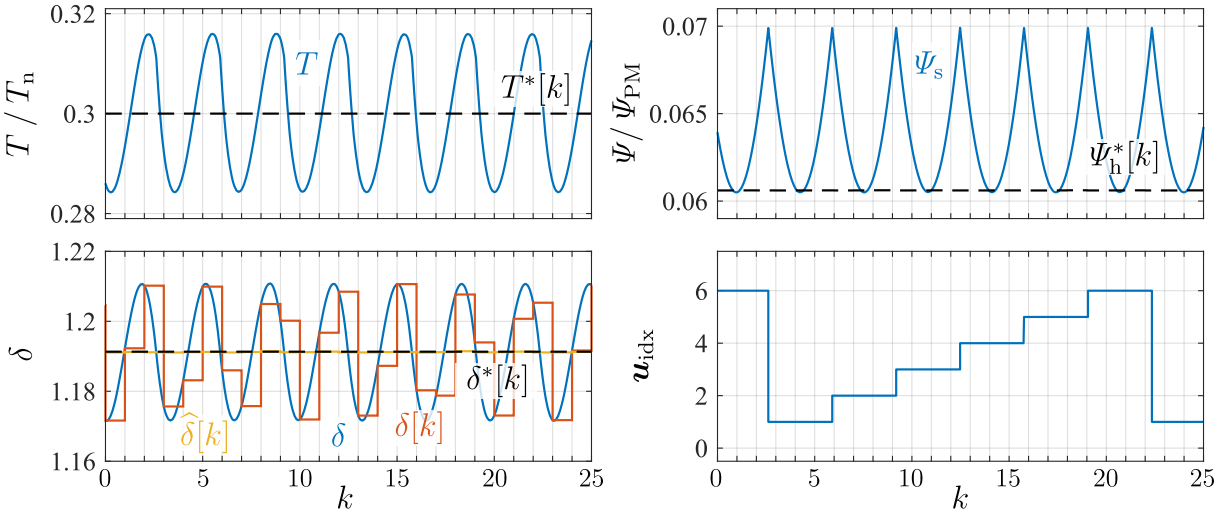


Fig. 3.22: Steady-state torque (top left), load angle (bottom left), flux amplitude (top right), and switching state index (bottom right) response during steady-state MPDSC operation. Operating point: $n = 1.5n_\mathrm{n}$, $T^* = 0.3T_\mathrm{n}$

Lastly, Fig. 3.24 compares the average current amplitude between the values achieved with FOC and the proposed MPDSC strategy. The figure only shows operating points beyond the MTPC path since MPDSC is only intended for flux-weakening operation. The reason for this is apparent in the figure, as it can be seen that, moving towards lower speeds, the dashed and solid contour lines converge for the MTPC operation, after which operating at higher flux would no longer yield an advantage. For increasing speeds, however, the MPDSC method shows its potential by gaining two clear improvements over FOC due to the optimal voltage utilization: on the one hand, the required current amplitude for

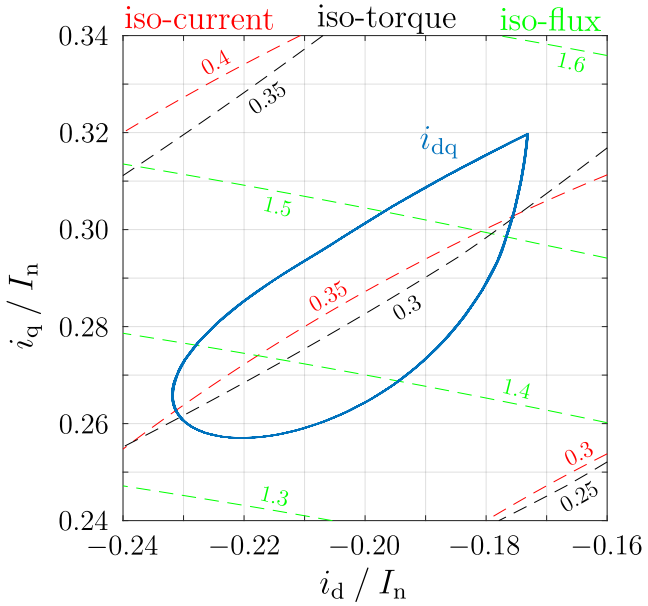


Fig. 3.23: Current trajectory in dq-coordinates during steady-state MPDSC operation. Operating point: $n = 1.5n_n$, $T^* = 0.3T_n$

operating at a given speed and torque is lower, and on the other, the maximum torque achievable at any given speed is increased.

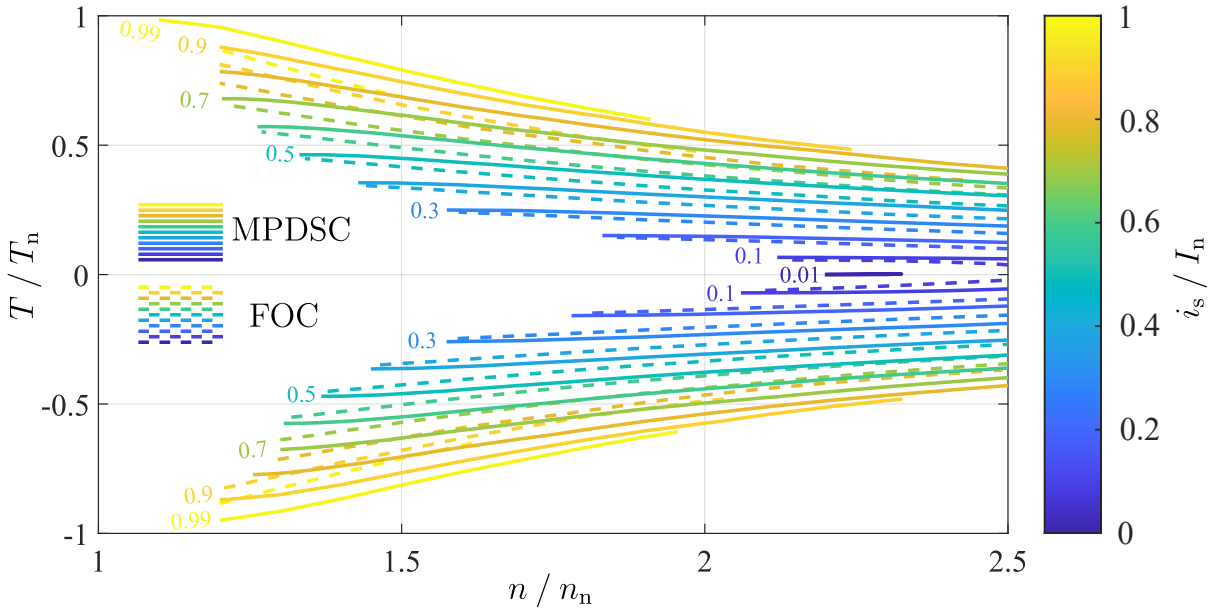


Fig. 3.24: Contour of average current amplitude during MPDSC and FOC steady-state operation throughout all torque-speed operating points in the flux weakening region

3.3.2 Torque Transient Response

The torque tracking response for an example speed in the flux weakening range ($n = 2n_\mathrm{n}$) is shown in Fig. 3.25. The torque reference (blacked dashed line) evolves between MTPC, its peak value and their average for the first six columns. The last two columns show a transient between intermediate values in the flux weakening range at this speed. The upper plots show motoring operation and the lower plots generating operation. The response of MPDSC is shown in a blue line, and the response of FOC is shown in a semi-transparent orange dotted line. It is once more evident that the maximum and minimum torque achievable is increased for MPDSC operation. The torque transient response shows adequate performance, with occasional undershoots at the beginning of the transient due to the necessary increase of flux amplitude to reduce load angle (e.g,. first row second column). This transient flux amplitude deviation from the steady-state value at this speed also affects the torque reference for the maximum and minimum torque operation (cf. first and fifth columns). For transitioning to maximum torque operation, the flux momentarily decreases, affecting the estimation of maximum achievable torque and, thus, the set torque reference. The reverse effect takes place when transitioning to minimum torque. The dynamic performance of FOC and MPDSC is comparable.

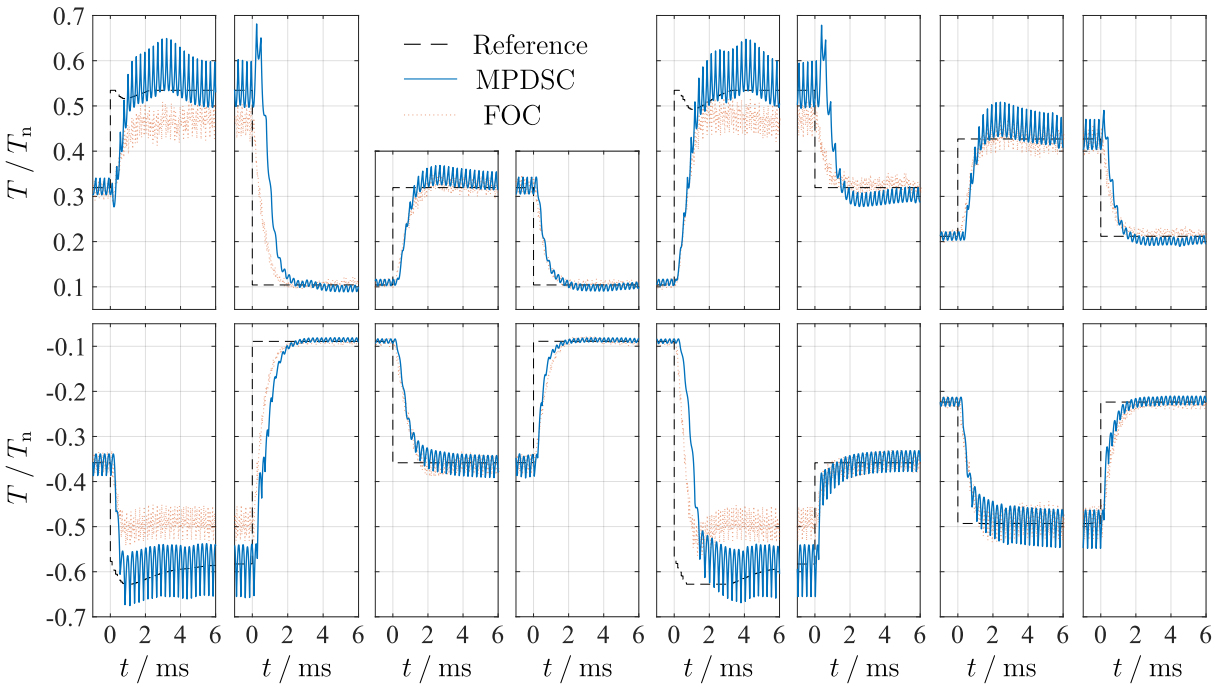


Fig. 3.25: Torque tracking response of MPDSC and FOC for motoring (top) and generating (bottom) operation for multiple torque reference step transitions (columns). Operating point: $n = 2n_\mathrm{n}$

For a more detailed observation of the controlled and uncontrolled variables, the transients depicted in the last two columns are shown in Fig. 3.26 and 3.27 for motoring and generating operation respectively, with semi-transparent lines for the corresponding FOC

response. It can be observed that the load angle reference is isolated from the flux amplitude transient through the LPF, and the flux amplitude reference is accurately achieved with a step delay once one of the line-to-line fluxes can reach the reference. The dynamic performance between FOC and MPDSC is shown to be similar, with notable differences occurring in their steady-state operating points for flux amplitude, load angle, and current amplitude.

3.3.3 Speed Transient Response

The MPDSC response to a speed transient is depicted in Fig. 3.28, for full and partial load operation, both for motoring and generating conditions, from a speed of $1.5n_{\mathrm{n}}$ to $2.5n_{\mathrm{n}}$ and back. The results corresponding to FOC are also depicted with semi-transparent lines for reference. The proposed method is capable of following the speed transient with negligible error in torque during the rapid speed change, whose rate of change is set to $0.4n_{\mathrm{n}}$/s. The tracking under these conditions is superior to that of FOC, as evidenced by the behavior when the speed ramp begins and ends. Lastly, this figure further demonstrates the superior peak torque capabilities of MPDSC due to its optimal voltage utilization.

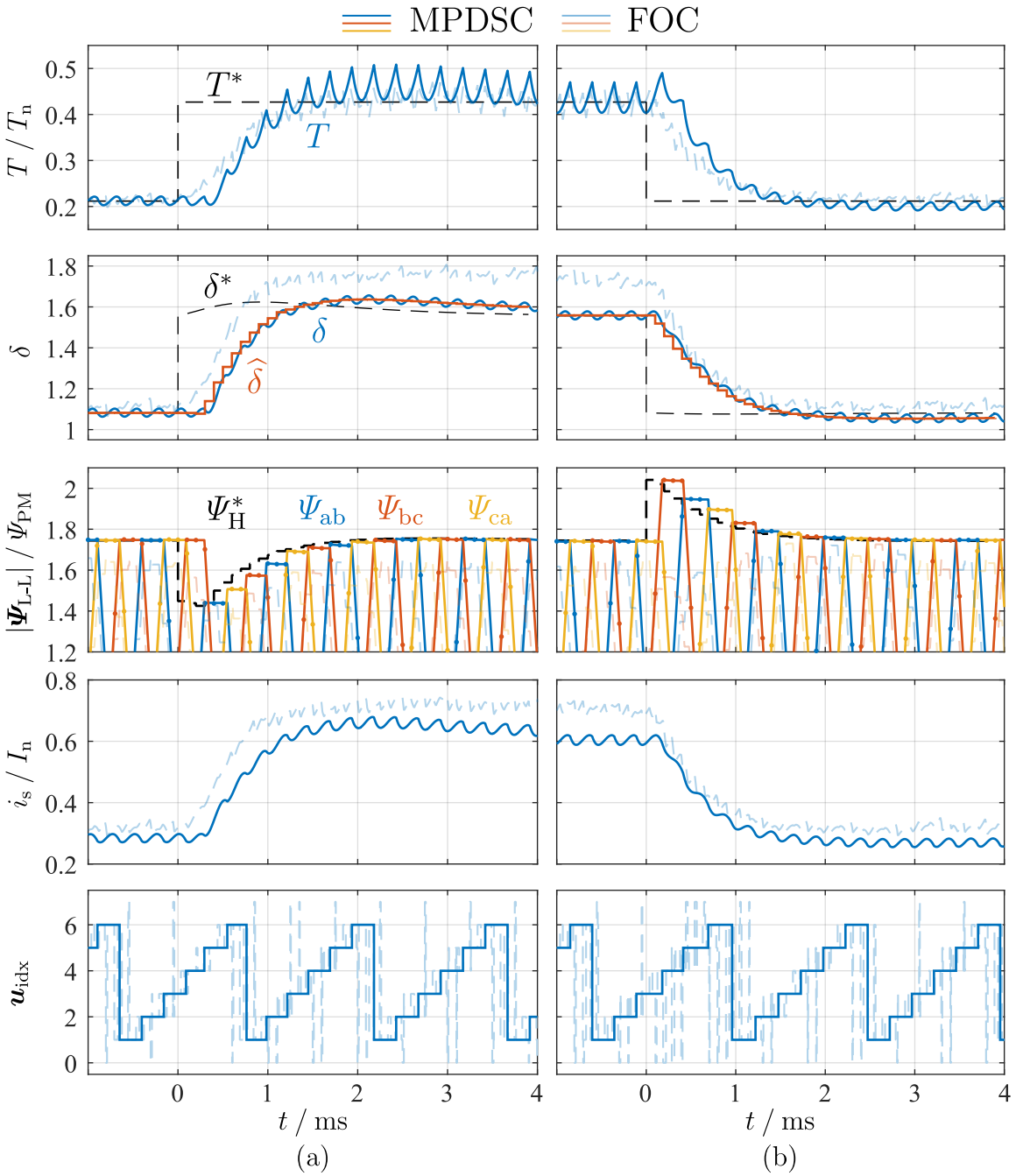


Fig. 3.26: Torque tracking response of MPDSC and FOC in motoring operation for up (a) and down (b) step torque reference change. From top to bottom: torque, load angle, line-to-line flux amplitude, current amplitude, and switching state index. Operating point: $n = 2n_\mathrm{n}$

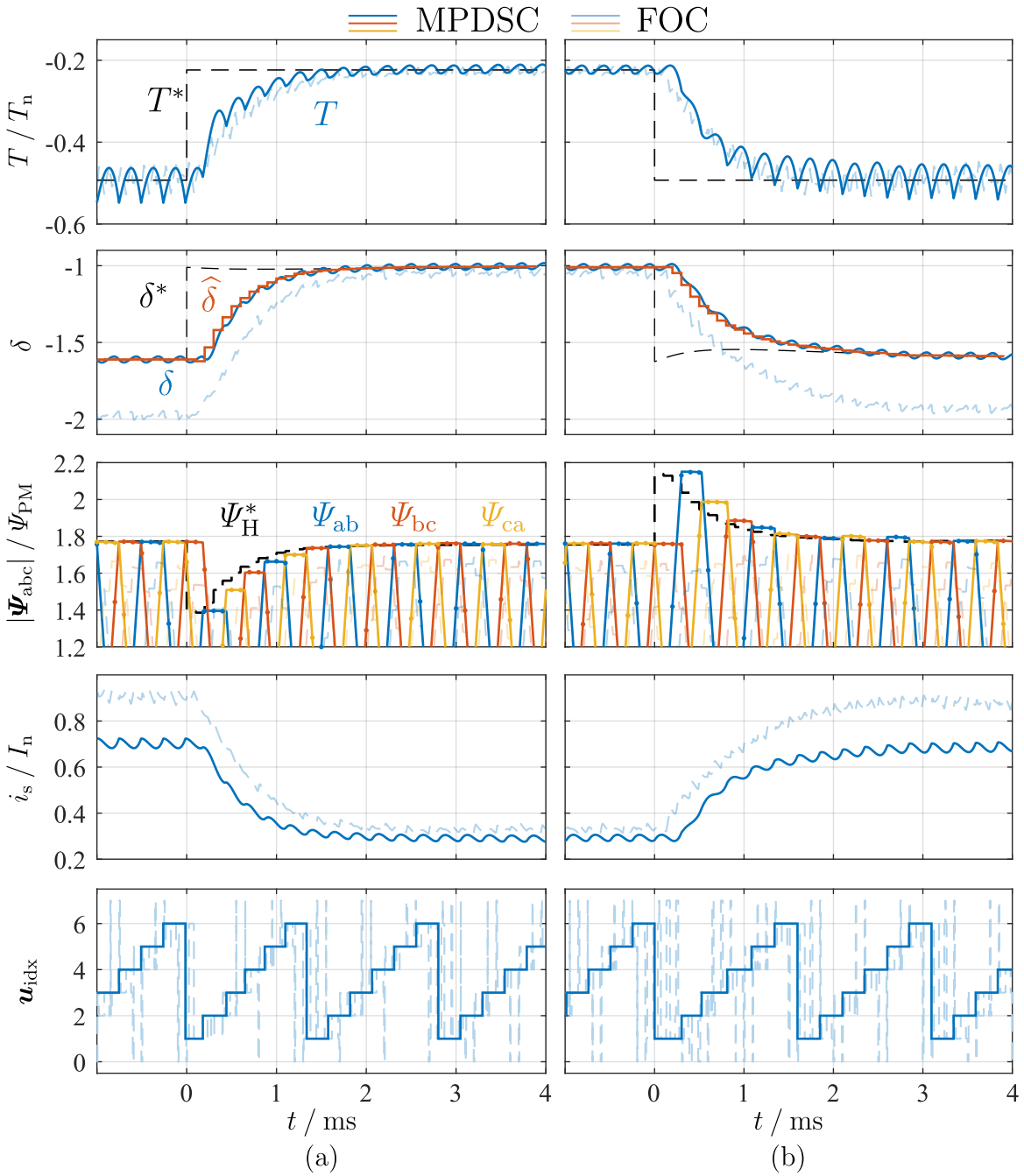


Fig. 3.27: Torque tracking response of MPDSC and FOC in generating operation for up (a) and down (b) step torque reference change. From top to bottom: torque, load angle, line-to-line flux amplitude, current amplitude, and switching state index. Operating point: $n = 2n_\mathrm{n}$

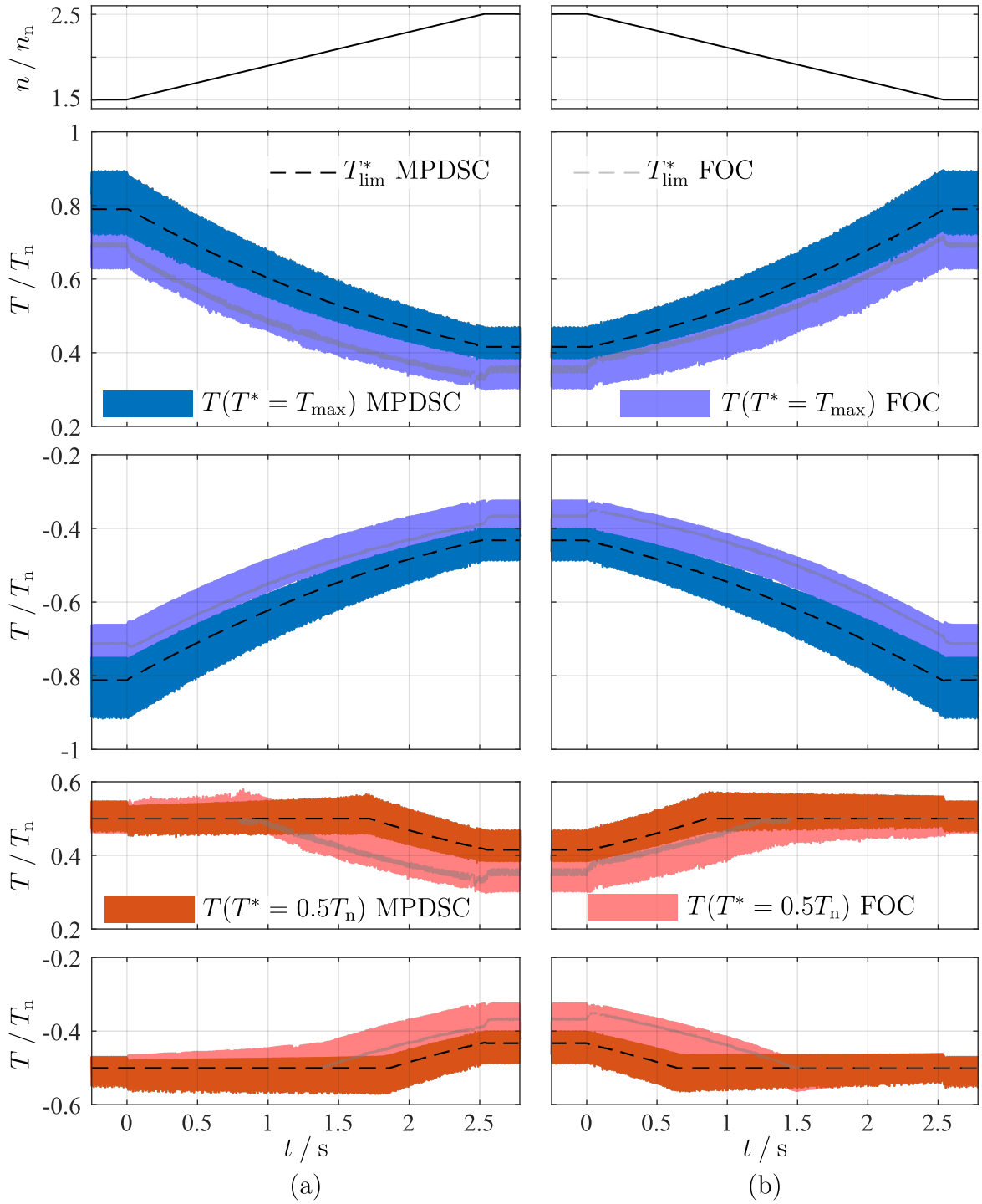


Fig. 3.28: Speed transient responses of MPDSC (solid) and FOC (semi-transparent) for a speed ramp up (a) and down (b). From top to bottom: speed, torque for full load (blue) in motoring operation, in generating operation, torque for partial load (orange) in motoring operation, and in generating operation

3.4 Experimental Results

The MPDSC strategy has been evaluated in a laboratory test bench for a transportation-grade highly utilized PMSM. A speed-controlled induction machine provides the mechanical load. The testbench is equipped with a rapid-control-prototyping system where the control strategy is implemented. Comprehensive details of the experimental setup are provided in App. B.

The implementation described in this document and employed for the simulation results incorporates several minor refinements compared to the version used for experimental evaluation. The scope and impact of these refinements on the observed performance are limited, full details are provided in App. B. These updates were introduced during the later stages of the research and could not be experimentally assessed due to the unavailability of the device under test. Their introduction was primarily motivated by the objectives of adopting more formally rigorous procedures, ensuring completeness in the algorithm description, and enhancing FOC operation for simulation-based comparison.

3.4.1 Computational Load

Turnaround times for individual control modules were quantified by compiling controller variants removing targeted sections[5]. Results are listed in Table 3.5[6]. The MPDSC exhibits execution times comparable with FOC, with voltage estimation dominating due to its iterative current prediction. Further algorithmic streamlining could mitigate this cost. The total computational load remains comparable to conventional control strategies, confirming the feasibility of MPDSC for low-cost micro-controller implementation in industrial and transportation applications.

3.4.2 Steady-State Operation

The operation during six-step is characterized by minimum switching frequency (equal to the fundamental frequency). In order to evaluate the steady-state six-step sequence, the time interval between switching events was calculated from the measured line-to-line voltage data at multiple torque-speed operating points as indicated in Fig. 3.29 and

$$\boldsymbol{T}_{\mathrm{swi}} = [T_{\mathrm{swi,1}}\, T_{\mathrm{swi,2}}\, ...\, T_{\mathrm{swi,n}}], \tag{3.41}$$

$$\rho_{\mathrm{Worst\ case}} = \frac{\max(\boldsymbol{T}_{\mathrm{swi}}) - \min(\boldsymbol{T}_{\mathrm{swi}})}{\mu(\boldsymbol{T}_{\mathrm{swi}})}, \tag{3.42}$$

$$\rho_{95\%} = \frac{p_{97.5}(\boldsymbol{T}_{\mathrm{swi}}) - p_{2.5}(\boldsymbol{T}_{\mathrm{swi}})}{\mu(\boldsymbol{T}_{\mathrm{swi}})}, \tag{3.43}$$

[5]Internal compilation protocols may produce aggregate turnaround times for complete systems (e.g., MPDSC) that are shorter than the sum of their individual module times.

[6]Ancillary systems comprise ADC input and command output processes, sensor data processing, PLL, and error sequence control for safe operation.

Task	μ	σ
Operating point selection	0.70 µs	0.28 µs
Load angle control	0.61 µs	0.26 µs
MPFC	2.41 µs	0.26 µs
Voltage estimation	3.34 µs	0.26 µs
Flux estimation	1.56 µs	0.30 µs
Total MPDSC	6.19 µs	0.25 µs
Total FOC	3.05 µs	0.24 µs
Ancillary systems	30.73 µs	0.03 µs
Complete implementation	38.78 µs	0.22 µs
Sampling period	100.00 µs	

Tab. 3.5: Turnaround times for real-time implementation of MPDSC (μ is the mean value and σ is the standard deviation of the data collected)

where $T_{\mathrm{swi},j}$ is the j^{th} observed time interval between switching events, p_m is the m^{th} percentile and ρ is the range of time intervals between switching events in the measurement.

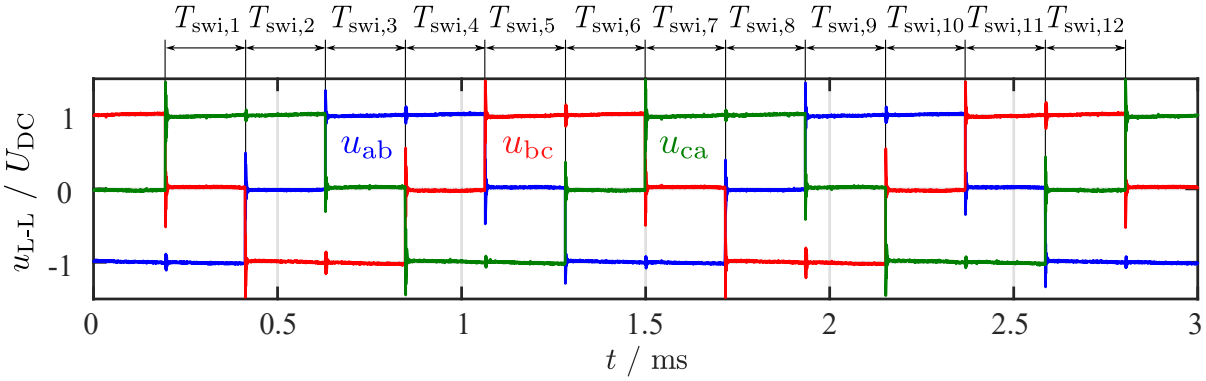


Fig. 3.29: Switching interval estimation from line-to-line voltage measurements

The relative worst case variation (3.42) and the range amplitude containing 95 % of the observed time intervals between switching events (3.43), measured within a 0.5 s time window, are shown in Fig. 3.30. The time for which any particular active voltage is applied remains in a 3.5 % band with respect to the average value. Moreover, once outliers are removed, 95 % of the active vectors are applied for a time within ±1 % of the average. This indicates the robustness of the proposed MPDSC as a six-step control strategy, i.e., the operating point does not change significantly beyond the inherent six-step operation ripple. In contrast, observing Fig. 21b in [34], the worst case variation for

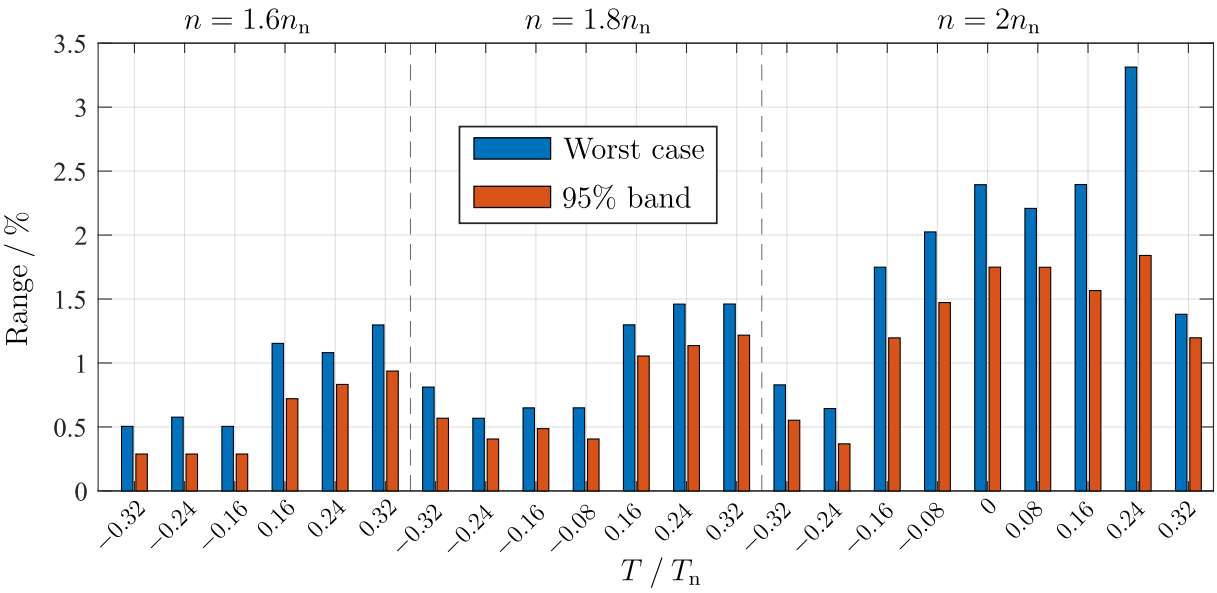


Fig. 3.30: Deviation from perfect six-step during steady-state operation in MPDSC

that implementation is approximately[7] 33 % and 11 %, in the top and bottom subplots, respectively.

Fig. 3.31 offers an example of steady-state six-step operation with MPDSC in the flux-weakening region. The line-to-line voltage measurement acquired with differential voltage probes shows that the six-step sequence is kept. A small error exists in flux linkage amplitude control, primarily due to slight inverter model and flux linkage prediction inaccuracies. This error introduces some disturbances in load angle control, for which the controller compensates. Geometric deviations in the machine construction from the idealized configuration may also introduce some of this variation. The deviation in torque steady state from the measurement remains small (approx. 2 %). A similar example in motoring operation is shown in Fig. 3.32 for a slightly lower speed. This experiment presents a higher reference torque deviation, stemming presumably from a deviation in rotor temperature between the two tests, leading to a difference in the PM flux linkage. The effect of parameter estimation errors is explored in detail in Ch. 6. The dq-current operating point from this experiment is presented in Fig. 3.33, resembling the characteristic tear-drop shape with slight deviations.

A summary of the maximum torque achieved at different speeds for MPDSC and FOC in the motoring and generating range can be seen in Fig. 3.34, demonstrating the benefits of MPDSC over FOC maximum torque output in the flux-weakening region. The benefits of the higher voltage utilization are clear, as MPDSC can operate at a significantly higher torque (up to 15 % increase) under the same operating conditions. The torque enhancement is superior in the motoring region. For $n/n_\mathrm{n} = 1$, the maximum torque

[7] This estimation is obtained by graphically measuring the zero-state time in the upper subplot, and the time between rising and falling edges in the lower subplot.

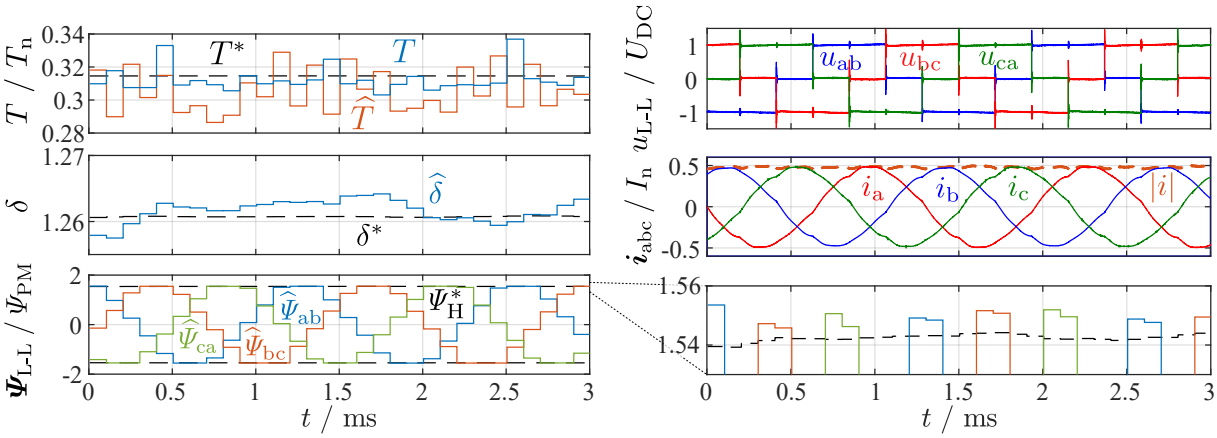


Fig. 3.31: Steady-state MPDSC operation at $2.2n_\mathrm{n}$ in the motoring region. From top to bottom, left column: torque, load angle, and line-to-line fluxes. From top to bottom, right column: line-to-line voltages, phase currents, and zoomed in view of line-to line fluxes. The line-to-line voltages and phase currents are measured at 5 MHz.

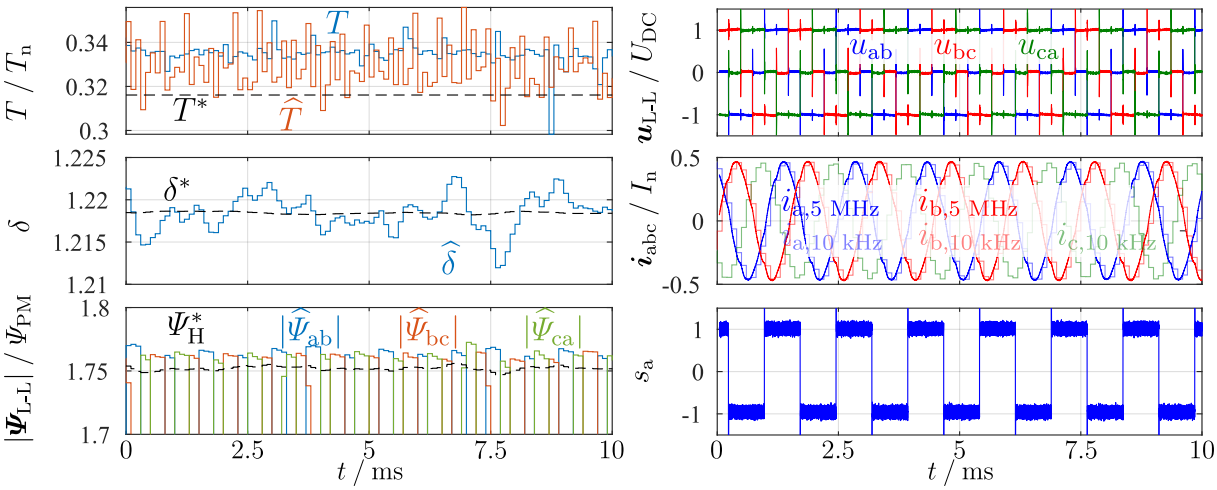


Fig. 3.32: Steady-state MPDSC operation at $2n_\mathrm{n}$ in the motoring region. From top to bottom, left column: torque, load angle, and line-to-line flux. From top to bottom, right column: line-to line voltages, phase currents, and a-switching pulses. The line-to-line voltages, switching pulses, and phase currents are measured at 5 MHz.

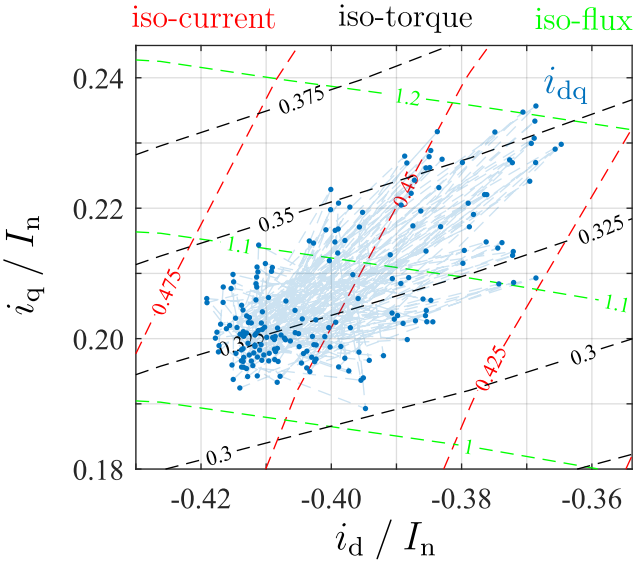


Fig. 3.33: Steady-state MPDSC operation at $2n_n$ in the motoring region

generation is equivalent for MPDSC and FOC, as voltage utilization would no longer be the limiting factor. Conversely, in the flux-weakening region and under the same external operating conditions (i.e., DC-bus voltage, speed), MPDSC benefits from current amplitude reduction due to better voltage utilization. This is also evidenced by the results in Fig. 3.35, depicting the contours of equal current amplitude achieved by fitting a surface through the thin plate interpolation and extrapolation method. The original data points are depicted with markers as indicated by the figure legend.

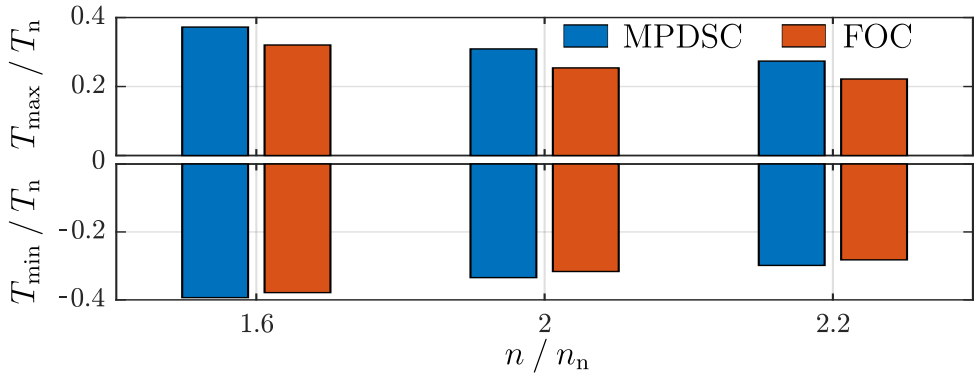


Fig. 3.34: Maximum and minimum achievable torque by MPDSC and FOC (limited to the linear modulation region) at a current amplitude $|\boldsymbol{i}_{dq}| = 0.4I_{max}$ for motoring (top) and generating (bottom) operation

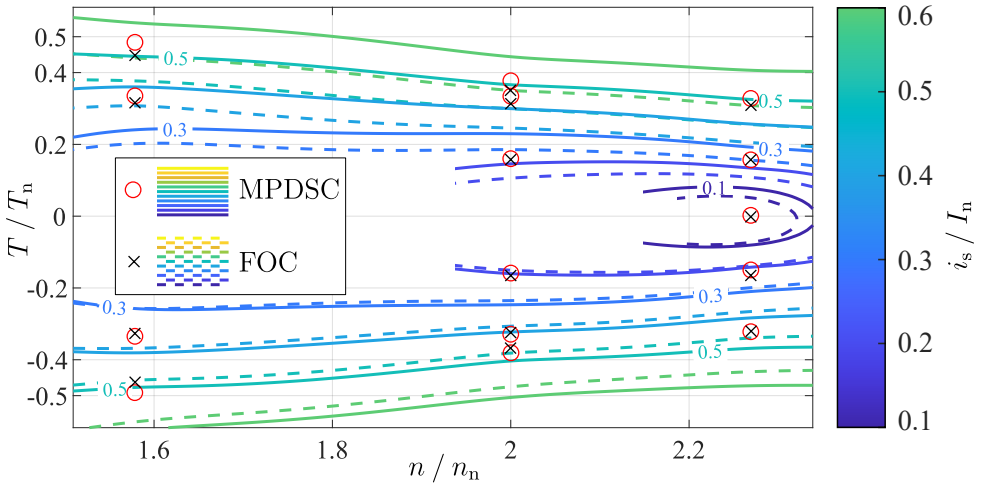


Fig. 3.35: Contour of fitted surface of average current amplitude during MPDSC and FOC steady-state operation for several torque-speed operating points in the flux weakening region

3.4.3 Torque-Transient Operation

Examples of the response to a change in torque reference with MPDSC and conventional FOC can be observed for two different speeds in the flux-weakening region in Fig. 3.36 and 3.37, for motoring and generating operation, respectively. The electromagnetic torque estimation from the measured dq-currents and the machine identified characteristics is shown here instead of the measured torque, due to the slow response of the torque transducer and mechanical resonance at the shaft. During the transient, the angular frequency of the stator flux linkage is adapted through its amplitude to obtain the desired change in load angle. The dynamic capabilities are very satisfactory, achieving the desired torque with a short rise time (approx. 2.3 ms) from the applied reference step.

These figures also depict the performance of FOC, limited to the linear modulation region, regarding torque response and measured current amplitude. The dynamic performance of MPDSC is superior to that of the implemented FOC. Moreover, the current to achieve the same final torque is smaller with MPDSC.

These sharp torque transients introduce a significant disturbance in the DC-bus voltage, as evidenced by Fig. 3.38, as well as by the phase voltage measurement in Fig. 3.36 and 3.37. However, the control strategy shows robustness against this disturbance, with only a slight deviation of the torque operating point during the DC-bus voltage transient (e.g., near 10 ms in Fig. 3.37). Further analysis of robustness against disturbance rejection is carried out in Ch. 6.

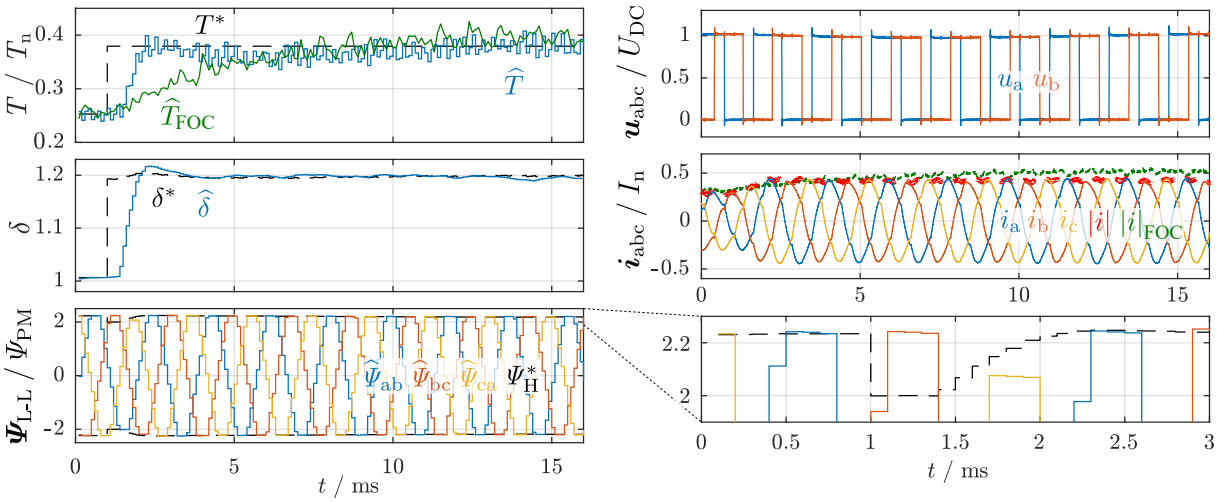


Fig. 3.36: Torque transient in the motoring region for MPDSC and FOC at $1.6n_\mathrm{n}$. From top to bottom, left column: torque, load angle, and line-to-line fluxes. From top to bottom, right column: phase voltages, phase currents, and zoomed in view of line-to line fluxes. Phase currents and voltages are measured at 5 MHz. All variables refer to MPDSC unless otherwise stated.

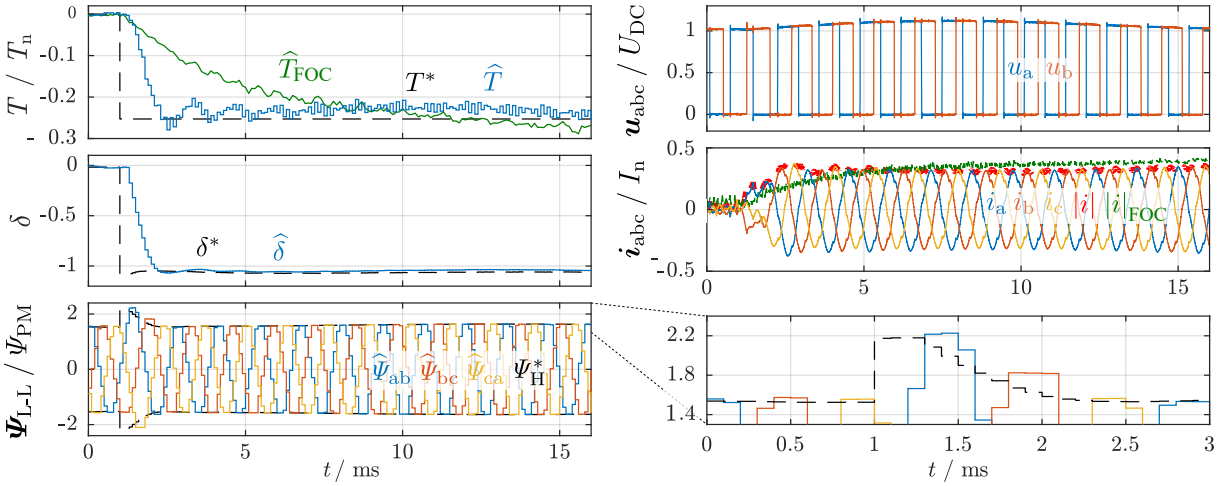


Fig. 3.37: Torque transient in the generating region during MPDSC and conventional FOC operation at $2.2n_\mathrm{n}$. From top to bottom, left column: torque, load angle, and line-to-line fluxes. From top to bottom, right column: phase voltages, phase currents, and zoomed in view of line-to line fluxes. Phase currents and voltages are measured at 5 MHz. All variables refer to MPDSC unless otherwise stated.

3.4.4 Speed-Transient Operation

The response to a speed ramp for a fixed torque reference is depicted in Fig. 3.39. The estimated torque is given here instead of the measured one, since during the ramp up an

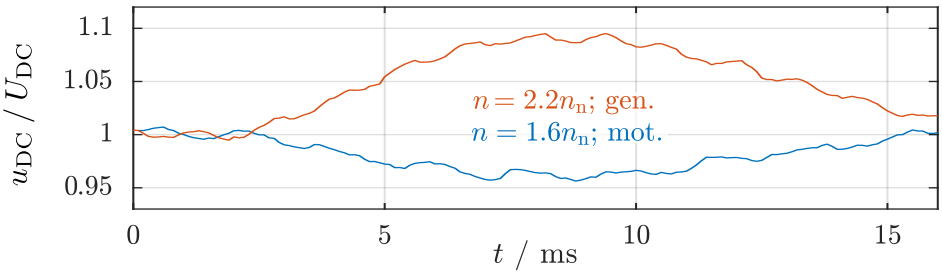


Fig. 3.38: DC-bus voltage evolution during the torque transient response shown in Fig. 3.36 and 3.37

offset is measured during the acceleration phase. These results show adequate response to speed transients maintaining torque tracking, and once more evidence the benefits of MPDSC in terms of reduced current amplitude.

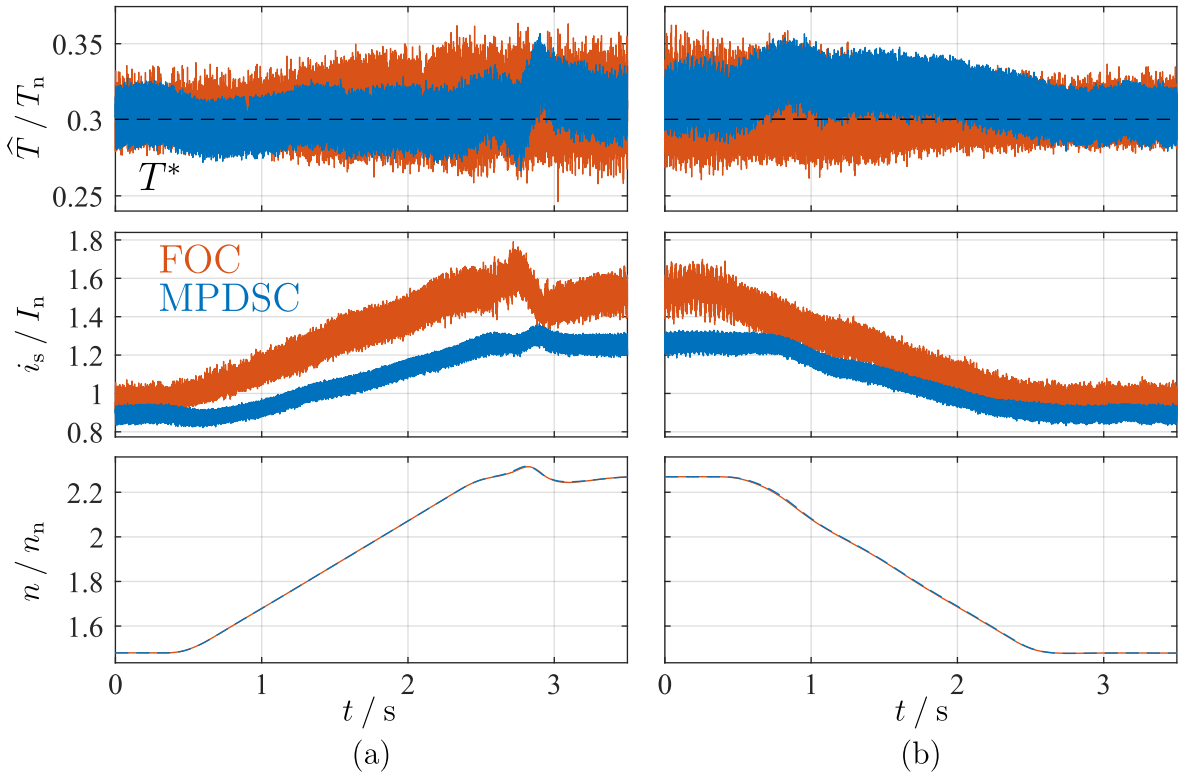


Fig. 3.39: Response to speed ramp up (a) and down (b) in the motoring region during MPDSC and FOC operation at $T^* = 0.3T_n$. From top to bottom: torque, current amplitude, and speed

3.5 Summary

This chapter outlines the MPDSC strategy as a maximum-voltage-utilization method for torque control in heavily utilized PMSMs, combining MPFC, load-angle regulation, nonlinear operating-point selection, and robust flux estimation to enable effective six-step operation in the flux-weakening region. Together, these modules create a real-time-capable control framework with computational effort and dynamic performance similar to conventional FOC, while delivering higher torque under voltage constraints and lower current for the same torque, as confirmed in simulation and experiments. Although MPDSC maintains stability and dynamic performance, it remains confined to six-step, above-base-speed operation, and is sensitive to parameter detuning, in particular to permanent magnet deviations originated by fluctuating rotor temperatures.

4 Fade-Over Strategy

The proposed MPDSC strategy is intended as a complementary addition to FOC, since this is the automotive industry standard for electric drive control. Thus, a critical part of the suggested algorithm is the necessary fade-over between control strategies, which if not handled correctly can introduce unwanted transients including severe current and torque overshoots. This transition is the focus of this chapter.

The main difference between the average operating point in MPDSC and FOC is, for a given torque, speed and DC-link voltage, the higher flux amplitude (and lower load angle) achievable with MPDSC due to its superior voltage utilization. As shown in Fig. 3.2, maintaining equal torque with higher flux amplitude requires a lower load angle. In order to provide an adequate transition between the two operating points, a strategy capable of continuously evolving between the linear voltage region and six-step operation is required. This is exemplified in Fig. 4.1, showing the transition from FOC to MPDSC. The reverse transition also poses problems when following a direct transition approach, as demonstrated later in the chapter.

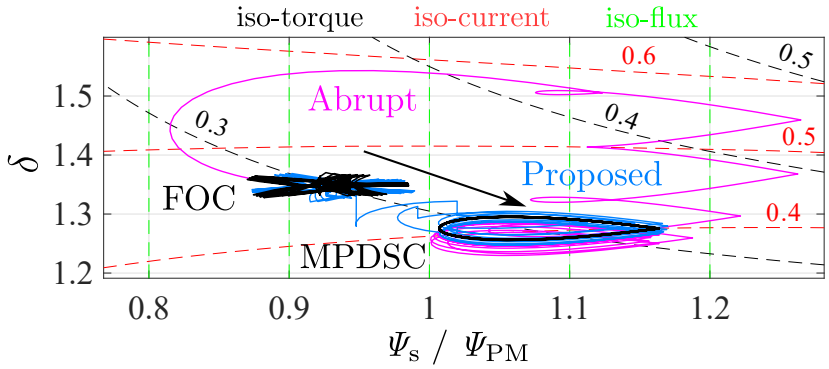


Fig. 4.1: Exemplary transition from FOC to MPDSC with an instantaneous switch-over (abrupt) and the proposed fade-over strategy, with the machine iso-torque, iso-current and iso-flux amplitude contours [OC2]. Operating point: $n = 2n_\mathrm{n}$, $T^* = 0.3T_\mathrm{n}$

When the transition is executed at an arbitrary instant without any fade-over strategy (abrupt scenario in magenta), a significant current, load angle, and torque overshoot

occurs, as can be observed when comparing with the machine contours. The overshoot is primarily caused by the rotor speed being significantly lower than flux rotational speed for six-step operation (cf. (3.4), (3.5)) due to the low flux amplitude at the switch-over instant. Additionally, the flux location at the start of the switch-over has a significant effect on the transient. An alternative fade-over strategy (proposed scenario in blue, explained in the following) can be applied to prevent unwanted transients, which accounts for the optimum flux location to start and end the fade-over, smoothly transitions the flux amplitude and load angle reference to minimize the final controller effort, and achieves flux and load angle control independently.

4.1 Fade-Over Control Strategy

The proposed fade-over control strategy is shown in Fig. 4.2 (orange). During MPDSC (green) operation, the structure is a nested control loop where the flux reference Ψ_h^* is the actuating variable of the load angle controller. During the transition, the load angle control is executed by intermittently stopping the flux rotation applying zero-voltage injection (ZVI). The zero voltage pulses are introduced at the start of each sampling period to counteract the load angle increase, thus maintaining the torque around the desired reference value. The MPFC maintains the peak line-to-line flux within the intended margin, as during regular MPDSC operation. The flux amplitude reference is generated by a transition scheme evolving between the expected steady-state operating points in FOC and MPDSC (more in Sec. 4.1.3). The integrators of the inactive controllers are

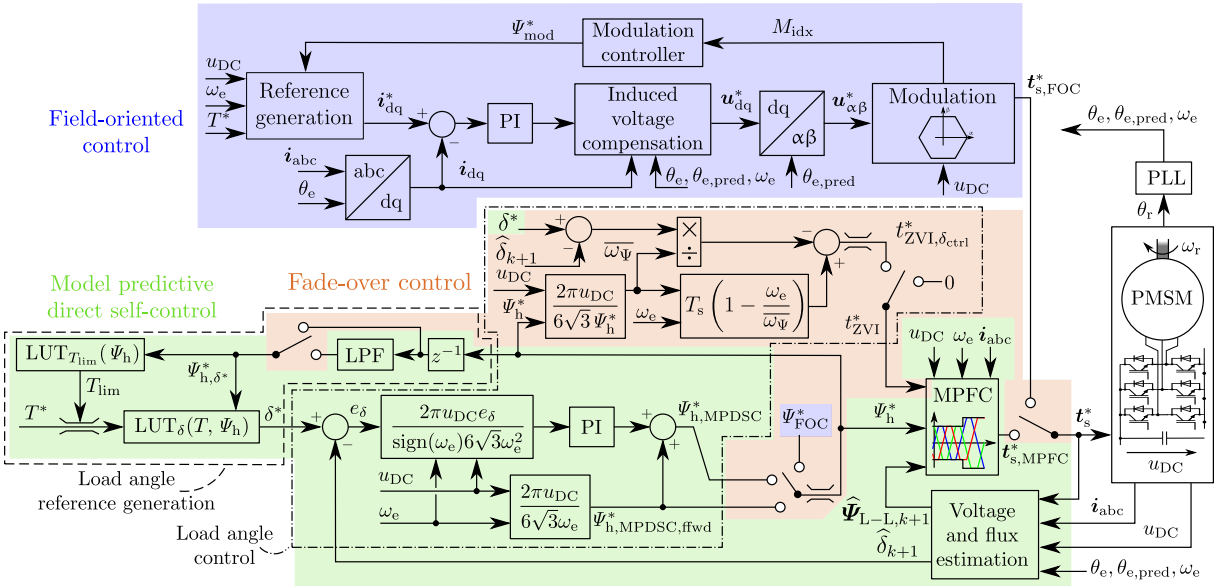


Fig. 4.2: Overview of the control strategy for integration of MPDSC (green) with the systems introduced for fade-over operation (orange) and FOC (blue). The signal selection is done according to Tab. 4.1.

deactivated to prevent windup phenomena, and they are initialized with the appropriate values to prevent unwanted transients before they restart operation. When the operation leaves FOC, the modulation controller flux correction Ψ^*_{mod} is latched until the FOC is active again.

4.1.1 Fade-Over Logic

The fade-over logic chain is represented in Fig. 4.3 and in the truth tables Tab. D.1, D.2, and D.3 in App. D. The outputs of this process are the logic signals c_{to} and c_{from}, which govern the control strategy selection as given by Tab. 4.1 in Sec. 4.1.3.

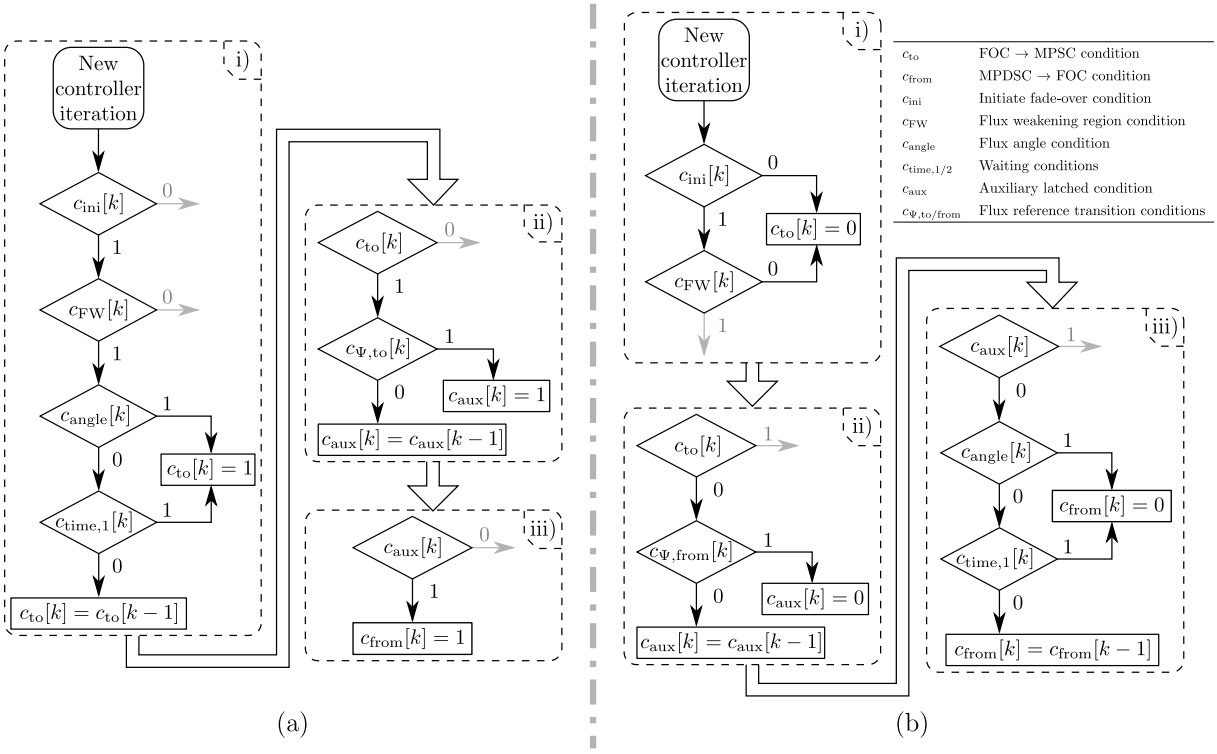


Fig. 4.3: Decision trees for fade-over logic from FOC to MPDSC (a) and vice-versa (b), separated in i) generation of c_{to}, ii) generation of c_{aux}, and iii) generation of c_{from}. Equivalent truth tables are available in App. D.

The decision tree in Fig. 4.3 is initiated by the user or by an upper level control strategy through the signal c_{ini}. The operation with MPDSC is only desirable in the flux-weakening region, as below a certain speed more efficient operation (i.e., MTPC) is obtained below the voltage limit. Thus, the signal c_{FW} is implemented to monitor whether the operation belongs to the flux weakening region. The error between the estimated flux amplitude limit for linear operation and the MTPC flux (Ψ_{MTPC}) is calculated as

$$e_{\mathrm{FW}}(z) = \frac{\Psi_{\mathrm{MTPC}} - \dfrac{u_{\mathrm{DC}}}{\omega_{\mathrm{e}}\sqrt{3}}}{(z-1)\dfrac{\tau_{\mathrm{filt}}}{T_{\mathrm{s}}} + 1}, \tag{4.1}$$

where τ_{filt} is a time constant for filtering (its tuning must be sufficiently slower than the sampling period, in this implementation it is chosen as 1 ms, i.e., $1000T_{\mathrm{s}}$, for achieving good noise rejection) and Ψ_{MTPC} is estimated with a LUT from the torque command (i.e., $\Psi_{\mathrm{MTPC}} = \mathrm{LUT}_{\Psi_s}(T^*)$). This error is used within a hysteresis comparison to generate c_{FW} as[1]

$$c_{\mathrm{FW}}[k] = 1 \quad \text{if } c_{\mathrm{FW}}[k-1] = 0 \ \wedge \ e_{\mathrm{FW}}[k] > 0.02\,\Psi_{\mathrm{PM}}, \tag{4.2a}$$
$$c_{\mathrm{FW}}[k] = 0 \quad \text{if } c_{\mathrm{FW}}[k-1] = 1 \ \wedge \ e_{\mathrm{FW}}[k] \leq 0, \tag{4.2b}$$
$$c_{\mathrm{FW}}[k] = c_{\mathrm{FW}}[k-1] \quad \text{otherwise.} \tag{4.2c}$$

The operating point in the αβ-flux trajectory (cf. Fig. 4.4) at which the transition starts and finishes was observed to be a critical factor for ensuring a smooth fade-over. For the transition from FOC to MPDSC, the flux will increase. The closest point between the quasi-circular and the hexagonal flux path is located at $\theta_s = \frac{\pi}{6} + N\frac{\pi}{3}$, with $N \in \mathbb{Z} \cap \{0, ..., 5\}$. By selecting this point for starting the transition, the flux amplitude naturally evolves in a favorable direction towards the hexagonal path. For the transition from MPDSC to FOC, the transition should also ideally end at a flux angle of $\theta_s = \frac{\pi}{6} + N\frac{\pi}{3}$, with $N \in \mathbb{Z} \cap \{0, ..., 5\}$. This provides the minimum flux amplitude during the hexagonal flux trajectory, and enables the FOC to take over with maximum voltage margin. For these reasons, the signal c_{angle} monitors whether the location of the flux is within a neighborhood of the desired value, as[2]

$$c_{\mathrm{angle}} = \left(\frac{\pi}{6} - \theta_{\mathrm{thr}}\right) \ \leq \ \mathrm{mod}\left(\angle \boldsymbol{\Psi}_{\alpha\beta}, \frac{\pi}{3}\right) \ \leq \ \left(\frac{\pi}{6} + \theta_{\mathrm{thr}}\right), \tag{4.3}$$

where θ_{thr} is the angle threshold. This parameter is tuned to $\pi/60$, chosen as a trade-off between being small enough to maintain the desired advantages and being large enough that the condition would be fulfilled with reasonable frequency (it corresponds to 10 % of the possible angles), enabling the criterion to be effective. Additionally, a time condition is assessed when the angle condition is evaluated ($c_{\mathrm{time},1}$, $c_{\mathrm{time},2}$, which are reset when c_{FW} and c_{aux} change their value, respectively) in order to prevent an infinite evaluation of this criterion. Their tuning is not critical, and for this implementation the waiting conditions were set to bypass the angle conditions after 20 electrical revolutions.

The auxiliary latched signal c_{aux} monitors whether the flux reference has reached its final value. It is obtained as described in Fig. 4.3 and Tab. D.2, from

$$c_{\Psi,\mathrm{to}}[k] = 1 \quad \text{if } \Psi_{\mathrm{h}}^*[k] = \Psi_{\mathrm{h,MPDSC}}^*[k], \tag{4.4a}$$
$$c_{\Psi,\mathrm{to}}[k] = 0 \quad \text{otherwise.} \tag{4.4b}$$

[1] The tuning for the hysteresis value limit (2% of the PM flux) was obtained empirically.

[2] The argument of the modulus operation is considered to range between 0 and 2π.

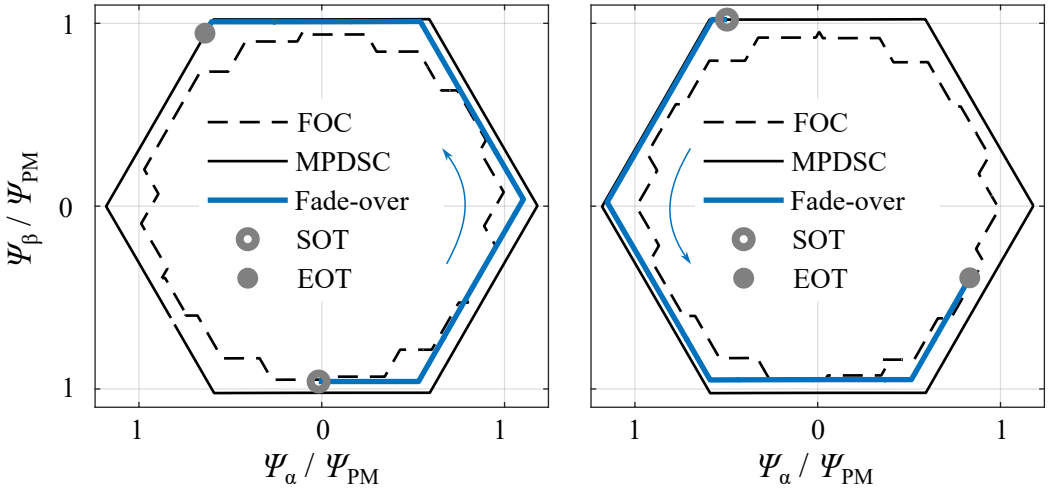


Fig. 4.4: Stator flux in the stationary reference frame during fade-over from FOC to MPDSC (a) and vice versa (b). The flux rotates counter-clockwise. SOT: start of transition, EOT: end of transition

$$c_{\Psi,\text{from}}[k] = 1 \quad \text{if } \Psi_\text{h}^*[k] = \Psi_{\text{h,FOC}}^*[k], \tag{4.5a}$$

$$c_{\Psi,\text{from}}[k] = 0 \quad \text{otherwise.} \tag{4.5b}$$

Thus, the fade-over from FOC to MPDSC starts after being initialized, if the operation is in the flux weakening region, and after the flux angle is suitable. It ends once the desired flux amplitude reference is reached. The fade-over from MPDSC to FOC starts when initialized or when exiting the flux-weakening region. It ends after reaching the desired flux amplitude reference and a suitable flux angle.

4.1.2 Load Angle Control through Zero-Voltage Injection

The control during the fade-over is based on controlling the flux amplitude through MPFC and the load angle through ZVI. For six-step operation at a flux amplitude near that of FOC, the load angle would increase due to the flux angular frequency being too high (cf. (3.5), Fig. 4.1). Instead, the stator flux rotation can be intermittently stopped by applying ZVI in order to control the load angle increase. Thus, the load angle control through ZVI is only possible as long as the flux amplitude is lower than the steady-state six-step flux amplitude, as it only enables control in one direction, i.e., to reduce the load angle amplitude for motoring operation and increase it for generating operation.

The time required for ZVI is calculated based on the discrete load angle plant model

$$\delta[k+2] \approx \hat{\delta}[k+1] + \hat{\bar{\omega}}_\Psi \cdot (T_\text{s} - t_\text{ZVI}) - \omega_\text{e} T_\text{s}, \tag{4.6}$$

where $\widehat{\overline{\omega}}_\Psi$ is the estimated average flux rotational frequency during six-step operation with a given flux amplitude (cf. (3.4)). For an accurate deadbeat control of the load angle, the ZVI time is calculated as

$$t^*_{\mathrm{ZVI},\delta_{\mathrm{ctrl}}} = T_\mathrm{s}\left(1 - \frac{\omega_\mathrm{e}}{\widehat{\overline{\omega}}_\Psi}\right) - \frac{(\delta^* - \widehat{\delta}_{\mathrm{rip,ref}}[k+1]) - (\widehat{\delta}[k+1] - \widehat{\delta}_{\mathrm{rip,pred}}[k+1])}{\widehat{\overline{\omega}}_\Psi}. \tag{4.7}$$

This necessitates the compensation of the load angle ripple due to the hexagonal flux path for both the reference $\widehat{\delta}_{\mathrm{rip,ref}}[k+1]$ and the predicted $\widehat{\delta}_{\mathrm{rip,pred}}$ value, calculated analogously to (3.40), as

$$\widehat{\delta}_{\mathrm{rip,pred}}[k+1] = \mathrm{mod}\left(\widehat{\theta}_\mathrm{s}[k+1], \frac{\pi}{3}\right) - \frac{2\pi \tan\left(\mathrm{mod}\left(\widehat{\theta}_\mathrm{s}[k+1], \frac{\pi}{3}\right)\right)}{3\left(\sqrt{3} + \tan\left(\mathrm{mod}\left(\widehat{\theta}_\mathrm{s}[k+1], \frac{\pi}{3}\right)\right)\right)}, \tag{4.8}$$

$$\widehat{\delta}_{\mathrm{rip,ref}}[k+1] = \mathrm{mod}\left(\widehat{\theta}_\mathrm{s}[k+1] + T_\mathrm{s}\omega_\mathrm{e}, \frac{\pi}{3}\right) - \frac{2\pi \tan\left(\mathrm{mod}\left(\widehat{\theta}_\mathrm{s}[k+1] + T_\mathrm{s}\omega_\mathrm{e}, \frac{\pi}{3}\right)\right)}{3\left(\sqrt{3} + \tan\left(\mathrm{mod}\left(\widehat{\theta}_\mathrm{s}[k+1] + T_\mathrm{s}\omega_\mathrm{e}, \frac{\pi}{3}\right)\right)\right)}. \tag{4.9}$$

This results in the performance depicted in Fig. 4.5 (a). The remaining steady-state error in torque reference tracking could be further compensated by correcting the load angle reference according to the expected average ripple due to ZVI. However, this strategy results in highly fluctuating ZVI times, and relies on very accurate flux and load angle estimation.

To bring about a ZVI time with less ripple, thus enhancing robustness, the control is executed instead as shown in Fig. 4.2 according to

$$t^*_{\mathrm{ZVI},\delta_{\mathrm{ctrl}}} = T_\mathrm{s}\left(1 - \frac{\omega_\mathrm{e}}{\widehat{\overline{\omega}}_\Psi}\right) - \frac{\delta^* - (\widehat{\delta}[k+1] - \widehat{\delta}_{\mathrm{rip,pred}}[k+1])}{\widehat{\overline{\omega}}_\Psi}, \tag{4.10}$$

where the load angle ripple is only compensated in the predicted load angle, and which results in the performance depicted in Fig. 4.5 (b). Thus, with a constant load angle reference the ZVI time stays mostly constant, but a steady-state error remains for load angle control. This is considered preferable, as it still provides sufficiently accurate reference tracking for the short fade-over period, which is the main concern of this control strategy. Finally, the calculated value ($t^*_{\mathrm{ZVI},\delta_{\mathrm{ctrl}}}$) is limited to prevent pulses too short for the inverter to supply.

4.1.3 Flux Amplitude Reference

The flux reference fed to the MPFC smoothly transitions from the value at the start of the fade-over to the expected final value (Ψ^*_h), following a maximum rate of change (tuned empirically to $0.15\,\Psi_\mathrm{PM}/\mathrm{ms}$). The reference setting according to the fade-over logic signals is given in Tab. 4.1.

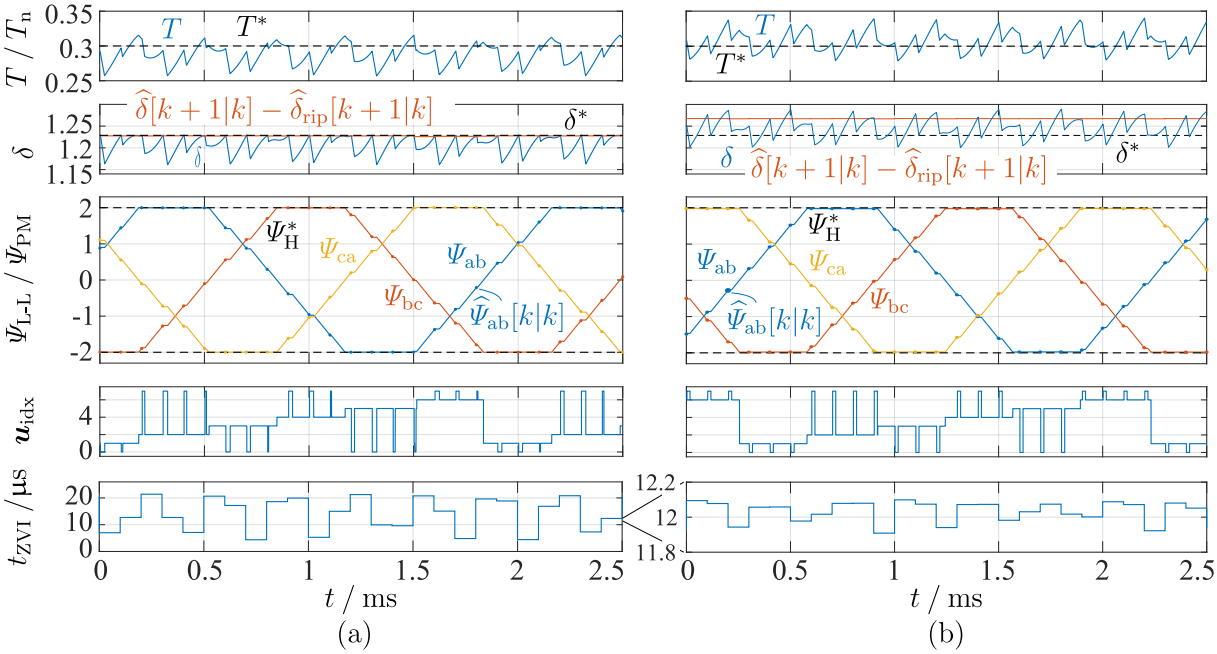


Fig. 4.5: Example operation of MPDSC with ZVI for accurate deadbeat load angle control (a) and for low ripple ZVI time (b). From top to bottom: torque, load angle, line-to-line flux, switching state index, and ZVI time

$c_{\text{to}}[k]$	$c_{\text{from}}[k]$	Control Strategy	$\Psi^*_{\text{h}}[k]$	Ψ^*_{h} rate limit	$\Psi^*_{\text{h},\delta^*}[k]$	$t^*_{\text{ZVI}}[k]$	$t^*_{\text{s}}[k]$
0	0	FOC	$\Psi^*_{\text{FOC}}[k]$	-	-	-	$t^*_{\text{s,FOC}}[k]$
1	0	F→M	$\Psi^*_{\text{h,MPDSC,ffwd}}[k]$	Yes	$\Psi^*_{\text{h}}[k-1]$	$t^*_{\text{ZVI},\delta_{\text{ctrl}}}[k]$	$t^*_{\text{s,MPFC}}[k]$
1	1	MPDSC	$\Psi^*_{\text{h,MPDSC}}[k]$	-	LPF($\Psi^*_{\text{h}}[k-1]$)	0	$t^*_{\text{s,MPFC}}[k]$
0	1	M→F	$\Psi^*_{\text{FOC}}[k]$	Yes	$\Psi^*_{\text{h}}[k-1]$	$t^*_{\text{ZVI},\delta_{\text{ctrl}}}[k]$	$t^*_{\text{s,MPFC}}[k]$

Tab. 4.1: Control strategy, reference setting and command selection according to fade-over logic

4.1.4 MPFC with Zero-Voltage Injection

The flux amplitude is controlled during the fade-over by the same MPFC system used by MPDSC, adapted to account for the ZVI, as

$$\hat{\boldsymbol{\Psi}}_{\text{L-L}}[k+2] = \hat{\boldsymbol{\Psi}}_{\text{L-L}}[k+1] + (1 - \frac{t_{\text{ZVI}}}{T_{\text{s}}})\Delta\hat{\boldsymbol{\Psi}}_{\text{L-L}}[k]. \tag{4.11}$$

The switching time commands are modified to introduce the zero-voltage pulse at the beginning of the sampling period according to the zero-voltage vector that will require

the least switching events. Tab. E.1 and E.2 in App. E show the introduction of ZVI in the switching time generation of the MPFC algorithm.

4.1.5 Load Angle Reference Selection

The load angle reference is calculated from the flux amplitude reference through the same LUT used for MPDSC operation as given in Tab. 4.1 and Fig. 4.2. For fade-over control, the LPF is not applied, since the flux amplitude control and the load angle control are not part of the same nested loop, and thus do not need decoupling.

4.2 Simulation Results

The fade-over response of the system in simulation is shown in Fig. 4.6, in terms of the evolution of the dq-current operating point, and in Fig. 4.7 in terms of the flux amplitude, the load angle operating point, the voltage sequence and ZVI applied. The benefits with respect to the abrupt transition are evident in the figure, preventing severe current and torque deviations in both directions (note the normalized iso-current and iso-torque contours). The time response for the abrupt transition is not shown for simplicity, as the drawbacks evident in the dq-current paths are ample motivation for an improved fade-over strategy.

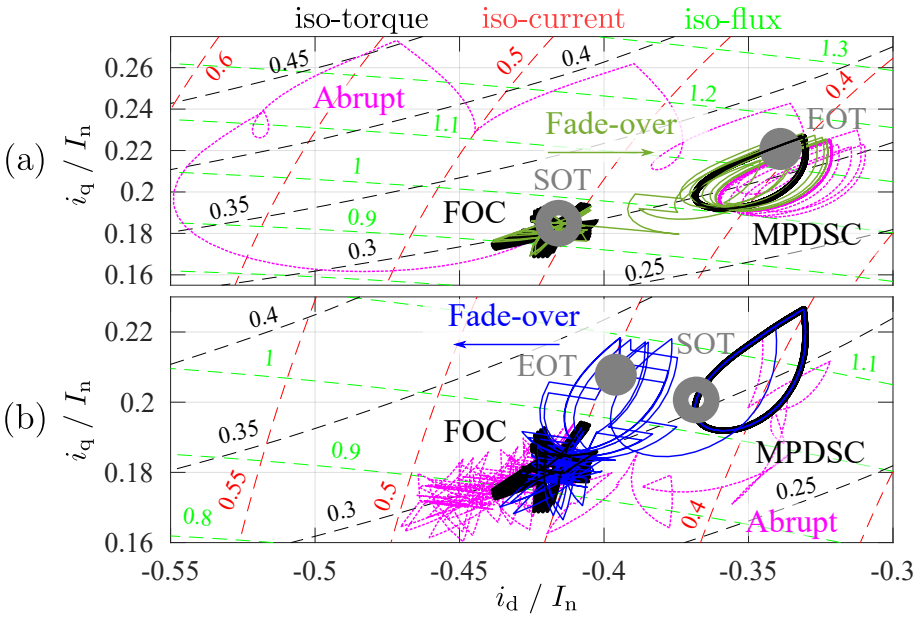


Fig. 4.6: Simulation evaluation of the fade-over strategy from FOC to MPDSC (a) and from MPDSC to FOC (b) in terms of the dq-current paths. SOT: start of transition, EOT: end of transition. Operating point: $n = 2n_n$, $T^* = 0.3T_n$

In the fade-over towards MPDSC, the introduction of ZVI enables the operating point to evolve to a higher flux amplitude while limiting the inherent increase in load angle. The

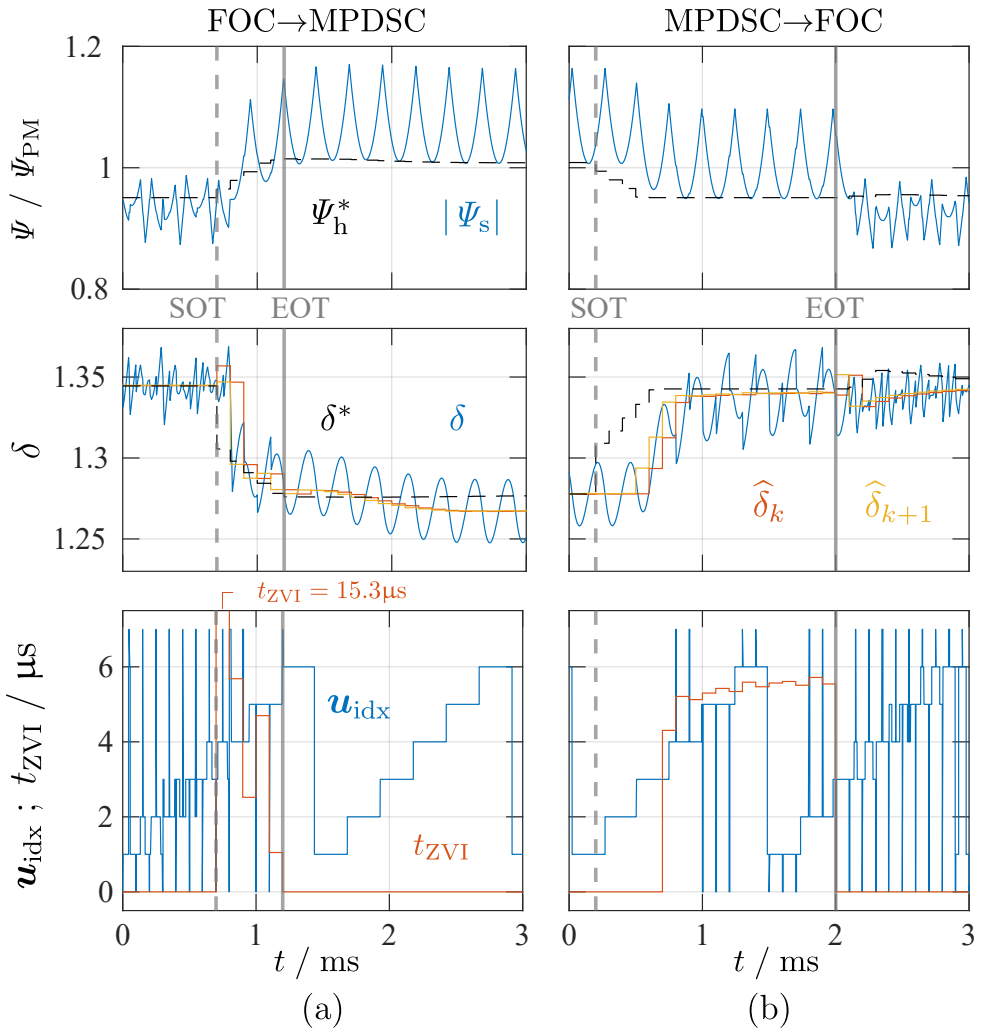


Fig. 4.7: Simulation evaluation of the fade-over strategy from FOC to MPDSC (a) and from MPDSC to MPDSC (b). From top to bottom: flux amplitude, load angle, and switching state index and ZVI time. SOT: start of transition, EOT: end of transition. Operating point: $n = 2n_\mathrm{n}$, $T^* = 0.3T_\mathrm{n}$

first ZVI pulse is the largest, and lies beyond the axis limits at 15.3 µs. After completing the fade-over towards MPDSC, the load angle controller then corrects the remaining operating-point deviation while maintaining six-step operation with small adjustments to the flux amplitude.

For the return to FOC, the flux is reduced so that the lower part of the flux ripple coincides with the reference flux amplitude during FOC. This operation is maintained until a convenient stator flux angle for switch-over is predicted (cf. Sec. 4.1.1). Note that the signals corresponding to SOT (start of transition) and EOT (end of transition), linked to c_to and c_from, are generated in the controller one sampling period in advance to the actual machine response.

The duration required for a complete fade-over was found to vary significantly with the operating conditions present at the instant the logic chain is initiated, particularly as a function of the flux angle and the flux amplitude reference difference between MPDSC and FOC. This duration is constrained by the $c_{\text{time},1}$ and $c_{\text{time},2}$ signals to a maximum of 20 electrical revolutions. Since the machine behavior during the transition is well defined, as demonstrated in the preceding sections, this delay between control strategies is not considered critical.

4.3 Experimental Results

The experimental evaluation of the transitions from FOC to MPDSC and vice versa are shown in Fig. 4.8 and 4.9. The change in modulation strategy is evidenced by the line-to-line voltage measurements presented. Both experiments demonstrate satisfactory behavior in terms of flux amplitude control and shown negligible torque or current deviations. In the transition from MPDSC to FOC a slight current overshoot occurs after FOC takes over. This is due to the correction applied by the modulation controller, as the final flux set point at the end of the transition was higher than the one expected for FOC operation.

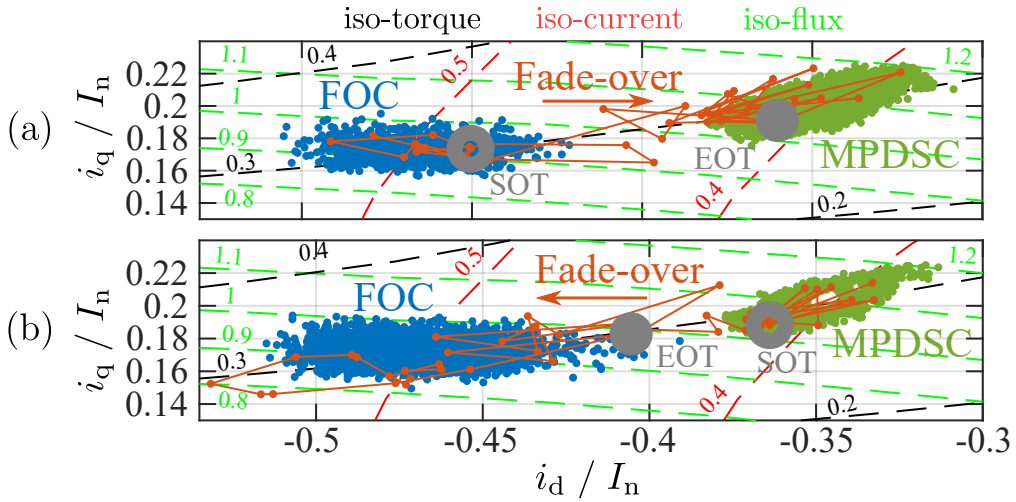


Fig. 4.8: Experimental evaluation of the fade-over from FOC to MPDSC (a) and from MPDSC to FOC (b) in terms of the dq-current path. SOT: Start of transition, EOT: end of transition. Operating point: $n = 2n_{\text{n}}$, $T^* = 0.3T_{\text{n}}$

Fig. 4.10 and 4.11 illustrate the fade-over between control strategies as the system enters and exits the flux-weakening region during speed-up (a) and speed-down (b) transients. Current and torque deviations remain within expected limits throughout the transition. The fade-over toward FOC remains for a longer time in the transition control method until conditions allow FOC to fully assume control. Nevertheless, in equivalent tests where flux-weakening detection was used as the sole transition criterion, noise in its identification

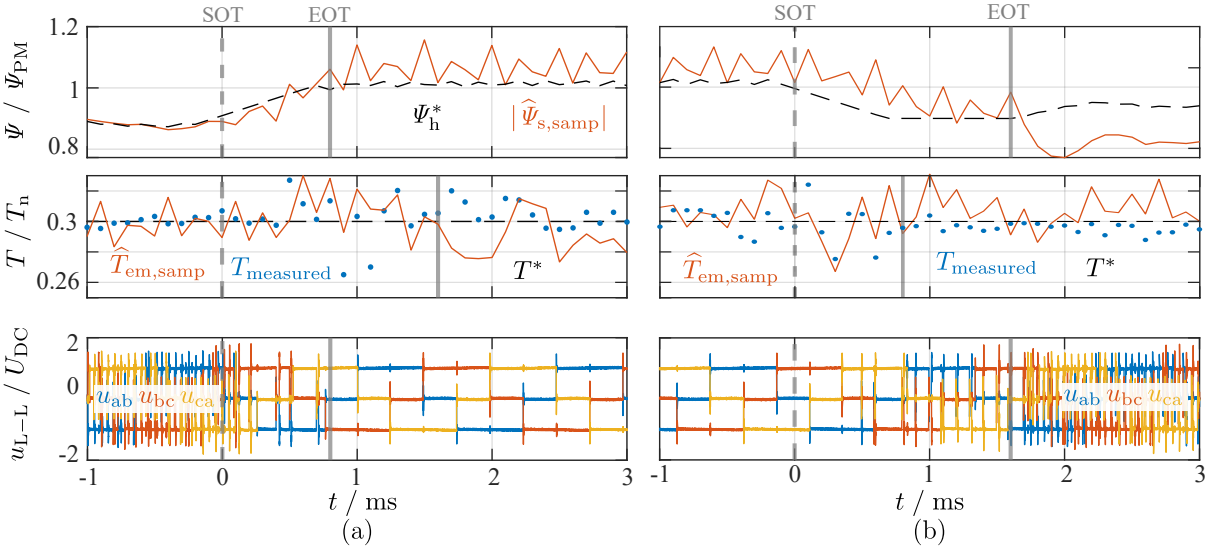


Fig. 4.9: Experimental evaluation of the fade-over from MPDSC to FOC (a) and from MPDSC to FOC (b). From top to bottom: flux amplitude, torque, and line-to-line voltage. SOT: start of transition, EOT: end of transition. Operating point: $n = 2n_n$, $T^* = 0.3T_n$

caused repeated switch-over between strategies. If this criterion were intended as the only trigger for the fade-over (i.e., transitioning to MPDSC whenever possible), additional filtering and protection would be necessary. In the present implementation, the transition is initiated by the user or an upper-level control strategy, with the flux-weakening criterion acting as a necessary but not sufficient condition for activating the decision logic chain (cf. Sec. 4.1.1).

4.4 Summary

This chapter presents a fade-over strategy that enables smooth, reliable transitions between conventional FOC and the proposed MPDSC method by independently regulating flux amplitude through MPFC, and load-angle through ZVI, to avoid torque and current overshoots. Simulation and experimental results showed that these resulting trajectories keep current and torque deviations within acceptable ranges, even during speed transients, although triggering the transition solely through flux-weakening detection proved susceptible to noise. Additional supervisory logic, filtering, and protective measures could further strengthen the robustness of the fade-over in practical applications.

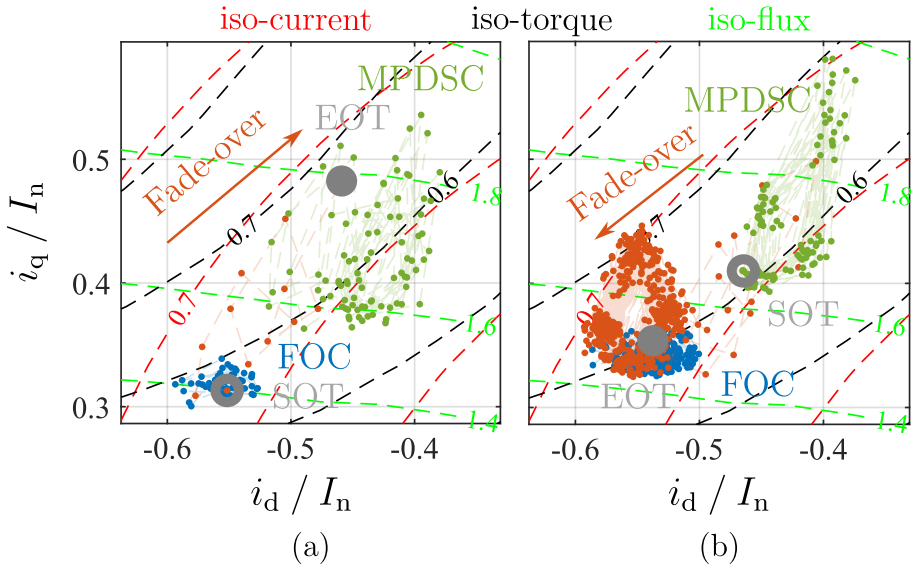


Fig. 4.10: Experimental evaluation of the fade-over from MPDSC to FOC (a) and from FOC to MPDSC (b) triggered by speed transients with $T^* = 0.6T_n$ in terms of the dq-current path

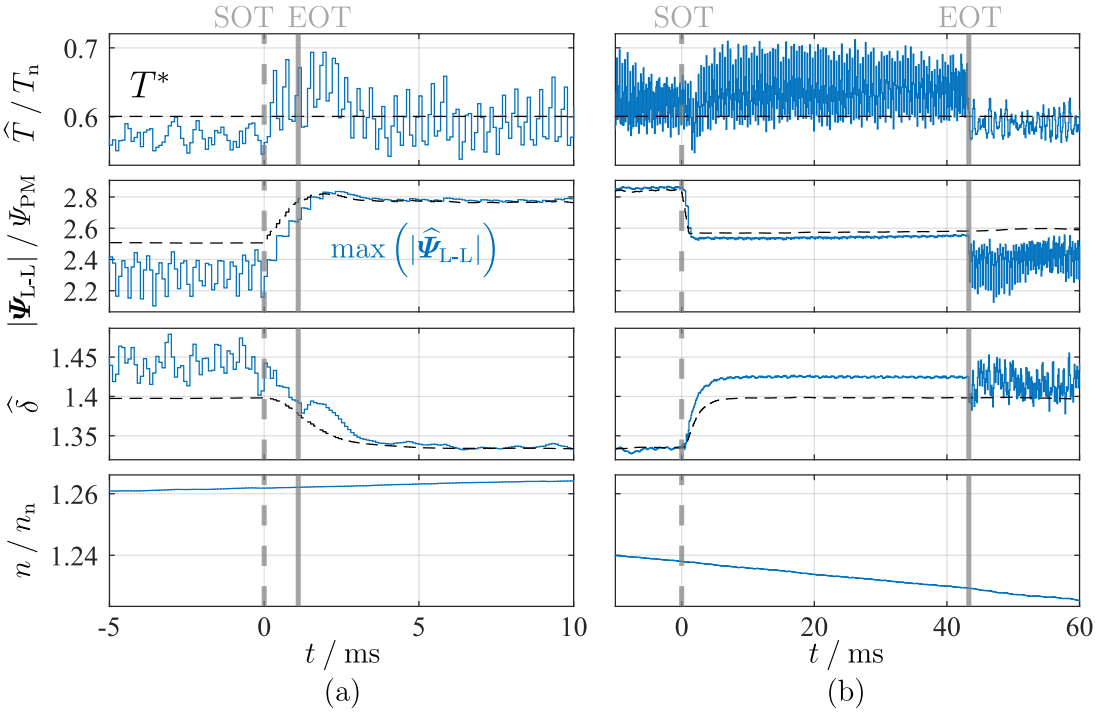


Fig. 4.11: Experimental evaluation of the fade-over from MPDSC to FOC (a) and from FOC to MPDSC (b) triggered by speed transients with $T^* = 0.6T_n$. From top to bottom: torque, line-to-line flux amplitude, estimated load angle, and speed

5 Alternative Switching Patterns

While six-step operation is very desirable in terms of voltage utilization, increasing the drive performance with respect to methods limited to the linear modulation region, it also introduces unwanted behavior in terms of harmonic content. To mitigate these issues, the proposed MPDSC can be enhanced to achieve different pulse patterns which may be beneficial depending on the control goals. One of these possibilities is the introduction of edge-modulated three-fold switching [35], [36]. This switching pattern, necessary modifications to the control structure and effect on performance are the focus of this chapter. The scope is limited to examining the integration of the three-fold modulation strategy within the MPDSC algorithm. It does not address the control policy governing the selection or timing of modulation factors, although the effect of specific folding ratios upon the harmonic content of various system variables is analyzed.

5.1 Three-Fold Switching Pattern

The three-fold switching pattern deviates from six-step by introducing a short modulation between adjacent voltage vectors instead of an immediate transition, as seen in Fig. 5.1(a). This creates an 18-corner flux path in the αβ-coordinates as shown in Fig. 5.1(b). During steady-state operation the inscribed circle amplitude Ψ_h remains the same as for six-step operation for the same speed and DC-bus voltage, since the perimeter of the hexagon remains unchanged by the choice of Ψ_f. In this work the folding ratio is defined as

$$k_\mathrm{f} = \frac{\Psi_\mathrm{f}}{\Psi_\mathrm{h}}, \tag{5.1}$$

with an increased folding ratio leading to an increased corner folding amplitude.

The modified flux path reduces the amplitude of the fundamental component of the stator flux. The amplitude of the fundamental component can be calculated as

$$|\boldsymbol{\Psi}_{\mathrm{s},1}| = \frac{6\sqrt{3}\,\Psi_\mathrm{h}}{\pi^2}\left(2\cos\left(\frac{\pi}{3}k_\mathrm{f}\right) - 1\right), \tag{5.2}$$

which is achieved by a Fourier analysis of the flux waveform under these conditions. On the other hand, it also has the potential to reduce the ripple in some variables.

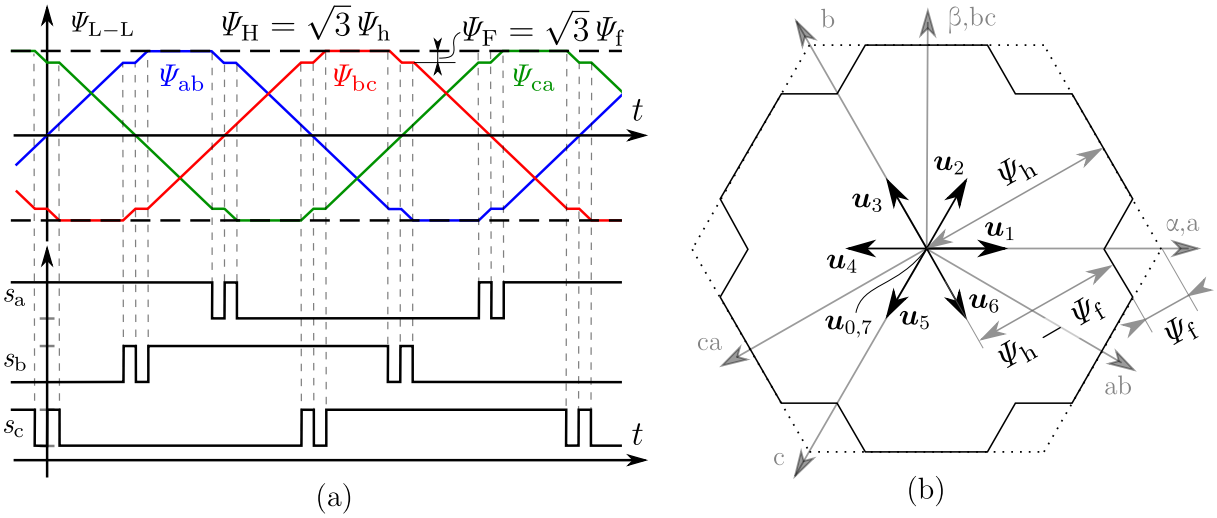


Fig. 5.1: Three-fold switching pattern analysis: (a) line-to-line flux and inverter leg states; (b) stator flux linkage trajectory

The geometry of the 18-corner flux trajectory normalized with respect to Ψ_h is presented in Fig. 5.2, where $\boldsymbol{\psi}_s$ is the normalized stator flux linkage vector, $\boldsymbol{\psi}_{s,1}$ is its fundamental component, θ_s and $\theta_{s,1}$ are their respective angles, and $\pm\varphi_{fold}$ are the angles at which the additional corners appear with respect to the corners of the original hexagonal flux path.

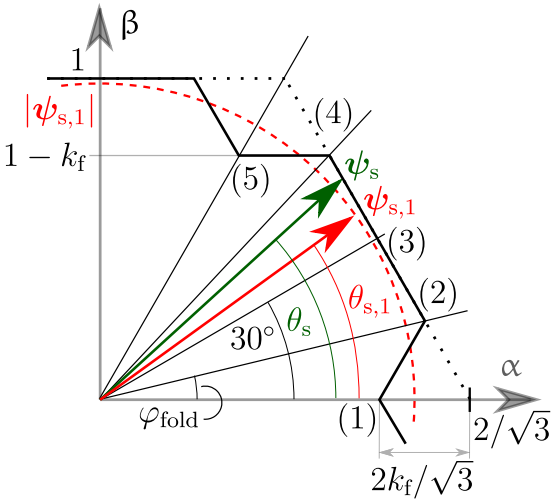


Fig. 5.2: Normalized 18-corner flux trajectory analysis

The angle at which the transition between flux paths takes place can be calculated as

$$\varphi_{fold} = \tan^{-1}\left(\frac{\sqrt{3}k_f}{2 - k_f}\right). \tag{5.3}$$

Based on this, the path in the first sector can be separated in three regions: (1)-(2), (2)-(4) and (4)-(5). The relation between the instantaneous stator flux angle and that of its fundamental component can be calculated in the first sector, following the same process as in Sec. 3.2.4.5, as

$$\theta_{s,1} = (1 - k_f)\frac{2\pi \tan\theta_s}{3(\sqrt{3} + \tan\theta_s)} \qquad \text{for } 0 < \theta_s < \varphi_{fold}, \tag{5.4a}$$

$$\theta_{s,1} = \frac{2\pi \tan\theta_s}{3(\sqrt{3} + \tan\theta_s)} \qquad \text{for } \varphi_{fold} < \theta_s < \frac{\pi}{3} - \varphi_{fold}, \tag{5.4b}$$

$$\theta_{s,1} = (1 - k_f)\frac{2\pi \tan\left(\frac{\pi}{3} - \theta_s\right)}{3(\sqrt{3} + \tan\left(\frac{\pi}{3} - \theta_s\right))} \qquad \text{for } \frac{\pi}{3} - \varphi_{fold} < \theta_s < \frac{\pi}{3}. \tag{5.4c}$$

These calculations must be referred from each sector of the flux path to the first sector for the equations to remain valid. Based on the above, the flux amplitude and load angle ripple evolution are represented in Fig. 5.3. The load angle ripple is defined as the angle difference between the stator flux linkage and its fundamental component, as in Sec. 3.2.4.5.

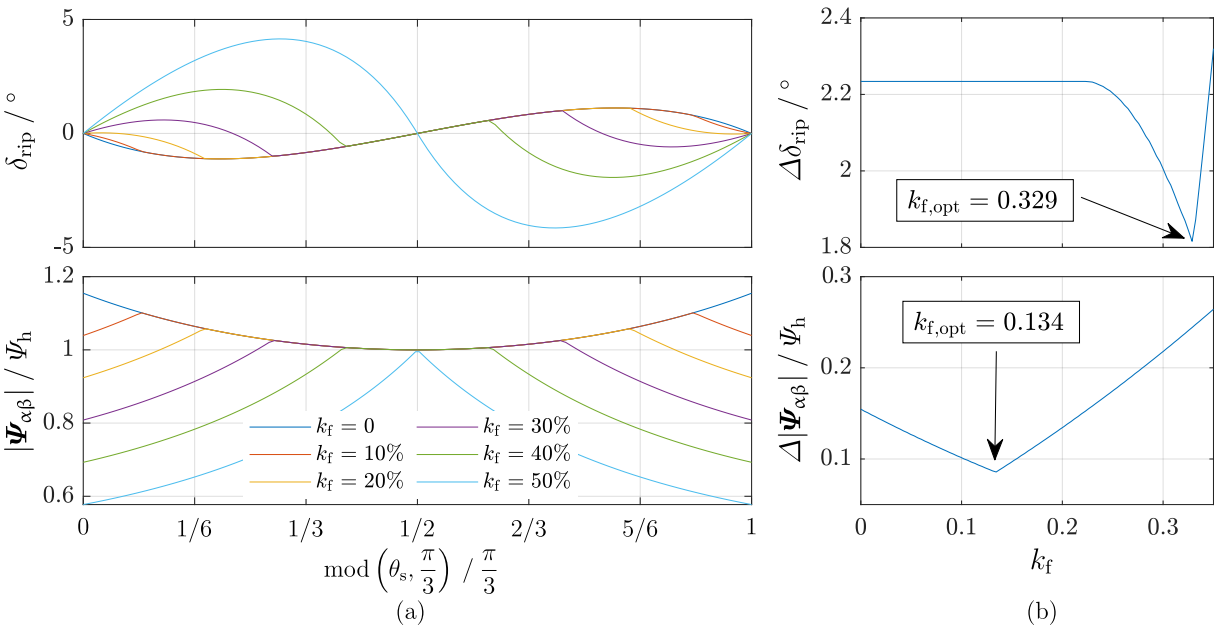


Fig. 5.3: Ripple with three-fold switching pattern according to k_f, in terms of the trajectory with respect to flux angle (a) and peak-to-peak ripple with respect to k_f (b) for the load angle (top) and the flux amplitude (bottom)

A key advantage of this modulation strategy, which may be of particular interest for certain applications, lies in the additional degree of freedom it provides for shaping the frequency content of the current on both the AC and DC sides of the inverter. Assuming a simplified machine model with $L_d = L_q = L_s$ and a normalized short-circuit current

defined as $\Psi_{\mathrm{PM}}/(L_{\mathrm{s}} I_{\mathrm{n}}) = k_{\mathrm{sc}}$, and based on (2.8b) and (2.13), the normalized current in the $\alpha\beta$-reference frame $\tilde{i}_{\alpha\beta}$ can be expressed as a function of the normalized flux $\tilde{\Psi}_{\alpha\beta}$ as

$$\tilde{i}_{\alpha\beta} = k_{\mathrm{sc}} \left(\tilde{\Psi}_{\alpha\beta} - \boldsymbol{T}_{\mathrm{dq}\to\alpha\beta}(\theta_{\mathrm{e}}) \, [1 \; 0]^{\top} \right). \tag{5.5}$$

Within this simplified framework and for constant speed, the fundamental component of the AC current depends on two contributions: a constant term associated with the PM flux, and a variable term determined by the flux trajectory. In contrast, higher-order harmonics are exclusively governed by the flux trajectory and can therefore be analyzed through the harmonic content of the α-flux, as illustrated in Fig. 5.4. In this figure, the top-left subplot depicts the fundamental harmonic component of the flux as a function of the flux-trajectory corner amplitude, while the remaining subplots show the harmonic components adjacent to the 6$^{\mathrm{th}}$, 12$^{\mathrm{th}}$, and 18$^{\mathrm{th}}$ orders, normalized with respect to the fundamental component. This analysis demonstrates that three-fold modulation can be effectively utilized to shape the harmonic content of the AC current. However, its impact is dependent on the specific system parameters, and therefore must be evaluated accordingly to ensure accurate and meaningful conclusions.

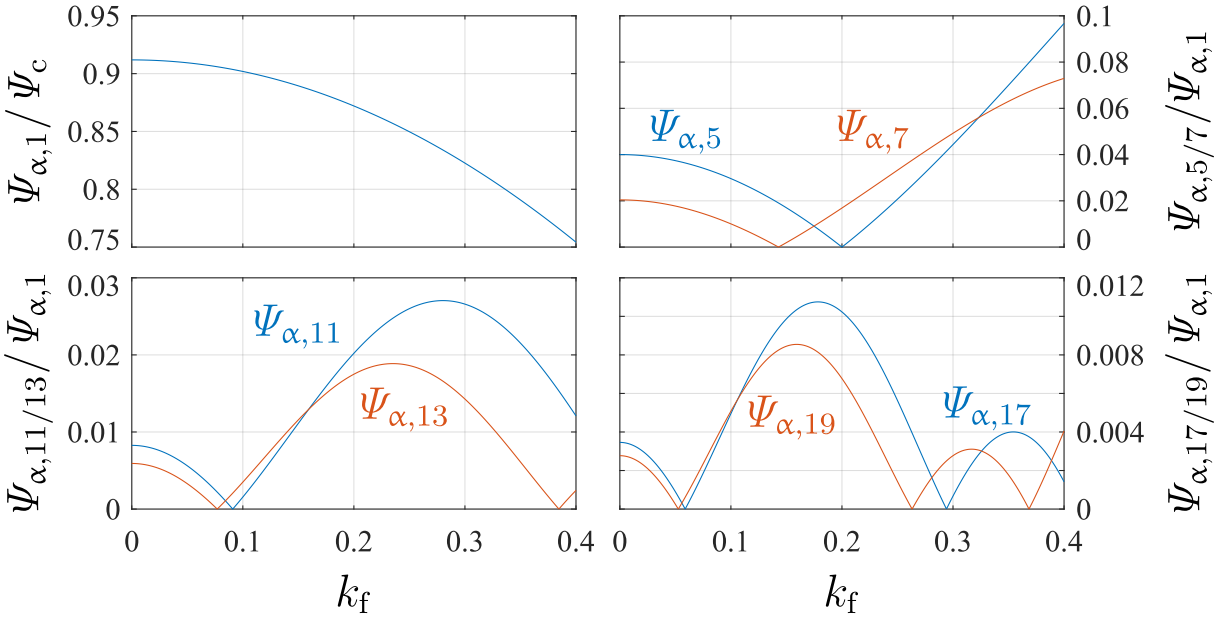


Fig. 5.4: Normalized fundamental (top left), 5$^{\mathrm{th}}$ and 7$^{\mathrm{th}}$ (top right), 11$^{\mathrm{th}}$ and 13$^{\mathrm{th}}$ (bottom left), and 17$^{\mathrm{th}}$ and 19$^{\mathrm{th}}$ (bottom right) harmonic components of the α-flux. The higher-order harmonics are equivalently present in the AC current according to (5.5).

Through the DC current, the modulation scheme directly influences the resulting DC-link voltage ripple through the DC-link impedance, and thus requires careful, application-specific analysis [45] to ensure the safe operation of other components, such as the battery in traction applications. The dominant DC current harmonics occur at multiples of six. For reference, Fig. 5.5 shows the amplitudes of the first three significant harmonics for an

ideal sinusoidal three-phase current system (unit amplitude) under varying phase angles between voltage and current, and different folding ratios in the three-fold modulation scheme.

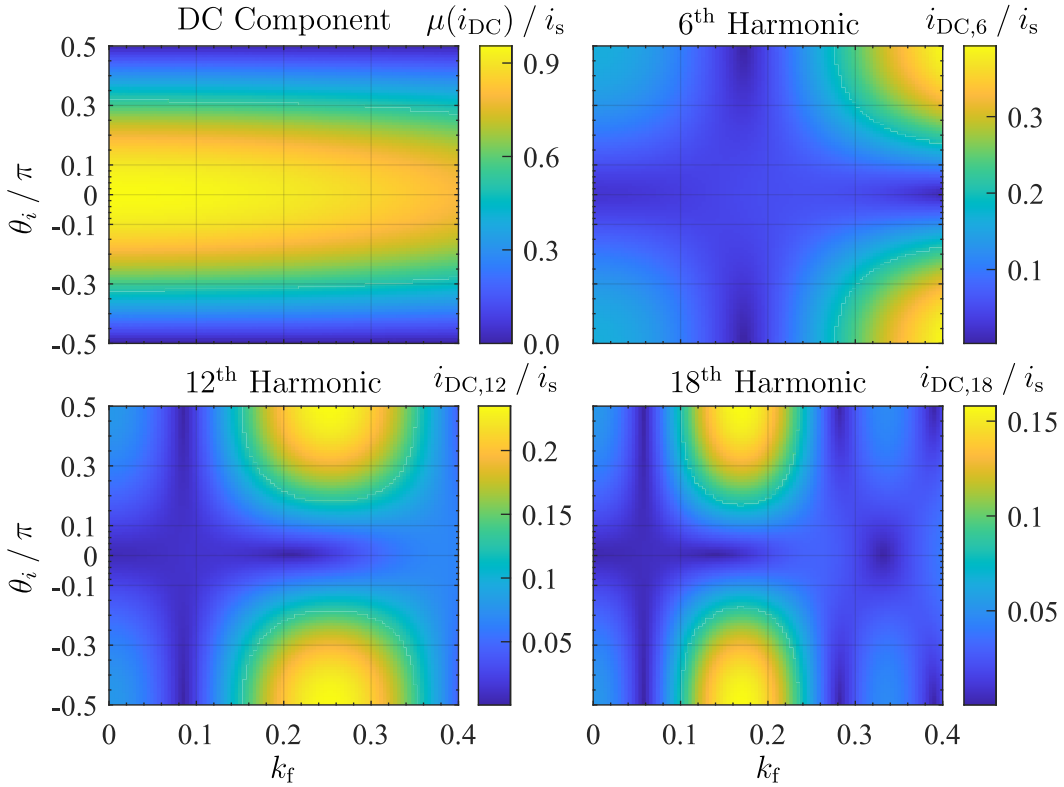


Fig. 5.5: Average value (μ) and harmonic content of the DC current for simplified scenario according to voltage-to-current angle and folding ratio

This simplified analysis does not account for the harmonic content of the line currents, nor the reduction in power output with increased k_f (i.e., for the same torque-speed operating point, increasing k_f would necessitate an increase in current amplitude to compensate for the fundamental component reduction in flux). Since no single hexagon shape minimizes ripple across all variables, the selection of k_f requires a trade-off between different performance objectives. As this choice is inherently application-specific, further optimization is beyond the scope of this work. Instead, the rest of this chapter focuses on effective implementation of a control strategy that can realize the proposed modulation approach within MPDSC.

5.2 Three-Fold MPDSC Control Strategy

To extend the MPDSC algorithm from six-step operation to three-fold switching, several approaches can be considered. One possibility is to treat the new thresholds defining the 18 corners independently, analogous to the original hexagonal flux trajectory. In this

case, for each of the six hexagon corners, three distinct flux-reference thresholds would be sequentially assigned along different axes. However, performing this within the existing control framework would demand an arbitrarily high sampling frequency for small values of the folded flux amplitude Ψ_f, since at most two of the three switching events could be computed within a single sampling period. To account for these additional thresholds without increasing the sampling frequency, more elaborate rules for flux prediction and switching time selection are required, depending on which thresholds are reached at a given instant. However, this solution may become more susceptible to noise, particularly when very small flux-reference thresholds are involved (e.g., during the second transition at low Ψ_f).

On the other hand, the complete switching sequence, regardless of its duration and including the possibility of spanning multiple sampling periods, can be calculated during the sampling period preceding the first switching event and then executed over the subsequent periods. In this way, the three-fold switching sequence can be derived directly from the MPFC algorithm without introducing additional thresholds for triggering switching events or increasing the sampling frequency. Instead, an auxiliary variable, hereafter referred to as the folding time t_f, is computed, and the switching sequence is generated accordingly for the successive sampling periods (see Sec. 5.2.2). The following subsections present the necessary modifications to the control structure for this approach, affecting flux estimation, reference setting, switching pulse generation, and switching time command generation. The overall MPDSC structure, adapted from those shown in Fig. 3.5 and 4.2, is shown in Fig. 5.6, with the introduced or modified blocks highlighted in blue. For clarity, the modifications related to fade-over with FOC, discussed in the previous chapter, are omitted here.

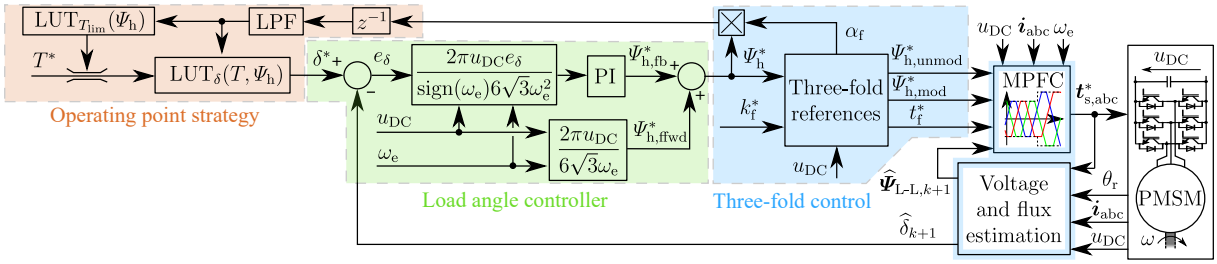


Fig. 5.6: Control diagram for torque control in the flux-weakening region with MPDSC enhanced for three-fold switching

5.2.1 Three-Fold Reference Generation

The reference folding ratio k^*_f is generated externally based on the desired control output. Some options for this choice are given in Tab. 5.1.

From the chosen folding ratio, the remaining variables are calculated as shown in Fig. 5.7. The folding time t_f is the time for which each of the active voltages is applied at the transition between sectors in the flux trajectory. This modulation is applied symmetrically,

Effect	k_f	Source
Maximum voltage utilization	0	
Minimum AC current 19^{th} harmonic component	0.053	Fig. 5.4
Minimum AC current 17^{th} harmonic component	0.059	Fig. 5.4
Minimum DC current 18^{th} harmonic component	0.06	Fig. 5.5
	0.0717	[36]
Minimum AC current 13^{th} harmonic component	0.077	Fig. 5.4
Minimum AC current 11^{th} harmonic component	0.091	Fig. 5.4
Minimum DC current 12^{th} harmonic component	0.08	Fig. 5.5
	0.1033	[36]
Minimum flux amplitude ripple	0.134	Fig. 5.3
Minimum AC current 7^{th} harmonic component	0.143	Fig. 5.4
Minimum DC current 6^{th} harmonic component	0.17	Fig. 5.5
	0.185	[36]
Minimum AC current 5^{th} harmonic component	0.200	Fig. 5.4
Minimum load angle ripple	0.329	Fig. 5.3

Tab. 5.1: Effect of different choices of folding ratios. The resulting AC and DC current harmonic content depends on the specific application parameters and operating conditions. Therefore the value of k_f is not uniquely determined by the the desired effect.

i.e., the duration of the pulses at each side of the middle switching event is the same. The folding time is calculated initially as

$$t^*_{\mathrm{f,unsat}} = \frac{k_{\mathrm{f,unsat}}\,\Psi^*_\mathrm{h}\sqrt{3}}{u_\mathrm{DC}}. \tag{5.6}$$

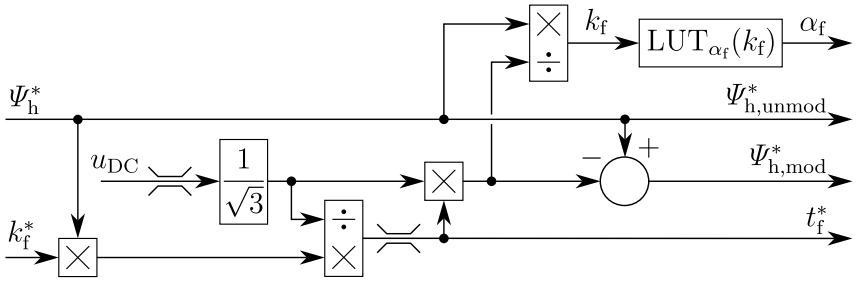


Fig. 5.7: Diagram of three-fold reference generation

The minimum folding time is given by the inverter limitations for short pulse synthesis (in the chosen implementation it is considered under 1 µs). The maximum folding time depends on the switching horizon, which can be best understood by considering an example objective switching sequence such as Fig. 5.8.

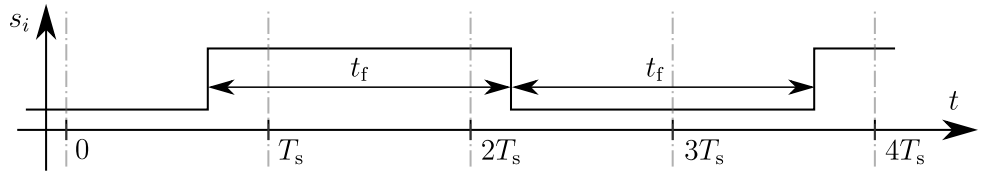


Fig. 5.8: Example switching sequence for three-fold modulation

Assuming correct flux prediction and voltage estimation, the first switching event on the sequence could happen at any point within the sampling period immediately after the switching time calculation (i.e., $t = 0$ to $t = T_\mathrm{s}$). After that, the modulation between the two adjacent voltage vectors takes place, with a total duration of $2t_\mathrm{f}$. Therefore, and considering the worst case scenario in which the first switching occurs just before T_s, the maximum folding time is

$$t_{\mathrm{f,max}} = (N_\mathrm{s} - 1)\frac{T_\mathrm{s}}{2}, \tag{5.7}$$

where N_s is the switching horizon, or the number of sampling periods for which the switching sequence will be calculated. The minimum switching horizon to achieve a given folding ratio at different speeds can be calculated from (5.6), (5.7) and (3.4) as

$$N_\mathrm{s} \geq 1 + \frac{2\pi k_\mathrm{f}}{3T_\mathrm{s}\omega_\mathrm{e}}. \tag{5.8}$$

Based on this, and to ensure that $k_\mathrm{f} \leq 0.3$ can be achieved in the full flux weakening range for the machine considered, a switching horizon $N_\mathrm{s} = 4$ was chosen.

After limiting the folding time, the modified flux reference is calculated as (5.9) and the true reference folding ratio as (5.10),

$$\Psi^*_{\mathrm{h,mod}} = \Psi^*_\mathrm{h} - t^*_\mathrm{f} \cdot \frac{u_\mathrm{DC}}{\sqrt{3}}, \tag{5.9}$$

$$k_\mathrm{f} = 1 - \frac{\Psi^*_{\mathrm{h,mod}}}{\Psi^*_\mathrm{h}}. \tag{5.10}$$

From k_f the fundamental component amplitude reduction gain α_fold is calculated as

$$\alpha_\mathrm{fold} = \frac{|\boldsymbol{\Psi}_{\mathrm{s},1}|}{\Psi_\mathrm{h}} = \frac{6\sqrt{3}}{\pi^2}\left(2\cos\left(\frac{\pi}{3}k_\mathrm{f}\right) - 1\right). \tag{5.11}$$

This relation could be calculated online or stored as a LUT for reduced computational effort. The load angle reference can be calculated as before based on the scaled flux amplitude set-point as shown in Fig. 5.6.

5.2.2 Switching Time Calculation

From the original flux reference Ψ_{H}^* (or $\Psi_{\mathrm{H,unmod}}^*$), the modified flux reference $\Psi_{\mathrm{H,mod}}^*$ and the calculated folding time reference t_{f}^*, the full switching sequence can be synthesized. This refers to the on and off times required to achieve the desired flux path throughout the sampling periods in the switching horizon. As an example, the flux in one of the line-to-line axes is considered in Fig. 5.9, leading to the switching pattern shown underneath.

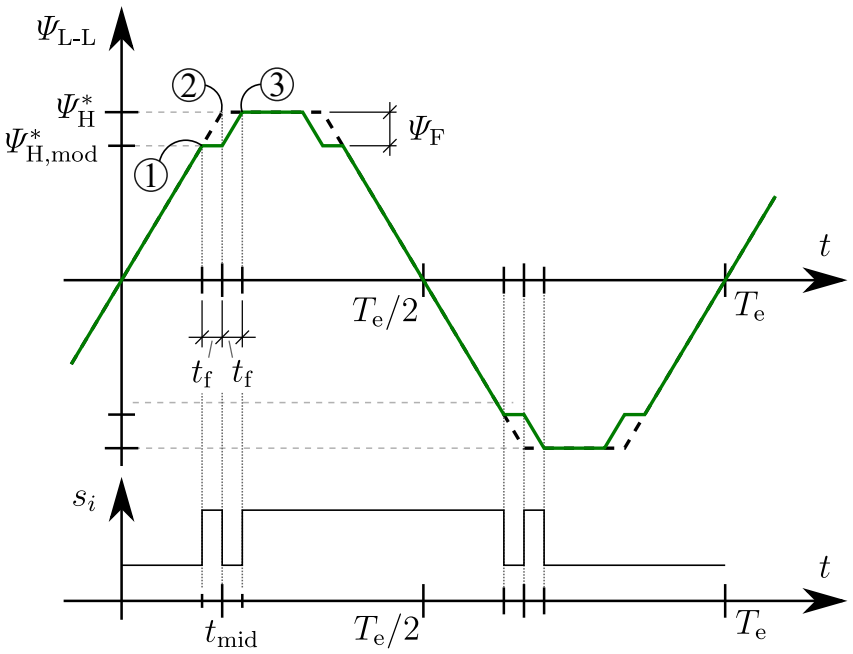


Fig. 5.9: Switching events according to the comparison between line-to-line flux and flux references for three-fold operation

The sequence of events for the calculation of the full switching time, which is composed of two switch-on times and two switch-off times, is as follows:

i. The two-steps ahead predicted line-to-line flux triggers the calculation of a new switching sequence when it surpasses $\Psi_{\mathrm{H,mod}}^*$, i.e., Ψ_{H}^* is replaced by $\Psi_{\mathrm{H,mod}}^*$ in the switching criteria calculation (3.12).
ii. The initial switching state determines the first time of the switching sequence, i.e., for the sequence highlighted in Fig. 5.9, the first switch-off time is set at 0.
iii. The time for the middle switching event t_{mid}^* (② in Fig. 5.9) is calculated identically to the standard MPDSC algorithm, i.e., by comparing the one-step-ahead flux prediction with the unmodified flux reference Ψ_{H}^*. In the example, this sets the second off-switching time.
iv. The remaining switching events (① and ③ in Fig. 5.9) are set symmetrically at $t_{\mathrm{mid}}^* - t_{\mathrm{f}}^*$ and $t_{\mathrm{mid}}^* + t_{\mathrm{f}}^*$, respectively.

The full switching sequence could, under inaccurate flux prediction, extend beyond or under the admissible limits. To prevent this, the special switching scenarios in Fig. 5.10 are considered as

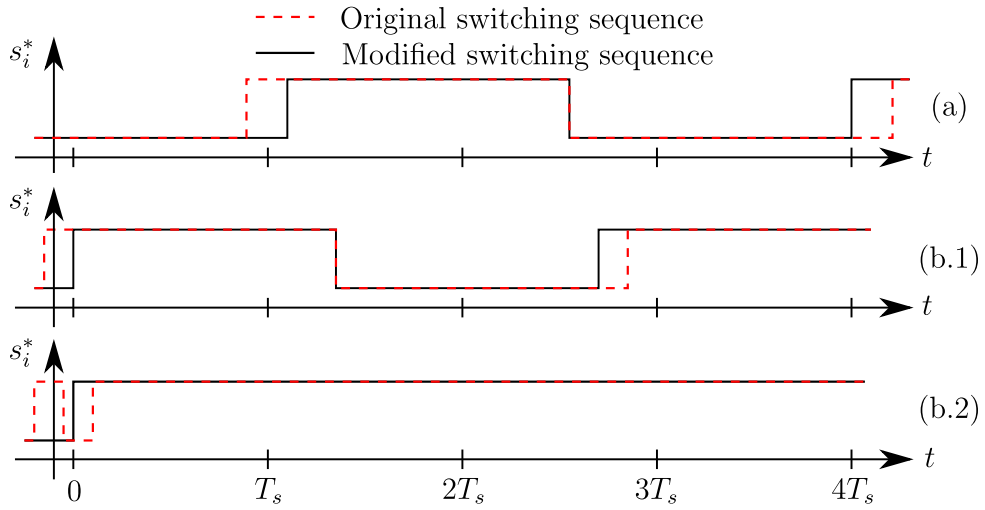


Fig. 5.10: Special scenarios requiring modification of the switching sequence for three-fold operation

a. The last switching event would happen after the end of the switching horizon: the middle switching event t^*_{mid} is maintained, and t^*_{f} is recalculated as

$$t^*_{\mathrm{f}} = N_{\mathrm{s}} T_{\mathrm{s}} - t^*_{\mathrm{mid}}. \tag{5.12}$$

The first and third switching events are set symmetrically at $t^*_{\mathrm{mid}} - t^*_{\mathrm{f}}$ and $t^*_{\mathrm{mid}} + t^*_{\mathrm{f}}$, respectively.

b.1. The first switching event would happen before the start of the first sampling period: the middle switching event t^*_{mid} is maintained, and t^*_{f} is recalculated as

$$t^*_{\mathrm{f}} = t^*_{\mathrm{mid}}. \tag{5.13}$$

The first and third switching events are set symmetrically at $t^*_{\mathrm{mid}} - t^*_{\mathrm{f}}$ and $t^*_{\mathrm{mid}} + t^*_{\mathrm{f}}$, respectively.

b.2. In the case in which $t^*_{\mathrm{mid}} < 0$, a command to switch to the final switching state is set at $t = 0$.

5.2.3 Switching Pulse Generation

From the full switching sequence $\boldsymbol{t}_i = \left[t_{\mathrm{on},1}, t_{\mathrm{on},2}, t_{\mathrm{off},1}, t_{\mathrm{off},2}\right]$, the individual switching time commands for the different sampling periods within the switching horizon $\boldsymbol{t}_{i,k}$ must be calculated. Time margin (T_{m}), and compensation of delay and interlock dead-time effects are implemented, analogously to Sec. 3.2.1.2 and 3.2.1.3. An example is shown in Fig. 5.11. For each of the individual sampling periods, the following steps are followed:

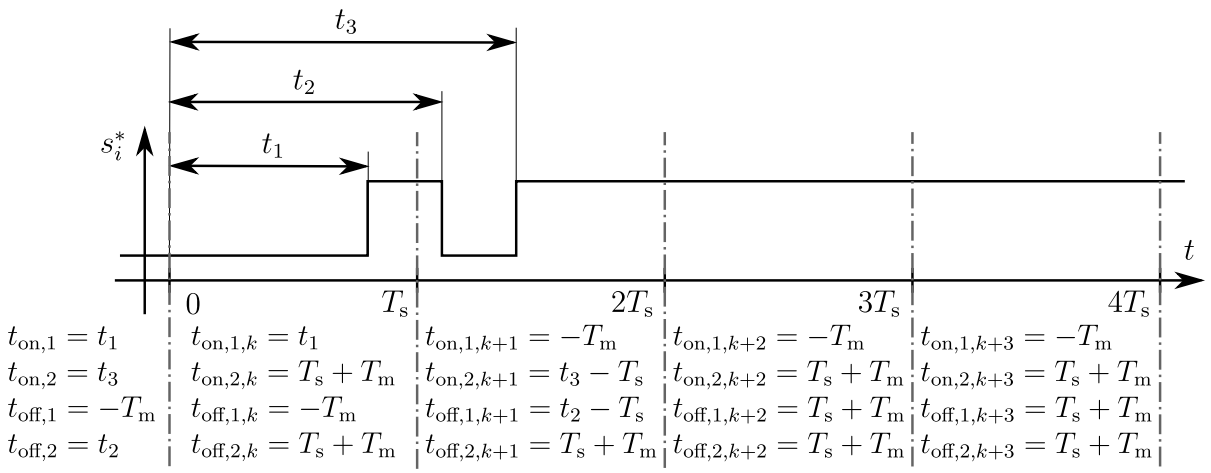


Fig. 5.11: Example of the split of full switching sequence between the sampling periods of the switching horizon

i. The time at the beginning of the sampling period is subtracted from the full switching sequence. In the example given in Fig. 5.11, for the first and second sampling periods this results in

$$\boldsymbol{t}_{i,k} \leftarrow \boldsymbol{t}_i = \left[t_1,\, t_3,\, -T_\mathrm{m},\, t_2\right], \tag{5.14a}$$

$$\boldsymbol{t}_{i,k+1} \leftarrow \boldsymbol{t}_i - T_\mathrm{s} = \left[t_1 - T_\mathrm{s},\, t_3 - T_\mathrm{s},\, -T_\mathrm{m} - T_\mathrm{s},\, t_2 - T_\mathrm{s}\right]. \tag{5.14b}$$

ii. The initial switching state is determined by the latest switching event before the start of the corresponding sampling period. The remaining switching events happening before the start of the sampling period are set to after T_s. In Fig. 5.11, for the second sampling period the past switching events are

$$\boldsymbol{t}_{i,k+1}\left(\boldsymbol{t}_{i,k+1} < 0\right) = \left[t_{\mathrm{on},1,k+1},\, t_{\mathrm{off},1,k+1}\right] = \left[t_1 - T_\mathrm{s},\, -T_\mathrm{m} - T_\mathrm{s}\right], \tag{5.15}$$

from which the latest switching event is

$$\max\left(\boldsymbol{t}_{i,k+1}\left(\boldsymbol{t}_{i,k+1} < 0\right)\right) = t_{\mathrm{on},1,k+1}, \tag{5.16}$$

resulting in the substitution

$$\left[t_{\mathrm{on},1,k+1},\, t_{\mathrm{off},1,k+1}\right] \leftarrow \left[-T_\mathrm{m},\, T_\mathrm{s} + T_\mathrm{m}\right]. \tag{5.17}$$

iii. The switching events beyond the end of the sampling period are set to after T_s. In Fig. 5.11, for the first sampling period

$$\boldsymbol{t}_{i,k} \leftarrow \left[t_1,\, T_\mathrm{s} + T_\mathrm{m},\, -T_\mathrm{m},\, T_\mathrm{s} + T_\mathrm{m}\right]. \tag{5.18}$$

iv. The switching events are reordered so that $t_{\mathrm{on},1} \leq t_{\mathrm{on},2}$ and $t_{\mathrm{off},1} \leq t_{\mathrm{off},2}$, resulting in the sequences observed in Fig. 5.11.

The individual switching sequences are then executed at the corresponding sampling period. If a new switching sequence is triggered as given in Sec. 5.2.2.1, the previous switching sequence is overwritten.

5.2.4 Voltage and Flux Estimation

The voltage and flux estimation remain unchanged from the methods introduced in Sec. 3.2.4. In contrast, the load-angle ripple estimation must account for the modified relationship between the instantaneous flux-linkage angle and its fundamental component, as given in (5.4) and illustrated in Fig. 5.3. This can be implemented either through online evaluation of the corresponding equations (5.4) or by means of offline-calculated LUTs for $\varphi_{\mathrm{fold}}(k_{\mathrm{f}})$ and $\theta_{\mathrm{s},1}(\theta_{\mathrm{s}})$ in each of the three sections of a flux-hexagon sector.

5.3 Simulation Results

The systems described in the sections above have been implemented and analyzed in simulation in order to validate the algorithm. The steady-state performance, transition to the new modulation scheme and torque-transient response are analyzed.

An example of steady-state operation of MPDSC with three-fold modulation at different ratios is shown in Fig. 5.12, with the path in the dq-current plane for each of the folding ratios represented in Fig 5.13. The modulation introduced shows little effect upon the torque ripple even for a folding ratio close to that of minimum flux linkage ripple, due to the six-step tear-shaped dq-current trajectory being in the direction of the torque isoline. The slight reduction in voltage utilization is evidenced in Fig. 5.13 by a deviation of the dq-current paths towards lower flux and higher current. Also, with the reduced flux amplitude a higher load angle is required to achieve the same torque as seen in Fig. 5.12. It should be noted that the load angle estimation method successfully removes the load angle ripple regardless of the modulation strategy. In terms of the DC current, the modulation scheme changes its shape and shifts its frequency components, but does not affect the overall ripple significantly at these folding ratios.

The transition from six-step modulation to three fold is represented in Fig. 5.14. The flux trajectory is immediately adapted from six-step ($k_{\mathrm{f}} = 0$) to the 18-corner shape (with $k_{\mathrm{f}} = 0.13$), and the torque shows very slight transient. This is due to the load angle reference generation responding slowly to the sudden change in the fundamental flux amplitude through the LPF in the operating point selection scheme. Full torque tracking accuracy is restored under 50 ms.

Finally, Fig. 5.15 and 5.16 show the torque transient response in motoring and generating operation for multiple folding ratios. The dynamic performance of the controller is barely affected by the change in modulation strategy. It is notable that the torque ripple for high load is reduced with the folding ratio minimizing the flux amplitude ripple.

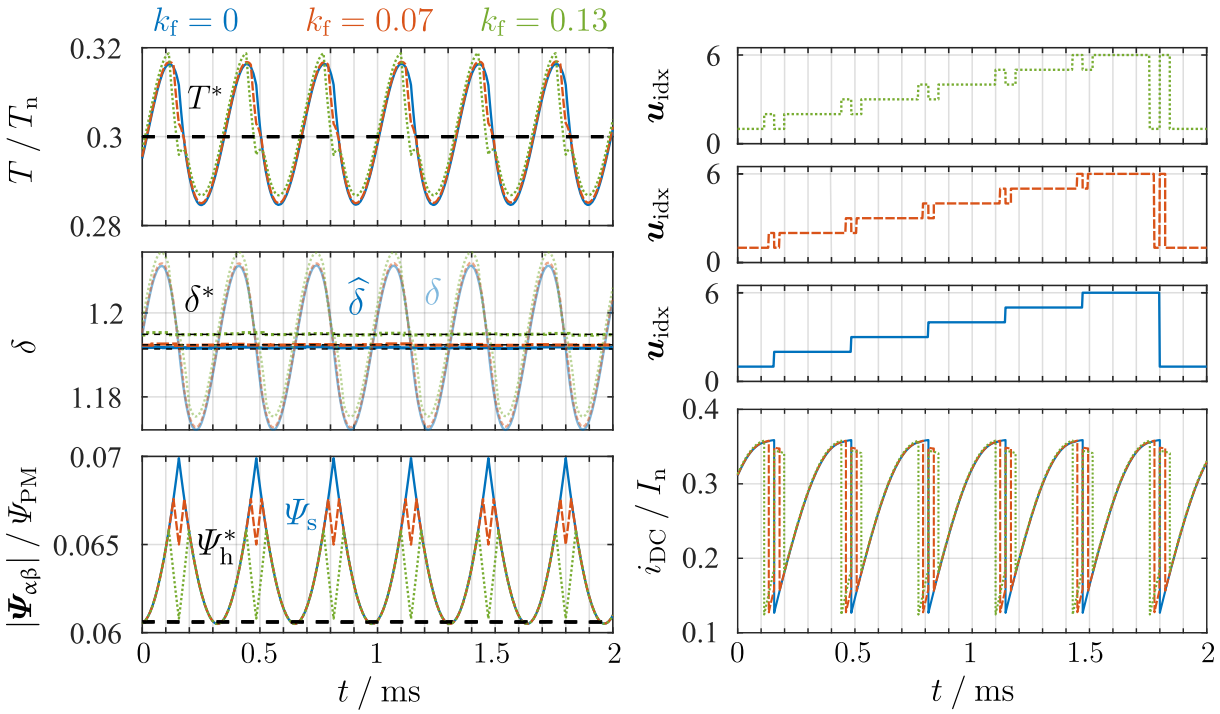


Fig. 5.12: Simulation steady-state operation example of MPDSC with multiple folding ratios at $n = 1.5n_n$, $T^* = 0.3T_n$. From top to bottom, left column: torque, load angle, flux amplitude. From top to bottom, right column: switching state index for various k_f values, and DC current

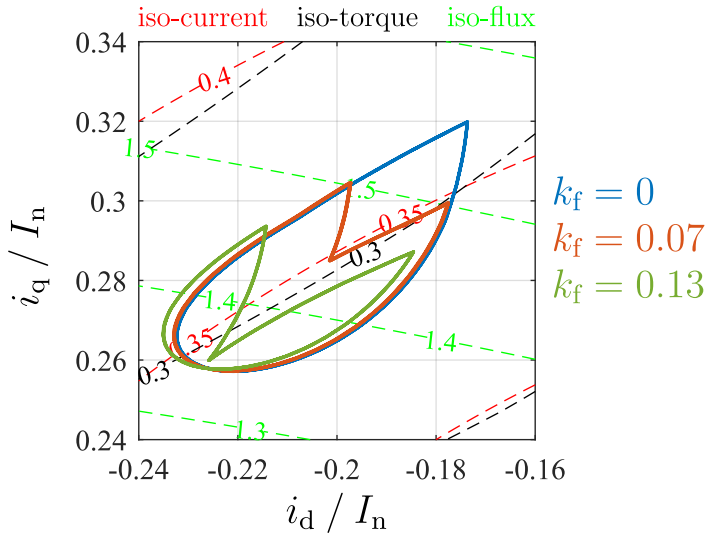


Fig. 5.13: Simulation steady-state operation example of dq-current trajectory of MPDSC with multiple folding ratios at $n = 1.5n_n$ and $T^* = 0.3T_n$

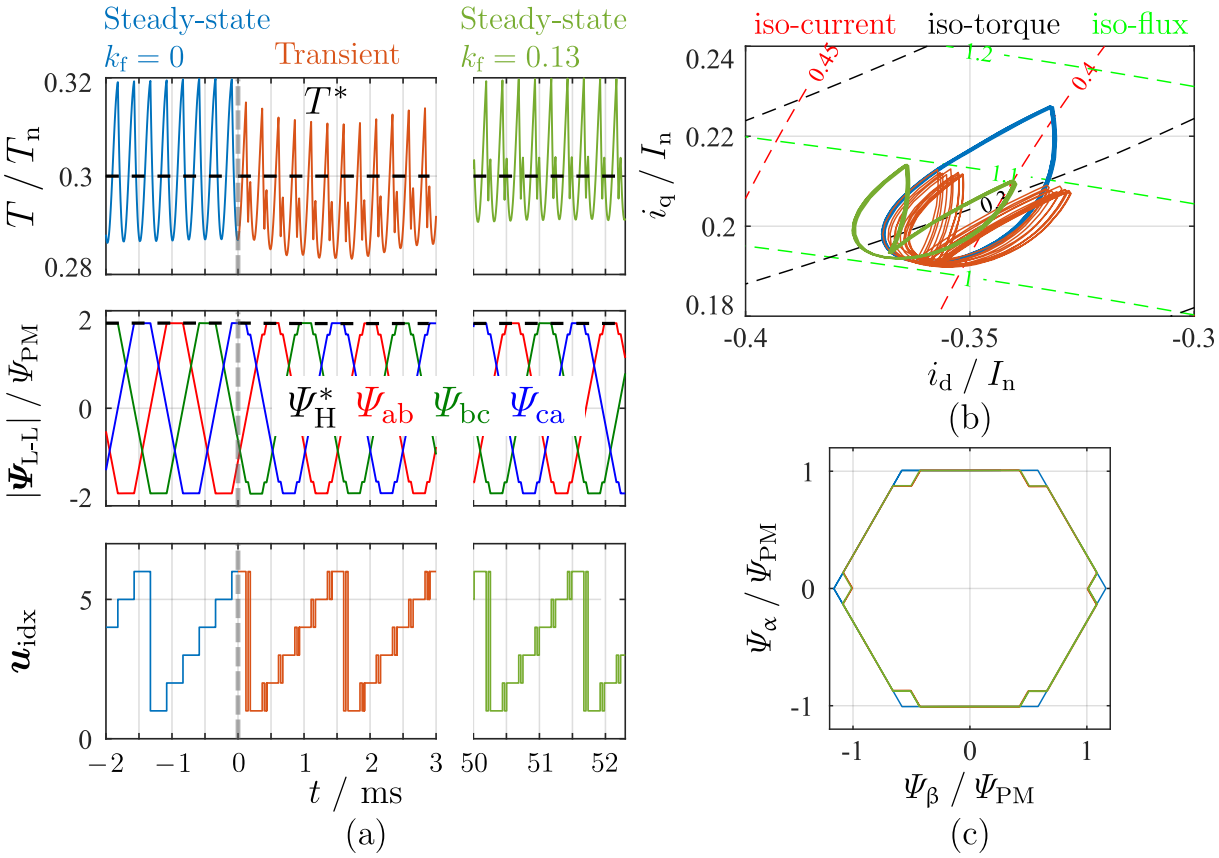


Fig. 5.14: Simulation example of transition in MPDSC between six-step and three-fold modulation at $n = 2n_n$ and $T^* = 0.3T_n$. From top to bottom in (a): torque, line-to-line flux amplitude, and switching state index; (b) dq-current path; and (c) αβ-flux trajectory

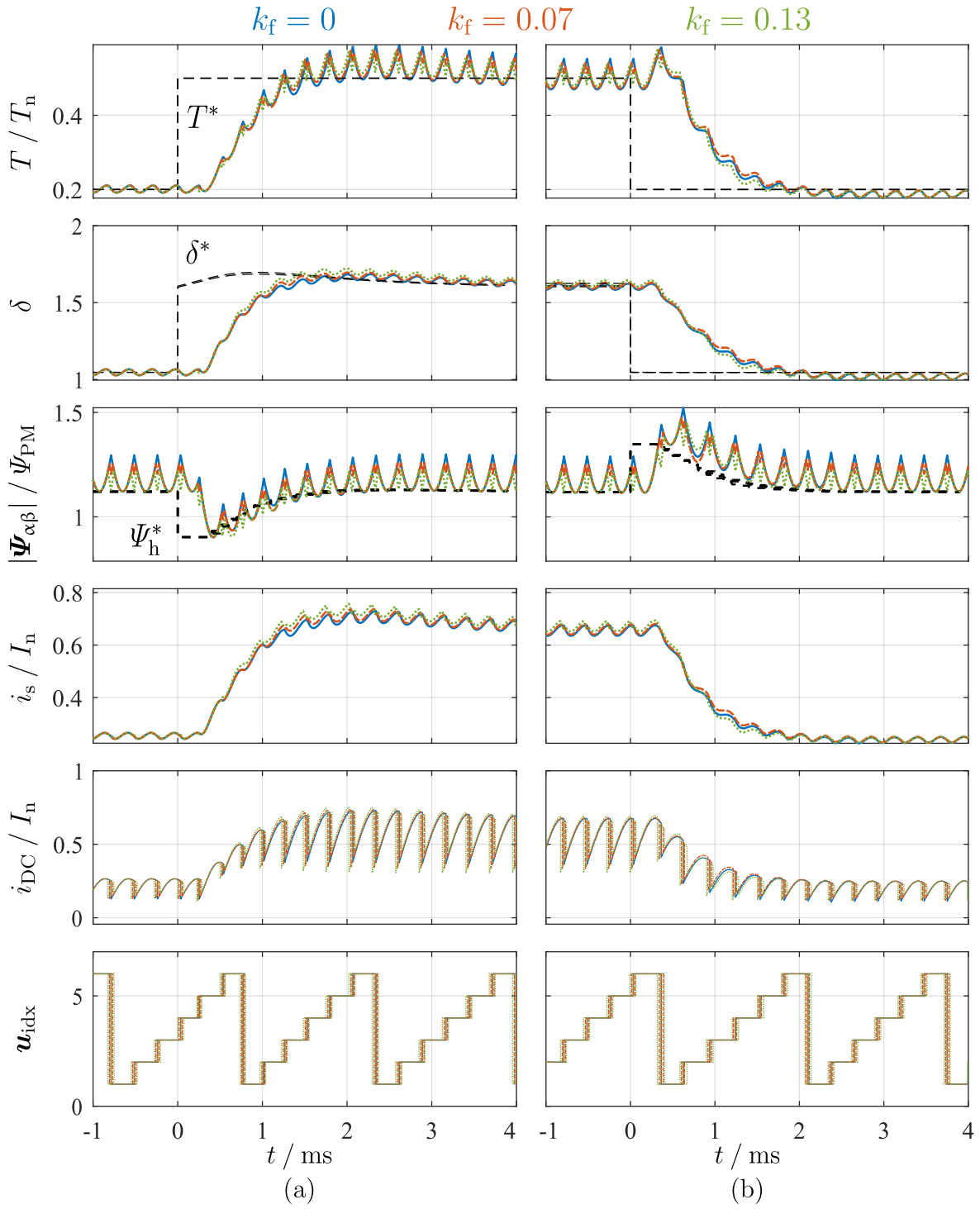


Fig. 5.15: Simulation torque transient example with MPDSC in the motoring region for up (a) and down (b) torque reference step with multiple folding ratios at $n = 1.8 n_\mathrm{n}$. From top to bottom: torque, load angle, line-to-line flux amplitude, current amplitude, DC current, and switching state index

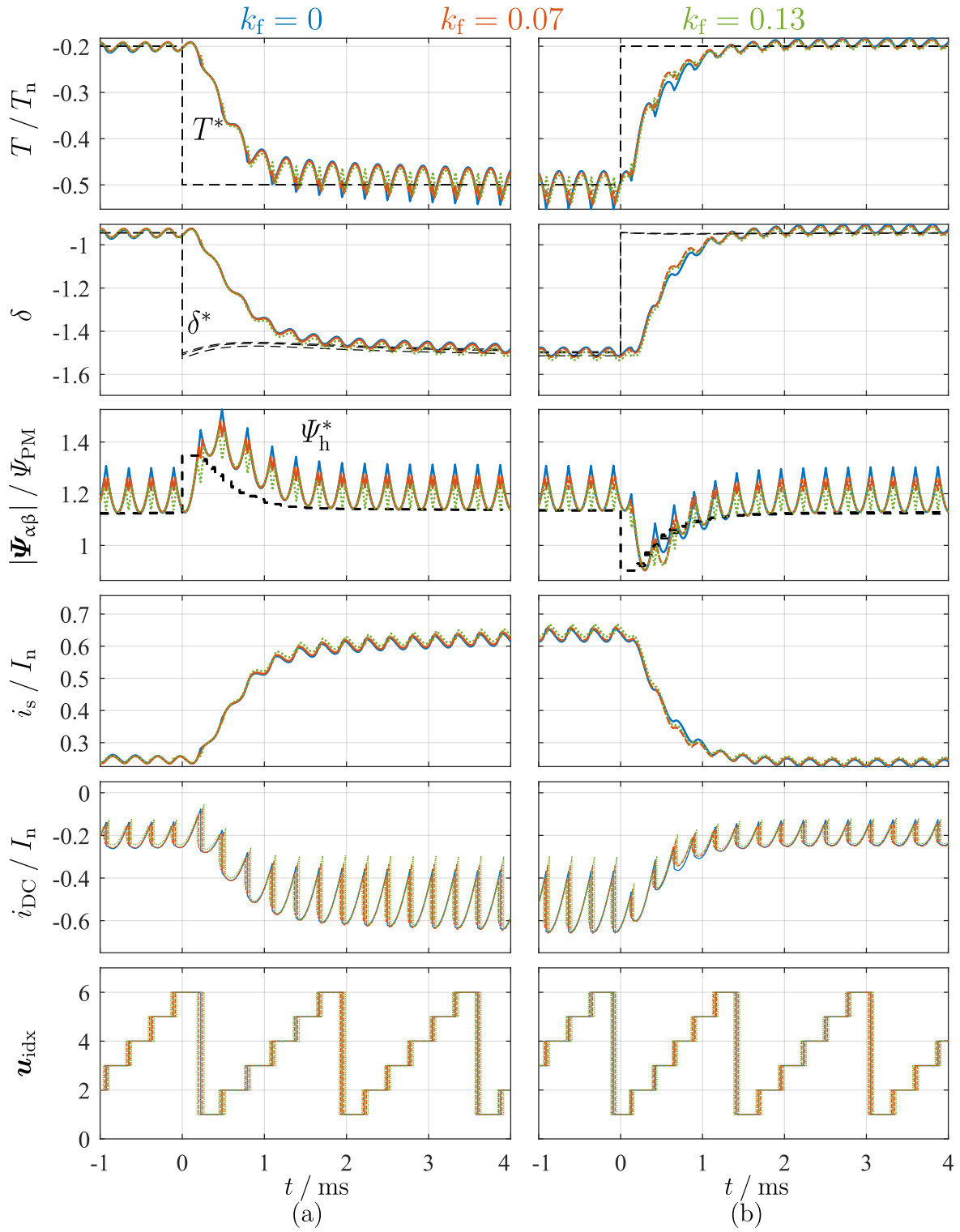


Fig. 5.16: Simulation torque transient example with MPDSC in the generating region for down (a) and up (b) torque reference step with multiple folding ratios at $n = 1.8n_\mathrm{n}$. From top to bottom: torque, load angle, line-to-line flux amplitude, current amplitude, DC current, and switching state index

5.4 Experimental Results

An example of the steady-state operation of MPDSC with three-fold modulation is shown in Fig. 5.17, with the corresponding dq-current path in Fig. 5.18. The three-fold modulation scheme is apparent in both the switching command and the line-to-line voltage measurements. The system behaves as expected, and the dq-current operating point exhibits the same shape as observed in simulation. The transition from six-step to three-fold modulation is presented in Fig. 5.19, which takes place smoothly with no significant stress on the operation or additional noise.

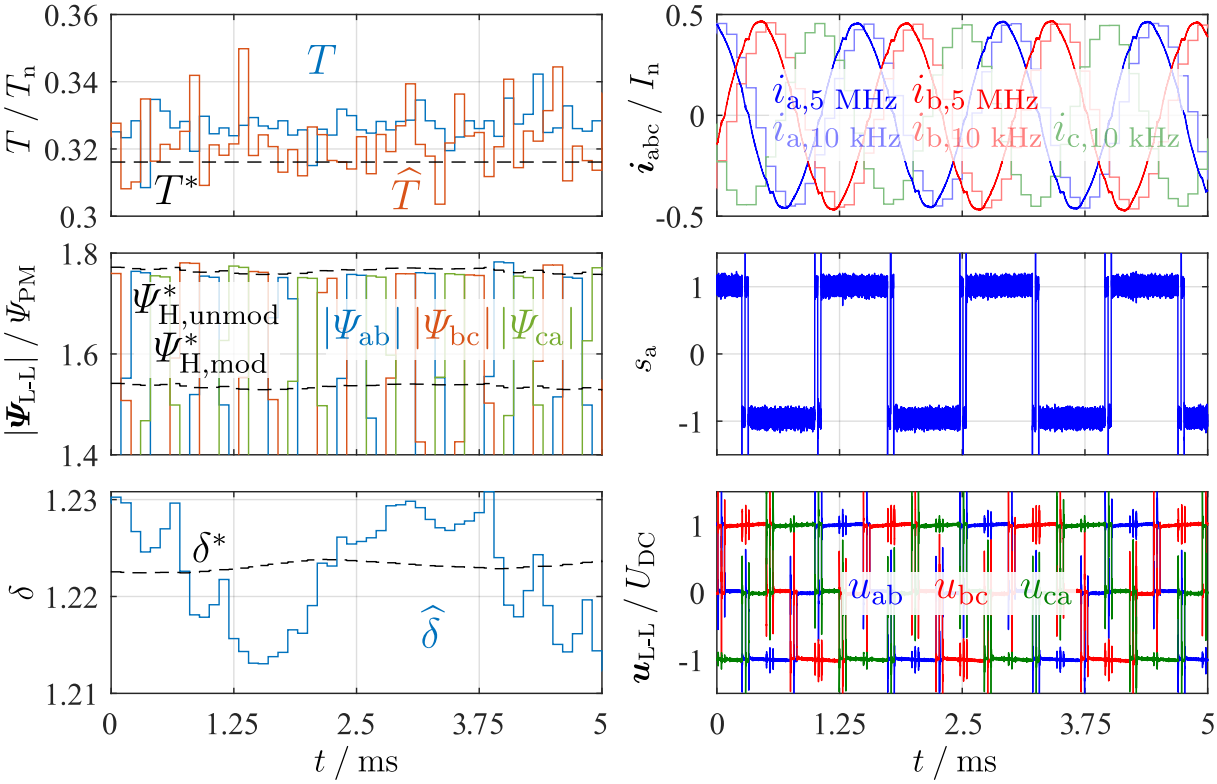


Fig. 5.17: Steady-state three-fold operation with $k_f = 0.13$ at $2n_n$ in the motoring region. From top to bottom, left column: torque, line-to-line flux, and load angle. From top to bottom, right column: phase currents, a-switching pulses, and line-to line voltages. The line-to-line voltages, switching pulses, and phase currents are measured at 5 MHz.

An example of the torque transient response is given in Fig. 5.20, comparing that of six-step with three-fold modulation for the plots on the left. The torque dip in both modulation methods around 7 ms is due to the DC-bus voltage oscillation immediately after the torque transient, the start of which can also be appreciated by observing the line-to-line voltage plot. The apparent ripple in the line-to-line flux amplitude is due to the intended 18-corner trajectory. No significant change in dynamic response is observed.

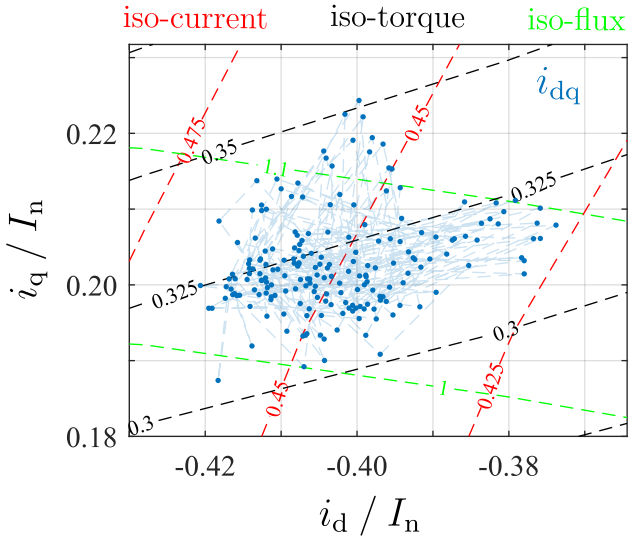


Fig. 5.18: Steady-state three-fold operation with $k_f = 0.13$ at $2n_n$ in the motoring region. The same operating point under six-step operation can be observed in Fig. 3.33.

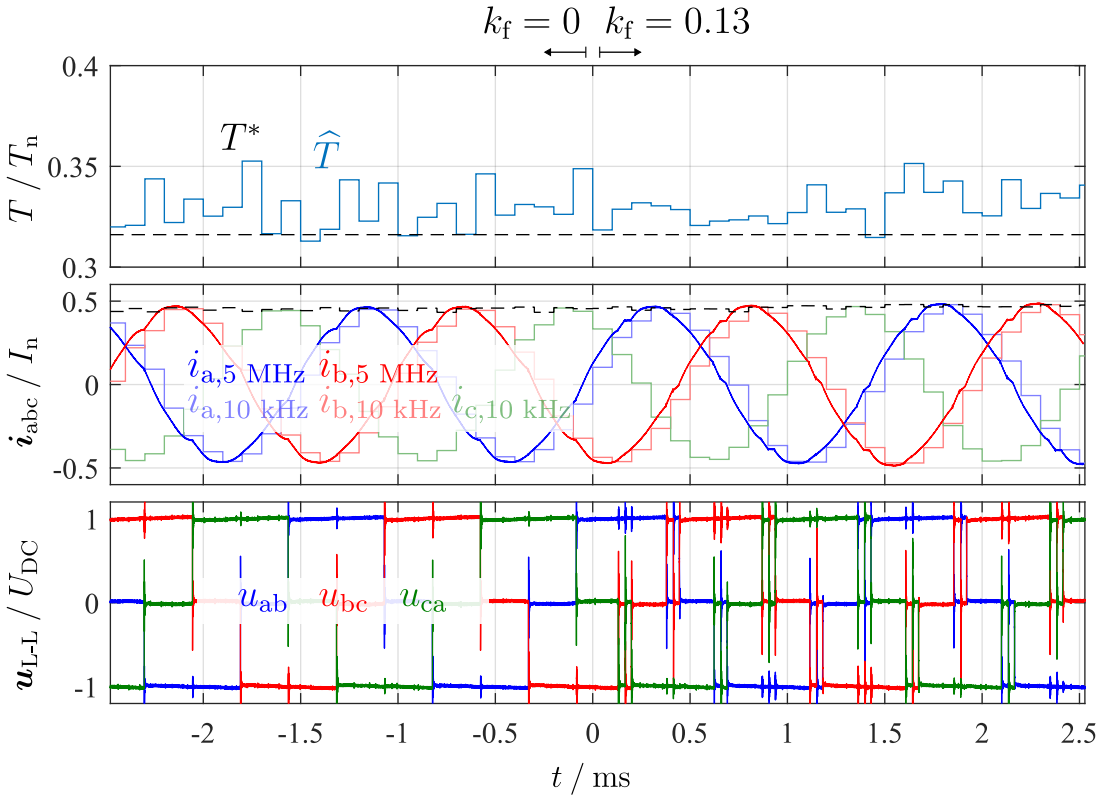


Fig. 5.19: Transition example from six-step to three-fold operation with $k_f = 0.13$ at $2n_n$ in the motoring region. From top to bottom: torque, phase currents, and line-to-line voltages. The line-to-line voltages and phase currents are measured at 5 MHz.

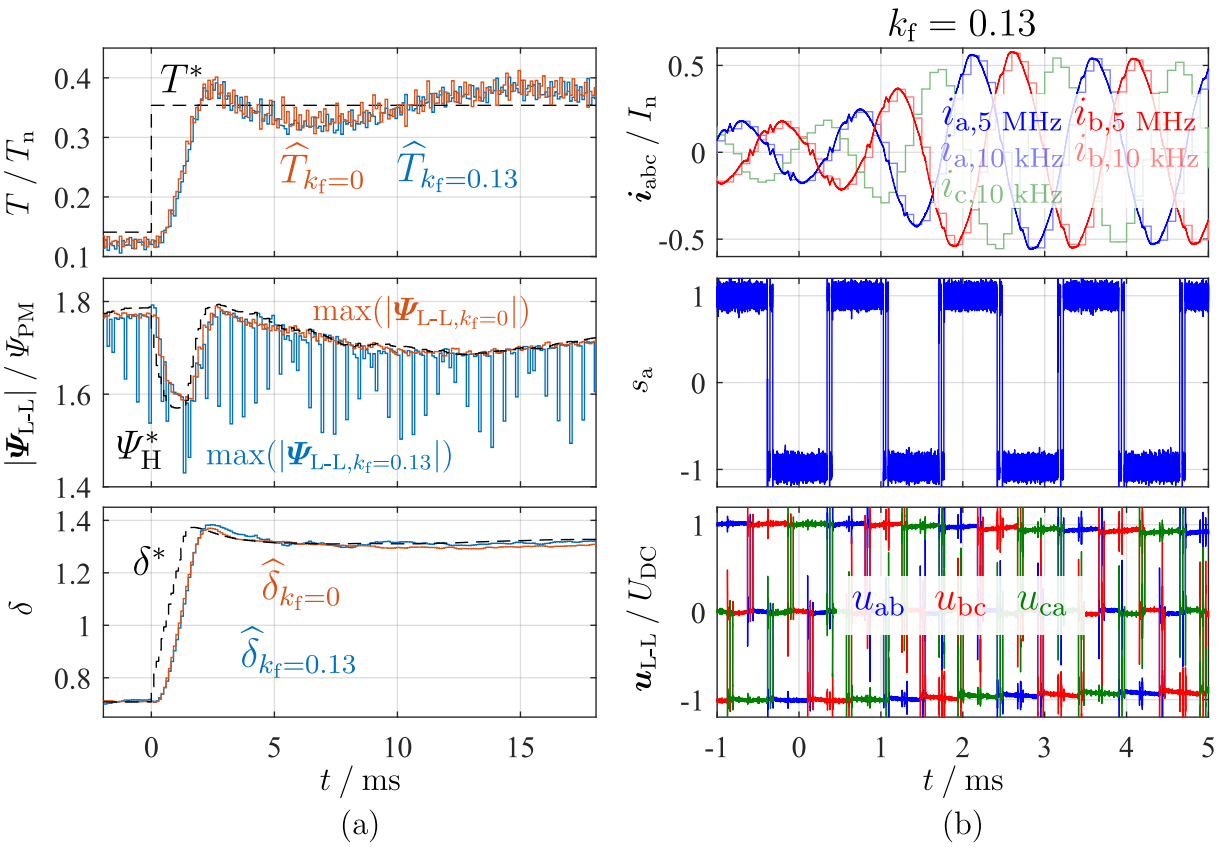


Fig. 5.20: Torque transient example with six-step and three fold operation with $k_\mathrm{f} = 0.13$ at $2n_\mathrm{n}$ in the motoring region. From top to bottom (a): torque, line-to-line flux, and load angle. From top to bottom (b) only for the three fold operation and measured at 5 MHz: phase currents, a-switching pulses, and line-to line voltages

5.5 Summary

This chapter extends MPDSC to accommodate three-fold switching patterns, showing that the framework can adapt to alternative flux sequences beyond six-step operation. The updated control structure compensates load-angle ripple, accounts for the reduced fundamental stator-flux component in operating-point selection, and generates the appropriate switching commands. Three-fold modulation offers flexibility by shaping the harmonic content in AC and DC variables, and reducing current or torque ripple depending on machine characteristics, operating point, and the chosen folding ratio. The implementation was validated through simulation and experimental tests. These results highlight the potential to generalize MPDSC to a broader family of flux patterns, allowing future implementations to optimize modulation for efficiency, torque, or harmonic objectives.

6 Robustness Analysis

Deviations between the models used to design control strategies and their real-world counterparts are inevitable. These discrepancies can arise from simplifying assumptions that neglect certain system behaviors, inaccurate model parametrization, or inherent limitations in the ability of the model to capture reality. Furthermore, controlled systems are subject to environmental disturbances, and the measurement instruments employed can introduce additional noise and inaccuracies. Consequently, a fundamental requirement for control strategies is their capacity to maintain reliable and robust performance under nonideal conditions. This consideration is particularly critical in transportation applications, where safety, efficiency, and passenger comfort must be ensured despite uncertain operating conditions and unpredictable external influences.

In much of the literature, studies on overmodulation and six-step operation are carried out under simplified conditions, typically assuming highly linear machines with large inductances (cf. Ch. 1). Furthermore, the robustness of ancillary systems for harmonic injection and reference adjustment under reduced voltage margin and uncertain parameter conditions is seldom addressed. In this work, the model was designed to capture the most significant factors affecting system performance: the nonlinear magnetic behavior of the machine, such as magnetic (cross-)saturation and low inductance values; as well as the nonideal behavior of the inverter in terms of reference pulse generation, delay, and interlock dead-time. The performance of the proposed control strategy and its enhancements has been validated through simulation across the entire operating range of the drive, under conditions where the model assumed for controller design accurately represents the system. When applied to the experimental setup, the proposed method generally achieved satisfactory performance in comparison with the industry-standard FOC. However, deviations were evident across several operating points. Most notably, steady-state torque exhibited variations that appeared to depend on the operating conditions, particularly the rotor temperature.

These observations motivated the investigation presented in this chapter. Rather than focusing on analytical evaluation of disturbance rejection and stability, which would require extensive simplifying assumptions and could yield unreliable results, the robustness of the system is assessed empirically through both simulation and experimental validation. In simulation, the model is modified to evaluate the effects of individual parameter

estimation errors (PEE) and sensor noise. These effects are further examined through a series of Monte Carlo simulations in which all relevant uncertainties are considered simultaneously. Additionally, the response to transients from exogenous sources is assessed in simulation. The experimental implementation inherently involves uncertain parameters and discrepancies between the design model and the actual controlled system. As such, the experimental results presented throughout this work serve as a practical demonstration of both the strengths and the limitations of the proposed strategy. To further evaluate robustness, moderate disturbances are intentionally introduced to the control strategy, measurements, and assumed model dynamics.

6.1 Simulation Evaluation

For clarity and conciseness, the following analysis considers a single operating point within the high-speed motoring region, as shown in Fig. 6.1. Variations in model parameters, as well as the injection of noise and disturbances, are applied and analyzed based on this reference profile. The investigation focuses on the steady-state performance of MPDSC and FOC, which are highlighted in yellow and illustrated in the second and third columns of Fig. 6.1, respectively.

The steady-state performance is evaluated with the following normalized metrics

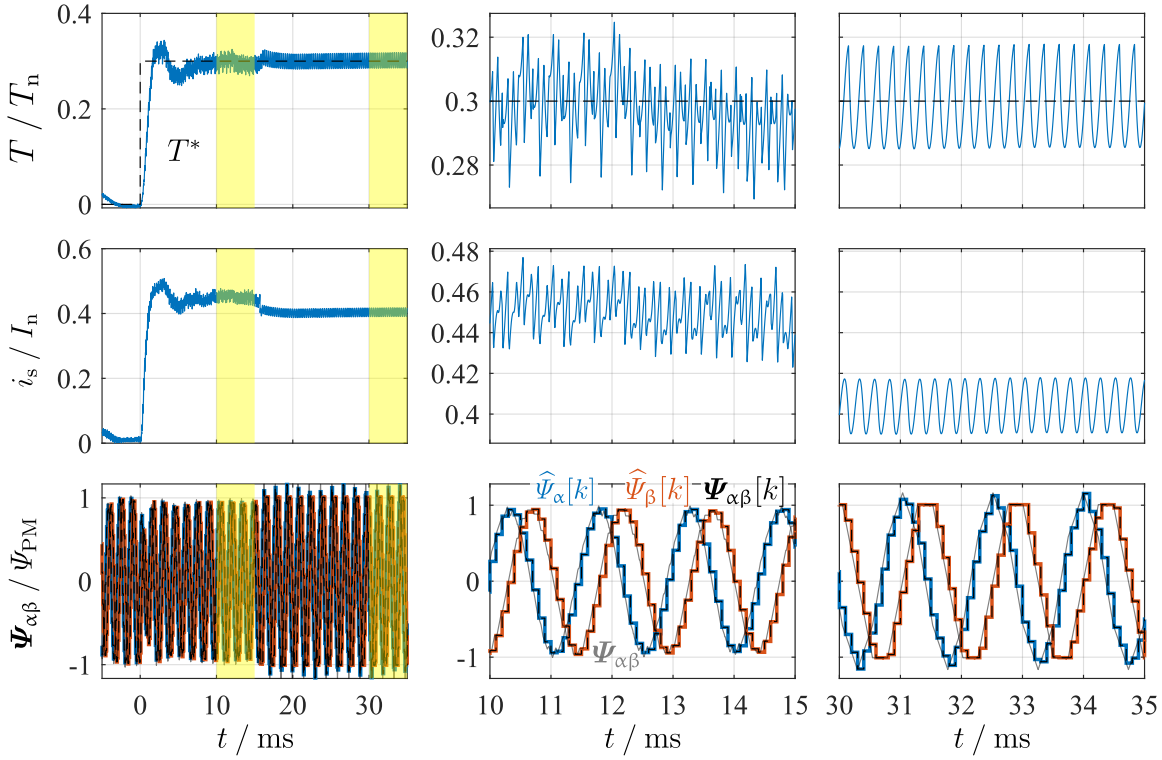
$$\mu_T = \mu\left(T\right)/T_\mathrm{n}, \tag{6.1}$$
$$\mu_I = \mu\left(i_\mathrm{s}\right)/I_\mathrm{n}, \tag{6.2}$$
$$\sigma_T = \mathrm{RMS}\left(T-\mu(T)\right)/T_\mathrm{n}, \tag{6.3}$$
$$\sigma_I = \mathrm{RMS}\left(i_\mathrm{s}-\mu(i_\mathrm{s})\right)/I_\mathrm{n}, \tag{6.4}$$
$$\mathrm{MAE}_T = \mu\left(|T-T^*|\right)/T_\mathrm{n}, \tag{6.5}$$
$$\mathrm{MAEE}_\delta = \mu\left(\left|\widehat{\delta}[k]-\delta[k]\right|\right), \tag{6.6}$$
$$\mathrm{MAEE}_\Psi = \mu\left(\left|\max\left(\left|\widehat{\boldsymbol{\Psi}}_\mathrm{L\text{-}L}[k]\right|\right)-\max\left(|\boldsymbol{\Psi}_\mathrm{L\text{-}L}[k]|\right)\right|\right)/\Psi_\mathrm{PM}, \tag{6.7}$$

to account for the mean μ operating point for torque and current amplitude, the standard deviation σ (i.e., the root-mean-square (RMS) value after removing the mean component) for those same variables, the mean-absolute error (MAE) for torque reference tracking, and the mean-absolute estimation error (MAEE) for the load angle and the maximum absolute line-to-line flux value (i.e., the controlled variables in MPDSC).

6.1.1 Parameter Estimation Errors

6.1.1.1 Machine Parameters

Deviation in the machine PM flux, inductances and resistances are considered as a bias Δ in the parameters, defined as



(a) Full simulation (b) FOC steady state (c) MPDSC steady state

Fig. 6.1: Baseline operating point for simulation-based robustness and disturbance rejection analysis. From top to bottom: torque, current amplitude, and flux linkage. Operating point $n = 2n_\mathrm{n}$, $T^* = 0.3T_\mathrm{n}$. Yellow boxes in (a) are detailed in (b) and (c), indicating the steady-state intervals for FOC and MPDSC.

$$\Psi'_\mathrm{PM} = \Psi_\mathrm{PM,0} + \Delta_{\Psi_\mathrm{PM}}\,, \quad \Delta_{\Psi_\mathrm{PM}} = \alpha_{\Psi_\mathrm{PM}}\Psi_\mathrm{PM,0}, \tag{6.8a}$$

$$L'_\mathrm{d} = L_\mathrm{d,0} + \Delta_{L_\mathrm{d}}, \quad \Delta_{L_\mathrm{d}} = \alpha_{L_\mathrm{d}}L_\mathrm{d,0}, \tag{6.8b}$$

$$L'_\mathrm{q} = L_\mathrm{q,0} + \Delta_{L_\mathrm{q}}, \quad \Delta_{L_\mathrm{q}} = \alpha_{L_\mathrm{q}}L_\mathrm{q,0}, \tag{6.8c}$$

$$R'_\mathrm{s} = R_\mathrm{s,0} + \Delta_{R_\mathrm{s}}, \quad \Delta_{R_\mathrm{s}} = \alpha_{R_\mathrm{s}}R_\mathrm{s,0}, \tag{6.8d}$$

with the subscript 0 indicating the original lumped parameters of the machine and the superscript $'$ indicating the modified parameters. The deviation factor α relates the bias with the lump parameters. The derivation of the machine model considering simultaneously nonlinear current-to-flux mapping and parameter deviations relative to the lump parameters as described above is detailed in App. F.

The effects of a change in the considered machine parameters in a range $\alpha \in [-0.25,\ 0.25]$ is shown in Fig. 6.2 with opaque thick lines. The effect of changing the stator resistance is negligible for both control strategies. Significant changes occur for torque tracking performance (MAE_T) of MPDSC for changes in d-inductance and PM flux. This is consistent with the observation during experimental evaluation, where the torque tracking

performance varied according to the temperature of the rotor[1]. This torque deviation is accompanied by a change in torque ripple proportional to the average torque change. As the flux estimation seems to be moderately robust to parameter estimation errors, thanks to the Gopinath-style implementation of the flux observer, the deviation in torque tracking was attributed to inaccuracies in the operating point selection algorithm. To a lesser extent, the torque accuracy is also degraded for FOC under d-inductance and PM flux deviations, and to an even larger extent than for MPDSC in the case of q-inductance deviations. The average current operating point varies very little in FOC, while MPDSC is affected due to the changing $\boldsymbol{i}_{\mathrm{dq}}(\boldsymbol{\Psi}_{\mathrm{dq}})$ relationship. The current ripple remains higher in FOC due to the effect of the switching ripple in this operating point (cf. Fig. 6.1).

A torque reference adaptation based on torque estimation is implemented to assess the feasibility of improving the robustness through an enhanced operating point selection strategy . This approach is intended solely as a proof of concept, and further investigation and tuning would be required to generalize its conclusions. The torque estimation is performed based on the flux estimation as

$$\widehat{T}[k] = \frac{3p}{2}\left(\widehat{\Psi}_{\alpha}[k] i_{\beta}[k] - \widehat{\Psi}_{\beta}[k] i_{\alpha}[k]\right). \tag{6.9}$$

The torque reference is adjusted through a closed-loop scheme using an I-controller that compares the estimated torque with the original reference, as

$$\Delta T^*[k] = \Delta T^*[k-1] + K_{\mathrm{I},T} T_{\mathrm{s}} \left(T^*_{\mathrm{original}}[k-1] - \widehat{T}[k-1]\right), \tag{6.10a}$$

$$T^*[k] = T^*_{\mathrm{original}}[k] + \Delta T^*[k]. \tag{6.10b}$$

The integral gain $K_{\mathrm{I},T}$ is tuned manually as $K_{\mathrm{I},T} = 200\,\mathrm{s}^{-1}$ to provide a slow adaptation. The integrator is initialized to zero when the torque reference or the control strategy change.

Fig. 6.2 includes the performance indicators for steady-state operation with the torque reference adaptation with thin semi-transparent lines. This simple enhancement enables the near total removal of the torque tracking error for both control strategies. It should be noted, however, that this performance has only been demonstrated in simulation, and effects not captured by the implemented model or the parameter deviations considered could introduce estimation (and thus reference correction) errors. The effect of the reference adaptation on the other performance metrics is negligible, with the exception of torque ripple in MPDSC. This change presumably stems from the different nature of the torque ripple during six-step operation for different areas of the machine, and the corresponding relative influence of load angle and flux amplitude ripple upon it.

6.1.1.2 Inverter Parameters

The inverter model (cf. App. A.3) considers both signal propagation delay $T_{\mathrm{del}} = 2.56\,\mu\mathrm{s}$ and interlock dead-time $T_{\mathrm{dt}} = 3\,\mu\mathrm{s}$, based on testbench measurements. These values are

[1]Rotor temperature was not measured, this statement is based on qualitative observation of the operating conditions after maintaining a certain operating point for an extended amount of time.

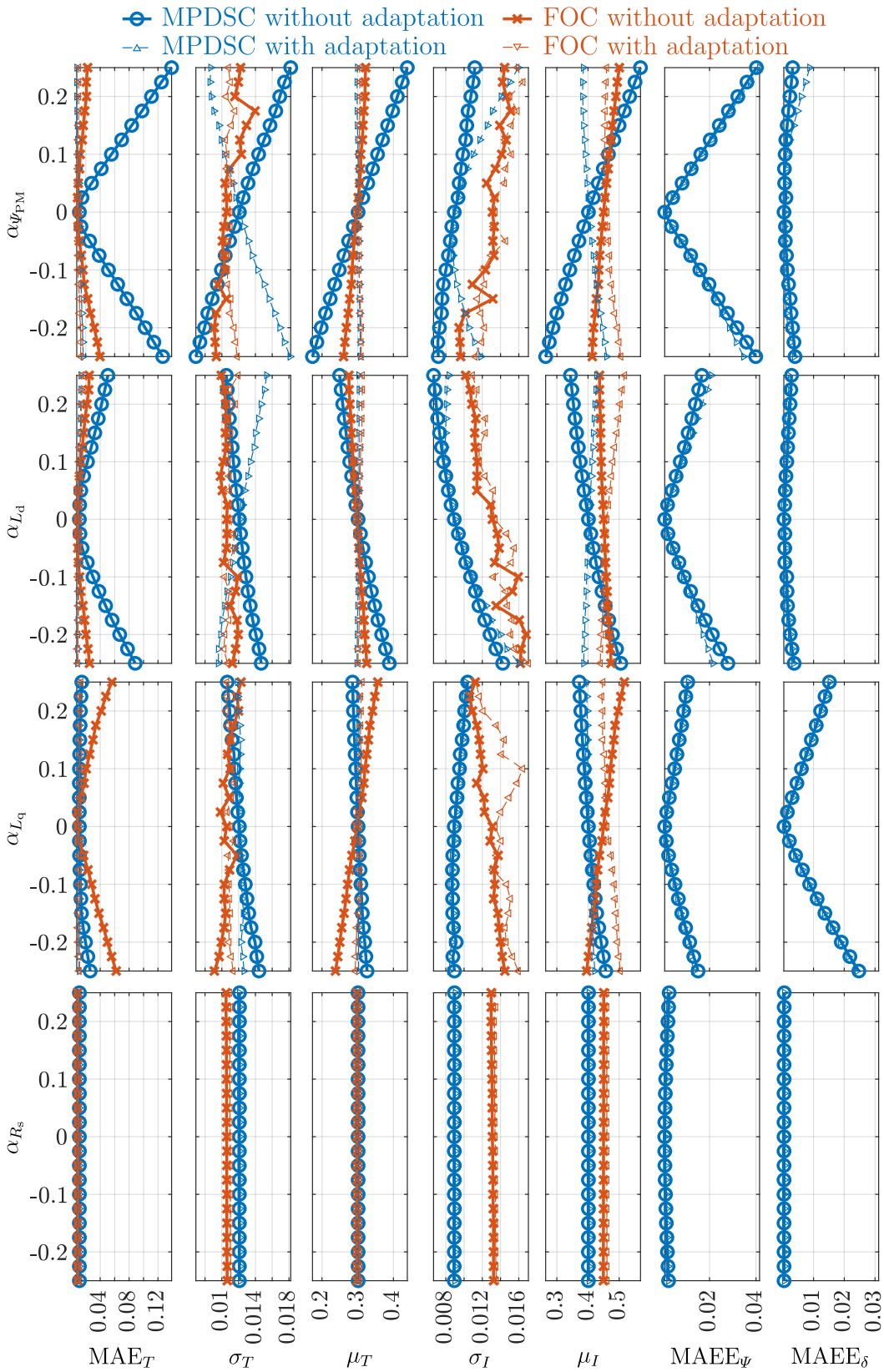


Fig. 6.2: Steady-state performance with machine parameter estimation errors (from top to bottom) in PM flux, d-inductance, q-inductance, and resistance, in terms of the metrics (from left to right) (6.1) to (6.7), with and without toque reference adaptation

varied as $T'_{\mathrm{del}}, T'_{\mathrm{dt}} \in [0, 6]$ µs, and their effect is given in Fig. 6.3. The overall effect upon the performance of both control strategies is not very significant, nor is the effect of torque reference adaptation based on the torque estimation. It should be noted that these results correspond to a change in the model parameters, while the controller remains unaffected, i.e., for $T'_{\mathrm{del}} < T_{\mathrm{del}}$ and $T'_{\mathrm{dt}} < T_{\mathrm{dt}}$ these effects are being overcompensated by the control strategy[2].

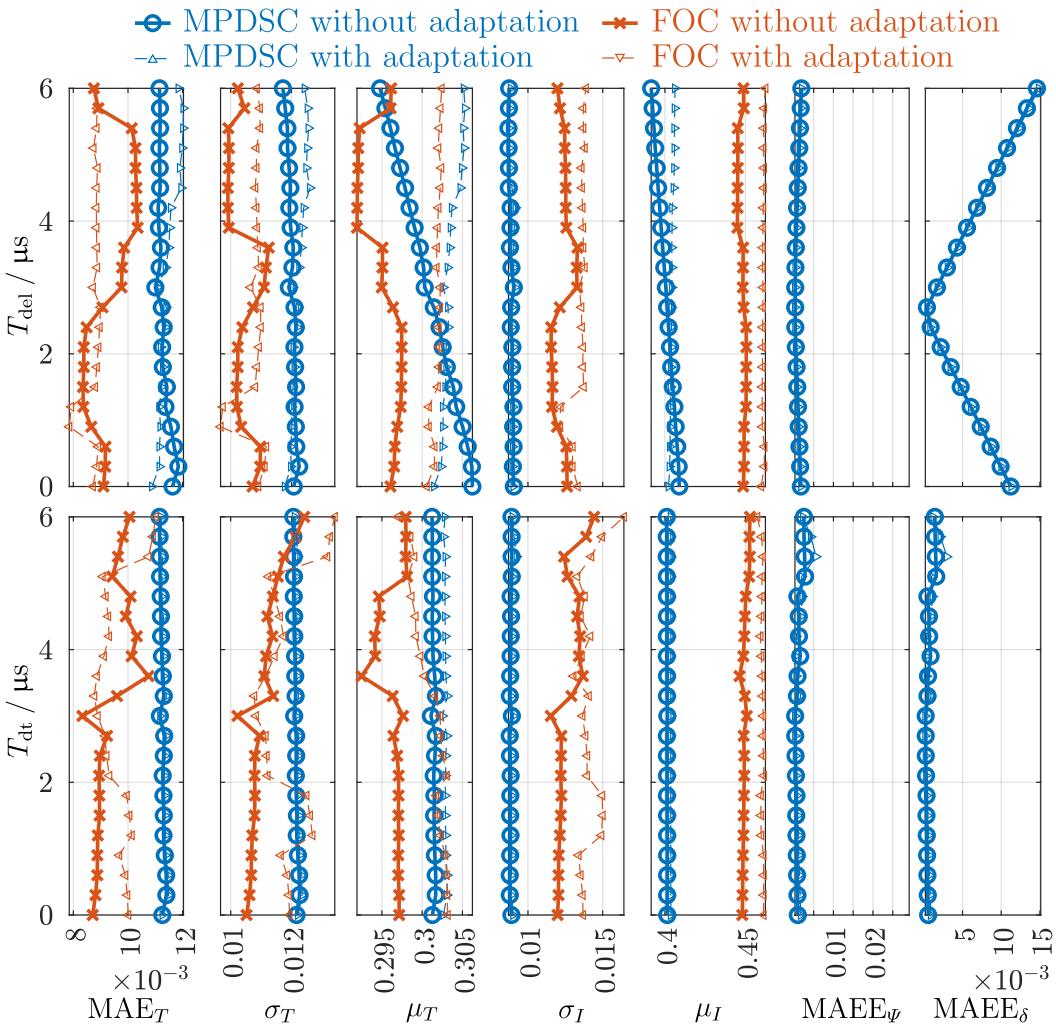


Fig. 6.3: Steady-state performance with estimation errors (from top to bottom) in inverter delay time and interlock deadtime, in terms of the metrics (from left to right) (6.1) to (6.7), with and without toque reference adaptation

[2]A clear difference could be observed in results between ideal and nonideal inverter modeling without compensation of these effects, especially for voltage synthesis in FOC. The assumed and/or actual existence of inverter nonlinearities distorts the voltage waveforms provided to the machine model. Ideal inverter model results are, however, omitted from this investigation as they provide a baseline too unrealistic for relevant comparison.

6.1.2 Sensor Noise

The control method relies upon the information from multiple sensors, namely angular position, DC bus voltage, and current sensors, which are subject to noise[3]. For the current measurement, two scenarios are considered: noise in just one of the sensors or in all three of them (independently seeded). For the DC-bus voltage and current measurements, Gaussian noise is injected so that the reading of each sensor y' is given to the control task as

$$y' = y + \max\left(|y|, y_{\text{thr}}\right) \cdot k_y \cdot \epsilon \quad , \epsilon \sim \mathcal{N}(0,1), \tag{6.11}$$

where y is the true value, y_{thr} a minimum threshold to ensure noise injection when the measurement is near zero (e.g., for the current measurements this was set at $i_{\text{thr}} = 0.025 I_{\text{n}}$), and $k_y \in [0, 0.25]$ varies the amplitude of the noise injected in different simulations, i.e., considering up to 25 % relative error to be the standard deviation in the measured quantities. For the resolver angle measurement, it is done in terms of additive noise as

$$\theta'_{\text{r}} = \theta_{\text{r}} + \frac{\pi}{3} k_{\theta_{\text{r}}} \epsilon \quad , \epsilon \sim \mathcal{N}(0,1), \tag{6.12}$$

i.e., considering a up to 25 % of the angle span of a sector, or $\pi/12$, to be the standard deviation in angle measurement. The results are given in Fig. 6.4. The noise in DC-bus voltage measurement introduces the largest effect on MPDSC performance, affecting all metrics considered. The effect of noise injections in the other sensors has a generally larger effect on FOC than MPDSC, particularly noticeable with angle measurement noise.

6.1.3 Monte Carlo Simulations

In the previous sections the parameters and sensor noise amplitude have been varied individually for a clear assessment of their effect upon the performance metrics. However, in a real scenario, it is likely that deviations occur simultaneously, albeit to a small extent if the model has been appropriately parameterized. In order to stress the system to a large extent, all parameters and noise amplitudes are varied across 200 simulations simultaneously via Latin hypercube sampling (LHS)[4] within the ranges $\alpha \in [-0.2,\ 0.2]$, $T'_{\text{del}}, T'_{\text{dt}} \in [0, 6]$ µs, and $k_y \in [0, 0.1]$. Fig. 6.5 provides a visualization of the distribution of each of the parameter variations with respect to each other for this set of tests, with each translucent point representing a single simulation and lines depicting the median across 10 equal width windows. The results show that the LHS method achieves a consistent and balanced distribution across the parameter space, with the median remaining close to the midpoint of the range[5].

[3]Sensor noise is commonly modeled as zero-mean Gaussian due to the aggregation of independent physical noise sources and the applicability of the central limit theorem. This assumption is widely used in filtering frameworks, e.g., [46]. In this study, noise is applied multiplicatively, analogous to [47], to represent relative error and improve interpretability of the noise amplitude.

[4]Proposed in [48] and implemented via MATLAB's *lhsdesign* function

[5]The thickness of the diagonal lines is due to the superposition of individual simulation markers.

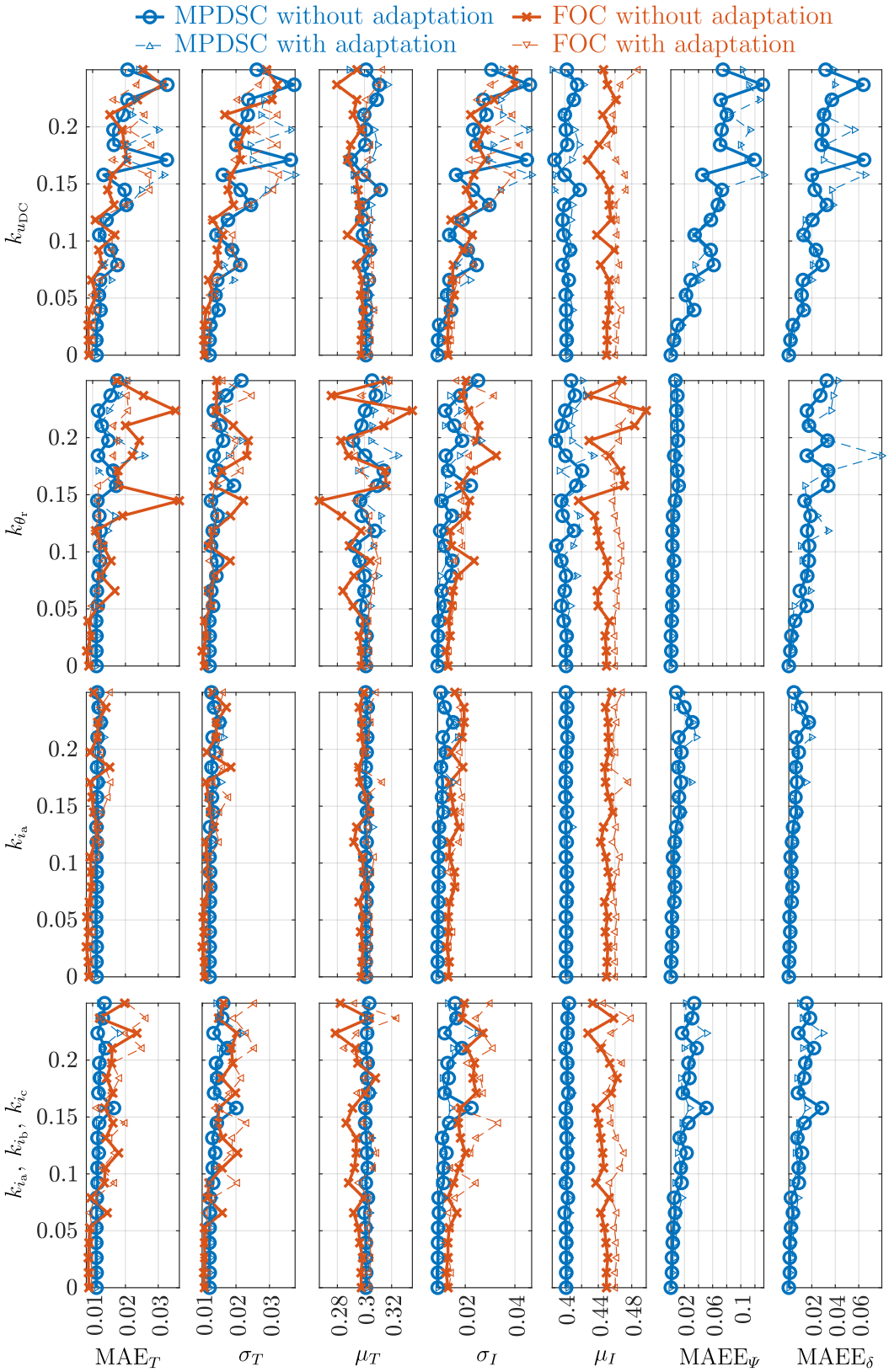


Fig. 6.4: Steady-state performance with noise injection (from top to bottom) in DC voltage, angle, one current, and all current measurements, in terms of the metrics (from left to right) (6.1) to (6.7), with and without toque reference adaptation

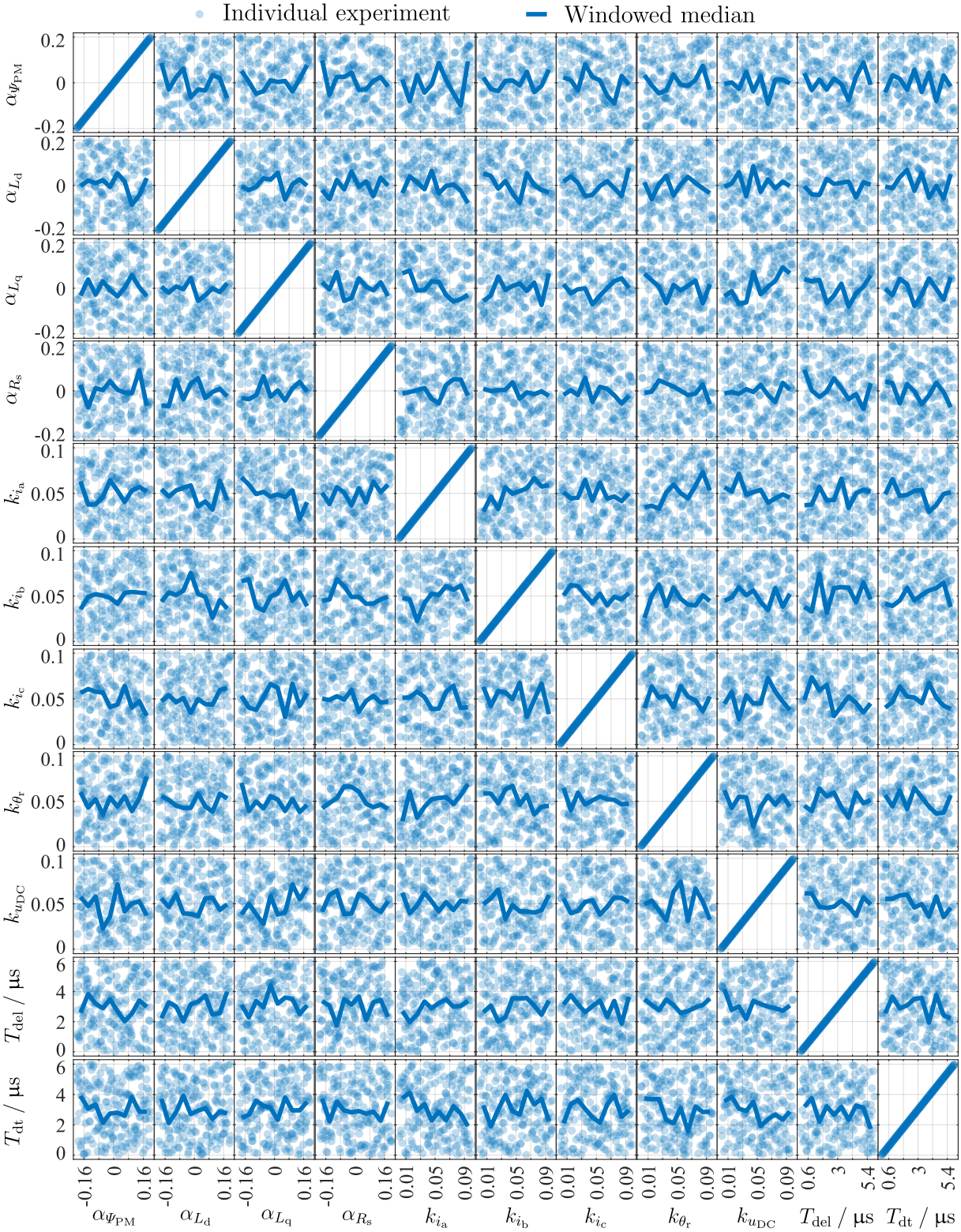


Fig. 6.5: Distribution of varied parameters for Monte Carlo simulations (from top to bottom, and from left to right) for PEE in PM flux, d-inductance, q-inductance, and stator resistance, sensor noise in phase currents, angle, and DC voltage measurement, and estimation errors in inverter delay and interlock deadtime.

The performance indicators for MPDSC and FOC steady-state operation are presented in Fig. 6.6. The indicators exhibiting the strongest correlation with parameter variations are highlighted in green. Variations in PM flux and d-axis inductance have a significant impact on MPDSC operation, whereas q-axis inductance shows a stronger influence on FOC. The effect of DC-bus voltage measurement noise is similar for both control strategies. These observations are consistent with the results discussed in previous sections regarding the individual variation of each disturbance source. Overall, FOC demonstrates lower sensitivity to parameter variations and generally superior performance metrics.

Fig. 6.7 also presents the results obtained after the introduction of the torque reference adaptation based on a torque estimation. This enhancement substantially reduces the impact of parameter variations on torque tracking, as evidenced by the change in y-axis scaling for MAE_T. The influence of PM flux is notably diminished, with most of the correlation effectively eliminated. Qualitatively, the adaptation reduces the standard deviation of the performance metrics more effectively for MPDSC than for FOC. For instance, the average torque and current values in MPDSC exhibited greater dispersion before adaptation, whereas after adaptation the remaining spread is primarily associated with FOC. The influence of DC-bus voltage measurement noise, however, persists following the adaptation.

The evolution of torque and current amplitude with time throughout all the tests was analyzed, with their average and envelope values represented in Fig. 6.8. It is most remarkable that both operating strategies maintained stable operation, with torque values within a neighborhood of the torque reference, under the greatly disturbed conditions of the simulations performed. This representation also highlights that the transition to and from MPDSC could be reliably performed, albeit with unwanted transients due to the deviation between expected and actual drive parameters and uncertain measurements. The torque reference adaptation chosen does not improve the fade-over significantly, as the modification resets when a fade-over is triggered.

6.1.4 Response to Exogenous Transients

6.1.4.1 DC-Bus Voltage

The DC link is influenced by the inverter, the power supply, and any other systems connected to it (e.g., additional drive systems). Consequently, the controller must exhibit robustness to variations in the DC-bus voltage. This aspect is evaluated here by introducing changes from the same operating point analyzed in the previous sections. The response to step changes[6] in DC-bus voltage are illustrated in Fig. 6.9, where both control methods display similar transient behavior and promptly return to steady-state operation.

Fig. 6.10 presents the system responses to sinusoidal disturbances with frequencies of $f_{\mathrm{dis}} = f_{\mathrm{e}}/10$ and $f_{\mathrm{dis}} = 6f_{\mathrm{e}}$, shown on the left and right, respectively. The high-frequency

[6] Although such a step change would be unrealistic in practice due to the presence of the DC link capacitor, it is considered here to impose maximum stress on the system.

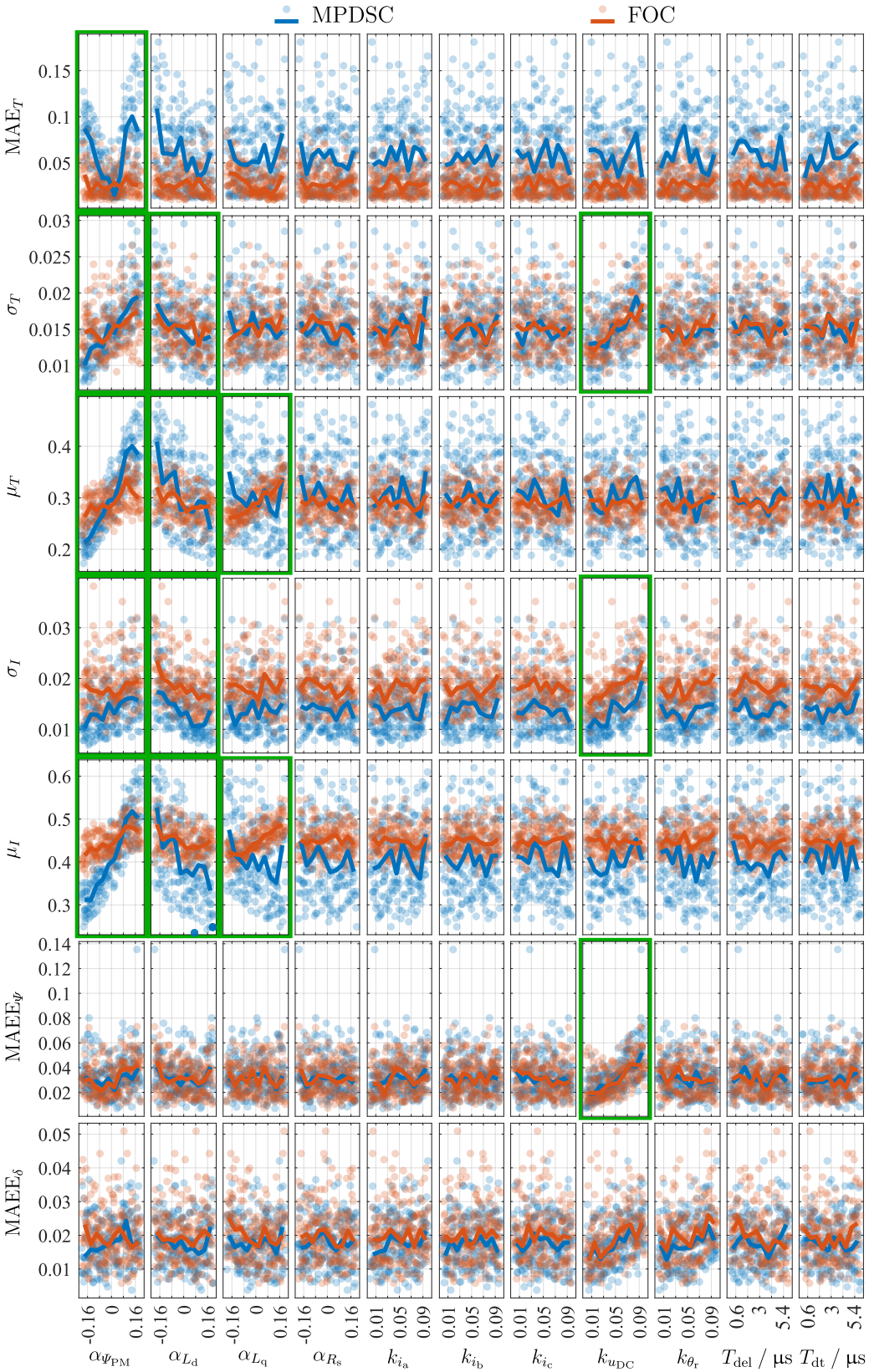


Fig. 6.6: Steady-state performance of MPDSC and FOC for Monte Carlo simulations in terms of the metrics (from top to bottom) (6.1) to (6.7). Green boxes highlight the strongest correlations.

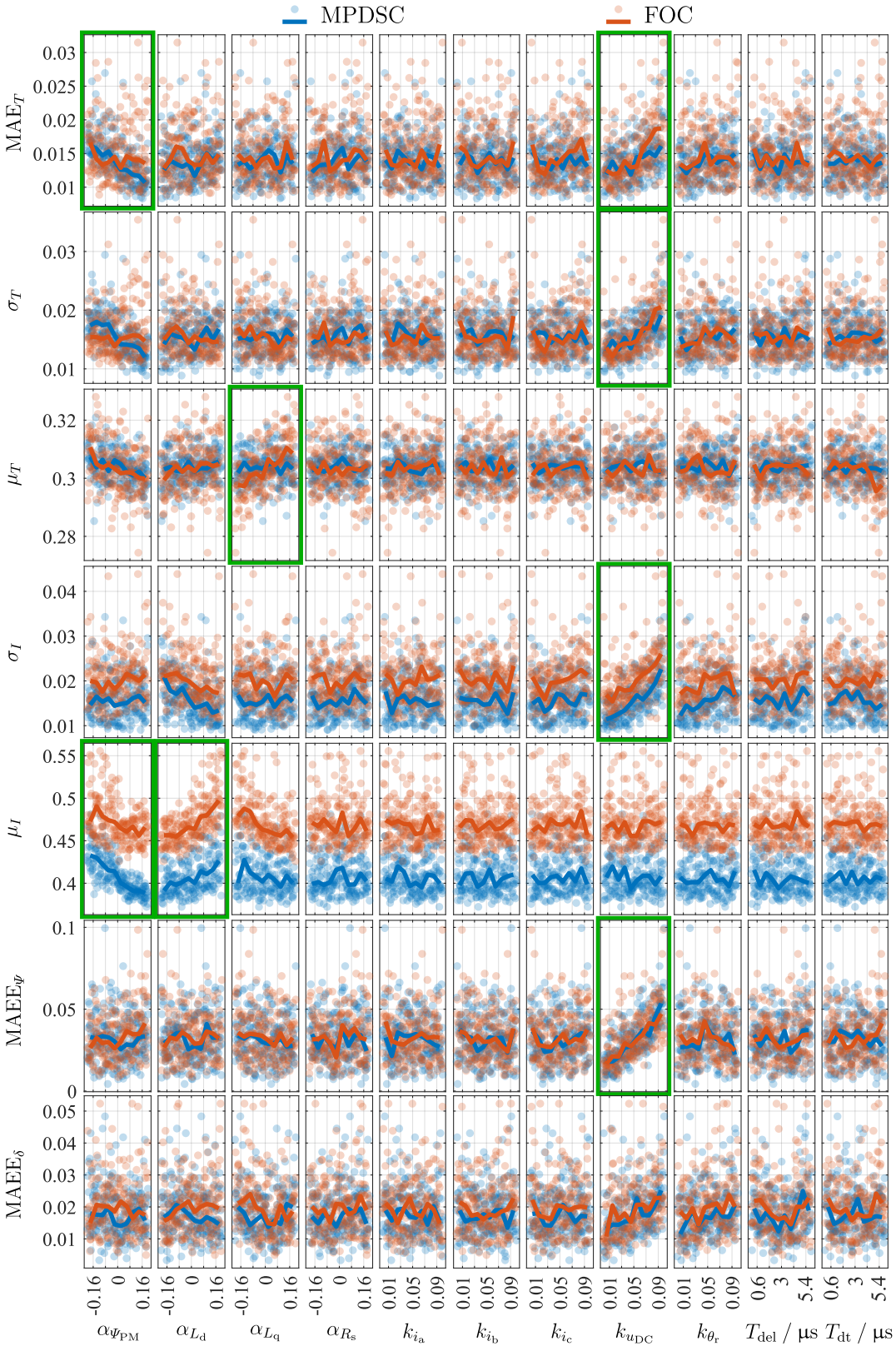
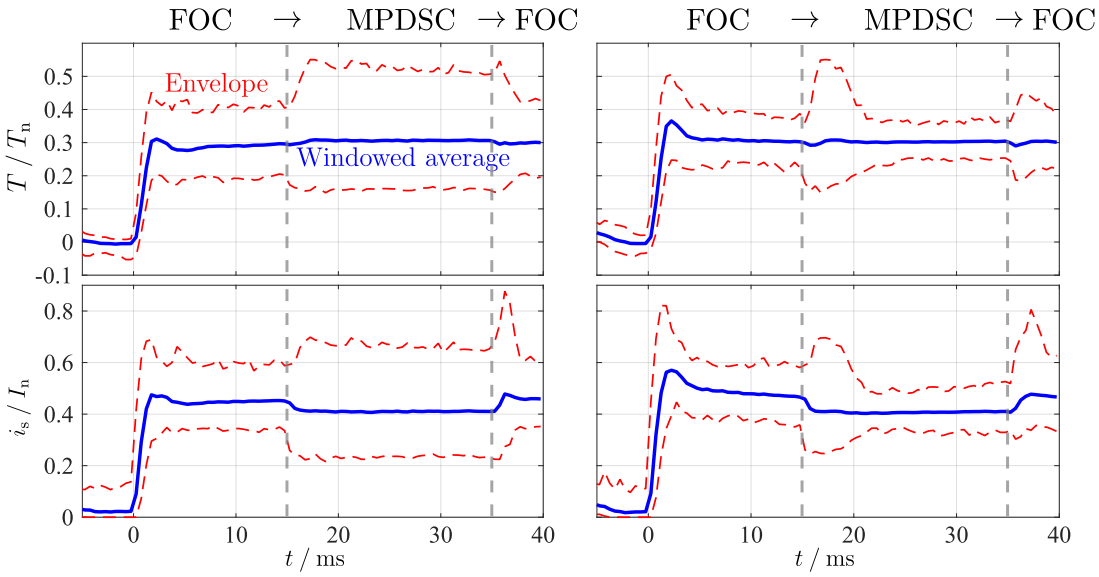


Fig. 6.7: Steady-state performance of MPDSC and FOC with torque reference adaptation for Monte Carlo simulations in terms of the metrics (from top to bottom) (6.1) to (6.7). Green boxes highlight the strongest correlations.



(a) Without observer (b) With observer

Fig. 6.8: Time evolution of torque (top) and current amplitude (bottom) average, maximum and minimum values across all Monte Carlo simulations with (a) unmodified reference, and (b) adapted torque reference

disturbance has negligible influence on either control strategy. In contrast, the low-frequency oscillation induces an oscillatory torque response in MPDSC. This effect arises from variations in flux amplitude under these conditions, which are fed to the operating point selection mechanism responsible for generating the load angle reference via an LPF. The filtering introduces a lag in the selected load angle with respect to its instantaneous appropriate value.

6.1.4.2 Speed

Since these control methods are dedicated solely to torque regulation, the mechanical shaft speed evolves according to the connected load. Consequently, variations in this variable are expected and must be appropriately managed. Due to the rotational inertia of the load in the final application, changes in mechanical speed are generally slow. In this analysis, a maximum rate of change of $2n_n/s$ is considered.

The quasi-step change response is illustrated in Fig. 6.11, where MPDSC demonstrates significantly better recovery following a speed increase compared to FOC, while the effect of a speed decrease is less pronounced in FOC. The responses to oscillatory speed disturbances at $f_{dis} = f_m/10$ and $f_{dis} = f_m$, with amplitudes selected to comply with the specified maximum rate of change, are presented in the left and right columns of Fig. 6.12, respectively. Here MPDSC exhibits a more stable response, even under conditions where the oscillations strongly influence the resulting torque, compared to FOC, for which the resulting torque even changes sign (cf. slow oscillation response, $t \approx 50\,\text{ms}$).

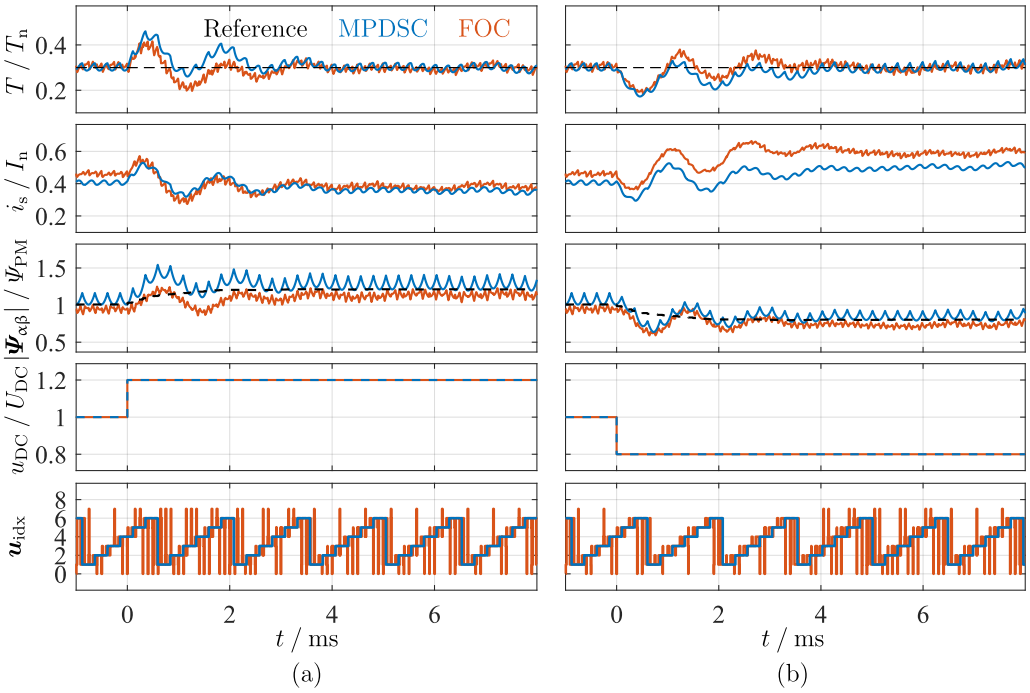


Fig. 6.9: Time response to a step up (a) and down (b) in DC-bus voltage. From top to bottom: torque, current amplitude, flux amplitude, DC-bus voltage, and switching state index

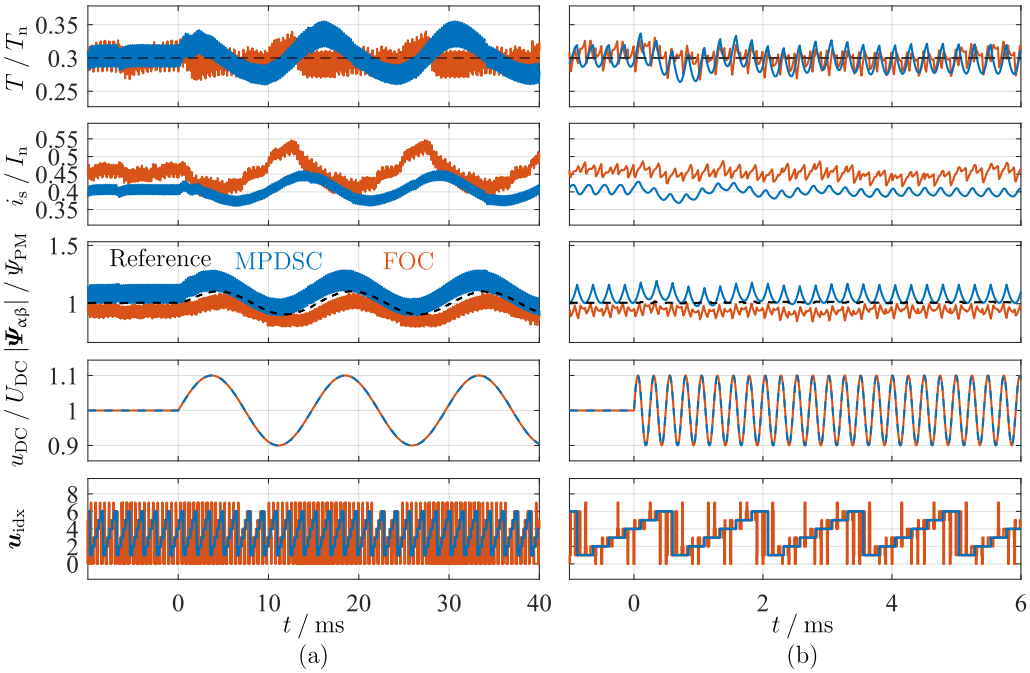


Fig. 6.10: Time response to slow (a) and fast (b) sinusoidal disturbance in DC-bus voltage. From top to bottom: torque, current amplitude, flux amplitude, DC-bus voltage, and switching state index

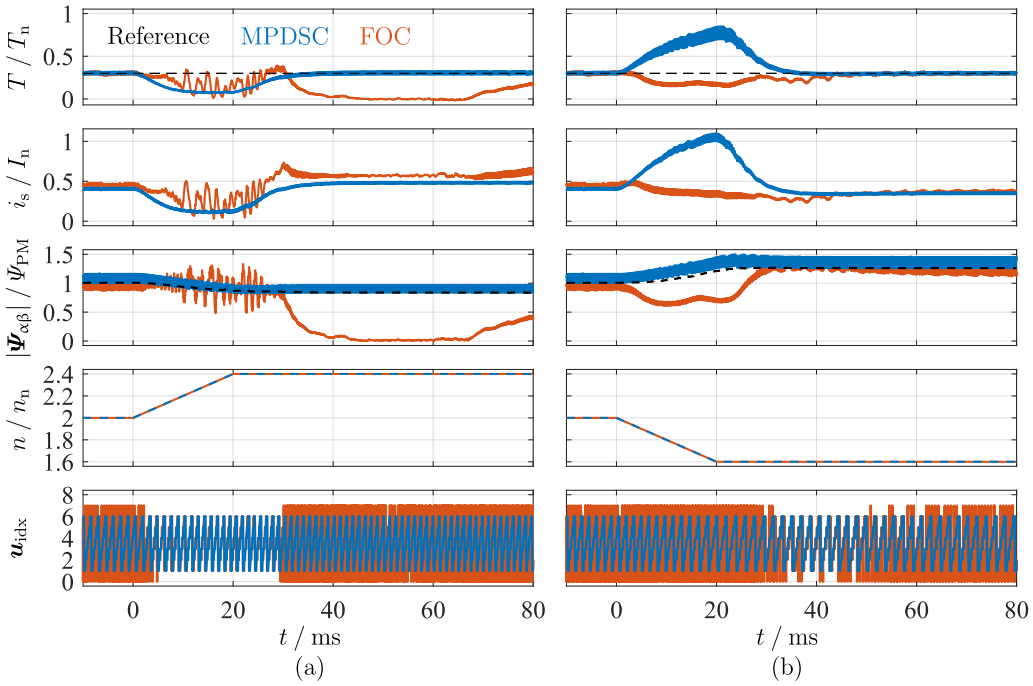


Fig. 6.11: Time response to ramp up (a) and down (b) changes in speed. From top to bottom: torque, current amplitude, flux amplitude, speed, and switching state index

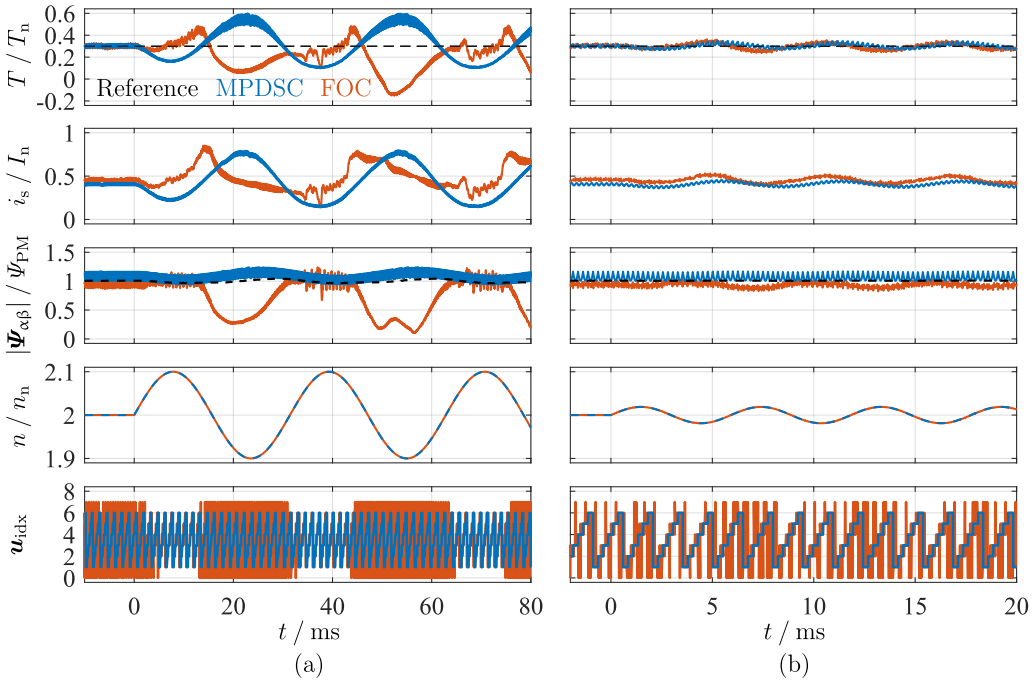


Fig. 6.12: Time response to slow (a) and fast (b) sinusoidal disturbances in speed. From top to bottom: torque, current amplitude, flux amplitude, speed, and switching state index

6.2 Experimental Results

The simulation analysis allows for the direct incorporation of multiple modifications to the model with which the controller interacts. In experimental evaluation, however, such alterations to the machine are not feasible, and the controller parameters are kept constant to ensure comparability between tests. Nevertheless, the experimental results presented throughout the other chapters provide practical evidence of the system's robustness against minor parameter estimation errors in the drive model. Sensor noise is also inherently present within the measurement chain, from sensing to sampling. It has been shown that sudden changes in the operating point cause short-term deviations in the DC-bus voltage and speed, which are subsequently compensated as the corresponding control systems adapt to the new operating conditions. Moreover, several examples of speed transients have been discussed, further demonstrating the system's robustness to mechanical disturbances.

Further experimental evidence of the system's performance under sensor noise and DC-bus voltage variations is presented in Fig. 6.13 and Fig. 6.14, respectively. For safety reasons, the testbench implementation was not subjected to disturbances of the same magnitude as those applied in simulation. The results in Fig. 6.13 indicate that increased noise in the DC-bus voltage measurement and rotor angle has a large impact on the MPDSC control variables. The effect on torque tracking is more difficult to evaluate, as the normal operation already exhibits a wide spread of values, largely independent of the introduced noise. Nonetheless, the control strategy maintains system operation within acceptable limits. For the DC-bus voltage transients shown in Fig. 6.14, the controller demonstrates an appropriate response to the applied disturbances, consistent with the results obtained in the previous section.

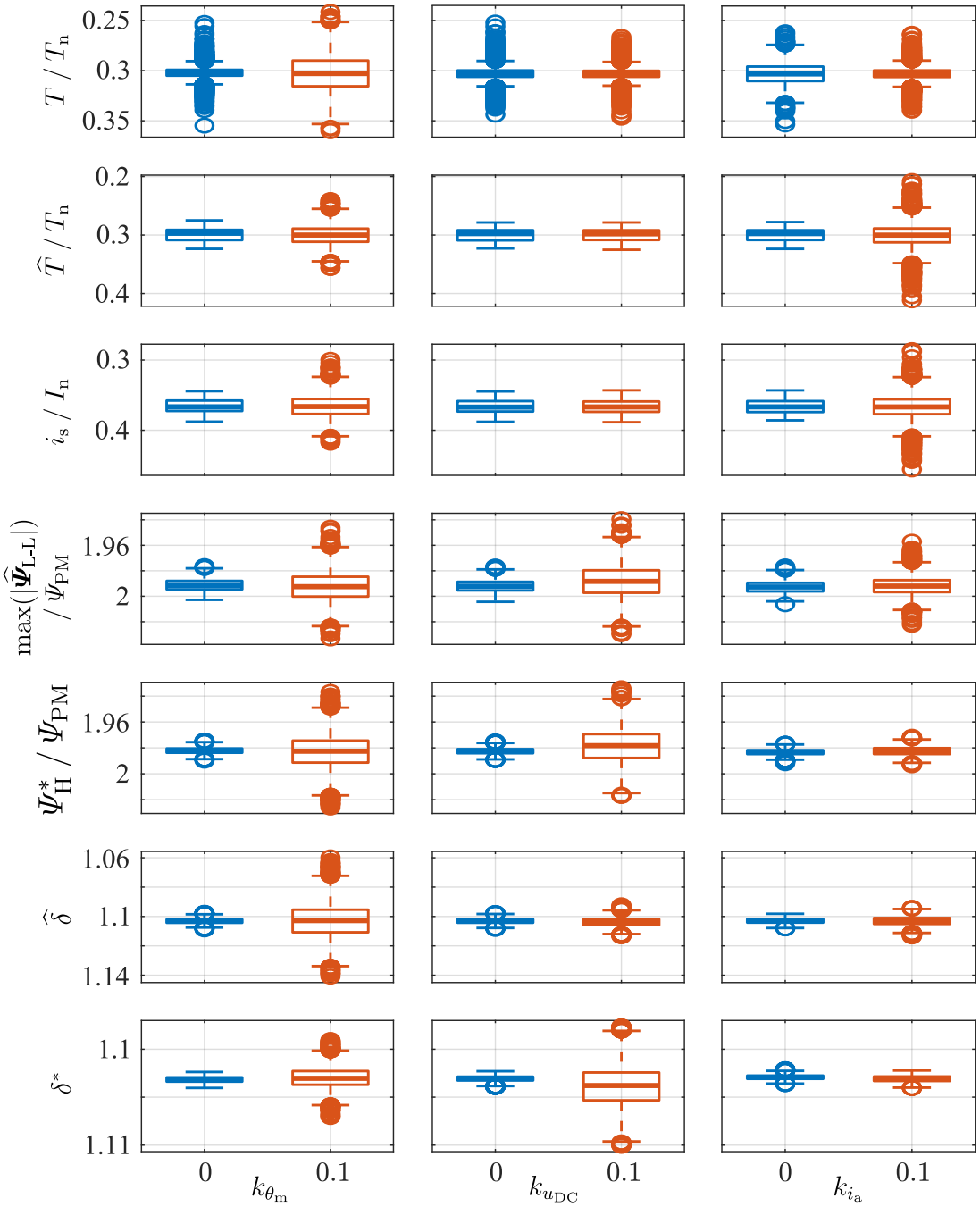


Fig. 6.13: Experimental steady-state MPDSC results with (orange) and without (blue) sensor noise injection in (from left to right) angle, DC voltage, and current measurement, in terms of (from top to bottom) torque, estimated torque, current amplitude, line-to-line flux amplitude, flux reference, estimated load angle, and load angle reference. Operating point $n = 1.8n_\mathrm{n}$, $T^* = 0.3T_\mathrm{n}$

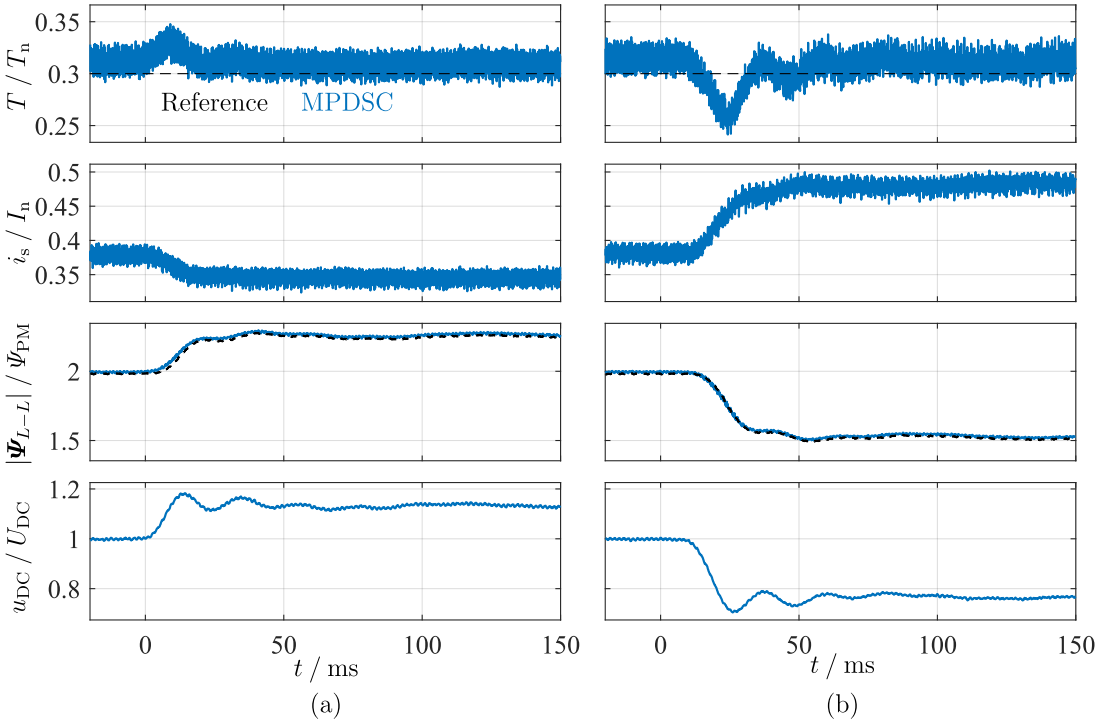


Fig. 6.14: Experimental results of MPDSC response to DC-bus voltage disturbance injection for voltage increase (a) and decrease (b). From top to bottom: torque, current amplitude, line-to-line flux amplitude, and DC-bus voltage. Operating point $n = 1.8n_n$, $T^* = 0.3T_n$

6.3 Summary

This chapter examines how parameter estimation errors, sensor noise, and external disturbances affect MPDSC, using targeted tests and Monte Carlo simulations to assess robustness under realistic conditions. The analysis showed that deviations in PM flux and d-axis inductance challenge the operating-point selection, but a torque-reference adaptation based on online torque estimation substantially reduced these errors. Noise on the DC-bus voltage was also found to influence torque tracking and flux estimation. While FOC generally delivered better torque tracking, MPDSC remained stable under combined disturbances and maintained acceptable performance. Future improvements may focus on more adaptive operating-point selection and broader comparisons with alternative overmodulation and six-step control strategies.

7 Conclusions

This work has developed, analyzed, and validated through simulation and experimental results a complementary control strategy to FOC for maximum voltage utilization of PMSM drives. The proposed MPDSC strategy enables six-step operation in the flux-weakening range while maintaining computational efficiency, real-time feasibility, dynamic performance, and robustness comparable to conventional FOC.

A literature review revealed the limitations of existing methods for maximum voltage utilization, particularly in relation to the challenging conditions of highly utilized drives. Additionally, industrial standard favors maintaining FOC for the linear modulation range due to its established methodology, suitable dynamic performance, robustness, and reliability. Accordingly, MPDSC was developed as a complementary strategy, conceptualized as a discrete-time modification of DSC to achieve six-step operation while retaining FOC as the primary strategy for linear modulation operation.

The MPDSC framework integrates an MPFC scheme regulating the stator flux trajectory in stationary coordinates, a load-angle controller ensuring stability across operating points and accurate reference tracking, an operating-point selection mechanism accounting for machine nonlinearities, and a flux estimation scheme providing accurate feedback closed loop control. Together, these elements enable effective torque control with maximum voltage utilization, yielding an increase peak torque and power performance, and lower copper losses for partial load operation.

A fade-over strategy was introduced to ensure smooth transitions between FOC and MPDSC. By independently controlling flux amplitude and load-angle, the transition was achieved without significant torque or current deviations, even under dynamic speed changes. MPDSC has also been enhanced through the incorporation of three-fold switching patterns. This extension underlines the potential for generalizing MPDSC to accommodate diverse flux modulation patterns, reducing ripple in current and torque, and tailoring drive behavior according to performance objectives.

Finally, practical robustness under realistic, nonideal conditions was addressed. Monte Carlo simulations and experimental evaluations confirmed that MPDSC remains stable despite parameter deviations, measurement noise, inverter non-linearities, and environmental disturbances.

The following main conclusions can be extracted from this work:

- Operating at the voltage limit is simplified by using flux control instead of current control. In the stationary reference frame, the flux–voltage relationship is largely independent of machine parameters, making the flux trajectory easy to predict. This is exploited here in the MPFC and for load angle ripple compensation. Related work that leverages the same principle includes [26], which enhances MPC to handle six-step harmonics, and [31], which extends deadbeat control to incorporate the flux trajectory.
- Considering the load angle as the controlled variable instead of a torque controller prevents potential instability when the torque derivative with respect to flux changes sign, which can occur at low load for high-salience machines or at low flux after the MTPF point. However, for a given flux amplitude, the load angle's dependence on the torque reference is highly sensitive to PM flux variations.
- The presented algorithm can operate with a very low number of measurement samples per electrical rotation (up to three), thanks to its inherent robustness, the predictive nature of the MPFC, and the use of load angle prediction for control. Furthermore, this feature is achieved with arbitrary sampling instants, not requiring the synchronization with the switching events.
- Using a MPFC approach with switching time as the actuating variable, rather than only triggering different voltage vectors instantaneously as in [34] or typical FCS applications, avoids variability in the hexagonal flux path. The resulting steady-state operating point is highly robust, with deviations below 2 % of the ideal six-step operation in terms of variation in switching intervals.
- The proposed strategy, utilizing six-step operation, achieves 12.5 % increase in voltage utilization in steady state with respect to the baseline FOC, which maintains a 2 % voltage margin with the linear voltage limit.
- The method discussed in this work achieves dynamic response and real-time implementation turnaround time similar to those of the industry standard FOC.
- The fade-over to FOC demonstrates the viability of the strategy as a complementary addition to industry standard.
- The inclusion of alternative switching patterns enables the introduction of optimal pulse patterns to achieve objectives beyond maximum voltage utilization.
- While conventional FOC exhibited superior torque tracking in some scenarios, MPDSC maintained acceptable performance under severe stress, demonstrating its practical viability. Torque reference adaptation and robust operating-point selection were shown to significantly mitigate the impact of parameter uncertainties.

7.1 Outlook

Future work may focus on several avenues to enhance the practical applicability and performance of MPDSC:

- Robust operating-point selection: Developing adaptive, system-identification-based algorithms to reduce sensitivity to parameter deviations and nonlinearities would improve torque-tracking accuracy and reliability. This could be achieved using system identification methods that leverage the excitation inherent in six-step operation and account for drive nonlinearities, as in [43]. Incorporating additional optimization criteria, such as iron-loss minimization, could further enhance efficiency.
- Transition logic enhancement: The developed transition between FOC and MPDSC provides a reliable changeover between the two control strategies. Further improvements could focus on reducing sensitivity to machine parameters, measurement noise, and transient fluctuations in the variables used in the transition criteria (e.g.,magnetic flux linkage amplitude). This could be achieved through appropriately designed filtering, careful tuning of the parameters (e.g., hysteresis threshold values) according to the specific drive conditions, or supervisory logic to prevent undesired or repeated switching under rapidly changing operating conditions.
- Generalized flux modulation: Extending MPDSC to support flux modulation patterns beyond six-step and three-fold switching could enable simultaneous optimization of efficiency, torque ripple, and harmonic content across the full operating range. Similar approaches [31] have been developed concurrently to this work toward the same goal.

  The consideration of optimal switching patterns through their effect on the flux trajectory is explored in [49] (see Fig. 7.1 (a)). Such flux patterns can be treated as line-to-line flux references, as done for three-fold operation, aiming to realize MPDSC for general flux patterns. For ease of implementation, simplifying constraints could include:
  - Symmetry between highlighted sectors (with respect to line-to-line axes, cf. Fig. 7.1 (b))
  - Symmetry within each sector (with respect to abc-axes, cf. Fig. 7.1 (b))
  - Modulation only between adjacent voltage vectors (e.g., in sector I, between vectors 2 and 3; in sector II, between vectors 3 and 4)
  - Voltage at the intersection of the flux path with line-to-line axes coinciding with the six-step sequence voltage
  - Switch-over points between possible trajectories occurring at the intersection of the flux path with line-to-line axes

  The algorithm can retain the proposed controller structure by determining the outer amplitude of the flux path via the load angle controller. Modifications are required to account for different switching-event cases (1, 3, 5, ... corners) and for switching-time calculation. Several options can be considered, e.g., as illustrated in Fig. 7.2:
  (a) Feed-forward calculation of the full switching sequence, triggered by detection of the first threshold. Times to reach various line-to-line flux references are then evaluated, and the full sequence is determined using flux pattern symmetry, analogous to three-fold implementation.
  (b) Recalculation of the switching sequence at each sampling instant, based on the current switching state, previously executed commands, and additional reference thresholds on other line-to-line axes not previously considered.

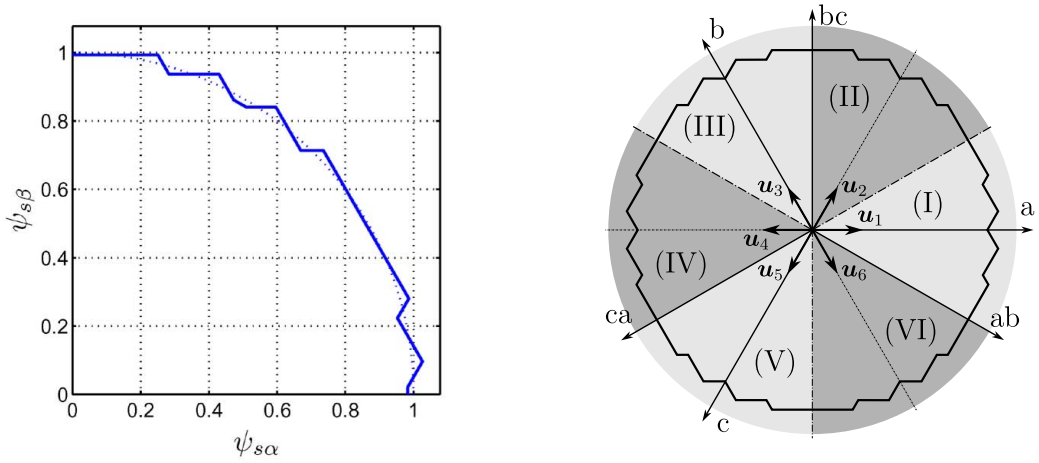


Fig. 7.1: (a) Consideration of optimal switching patterns via flux trajectory [49] and (b) diagram for proposed flux pattern consideration for MPDSC

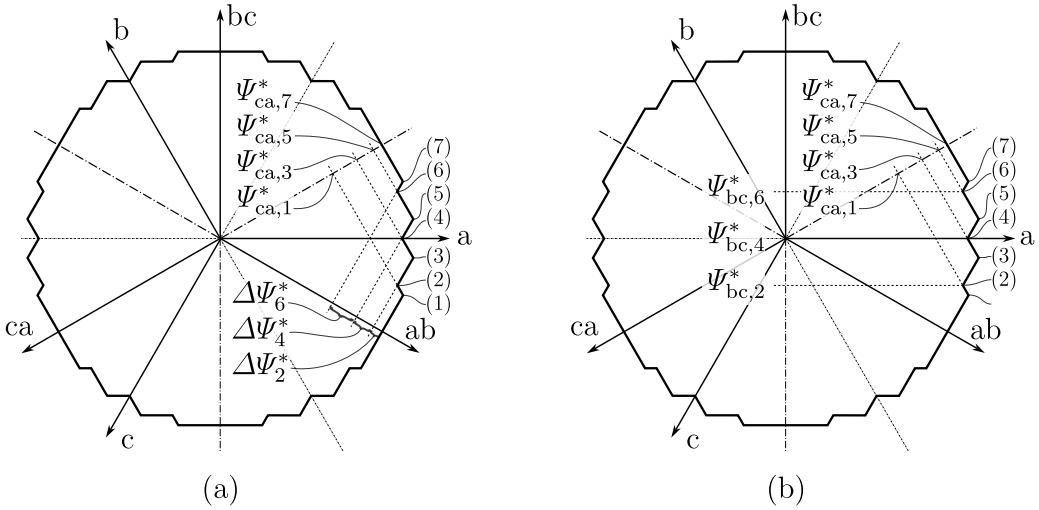


Fig. 7.2: Options for MPDSC general flux pattern switching sequence determination implementation

- Comparative evaluation: Systematic experimental comparison under a common drive setup with other maximum-voltage utilization strategies, including overmodulation and six-step PMSM control methods, would clarify trade-offs in robustness, efficiency, and dynamic performance, highlighting the most suitable approach for industrial adoption.

Bibliography

List of peer-reviewed publications with own contributions (OC)

[OC1] M. Peña, M. Meyer, O. Wallscheid, and J. Böcker, "Model predictive direct self-control for six-step operation of permanent-magnet synchronous machines," *IEEE Transactions on Power Electronics*, vol. 38, no. 10, pp. 12 416–12 429, 2023.

[OC2] M. Peña, M. Meyer, O. Wallscheid, and J. Böcker, "Fade-over strategy for use of model predictive direct self-control with field-oriented control," in *2023 IEEE International Electric Machines and Drives Conference (IEMDC)*, 2023, pp. 1–7.

References

[1] A. T. De Almeida, F. J. T. E. Ferreira, and J. A. Fong, "Standards for efficiency of electric motors," *IEEE Industry Applications Magazine*, vol. 17, no. 1, pp. 12–19, 2011.

[2] IEA, *Global ev outlook 2025*. [Online]. Available: https://www.iea.org/reports/global-ev-outlook-2025

[3] B. Şengül and H. Mostofi, "Impacts of e-micromobility on the sustainability of urban transportation—a systematic review," *Applied Sciences*, vol. 11, no. 13, 2021. [Online]. Available: https://www.mdpi.com/2076-3417/11/13/5851

[4] F. Blaschke, "The principle of field orientation as applied to the new transvector closed-loop control system for rotating-field machine," *Siemens review*, vol. 34, pp. 217–220, 1772.

[5] I. Takahashi and T. Noguchi, "A new quick-response and high-efficiency control strategy of an induction motor," *IEEE Transactions on Industry Applications*, vol. IA-22, no. 5, pp. 820–827, 1986.

[6] M. Depenbrock, "Direct self-control (dsc) of inverter-fed induction machine," *IEEE Transactions on Power Electronics*, vol. 3, no. 4, pp. 420–429, Oct. 1988.

[7] J. Holtz, "A predictive controller for the stator current vector of ac machines fed from a switched voltage source," *IPEC-Tokyo, 1983*, pp. 1665–1675, 1983.

[8] D. F. Schroder and R. Kennel, "Model-control promc—a new control strategy with microcomputer for drive applications," *IEEE Transactions on Industry Applications*, vol. IA-21, no. 5, pp. 1162–1167, Sep. 1985.

[9] P. Karamanakos, E. Liegmann, T. Geyer, and R. Kennel, "Model predictive control of power electronic systems: Methods, results, and challenges," *IEEE Open Journal of Industry Applications*, vol. 1, pp. 95–114, 2020.

[10] M. Schenke, B. Haucke-Korber, and O. Wallscheid, "Finite-set direct torque control via edge-computing-assisted safe reinforcement learning for a permanent-magnet synchronous motor," *IEEE Transactions on Power Electronics*, vol. 38, no. 11, pp. 13 741–13 756, 2023.

[11] Y. Kwon, S. Kim, and S. Sul, "Six-step operation of pmsm with instantaneous current control," *IEEE Transactions on Industry Applications*, vol. 50, no. 4, pp. 2614–2625, Jul. 2014.

[12] I. Ralev, T. Lange, and R. W. De Doncker, "Wide speed range six-step mode operation of ipmsm drives with adjustable dc-link voltage," in *2014 17th International Conference on Electrical Machines and Systems (ICEMS)*, Oct. 2014, pp. 2987–2993.

[13] A. M. Khambadkone and J. Holtz, "Compensated synchronous pi current controller in overmodulation range and six-step operation of space-vector-modulation-based vector-controlled drives," *IEEE Transactions on Industrial Electronics*, vol. 49, no. 3, pp. 574–580, Jun. 2002.

[14] J. Liu, W. Zhang, F. Xiao, C. Lian, and S. Gao, "Six-step mode control of ipmsm for railway vehicle traction eliminating the dc offset in input current," *IEEE Transactions on Power Electronics*, vol. 34, no. 9, pp. 8981–8993, Sep. 2019.

[15] W. Peters, O. Wallscheid, and J. Böcker, "Optimum efficiency control of interior permanent magnet synchronous motors in drive trains of electric and hybrid vehicles," in *2015 17th European Conference on Power Electronics and Applications (EPE'15 ECCE-Europe)*, 2015, pp. 1–10.

[16] T. Huber, W. Peters, and J. Böcker, "Voltage controller for flux weakening operation of interior permanent magnet synchronous motor in automotive traction applications," *2015 IEEE International Electric Machines and Drives Conference (IEMDC)*, May 2015.

[17] W. Peters and J. Böcker, "Discrete-time design of adaptive current controller for interior permanent magnet synchronous motors (IPMSM) with high magnetic saturation," in *IECON 2013 - 39th Annual Conference of the IEEE Industrial Electronics Society*, IEEE, Nov. 2013, pp. 6608–6613.

[18] F. Briz, A. Diez, M. Degner, and R. Lorenz, "Current and flux regulation in field-weakening operation [of induction motors]," *IEEE Transactions on Industry Applications*, vol. 37, no. 1, pp. 42–50, Jan. 2001.

[19] T. Kwon, G. Choi, M. Kwak, and S. Sul, "Novel flux-weakening control of an ipmsm for quasi-six-step operation," *IEEE Transactions on Industry Applications*, vol. 44, no. 6, pp. 1722–1731, Nov. 2008.

[20] J. Holtz, W. Lotzkat, and A. M. Khambadkone, "On continuous control of pwm inverters in the overmodulation range including the six-step mode," *IEEE Transactions on Power Electronics*, vol. 8, no. 4, pp. 546–553, Oct. 1993.

[21] S. Bolognani and M. Zigliotto, "Novel digital continuous control of svm inverters in the overmodulation range," *IEEE Transactions on Industry Applications*, vol. 33, no. 2, pp. 525–530, Mar. 1997.

[22] Dong-Choon Lee and G-Myoung Lee, "A novel overmodulation technique for space-vector pwm inverters," *IEEE Transactions on Power Electronics*, vol. 13, no. 6, pp. 1144–1151, Nov. 1998.

[23] G. Narayanan and V. T. Ranganathan, "Extension of operation of space vector pwm strategies with low switching frequencies using different overmodulation algorithms," *IEEE Transactions on Power Electronics*, vol. 17, no. 5, pp. 788–798, Sep. 2002.

[24] S. Kim and J. Seok, "Maximum voltage utilization of ipmsms using modulating voltage scalability for automotive applications," *IEEE Transactions on Power Electronics*, vol. 28, no. 12, pp. 5639–5646, Dec. 2013.

[25] A. Brosch, O. Wallscheid, and J. Böcker, "Model predictive control of permanent magnet synchronous motors in the overmodulation region including six-step operation," *IEEE Open Journal of Industry Applications*, vol. 2, pp. 47–63, 2021.

[26] A. Brosch, O. Wallscheid, and J. Böcker, "Model predictive torque control for permanent- magnet synchronous motors using a stator- fixed harmonic flux reference generator in the entire modulation range," *IEEE Transactions on Power Electronics*, vol. 38, no. 4, pp. 4391–4404, 2023.

[27] J. Holtz, "Advanced pwm and predictive control—an overview," *IEEE Transactions on Industrial Electronics*, vol. 63, no. 6, pp. 3837–3844, 2016.

[28] P. Karamanakos and T. Geyer, "Guidelines for the design of finite control set model predictive controllers," *IEEE Transactions on Power Electronics*, vol. 35, no. 7, pp. 7434–7450, 2020.

[29] F. Toso, P. G. Carlet, A. Favato, and S. Bolognani, "On-line continuous control set mpc for pmsm drives current loops at high sampling rate using qpoases," in *2019 IEEE Energy Conversion Congress and Exposition (ECCE)*, 2019, pp. 6615–6620.

[30] G. Pei, L. Li, X. Gao, J. Liu, and R. Kennel, "Predictive current trajectory control for pmsm at voltage limit," *IEEE Access*, vol. 8, pp. 1670–1679, 2020.

[31] H. El Khatib, D. Gerling, and M. Saur, "Deadbeat flux vector control as a one single control law operating in the linear, overmodulation, and six-step regions with time-optimal torque control," *IEEE Open Journal of Industry Applications*, vol. 3, pp. 247–270, 2022.

[32] A. Tripathi, A. M. Khambadkone, and S. K. Panda, "Stator flux based space-vector modulation and closed loop control of the stator flux vector in overmodulation into six-step mode," *IEEE Transactions on Power Electronics*, vol. 19, no. 3, pp. 775–782, May 2004.

[33] M. S. Petit, B. Sarlioglu, R. D. Lorenz, B. S. Gagas, and C. W. Secrest, "Deadbeat flux vector control for dynamic six-step operation of synchronous machines," in *2019 IEEE Transportation Electrification Conference and Expo (ITEC)*, 2019, pp. 1–6.

[34] B. Han, J.-S. Lee, Y. Bak, and K.-B. Lee, "Six-step operation strategy for direct self-control method of interior permanent magnet synchronous motors based on torque angle," *J. Power Electron*, vol. 21, no. 9, pp. 1352–1364, Jul. 2021.

[35] A. Steimel, "Direct self-control and synchronous pulse techniques for high-power traction inverters in comparison," *IEEE Transactions on Industrial Electronics*, vol. 51, no. 4, pp. 810–820, Aug. 2004.

[36] A. Steimel and J. Wiesemann, "Further development of direct self control for application in electric traction," in *Proceedings of IEEE International Symposium on Industrial Electronics*, vol. 1, 1996, 180–185 vol.1.

[37] M. Janssen and A. Steimel, "Direct self control with minimum torque ripple and high dynamics for a double three-level GTO inverter drive," *IEEE Transactions on Industrial Electronics*, vol. 49, no. 5, pp. 1065–1071, Oct. 2002.

[38] C. Calleja, A. Lopez-de-Heredia, H. Gaztanaga, T. Nieva, and L. Aldasoro, "Validation of a modified direct-self control strategy for PMSM in railway-traction applications," *IEEE Transactions on Industrial Electronics*, vol. 63, no. 8, pp. 1–1, 2016.

[39] D. Seidl, D. Kaiser, and R. Lorenz, "One-step optimal space vector pwm current regulation using a neural network," in *Proceedings of 1994 IEEE Industry Applications Society Annual Meeting*, vol. 2, 1994, 867–874 vol.2.

[40] D. Schroeder and J. Böcker, *Elektrische Antriebe - Regelung von Antriebssystemen*, 5th ed. 2021. Berlin, Heidelberg : Springer Berlin Heidelberg, 2021. [Online]. Available: https://dx.doi.org/10.1007/978-3-662-62700-6

[41] W. Peters, O. Wallscheid, and J. Böcker, "A precise open-loop torque control for an interior permanent magnet synchronous motor (ipmsm) considering iron losses," in *IECON 2012 - 38th Annual Conference on IEEE Industrial Electronics Society*, 2012, pp. 2877–2882.

[42] M. Meyer, *Wirkungsgradoptimierte Regelung hoch ausgenutzter Permanentmagnet-Synchronmaschinen im Antriebsstrang von Automobilen [Elektronische Ressource]*. 2010, Paderborn, Univ., Diss., 2010, Open Access.

[43] A. Brosch, O. Wallscheid, and J. Böcker, "Long-term memory recursive least squares online identification of highly utilized permanent magnet synchronous motors for finite-control-set model predictive control," *IEEE Transactions on Power Electronics*, vol. 38, no. 2, pp. 1451–1467, 2023.

[44] P. Jansen and R. Lorenz, "A physically insightful approach to the design and accuracy assessment of flux observers for field oriented induction machine drives," in *Conference Record of the 1992 IEEE Industry Applications Society Annual Meeting*, IEEE, 1992, 570–577 vol.1.

[45] C. Rettner, G. Jacob, M. Schiedermeier, A. Apelsmeier, and M. März, "Voltage ripple analysis based on dc-link current harmonics for voltage source inverters," in *2019 20th Workshop on Control and Modeling for Power Electronics (COMPEL)*, 2019, pp. 1–6.

[46] R. E. Kalman, "A new approach to linear filtering and prediction problems," *Journal of Basic Engineering*, vol. 82, no. 1, pp. 35–45, Mar. 1960.

[47] X. Wang, M. Fu, and H. Zhang, "Target tracking in wireless sensor networks based on the combination of kf and mle using distance measurements," *IEEE Transactions on Mobile Computing*, vol. 11, no. 4, pp. 567–576, 2012.

[48] M. D. McKay, R. J. Beckman, and W. J. Conover, "A comparison of three methods for selecting values of input variables in the analysis of output from a computer code," *Technometrics*, vol. 21, no. 2, pp. 239–245, 1979. Accessed: Oct. 16, 2025. [Online]. Available: http://www.jstor.org/stable/1268522

[49] T. Geyer, N. Oikonomou, G. Papafotiou, and F. D. Kieferndorf, "Model predictive pulse pattern control," *IEEE Transactions on Industry Applications*, vol. 48, no. 2, pp. 663–676, Mar. 2012.

Appendix

A Simulation Setup

The drive model and control task are implemented in MATLAB Simulink according to the diagram in Fig. A.1, with a variable-step size (i.e., emulating continuous time) and the control task triggered at fixed frequency. It consists of

- Control task: triggered every T_s, with sampled inputs and zero-order-hold outputs.
- Pulse generation: further details are given in Sec. A.2. It transforms the switching time commands ($\boldsymbol{t}^*_{\mathrm{s,abc}}$) into switching pulse commands for each of the semiconductors ($\boldsymbol{s}_{\mathrm{abc}}$).
- Inverter model: full details are given in Sec. A.3. It includes safety interlock dead-time effects, as well as the corresponding passive rectifier operation during the off-state of the semiconductors.
- The machine model is implemented according to Sec. A.1.

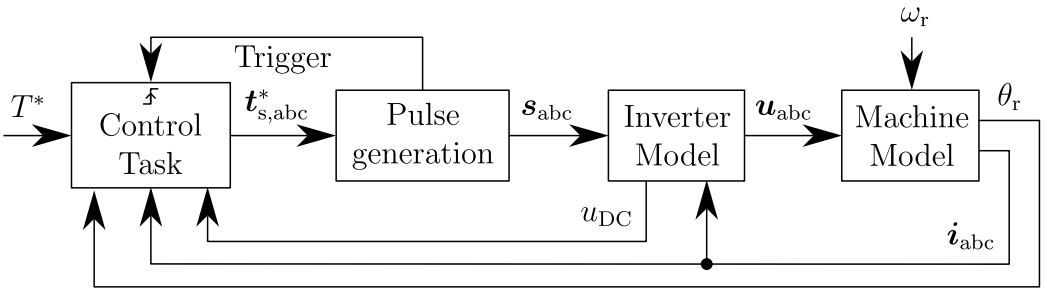


Fig. A.1: Schematic representation of the simulation model for evaluation

A.1 Machine Model for Simulation Evaluation

The machine model for simulation evaluation is represented in Fig. A.2. It takes as input the inverter voltages and mechanical speed, and outputs the torque, phase currents, and rotor angle signals. The speed is considered as an external input. Internally, the machine model is implemented in the dq-reference frame, interfaced with its inputs and outputs through reference frame transformations.

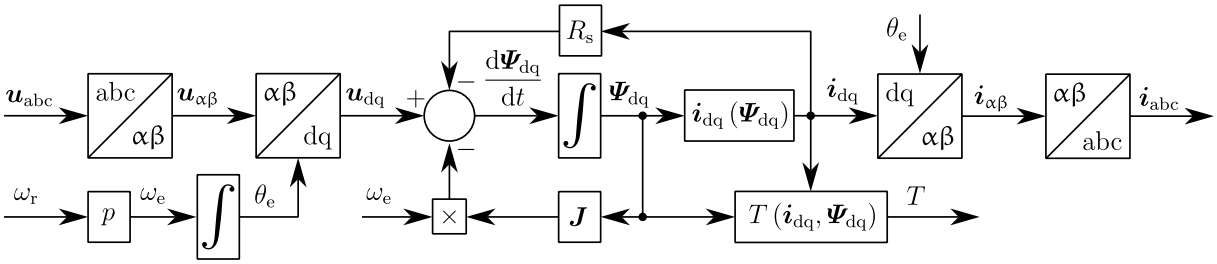


Fig. A.2: Schematic representation of the machine model for simulation evaluation

The magnetic behavior is encoded in the current-to-flux relationship $\boldsymbol{i}_{\mathrm{dq}}(\boldsymbol{\Psi}_{\mathrm{dq}})$, implemented with 2D-LUTs considering (cross-)saturation. The flux maps can be seen in Fig. 2.5. The lump parameters of the drive model are summarized in Tab. A.1.

PMSM Rated Values and Parameters					
Nominal torque	T_{n}	310 Nm	Stator phase resistance	R_{s}	3.3 mΩ
Nominal power	P_{n}	160 kW	d-axis inductance	L_{d}	79 µH
Nominal speed	n_{n}	5000 min^{-1}	q-axis inductance	L_{q}	151 µH
Maximum current	I_{max}	840 A	Permanent magnet flux	Ψ_{PM}	45 mVs
Pole pairs	N_{p}	4			
Inverter and controller					
DC-link voltage		U_{DC}			320 V
Controller update frequency		f_{s}			10 kHz

Tab. A.1: PMSM, inverter, and controller parameters

A.2 Pulse Generation for Simulation Evaluation

The switching pulses are generated by an S-function, emulating the behavior of the pulse generation module. This enables the accurate placement of simulation steps in a quasi-continuous environment at the precise instant in which the pulse edge should occur. It takes as input the switching times commanded by the control strategy $\boldsymbol{t}^*_{\mathrm{s,abc}}$ and outputs the switching pulse commands for each of the semiconductors $\boldsymbol{s}_{\mathrm{abc}}$ as well the trigger signal for the execution of the control task. For an accurate depiction of the inverter delay, this effect is also included in the switching pulse generation, despite formally being part of the inverter model. Its functionality is summarized in Fig. A.3.

A.3 Inverter Model for Simulation Evaluation

The inverter feeding the stator circuit is controlled via the switching commands $s_{p,\mathrm{up}}, s_{p,\mathrm{down}} \in \{0, 1\}$, with $p \in \{\mathrm{a,b,c}\}$. For each, zero switching command states are

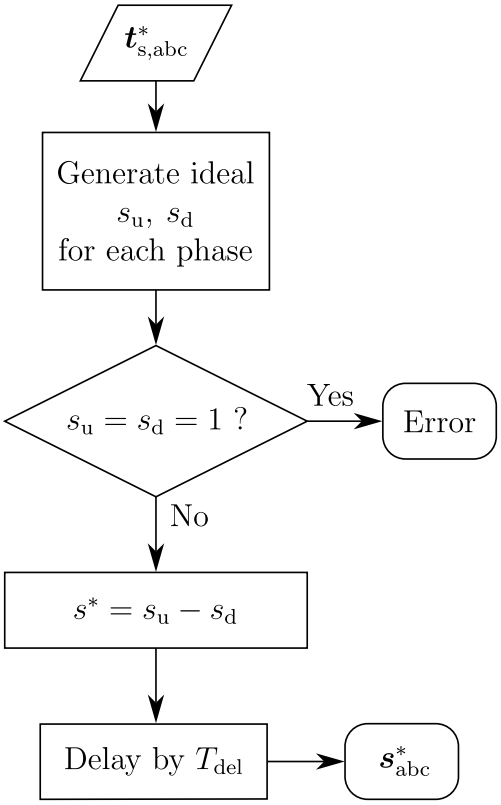


Fig. A.3: Switch pulse generation implemented in S-function. Time indexes are omitted for simplicity.

considered to avoid short circuiting the DC bus, with $s_p = s_{p,\mathrm{up}} - s_{p,\mathrm{down}},\ s_p \in \{-1, 0, 1\}$. The switching pulse commands from the pulse generation are processed to ensure sufficient dead-time between active opposite leg states as Fig. A.4.

During the zero-command state (i.e., both semiconductors in one inverter leg are off) the voltage is set according to the passive rectifier behavior through the anti parallel diodes. Thus, in the inverter model,

$$\text{if } s_p \neq 0 \ : \ u_p = s_p u_{\mathrm{DC}}/2, \tag{A.1a}$$

$$\text{if } s_p = 0 \ : \ u_p = -\mathrm{sign}(i_p) u_{\mathrm{DC}}/2. \tag{A.1b}$$

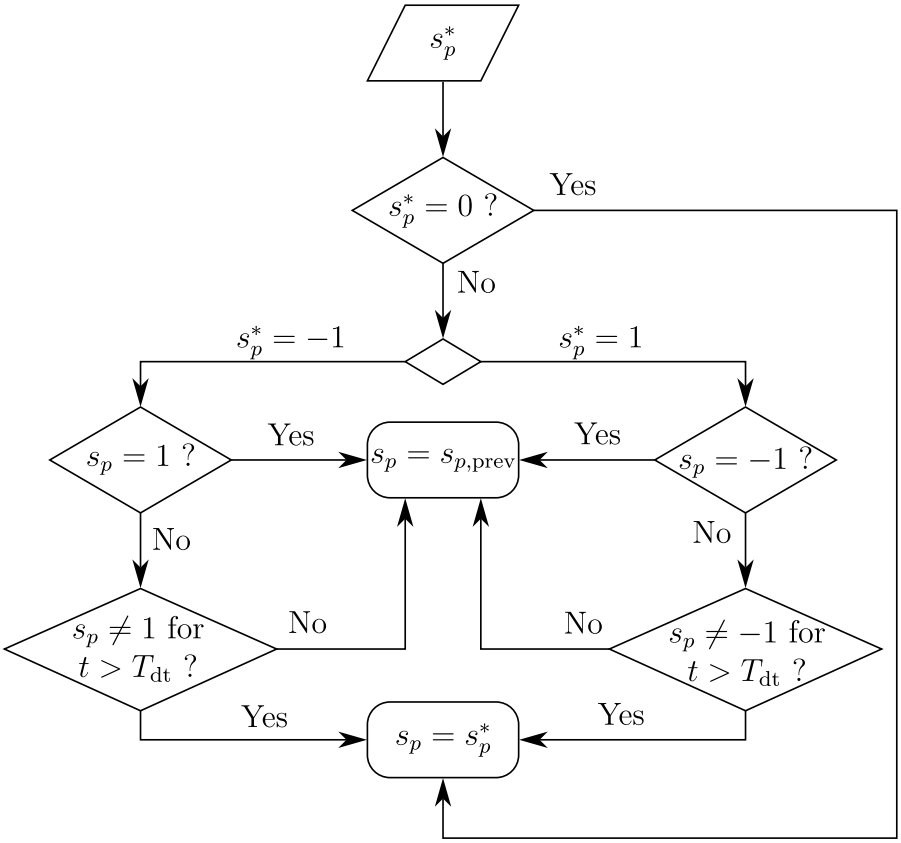


Fig. A.4: Delay and dead-time implemented in quasi-continuous time. Time indexes are omitted for simplicity.

B Experimental Evaluation

The electrical drive system under test is a highly utilized IPMSM intended for a traction application (see rated parameters in Tab. A.1) with a two-level IGBT inverter equipped with current transducers. The load is a speed-controlled IM, mechanically coupled with the test motor. The control strategy was implemented in a rapid-control-prototyping (RCP) system. Most measurements shown in this document are recorded through the analog-to-digital converters (ADC) of the RCP system, which are synchronized with the control task and executed at a fixed frequency of 10 kHz. Additionally, measurements from current and differential voltage probes were captured in an oscilloscope for observation of high-frequency phenomena, sampling at 5 MHz. Lastly, the testbench is equipped with a torque transducer, whose measurements are only relevant for steady-state analysis due to the limited bandwidth of the sensor and mechanical resonance at the shaft's connection. For transient behavior analysis, the estimated torque from the stored machine data and dq-current operating point is used. The test bench is shown in Fig. B.1, and the specific equipment and specifications for each of the systems described above is given in Tab. B.1.

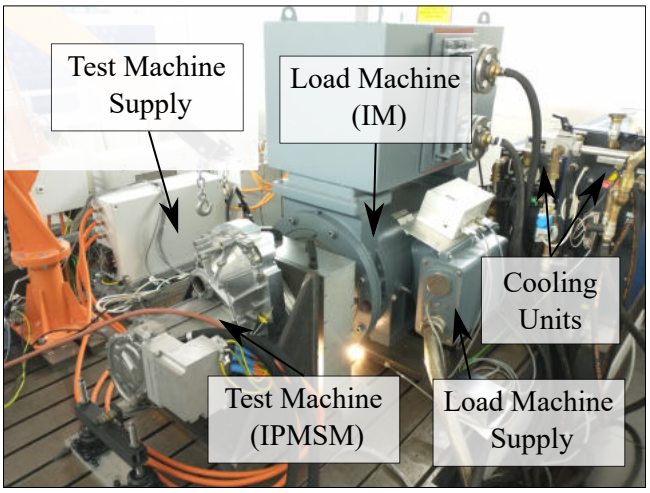


Fig. B.1: Test bench setup for experimental evaluation

System	Equipment	Specifications
Load machine (IM)	Schorch LU8250M-AZ83Z-Z	$n_{\max} = 12000\,\mathrm{min}^{-1}$
Two-level IGBT inverter	Semikron 3xSkiiP 1242GB120-4D	$f_{\mathrm{switching}} = 10\,\mathrm{kHz}$
RCPs (test and load drives)	dSPACE DS1006MC	$f_{\mathrm{sampling}} = 10\,\mathrm{kHz}$
Torque transducer	HBM-T10FS	
Oscilloscope	Yokogawa DL850	$f_{\mathrm{sampling}} = 5\,\mathrm{MHz}$
Current probes	Iwatsu SS-270	
Differential voltage probes	Bumblebee 1000V CAT III	

Tab. B.1: Testbench systems

The DC-link current must be limited to 500 A due to the testbench implementation. This restriction, with the range of DC-bus voltage values used for the tests (approx. 320 V), prevents MTPF operation in the deep flux-weakening range for the studied machine.

The control method implemented for the experimental evaluation was not fully identical to the approach described in this document. Several minor enhancements were introduced at a later stage of the investigation. However, before the experimental tests with the fully updated implementation could be completed, the machine became unavailable. These enhancements are relatively minor in scope and were incorporated primarily to ensure completeness in the algorithm description and to adopt more formally accurate methodologies. An example of the effect of the modifications upon MPDSC torque transient control and FOC steady-state operation is shown in Fig. B.2 and B.3, respectively. Specifically, the modifications include:

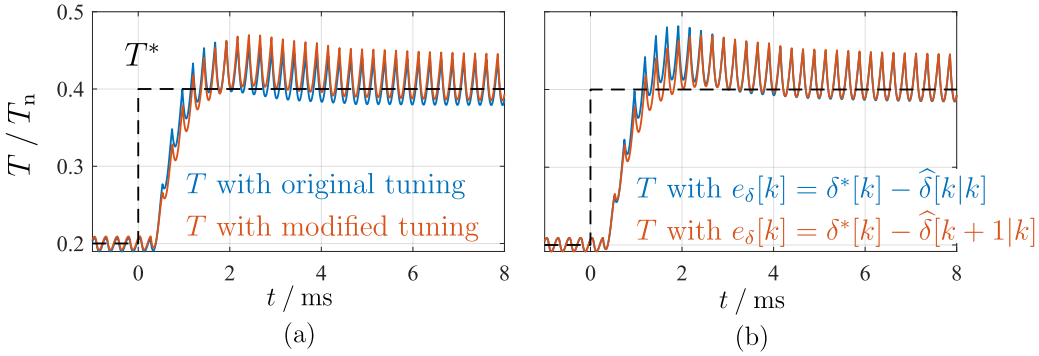


Fig. B.2: Effect of the changes introduced for MPDSC control in terms of (a) load angle controller tuning and (b) usage of load angle estimation or prediction for control

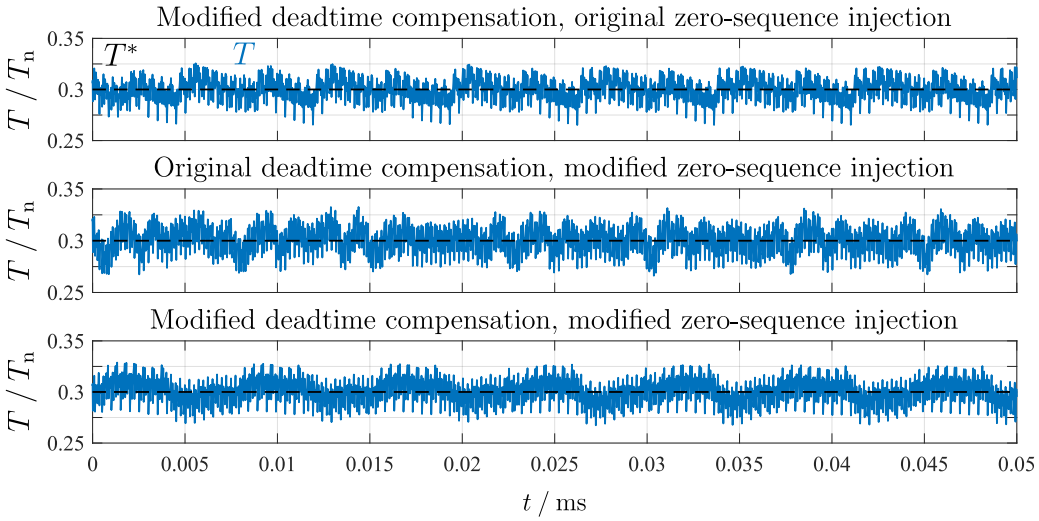


Fig. B.3: Effect of the changes introduced for FOC control in terms of deadtime compensation and zero-sequence injection

- Retuning of the load angle controller gains, from the original $K_\mathrm{P} = -1.9 \cdot 10^3\,\mathrm{s}^{-1}$ and $K_\mathrm{I} = -6 \cdot 10^4\,\mathrm{s}^{-2}$, which were based on a similar analysis to the one discussed in Sec. 3.2.2.2 and then further adapted empirically.
- Use of the predicted load angle in place of the estimated load angle as the controlled variable for load-angle control.
- Minor adjustments to the dead-time compensation strategy and the corresponding voltage estimation.
- Application of flat-top modulation with zero-sequence component injection for FOC.

C Voltage estimation algorithm

Algorithm C.1 Voltage estimation for each phase

Inputs: $\boldsymbol{t}_\mathrm{s}^*$, $i[k]$, $\widehat{i}[k+1]$, $s_\mathrm{u,last}$, $s_\mathrm{d,last}$, $t_\mathrm{u,last}$, $t_\mathrm{d,last}$, u_res
Outputs: $\widehat{u}$, $s_\mathrm{u,last}$, $s_\mathrm{d,last}$, $t_\mathrm{u,last}$, $t_\mathrm{d,last}$, u_res

1: Generate reference switching sequence $\boldsymbol{s}_\mathrm{u}^*$, $\boldsymbol{s}_\mathrm{d}^*$ for "up" and "down" semiconductor with corresponding $\boldsymbol{t}_\mathrm{u}^*, \boldsymbol{t}_\mathrm{d}^*$ following $\boldsymbol{t}_\mathrm{s}^* < T_\mathrm{s}$

2: To each "up" and "down" sequence, add the previous last state and last state, i.e.
$\boldsymbol{s}_\mathrm{u/d}^* \leftarrow [s_\mathrm{u/d,last},\ \boldsymbol{s}_\mathrm{u/d}^*,\ \boldsymbol{s}_\mathrm{u/d}^*(\mathrm{end})]$
$\boldsymbol{t}_\mathrm{u/d}^* \leftarrow [t_\mathrm{u/d,last},\ \boldsymbol{t}_\mathrm{u/d}^*,\ T_\mathrm{s}]$

3: Defining evaluated semiconductor $e \leftarrow u$, and complementary semiconductor $c \leftarrow d$
For each t_e **in** $\boldsymbol{t}_\mathrm{e}^*$ **with** $0 < t_\mathrm{e} < T_\mathrm{s}$:
Identify t_c as last $\boldsymbol{t}_\mathrm{c}^*$ with $t_\mathrm{c} \leq t_\mathrm{e}$
Identify s_c as last $\boldsymbol{s}_\mathrm{c}^*(t_\mathrm{c})$
If $\boldsymbol{s}_\mathrm{e}^*(t_\mathrm{e}) = 0$: Set $\boldsymbol{s}_\mathrm{e}(t_\mathrm{e}) = 0$
Else if $\boldsymbol{s}_\mathrm{e}^*(t_\mathrm{e}) = 1$:
If $s_\mathrm{c} = 1$: Ignore $\boldsymbol{s}_\mathrm{e}^*(t_\mathrm{e})$
Else if $s_\mathrm{c} = 0$:
If $t_\mathrm{e} \geq t_\mathrm{c} + T_\mathrm{dt}$: Set $\boldsymbol{s}_\mathrm{e}(t_\mathrm{e}) = 1$
Else if $t_\mathrm{e} < t_\mathrm{c} + T_\mathrm{dt}$:
If $t_\mathrm{e,next} \leq t_\mathrm{c} + T_\mathrm{dt}$: Ignore $\boldsymbol{s}_\mathrm{e}^*(t_\mathrm{e})$ and $\boldsymbol{s}_\mathrm{e}^*(t_\mathrm{e,next})$
Else if $t_\mathrm{e,next} > t_\mathrm{c} + T_\mathrm{dt}$: Set $\boldsymbol{s}_\mathrm{e}(t_\mathrm{c} + T_\mathrm{dt}) = 1$
End if
End if
End if
End if
End for

4: Defining evaluated semiconductor $e \leftarrow d$, and complementary semiconductor $c \leftarrow u$, repeat 3.

5: Remove redundant switching commands from $\boldsymbol{s}_\mathrm{u}$ and $\boldsymbol{s}_\mathrm{d}$

6: Replace, for both up and down semiconductors, $\boldsymbol{s}_\mathrm{u/d}(t < 0)$ with last state $\boldsymbol{s}_\mathrm{u/d}(t < 0)$ at $t = 0$, i.e.,
$\boldsymbol{s}_\mathrm{u/d}(0) \leftarrow \text{last } \boldsymbol{s}_\mathrm{u/d}(t < 0)$
$\boldsymbol{s}_\mathrm{u/d} \leftarrow \boldsymbol{s}_\mathrm{u/d}(t \geq 0)$

7: Store $s_\mathrm{u/d,last} \leftarrow \boldsymbol{s}_\mathrm{u/d}[\mathrm{end}]$; $t_\mathrm{u/d,last} \leftarrow \boldsymbol{t}_\mathrm{u/d}[\mathrm{end}] - T_\mathrm{s}$

1: Combine and order $\boldsymbol{t}_\mathrm{u}$ and $\boldsymbol{t}_\mathrm{d}$ into $\boldsymbol{t}_\mathrm{s}$; initialize $\widehat{u} \leftarrow u_\mathrm{res}$; $u_\mathrm{res} \leftarrow 0$
For each t **in** $\boldsymbol{t}_\mathrm{s}[:\mathrm{end}-1]$:
If $s = \boldsymbol{s}_\mathrm{u}(t) = \boldsymbol{s}_\mathrm{d}(t) = 1$: Trigger error
Else:
$s = \boldsymbol{s}_\mathrm{u}(t) - \boldsymbol{s}_\mathrm{d}(t)$
If $s = 0$:
$i_\mathrm{s} = i[k] + \dfrac{\widehat{i}[k+1] - i[k]}{T_\mathrm{s}} \dfrac{t + t_\mathrm{next}}{2}$
If $i_\mathrm{s} \geq 0$: Set $s = -1$
Else if $i_\mathrm{s} < 0$: Set $s = 1$
End if
End if
If $t_\mathrm{next} \leq T_\mathrm{s} - T_\mathrm{del}$:
$\widehat{u} \leftarrow \widehat{u} + s \dfrac{t_\mathrm{next} - t}{T_\mathrm{s}} \dfrac{u_\mathrm{DC}}{2}$
Else if $t_\mathrm{next} > T_\mathrm{s} - T_\mathrm{del}$:
$u_\mathrm{res} \leftarrow u_\mathrm{res} + s \dfrac{t_\mathrm{next} - t}{T_\mathrm{s}} \dfrac{u_\mathrm{DC}}{2}$
If $t < T_\mathrm{s} - T_\mathrm{del}$:
$\widehat{u} \leftarrow \widehat{u} + s \dfrac{T_\mathrm{s} - T_\mathrm{del} - t}{T_\mathrm{s}} \dfrac{u_\mathrm{DC}}{2}$
End if
End if
End if
End for
2: Store u_res

D Fade Over Logic Truth Tables

$c_{\text{ini}}[k]$	$c_{\text{FE}}[k]$	$c_{\text{angle}}[k]$	$c_{\text{time,1}}[k]$	$c_{\text{to}}[k]$
0	-	-	-	0
1	0	-	-	0
1	1	1	-	1
1	1	0	1	1
1	1	0	0	$c_{\text{to}}[k-1]$

Tab. D.1: Fade over logic for the generation of the c_{to} signal

$c_{\text{to}}[k]$	$c_{\Psi,\text{to}}[k]$	$c_{\Psi,\text{from}}[k]$	$c_{\text{aux}}[k]$
0	-	0	$c_{\text{aux}}[k-1]$
0	-	1	0
1	0	-	$c_{\text{aux}}[k-1]$
1	1	-	1

Tab. D.2: Fade over logic for the generation of the c_{aux} signal

$c_{\text{aux}}[k]$	$c_{angle}[k]$	$c_{\text{time,2}}[k]$	$c_{\text{from}}[k]$
1	-	-	1
0	1	-	0
0	0	1	0
0	0	0	$c_{\text{from}}[k-1]$

Tab. D.3: Fade over logic for the generation of the c_{from} signal

E Switching Criteria Modification for ZVI

$c_\mathrm{i}[k-1]$	$c_\mathrm{i}[k]$	$t^*_{\mathrm{i,H,on}}$	$t^*_{\mathrm{i,H,off}}$	$t^*_{\mathrm{i,L,on}}$	$t^*_{\mathrm{i,L,off}}$	Condition	Sequence
0	0	$T_\mathrm{s}+t_\mathrm{m}$	$-t_\mathrm{m}$	$-t_\mathrm{m}$	$T_\mathrm{s}+t_\mathrm{m}$		off
0	1	$t_{\mathrm{i,on}}[k]$	$-t_\mathrm{m}$	$-t_\mathrm{m}$	$t_{\mathrm{i,on}}[k]$	$t_\mathrm{ZVI} <= t_{\mathrm{i,on}}[k]$	off-on
		t_ZVI	$-t_\mathrm{m}$	$-t_\mathrm{m}$	t_ZVI	$t_\mathrm{ZVI} > t_{\mathrm{i,on}}(k)$	off-on
1	1	t_ZVI	$T_\mathrm{s}+t_\mathrm{m}$	$T_\mathrm{s}+t_\mathrm{m}$	t_ZVI		off-on
1	0	t_ZVI	$t_{\mathrm{i,off}}[k]$	$t_{\mathrm{i,off}}[k]$	t_ZVI	$t_\mathrm{ZVI} <= t_{\mathrm{i,off}}[k]$	off-on-off
		$T_\mathrm{s}+t_\mathrm{m}$	$-t_\mathrm{m}$	$-t_\mathrm{m}$	$T_\mathrm{s}+t_\mathrm{m}$	$t_\mathrm{ZVI} > t_{\mathrm{i,off}}[k]$	off

Tab. E.1: Switching time command generation according to switching criteria and switching times in each phase for zero voltage injection from initial switching states 1 3 and 5, i.e., zero-voltage state 0

$c_\mathrm{i}(k-1)$	$c_\mathrm{i}(k)$	$t^*_{\mathrm{i,H,on}}$	$t^*_{\mathrm{i,H,off}}$	$t^*_{\mathrm{i,L,on}}$	$t^*_{\mathrm{i,L,off}}$	Condition	Sequence
0	0	$-t_\mathrm{m}$	t_ZVI	t_ZVI	$-t_\mathrm{m}$		on-off
0	1	Not valid, use state 0 instead (Tab. E.1)				$t_\mathrm{ZVI} <= t_{\mathrm{i,on}}(k)$	on-off-on
		$-t_\mathrm{m}$	$T_\mathrm{s}+t_\mathrm{m}$	$T_\mathrm{s}+t_\mathrm{m}$	$-t_\mathrm{m}$	$t_\mathrm{ZVI} > t_{\mathrm{i,on}}(k)$	on
1	1	$-t_\mathrm{m}$	$T_\mathrm{s}+t_\mathrm{m}$	$T_\mathrm{s}+t_\mathrm{m}$	$-t_\mathrm{m}$		on
1	0	$-t_\mathrm{m}$	$t_{\mathrm{i,off}}(k)$	$t_{\mathrm{i,off}}(k)$	$-t_\mathrm{m}$	$t_\mathrm{ZVI} <= t_{\mathrm{i,off}}(k)$	on-off
		$-t_\mathrm{m}$	t_ZVI	t_ZVI	$-t_\mathrm{m}$	$t_\mathrm{ZVI} > t_{\mathrm{i,off}}(k)$	on-off

Tab. E.2: Switching time command generation according to switching criteria and switching times in each phase for zero voltage injection from initial switching states 2 4 and 6, i.e., zero-voltage state 7

F Machine Parameter Deviations

The following shows the derivation of the machine model for consideration of deviations in the machine PM flux, inductances and resistances. The machine model is implemented in simulation in a quasi-continuous environment as

$$\boldsymbol{\Psi}_\mathrm{dq}(t) = \int \left(\boldsymbol{u}_\mathrm{dq}(t) - R_\mathrm{s}\boldsymbol{i}_\mathrm{dq}(\boldsymbol{\Psi}_\mathrm{dq}(t)) - \boldsymbol{J}\omega_\mathrm{e}(t)\boldsymbol{\Psi}_\mathrm{dq}(t)\right)\mathrm{d}t, \tag{F.2}$$

with $\boldsymbol{i}_\mathrm{dq}(\boldsymbol{\Psi}_\mathrm{dq})$ implemented via LUTs encoding the magnetic saturation. For considering the deviation in machine parameters, first a linear magnetic behavior is considered as

$$\boldsymbol{i}_{\mathrm{dq,0}}(\boldsymbol{\Psi}_{\mathrm{dq}}(t)) = \begin{bmatrix} \dfrac{\Psi_{\mathrm{d}}(t) - \Psi_{\mathrm{PM,0}}}{L_{\mathrm{d,0}}} \\ \dfrac{\Psi_{\mathrm{q}}(t)}{L_{\mathrm{q,0}}} \end{bmatrix} = \begin{bmatrix} i_{\mathrm{d,0}}(\Psi_{\mathrm{d}}(t)) \\ \\ i_{\mathrm{q,0}}(\Psi_{\mathrm{q}}(t)) \end{bmatrix}. \tag{F.3}$$

The bias Δ in parameters is defined as

$$\Psi'_{\mathrm{PM}} = \Psi_{\mathrm{PM,0}} + \Delta_{\Psi_{\mathrm{PM}}}, \quad \Delta_{\Psi_{\mathrm{PM}}} = \alpha_{\Psi_{\mathrm{PM}}} \Psi_{\mathrm{PM,0}}, \tag{F.4a}$$
$$L'_{\mathrm{d}} = L_{\mathrm{d,0}} + \Delta_{L_{\mathrm{d}}}, \qquad \Delta_{L_{\mathrm{d}}} = \alpha_{L_{\mathrm{d}}} L_{\mathrm{d,0}}, \tag{F.4b}$$
$$L'_{\mathrm{q}} = L_{\mathrm{q,0}} + \Delta_{L_{\mathrm{q}}}, \qquad \Delta_{L_{\mathrm{q}}} = \alpha_{L_{\mathrm{q}}} L_{\mathrm{q,0}}, \tag{F.4c}$$
$$R'_{\mathrm{s}} = R_{\mathrm{s,0}} + \Delta_{R_{\mathrm{s}}}, \qquad \Delta_{R_{\mathrm{s}}} = \alpha_{R_{\mathrm{s}}} R_{\mathrm{s,0}}, \tag{F.4d}$$

with the subscript 0 indicating the original lump parameters of the model and the superscript $'$ indicating the modified parameters. The flux-to-current mapping with the modified parameters results in

$$\begin{aligned} \boldsymbol{i}'_{\mathrm{dq}}(\boldsymbol{\Psi}_{\mathrm{dq}}(t)) &= \begin{bmatrix} \dfrac{\Psi_{\mathrm{d}}(t) - \Psi'_{\mathrm{PM}}}{L'_{\mathrm{d}}} \\ \dfrac{\Psi_{\mathrm{q}}(t)}{L'_{\mathrm{q}}} \end{bmatrix} = \begin{bmatrix} \dfrac{\Psi_{\mathrm{d}}(t) - (\Psi_{\mathrm{PM,0}} + \Delta_{\Psi_{\mathrm{PM}}})}{L_{\mathrm{d,0}} + \Delta_{L_{\mathrm{d}}}} \\ \dfrac{\Psi_{\mathrm{q}}(t)}{L_{\mathrm{q,0}} + \Delta_{L_{\mathrm{q}}}} \end{bmatrix} = \\ &\begin{bmatrix} \dfrac{(\Psi_{\mathrm{d}}(t) - \Delta_{\Psi_{\mathrm{PM}}}) - \Psi_{\mathrm{PM,0}}}{L_{\mathrm{d,0}} + \alpha_{L_{\mathrm{d}}} L_{\mathrm{d,0}}} \\ \dfrac{\Psi_{\mathrm{q}}(t)}{L_{\mathrm{q,0}} + \alpha_{L_{\mathrm{q}}} L_{\mathrm{q,0}}} \end{bmatrix} = \begin{bmatrix} \dfrac{(\Psi_{\mathrm{d}}(t) - \Delta_{\Psi_{\mathrm{PM}}}) - \Psi_{\mathrm{PM,0}}}{L_{\mathrm{d,0}}(1 + \alpha_{L_{\mathrm{d}}})} \\ \dfrac{\Psi_{\mathrm{q}}(t)}{L_{\mathrm{q,0}}(1 + \alpha_{L_{\mathrm{q}}})} \end{bmatrix} = \\ &\begin{bmatrix} i_{\mathrm{d,0}}(\Psi'_{\mathrm{d}}(t)) \dfrac{1}{1 + \alpha_{L_{\mathrm{d}}}} \\ \\ i_{\mathrm{q,0}}(\Psi'_{\mathrm{q}}(t)) \dfrac{1}{1 + \alpha_{L_{\mathrm{q}}}} \end{bmatrix}, \text{ with } \boldsymbol{\Psi}'_{\mathrm{dq}}(t) = \begin{bmatrix} \Psi'_{\mathrm{d}}(t) \\ \\ \Psi'_{\mathrm{q}}(t) \end{bmatrix} = \begin{bmatrix} \Psi_{\mathrm{d}}(t) - \Delta_{\Psi_{\mathrm{PM}}} \\ \\ \Psi_{\mathrm{q}}(t) \end{bmatrix}. \end{aligned} \tag{F.5}$$

Equivalently, the model including parameter deviations upon the nonlinear flux-to-current-mapping $\boldsymbol{i}_{\mathrm{dq,LUT}}(\boldsymbol{\Psi}_{\mathrm{dq}})$ is considered as

$$\boldsymbol{\Psi}_{\mathrm{dq}}(t) = \int \Big(\boldsymbol{u}_{\mathrm{dq}}(t) - R_{\mathrm{s}} \left(1 + \alpha_{R_{\mathrm{s}}}\right) \boldsymbol{i}'_{\mathrm{dq}}(\boldsymbol{\Psi}_{\mathrm{dq}}(t)) - \boldsymbol{J} \omega_{\mathrm{e}}(t) \boldsymbol{\Psi}_{\mathrm{dq}}(t) \Big) \mathrm{d}t, \tag{F.6a}$$

$$\boldsymbol{i}'_{\mathrm{dq}}(\boldsymbol{\Psi}_{\mathrm{dq}}(t)) = \begin{bmatrix} i_{\mathrm{d,LUT}} \left(\Psi_{\mathrm{d}}(t) - \alpha_{\Psi_{\mathrm{PM}}} \Psi_{\mathrm{PM,0}} \right) \dfrac{1}{1 + \alpha_{L_{\mathrm{d}}}} \\ \\ i_{\mathrm{q,LUT}} \left(\Psi_{\mathrm{q}}(t) \right) \dfrac{1}{1 + \alpha_{L_{\mathrm{q}}}} \end{bmatrix}. \tag{F.6b}$$

The effect of the parameter changes in L_{d}, L_{q}, and Ψ_{PM} on the current-to-flux maps are illustrated in Fig. F.1.

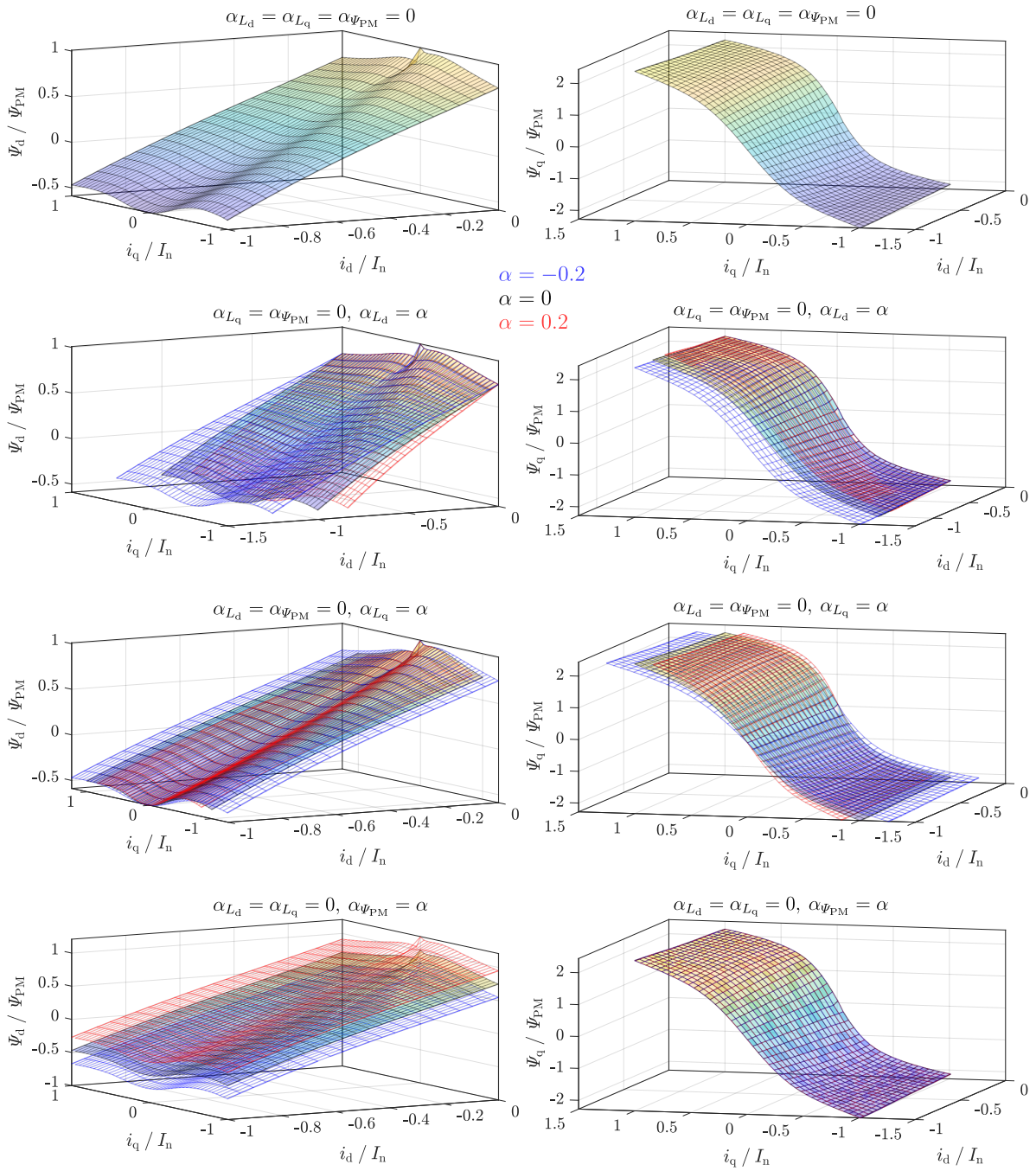


Fig. F.1: Effect of parameter changes in current-to-flux maps

Lists

List of Tables

2.1 Normalization values 11
2.2 Switching states 13

3.1 Switching criteria and switching times to be used in each phase according to rotation direction 32
3.2 Switching time command generation according to switching criteria and switching times in each phase 32
3.3 Switching time command generation according to switching criteria and switching times in each phase 37
3.4 Controller output depending on controller input sign and direction of rotation 38
3.5 Turnaround times for real-time implementation of MPDSC (μ is the mean value and σ is the standard deviation of the data collected) 56

4.1 Control strategy, reference setting and command selection according to fade-over logic 71

5.1 Effect of different choices of folding ratios. The resulting AC and DC current harmonic content depends on the specific application parameters and operating conditions. Therefore the value of k_f is not uniquely determined by the the desired effect. 83

A.1 PMSM, inverter, and controller parameters 126
B.1 Testbench systems 129
D.1 Fade over logic for the generation of the c_to signal 133
D.2 Fade over logic for the generation of the c_aux signal 133
D.3 Fade over logic for the generation of the c_from signal 133
E.1 Switching time command generation according to switching criteria and switching times in each phase for zero voltage injection from initial switching states 1 3 and 5, i.e., zero-voltage state 0 134
E.2 Switching time command generation according to switching criteria and switching times in each phase for zero voltage injection from initial switching states 2 4 and 6, i.e., zero-voltage state 7 134

List of Figures

1.1 Global electric car sales for battery electric vehicles (BEVs) and plug-in hybrid electric vehicles (PHEVs), 2014-2024 [2] 1
1.2 Operating regions for exemplary PMSM, highlighting the maximum torque and power output according to voltage utilization 3
1.3 Comparison of drives and control strategies used in the literature for six-step operation of PMSMs [OC1]: left - number of samples (each $T_s = 1/f_s$) per electrical revolution ($T_e = 1/f_e$); right - normalized current transient (with respect to I_{max}) achieved in one sampling period (T_s) when applying maximum voltage ($2u_{DC}/3$) considering nominal stator inductance (L_s) 7
1.4 Switching pulse generation by the DSC algorithm under ideal conditions in continuous time 8

2.1 Simplified diagram of an electric drive system 12
2.2 Three-phase two-level VSI 13
2.3 Operating regions and limits of inverter in the αβ-voltage plane 14
2.4 Single-pole PMSM schematic cross-section 15
2.5 Normalized d- (a) and q- (b) flux linkage maps 17
2.6 Operating regions of PMSMs in the dq-current plane 18
2.7 Simplified FOC control diagram 20
2.8 Modulation strategy for FOC 20
2.9 Flux control diagram for continuous-time implementation of DSC 21

3.1 Ideal flux path during six-step operation in PMSM 24
3.2 Torque relation with load angle depending on flux amplitude for the machine model considered, and example for higher saliency ratio 25
3.3 Event sequence for discrete-time implementation of MPDSC 27
3.4 Example of the switching pulse generation by the proposed MPFC. From top to bottom: ab-flux linkage (with reference, estimation, and prediction one and two-steps ahead), switching pulses in phases a, b, and c 27
3.5 Control diagram for torque control in the flux-weakening region with MPDSC 28
3.6 Model predictive flux control schematic 29
3.7 Switching pulse generation by the MPFC algorithm operating at 3.05 samples per electrical revolution. From top to bottom: ab-flux linkage, ab-switching condition, and switching pulses for phase b 30
3.8 Inverter leg diagram highlighting in red the current path (a) and dead-time compensation for turn-on (b) and turn-off (c) behavior depending on the PR operation. Desired switching behavior (top), necessary upper and lower semiconductor reference pulses for positive phase current (middle), and for negative phase current (bottom) 34
3.9 Load angle control diagram 35

3.10 Plant model for load angle controller tuning 35
3.11 Example MPFC response according to the instantaneous flux location when the new reference is applied 36
3.12 Control diagram depicting the control (G_{c}), plant (G_{plant}), open-loop (G_{OL}), and closed-loop (G_{CL}) transfer functions 37
3.13 Amplitude (top) and phase (bottom) frequency response of the open-loop transfer function for the whole range of speed and τ_{MPFC}, without (blue) and with (orange) the PI controller with the chosen zero location ($\tau_{\mathrm{n}} = 0.0092$) and $K_{\mathrm{p,c}} = 1$ 39
3.14 Crossover frequency of the open-loop transfer function (top) and maximum gain of the closed-loop transfer function (bottom) depending on the controller proportional gain, for the whole range of speed and τ_{MPFC} 40
3.15 Load angle reference generation diagram 41
3.16 Load angle reference generation LUT values with MTPF and MTPC loci . 42
3.17 Voltage and flux estimation and prediction diagram 43
3.18 Gopinath-style flux observer 44
3.19 Normalized flux path during six-step operation compared to its fundamental component 46
3.20 Load angle ripple estimation during six-step operation referred to the first sector of the flux hexagon trajectory 46
3.21 Phase voltage (a) and line-to-line flux (b) estimation and prediction (top), and error (bottom), during steady-state MPDSC operation. Operating point: $n = 1.5n_{\mathrm{n}}$, $T^* = 0.3T_{\mathrm{n}}$ 47
3.22 Steady-state torque (top left), load angle (bottom left), flux amplitude (top right), and switching state index (bottom right) response during steady-state MPDSC operation. Operating point: $n = 1.5n_{\mathrm{n}}$, $T^* = 0.3T_{\mathrm{n}}$. 48
3.23 Current trajectory in dq-coordinates during steady-state MPDSC operation. Operating point: $n = 1.5n_{\mathrm{n}}$, $T^* = 0.3T_{\mathrm{n}}$ 49
3.24 Contour of average current amplitude during MPDSC and FOC steady-state operation throughout all torque-speed operating points in the flux weakening region 49
3.25 Torque tracking response of MPDSC and FOC for motoring (top) and generating (bottom) operation for multiple torque reference step transitions (columns). Operating point: $n = 2n_{\mathrm{n}}$ 50
3.26 Torque tracking response of MPDSC and FOC in motoring operation for up (a) and down (b) step torque reference change. From top to bottom: torque, load angle, line-to-line flux amplitude, current amplitude, and switching state index. Operating point: $n = 2n_{\mathrm{n}}$ 52
3.27 Torque tracking response of MPDSC and FOC in generating operation for up (a) and down (b) step torque reference change. From top to bottom: torque, load angle, line-to-line flux amplitude, current amplitude, and switching state index. Operating point: $n = 2n_{\mathrm{n}}$ 53

3.28 Speed transient responses of MPDSC (solid) and FOC (semi-transparent) for a speed ramp up (a) and down (b). From top to bottom: speed, torque for full load (blue) in motoring operation, in generating operation, torque for partial load (orange) in motoring operation, and in generating operation 54
3.29 Switching interval estimation from line-to-line voltage measurements 56
3.30 Deviation from perfect six-step during steady-state operation in MPDSC . 57
3.31 Steady-state MPDSC operation at $2.2n_{\mathrm{n}}$ in the motoring region. From top to bottom, left column: torque, load angle, and line-to-line fluxes. From top to bottom, right column: line-to-line voltages, phase currents, and zoomed in view of line-to line fluxes. The line-to-line voltages and phase currents are measured at 5 MHz. 58
3.32 Steady-state MPDSC operation at $2n_{\mathrm{n}}$ in the motoring region. From top to bottom, left column: torque, load angle, and line-to-line flux. From top to bottom, right column: line-to line voltages, phase currents, and a-switching pulses. The line-to-line voltages, switching pulses, and phase currents are measured at 5 MHz. 58
3.33 Steady-state MPDSC operation at $2n_{\mathrm{n}}$ in the motoring region 59
3.34 Maximum and minimum achievable torque by MPDSC and FOC (limited to the linear modulation region) at a current amplitude $|\boldsymbol{i}_{\mathrm{dq}}| = 0.4I_{\max}$ for motoring (top) and generating (bottom) operation 59
3.35 Contour of fitted surface of average current amplitude during MPDSC and FOC steady-state operation for several torque-speed operating points in the flux weakening region 60
3.36 Torque transient in the motoring region for MPDSC and FOC at $1.6n_{\mathrm{n}}$. From top to bottom, left column: torque, load angle, and line-to-line fluxes. From top to bottom, right column: phase voltages, phase currents, and zoomed in view of line-to line fluxes. Phase currents and voltages are measured at 5 MHz. All variables refer to MPDSC unless otherwise stated. 61
3.37 Torque transient in the generating region during MPDSC and conventional FOC operation at $2.2n_{\mathrm{n}}$. From top to bottom, left column: torque, load angle, and line-to-line fluxes. From top to bottom, right column: phase voltages, phase currents, and zoomed in view of line-to line fluxes. Phase currents and voltages are measured at 5 MHz. All variables refer to MPDSC unless otherwise stated. 61
3.38 DC-bus voltage evolution during the torque transient response shown in Fig. 3.36 and 3.37 62
3.39 Response to speed ramp up (a) and down (b) in the motoring region during MPDSC and FOC operation at $T^* = 0.3T_{\mathrm{n}}$. From top to bottom: torque, current amplitude, and speed 62

4.1 Exemplary transition from FOC to MPDSC with an instantaneous switch-over (abrupt) and the proposed fade-over strategy, with the machine iso-torque, iso-current and iso-flux amplitude contours [OC2]. Operating point: $n = 2n_{\mathrm{n}}$, $T^* = 0.3T_{\mathrm{n}}$ 65

4.2 Overview of the control strategy for integration of MPDSC (green) with the systems introduced for fade-over operation (orange) and FOC (blue). The signal selection is done according to Tab. 4.1. 66

4.3 Decision trees for fade-over logic from FOC to MPDSC (a) and vice-versa (b), separated in i) generation of c_{to}, ii) generation of c_{aux}, and iii) generation of c_{from}. Equivalent truth tables are available in App. D. 67

4.4 Stator flux in the stationary reference frame during fade-over from FOC to MPDSC (a) and vice versa (b). The flux rotates counter-clockwise. SOT: start of transition, EOT: end of transition 69

4.5 Example operation of MPDSC with ZVI for accurate deadbeat load angle control (a) and for low ripple ZVI time (b). From top to bottom: torque, load angle, line-to-line flux, switching state index, and ZVI time 71

4.6 Simulation evaluation of the fade-over strategy from FOC to MPDSC (a) and from MPDSC to FOC (b) in terms of the dq-current paths. SOT: start of transition, EOT: end of transition. Operating point: $n = 2n_{\mathrm{n}}$, $T^* = 0.3T_{\mathrm{n}}$ 72

4.7 Simulation evaluation of the fade-over strategy from FOC to MPDSC (a) and from MPDSC to MPDSC (b). From top to bottom: flux amplitude, load angle, and switching state index and ZVI time. SOT: start of transition, EOT: end of transition. Operating point: $n = 2n_{\mathrm{n}}$, $T^* = 0.3T_{\mathrm{n}}$. 73

4.8 Experimental evaluation of the fade-over from FOC to MPDSC (a) and from MPDSC to FOC (b) in terms of the dq-current path. SOT: Start of transition, EOT: end of transition. Operating point: $n = 2n_{\mathrm{n}}$, $T^* = 0.3T_{\mathrm{n}}$. 74

4.9 Experimental evaluation of the fade-over from MPDSC to FOC (a) and from MPDSC to FOC (b). From top to bottom: flux amplitude, torque, and line-to-line voltage. SOT: start of transition, EOT: end of transition. Operating point: $n = 2n_{\mathrm{n}}$, $T^* = 0.3T_{\mathrm{n}}$ 75

4.10 Experimental evaluation of the fade-over from MPDSC to FOC (a) and from FOC to MPDSC (b) triggered by speed transients with $T^* = 0.6T_{\mathrm{n}}$ in terms of the dq-current path 76

4.11 Experimental evaluation of the fade-over from MPDSC to FOC (a) and from FOC to MPDSC (b) triggered by speed transients with $T^* = 0.6T_{\mathrm{n}}$. From top to bottom: torque, line-to-line flux amplitude, estimated load angle, and speed 76

5.1 Three-fold switching pattern analysis: (a) line-to-line flux and inverter leg states; (b) stator flux linkage trajectory 78

5.2 Normalized 18-corner flux trajectory analysis 78

5.3 Ripple with three-fold switching pattern according to k_{f}, in terms of the trajectory with respect to flux angle (a) and peak-to-peak ripple with respect to k_{f} (b) for the load angle (top) and the flux amplitude (bottom) . 79

5.4 Normalized fundamental (top left), 5^{th} and 7^{th} (top right), 11^{th} and 13^{th} (bottom left), and 17^{th} and 19^{th} (bottom right) harmonic components of the α-flux. The higher-order harmonics are equivalently present in the AC current according to (5.5). 80
5.5 Average value (μ) and harmonic content of the DC current for simplified scenario according to voltage-to-current angle and folding ratio 81
5.6 Control diagram for torque control in the flux-weakening region with MPDSC enhanced for three-fold switching 82
5.7 Diagram of three-fold reference generation 83
5.8 Example switching sequence for three-fold modulation 84
5.9 Switching events according to the comparison between line-to-line flux and flux references for three-fold operation 85
5.10 Special scenarios requiring modification of the switching sequence for three-fold operation 86
5.11 Example of the split of full switching sequence between the sampling periods of the switching horizon 87
5.12 Simulation steady-state operation example of MPDSC with multiple folding ratios at $n = 1.5n_{\text{n}}$, $T^* = 0.3T_{\text{n}}$. From top to bottom, left column: torque, load angle, flux amplitude. From top to bottom, right column: switching state index for various k_{f} values, and DC current 89
5.13 Simulation steady-state operation example of dq-current trajectory of MPDSC with multiple folding ratios at $n = 1.5n_{\text{n}}$ and $T^* = 0.3T_{\text{n}}$ 89
5.14 Simulation example of transition in MPDSC between six-step and three-fold modulation at $n = 2n_{\text{n}}$ and $T^* = 0.3T_{\text{n}}$. From top to bottom in (a): torque, line-to-line flux amplitude, and switching state index; (b) dq-current path; and (c) $\alpha\beta$-flux trajectory 90
5.15 Simulation torque transient example with MPDSC in the motoring region for up (a) and down (b) torque reference step with multiple folding ratios at $n = 1.8n_{\text{n}}$. From top to bottom: torque, load angle, line-to-line flux amplitude, current amplitude, DC current, and switching state index . . . 91
5.16 Simulation torque transient example with MPDSC in the generating region for down (a) and up (b) torque reference step with multiple folding ratios at $n = 1.8n_{\text{n}}$. From top to bottom: torque, load angle, line-to-line flux amplitude, current amplitude, DC current, and switching state index . 92
5.17 Steady-state three-fold operation with $k_{\text{f}} = 0.13$ at $2n_{\text{n}}$ in the motoring region. From top to bottom, left column: torque, line-to-line flux, and load angle. From top to bottom, right column: phase currents, a-switching pulses, and line-to line voltages. The line-to-line voltages, switching pulses, and phase currents are measured at 5 MHz. 93
5.18 Steady-state three-fold operation with $k_{\text{f}} = 0.13$ at $2n_{\text{n}}$ in the motoring region. The same operating point under six-step operation can be observed in Fig. 3.33. 94

5.19 Transition example from six-step to three-fold operation with $k_\mathrm{f} = 0.13$ at $2n_\mathrm{n}$ in the motoring region. From top to bottom: torque, phase currents, and line-to-line voltages. The line-to-line voltages and phase currents are measured at 5 MHz. 94
5.20 Torque transient example with six-step and three fold operation with $k_\mathrm{f} = 0.13$ at $2n_\mathrm{n}$ in the motoring region. From top to bottom (a): torque, line-to-line flux, and load angle. From top to bottom (b) only for the three fold operation and measured at 5 MHz: phase currents, a-switching pulses, and line-to line voltages 95

6.1 Baseline operating point for simulation-based robustness and disturbance rejection analysis. From top to bottom: torque, current amplitude, and flux linkage. Operating point $n = 2n_\mathrm{n}$, $T^* = 0.3T_\mathrm{n}$. Yellow boxes in (a) are detailed in (b) and (c), indicating the steady-state intervals for FOC and MPDSC. 99
6.2 Steady-state performance with machine parameter estimation errors (from top to bottom) in PM flux, d-inductance, q-inductance, and resistance, in terms of the metrics (from left to right) (6.1) to (6.7), with and without toque reference adaptation 101
6.3 Steady-state performance with estimation errors (from top to bottom) in inverter delay time and interlock deadtime, in terms of the metrics (from left to right) (6.1) to (6.7), with and without toque reference adaptation . 102
6.4 Steady-state performance with noise injection (from top to bottom) in DC voltage, angle, one current, and all current measurements, in terms of the metrics (from left to right) (6.1) to (6.7), with and without toque reference adaptation 104
6.5 Distribution of varied parameters for Monte Carlo simulations (from top to bottom, and from left to right) for PEE in PM flux, d-inductance, q-inductance, and stator resistance, sensor noise in phase currents, angle, and DC voltage measurement, and estimation errors in inverter delay and interlock deadtime. 105
6.6 Steady-state performance of MPDSC and FOC for Monte Carlo simulations in terms of the metrics (from top to bottom) (6.1) to (6.7). Green boxes highlight the strongest correlations. 107
6.7 Steady-state performance of MPDSC and FOC with torque reference adaptation for Monte Carlo simulations in terms of the metrics (from top to bottom) (6.1) to (6.7). Green boxes highlight the strongest correlations. 108
6.8 Time evolution of torque (top) and current amplitude (bottom) average, maximum and minimum values across all Monte Carlo simulations with (a) unmodified reference, and (b) adapted torque reference 109
6.9 Time response to a step up (a) and down (b) in DC-bus voltage. From top to bottom: torque, current amplitude, flux amplitude, DC-bus voltage, and switching state index 110

6.10 Time response to slow (a) and fast (b) sinusoidal disturbance in DC-bus voltage. From top to bottom: torque, current amplitude, flux amplitude, DC-bus voltage, and switching state index 110
6.11 Time response to ramp up (a) and down (b) changes in speed. From top to bottom: torque, current amplitude, flux amplitude, speed, and switching state index 111
6.12 Time response to slow (a) and fast (b) sinusoidal disturbances in speed. From top to bottom: torque, current amplitude, flux amplitude, speed, and switching state index 111
6.13 Experimental steady-state MPDSC results with (orange) and without (blue) sensor noise injection in (from left to right) angle, DC voltage, and current measurement, in terms of (from top to bottom) torque, estimated torque, current amplitude, line-to-line flux amplitude, flux reference, estimated load angle, and load angle reference. Operating point $n = 1.8n_{\mathrm{n}}$, $T^* = 0.3T_{\mathrm{n}}$ 113
6.14 Experimental results of MPDSC response to DC-bus voltage disturbance injection for voltage increase (a) and decrease (b). From top to bottom: torque, current amplitude, line-to-line flux amplitude, and DC-bus voltage. Operating point $n = 1.8n_{\mathrm{n}}$, $T^* = 0.3T_{\mathrm{n}}$ 114

7.1 (a) Consideration of optimal switching patterns via flux trajectory [49] and (b) diagram for proposed flux pattern consideration for MPDSC 118
7.2 Options for MPDSC general flux pattern switching sequence determination implementation 118

A.1 Schematic representation of the simulation model for evaluation 125
A.2 Schematic representation of the machine model for simulation evaluation . 126
A.3 Switch pulse generation implemented in S-function. Time indexes are omitted for simplicity. 127
A.4 Delay and dead-time implemented in quasi-continuous time. Time indexes are omitted for simplicity. 128
B.1 Test bench setup for experimental evaluation 129
B.2 Effect of the changes introduced for MPDSC control in terms of (a) load angle controller tuning and (b) usage of load angle estimation or prediction for control 130
B.3 Effect of the changes introduced for FOC control in terms of deadtime compensation and zero-sequence injection 130
F.1 Effect of parameter changes in current-to-flux maps 136